2014

# Electrochemical Reduction of CO2 on Supported Cu2O Catalysts

Joel Niño Galvez Bugayong
*Louisiana State University and Agricultural and Mechanical College*, jbugay1@lsu.edu

# ELECTROCHEMICAL REDUCTION OF $CO_2$ ON SUPPORTED $Cu_2O$ CATALYSTS

A Dissertation

Submitted to the Graduate Faculty of the
Louisiana State University and
Agriculture and Mechanical College
in partial fulfillment of the
requirements for the degree of
Doctor of Philosophy

in

The Department of Chemical Engineering

by
Joel Niño Galvez Bugayong
B.S., University of the Philippines Los Baños, 2004
M.S., Louisiana State University, 2011
December 2014

*This work is dedicated to my Mom who passed away in January of 2014.*

*You are deeply missed.*

# ACKNOWLEDGMENTS


Ph.D. Advisor
*Prof. Gregory L. Griffin*

Ph.D. Committee Members
*Prof. James J. Spivey*
*Prof. Robin L. McCarley*
*Prof. Francisco R. Hung*
*Prof. Krishnaswamy Nandakumar*
*(Prof. Martin Feldman)*

$CO_2$ Electrochemical Reduction Group (Experimentalist)
*Prof. John C. Flake*
*Prof. Richard L. Kurtz*
*Prof. Phillip T. Sprunger*
*Dr. Maoming Ren*
*Evan Andrews*
*Minh Le*
*Ziyu Zhang*
*Yuxin Fang*

Undergraduate Research Assistants
*Edward Alexander Thistlethwaite III*
*Diana A. Zacarias*
*Raymond Lam*
*Jason Haddad*
*Jon Wilson*
*Nicholas Ryan Abshire*
*Nick Grant Landwehr*
*Aamani Kura*

Staff Members of the Department of Chemical Engineering
*Joe Bell*
*Darla Dao*
*Danny Fontenot*
*Rachel Landry*
*Paul Rodriguez*
*Ellen Stevens*
*Robert Willis*

LSU Materials Characterization Center
*Dr. Congmei Cao*

My Family

*Dr. Patrisha J. Pham-Bugayong*
*Lorenzo Theodore P. Bugayong and future 2nd, 3rd or nth child*
*Adoracion C. Galvez-Bugayong*
*Rolando G. Bugayong*
*Jonathan G. Bugayong and family*
*Dr. Jennifer G. Bugayong-Luna and family*
*Ma. Joan G. Bugayong-Ocampo and family*
*Dr. Chay Binh Pham and Dr. Laura A. Julian-Pham*
*Alessandra J. Pham-Mondala and husband*

*Sunday*

*Fryday, Salmon, Mickey and Mouse*

*And to the Cornerstone, the Great I Am*

# TABLE OF CONTENTS

# ABSTRACT

We have examined Cu-based catalyst materials that enable the conversion of $CO_2$ to useful products such as fuels and chemical feedstocks by electrochemical reduction. In particular, we compared the electrocatalytic activity of supported $Cu_2O$ particles prepared using electrodeposition and wet chemical methods. The particles had cubic structure, ranging in size from 40 nm to 900 nm and consisting of low index planes. We observed significantly different product distribution on these catalysts compared to polycrystalline Cu, specifically for methane and ethylene formation. While Cu particles showed higher faradaic efficiency for methane formation compared to ethylene formation, we observed that $Cu_2O$ particles were more selective to ethylene than methane. For example, the $C_2H_4/CH_4$ ratio on Cu was 0.2 while the $C_2H_4/CH_4$ ratio on both electrodeposited $Cu_2O$ film and colloidal $Cu_2O$ particles was around 60.

The $Cu_2O$ particles were reducible and the derived particles consisted of higher number of low-coordinated active sites than Cu which we propose are responsible for the increased ethylene selectivity. At $-1.5V_{NHE}$, electrodeposited $Cu_2O$ film and colloidal $Cu_2O$ particles achieved highest average ethylene faradaic efficiency of 9.4% and 38% respectively while Cu foil only showed 1.2%. The colloidal $Cu_2O$ particles also exhibited better CO selectivity than Cu. While Cu showed 5.5% CO faradaic efficiency, colloidal $Cu_2O$ particles achieved highest average CO faradaic efficiency of 22%. Product distribution on $Cu_2O$ catalysts was primarily influenced by potential and was kinetically dynamic. Nafion mixed with $Cu_2O$ particles was shown to enhance and stabilize ethylene formation.

# CHAPTER 1
# CURRENT U.S. ENERGY STATUS AND OVERVIEW OF $CO_2$ ELECTROCHEMICAL REDUCTION

## 1.1. Introduction

Electrochemical conversion of $CO_2$ to liquid fuels and chemical feed stocks is an important research area aimed at developing feasible technologies that promote carbon neutral energy cycles (Lewis et al. 2006, Whipple et al. 2010). $CO_2$ is considered a greenhouse gas and though it only has a global warming potential (GWP) of 1 (compared to 25 for $CH_4$ and 298 for $N_2O$) (US Energy Information Administration | Emissions of Greenhouse Gases in the United States 2009), its impact in the environment is significant because of high emission rates from use of fossil fuel (coal, natural gas, crude oil).

Fossil fuels have dominated energy supply in the United States since 1973. In 2012, they accounted for 79% of total energy production and 82% of total energy consumption. In contrast, renewable sources accounted for only 11% of total energy production and 9% of total energy consumption (see Figure 1.1, 2012 Renewable Energy Data Book). Consequently, $CO_2$ emission rose from 4,735 million metric tons in 1975 to 6,023 million metric tons in 2007 (US Energy Information Administration 2013). $CO_2$ concentrations in the atmosphere also reached 390 ppm $CO_2$ in 2010, which is 39% above pre-industrial levels (IPCC Climate Change 2007: Synthesis Report).

Though production from renewable sources is increasing, our high dependence on fossil fuels will continue in the future because it remains the only reliable source that is able to meet our projected demand. If the use of fossil fuels is to continue, it is imperative that we develop commercially viable technologies that capture, store and recycle $CO_2$ waste. Studies by the Intergovernmental Panel on Climate Change suggest that in order to

maintain $CO_2$ atmospheric content to below 400 ppm, global $CO_2$ emissions must decrease by 50-80% from the level reported in 2000.

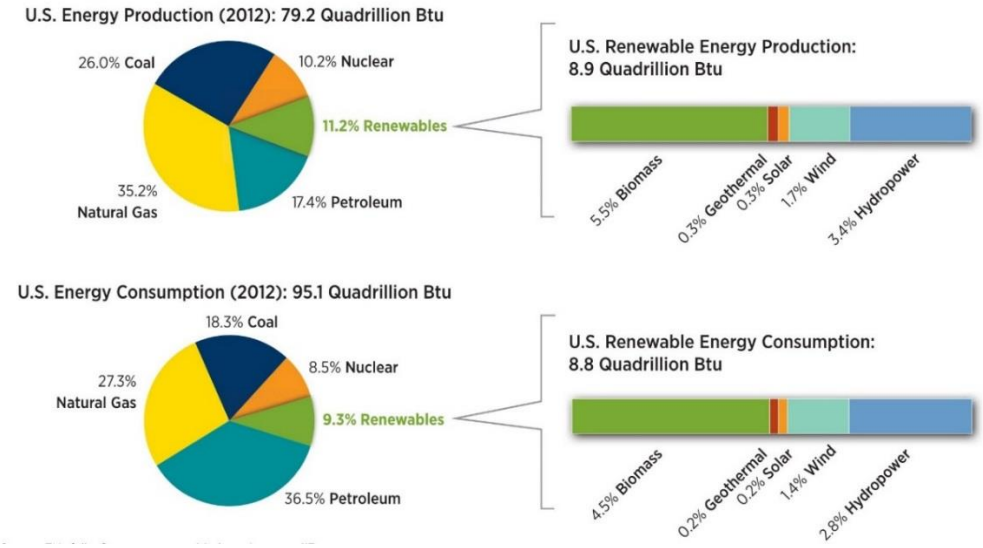


Figure 1.1. 2012 US energy production and consumption.
(Source: 2012 Renewable Energy Data Book, October 2013)

Carbon dioxide ($CO_2$) capture and storage (CCS) is one of the options considered to stabilize atmospheric greenhouse gas concentrations. It is a process consisting of the separation of $CO_2$ from industrial and energy-related sources, transport to a storage location in geological formations, in the ocean, and in mineral carbonates, isolated from the atmosphere for an extended period of time or reserved for future use in industrial processes. However, this technology requires an additional 10-40% energy penalty, used mostly for capture and compression of $CO_2$. There is also concern for potential $CO_2$ leakage. (IPCC, 2005 Special Report on CCS).

Alternative efforts to mitigate fossil fuel dependence include expanding production from renewable sources. Of these, biomass accounted for 49% of total renewable production (6% of total energy production) in 2011 (US EIA Monthly Energy Review

2013). Microalga are used for biofuel production because of their high dry weight oil content. However, sunlight to fuel efficiency is only about 1%. Additionally, large land and water areas are needed to increase supply (Roy et al. 2010).

Other renewable sources include hydroelectric power (4%), wind (2%), geothermal (<1%), and solar (<1%) (US EIA Monthly Energy Review 2013). Hydroelectric power and geothermal power plants have limited growth opportunity because these sources are natural fixtures (Lewis 2007). Nuclear energy source is also an alternative to fossil fuels. However, storage of nuclear waste is a problem. Likewise, when a nuclear power plant is damaged, it creates a serious health problem to surrounding community (Rapier and Thurber 2013).

On the other hand, wind and solar energy have greatest growth potential. For example, to meet the energy demands in the United States, a solar panel with an area of 400 km x 400 km will be required as shown in Figure 1.2 (Lewis 2007).


Figure 1.2. Representation of land requirement for solar panel to meet the energy demands in the United States. (Source: Lewis, N.S. 2007. "Powering the Planet." Engineering and Science No. 2, p. 22)

However these sources are intermittent and unpredictable, requiring electricity storage to minimize supply fluctuation (Whipple et al. 2010). Despite abundant sun power, solar energy is still limited by high manufacturing and grid installation costs (Lewis 2007).

Lastly, wind and solar energy are mainly used to supply electrical energy and have limited application to transportation fuels (Lewis et al. 2006).

### 1.2. Framework for Integrating $CO_2$ Electrochemical Reduction

In the future, we envision an energy cycle that utilizes electrochemical reduction as a process to recycle $CO_2$. The process flow is shown in Figure 1.3. In order for the technology to be sustainable, the required electricity to drive the reaction must come from non-fossil fuel sources such as solar energy, wind energy and nuclear energy. Purified $CO_2$ will be initially collected from fixed sources such as power plants. Products of $CO_2$ reduction will be collected, separated and purified through a separate set of unit operations while excess $CO_2$ will be recycled back to the reactor. Eventually, technology must also be developed to capture atmospheric $CO_2$ emitted by mobile sources such as automobiles and airplanes.

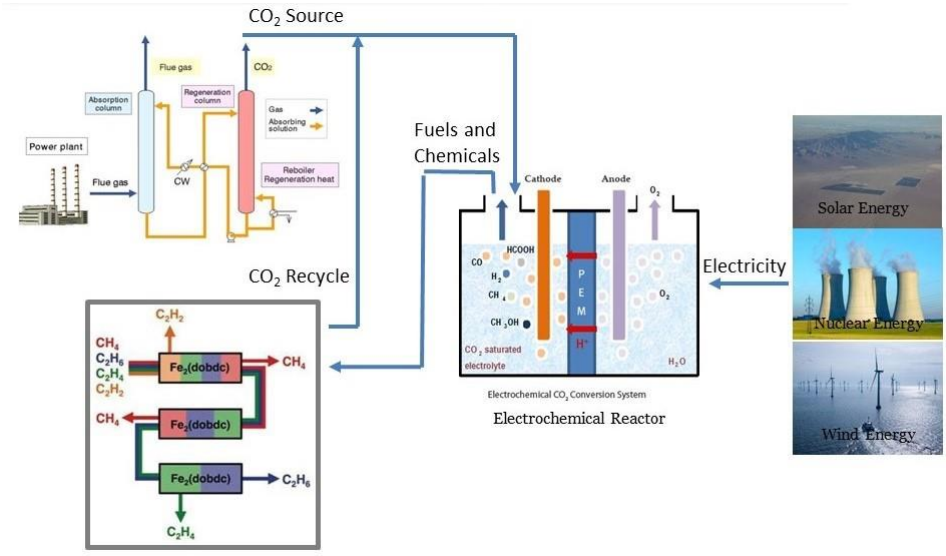


Figure 1.3. Framework for integrating $CO_2$ electrochemical reduction to existing energy infrastructure. (Image sources: (a) power plant - http://www.chiyoda-corp.com/, (b) electrochemical reactor - http://enpl.cau.ac.kr, (c) separation unit – http://alchemy.cchem.berkeley.edu/, (d) solar energy - http://en.wikipedia.org/wiki/Nevada_Solar_One, (e) nuclear energy – http://herguthlaboratories.wordpress.com, (f) wind energy - http://macaulay.cuny.edu/eportfolios/alternativeenergyinnewyork/wind-energy-in-nyc/.)

### 1.3. Statement of Problem and Research Objectives

We identify rising $CO_2$ content in the atmosphere as a critical condition that needs to be resolved. We present electrochemical reduction as a promising technology to control continued increase in $CO_2$ level by recycling them into fuels and chemical feedstocks. This technology aims to reduce our consumption of fossil fuels which would prevent further growth of $CO_2$ concentration in the atmosphere. We focus our work on developing electrocatalysts and understanding their catalytic activity towards $CO_2$ conversion. Particularly, we develop, synthesize and test foreign $Cu_2O$ particles deposited onto a support substrate.

In previous literature, Cu(I) was identified to have the unique ability to produce hydrocarbons and alcohols from $CO_2$. However, factors affecting selectivity among these $CO_2$ products remain unclear. Hence, further exploration into the surface of $Cu_2O$ is necessary. In this project, our main objective is to understand the role of oxide in copper during $CO_2$ conversion to CO, hydrocarbons and alcohols. To facilitate this goal, we will examine several factors that might be expected to affect the stability of the $Cu_2O$ electrode, including (1) influence of $Cu_2O$ particle morphology derived from applying various synthesis conditions, (2) effect of Nafion binder coating, (3) effect of CuO sublayer and (4) type of support substrate used; namely Toray carbon fiber paper, glassy carbon and copper.

### 1.4. Overview of Dissertation

Chapter 2 is a literature review that covers a brief highlight on $CO_2$ conversion processes and thermodynamics of $CO_2$ electrochemical reduction. It also covers details of experimental studies that have been done on copper and copper oxide, particularly,

contributions from the group of Hori, Kuhl, Schouten and Li. Computational studies are also reported, particularly, contributions from the group of Peterson and Nie. The contents are carefully selected and presented in a manner that tailors to the results and discussion on the electrocatalytic activity of $Cu_2O$.

Chapter 3 provides the general methodology that covers procedure for electrode fabrication and characterization, $CO_2$ reduction, electrochemical measurements, gas chromatography and data processing.

Afterwards, the main content of this work is then covered in Chapters 4, 5 and 6. Chapter 4 covers our study on polycrystalline copper. We studied the kinetics and potential dependency of $CO_2$ products on Cu foil to provide the most suitable comparison for our results on $Cu_2O$.

Chapter 5 covers our work on $Cu_2O$ films fabricated by electrochemical deposition. We studied the effect of oxide thickness on CO formation. We determined the kinetics of $CO_2$ reduction at a fix potential of $-1.5V_{NHE}$. We then examined the effect of Nafion and growing $Cu_2O$ films on a CuO substrate.

Chapter 6 covers our results on colloidal $Cu_2O$ particles synthesized by wet chemical reduction. In this chapter, we examined the reproducibility of product distribution on Toray supported $Cu_2O$ particles. We studied the effect of different preparation conditions; namely, (1) composition of NaOH, (2) synthesis aging time, (3) amount of Nafion. We also studied the effect of cyclic voltammetry. Finally, we compared the product distribution on two sets of $Cu_2O$ particles at different potentials. In this Chapter, we also studied the electrocatalytic activity of $Cu_2O$ particles supported on glassy carbon and copper.

Finally, we close the dissertation with Chapter 7 for summary, conclusion and recommendations where we highlight key results and provide over-all insights into the conversion of $CO_2$ on $Cu_2O$ catalysts. We then provided our suggestions for future experiments.

# CHAPTER 2
# REVIEW OF RELATED LITERATURE

## 2.1. Overview of $CO_2$ Conversion Technologies

Centi et al. (2013) published a paper outlining the prospect of integrating renewable energy sources on different $CO_2$ conversion technologies being developed for the chemical industry. In this dissertation, I referred to this material to highlight the important products that can be derived from $CO_2$ using different catalytic reactions. The reader is referred to the article published by Centi et al. (2013) for details on the current status and progress on these different $CO_2$ conversion technologies and how renewable energy sources may be integrated to existing infrastructures.

The list and names of $CO_2$ reactions are given below. The formation of CO and $H_2$ opens up pathway for the formation of $C_n$ hydrocarbons and oxygenates through the Fischer-Tropsch (Centi et al. 2013).

$$CO_2 + H_2O \leftrightarrow HCOOH + O_2$$

*(electrochemical, photoelectrochemical reduction)* [Eq. 2-1]

$$CO_2 + 4H_2 \leftrightarrow CH_4 + 2H_2O$$ *(Sabatier reaction)* [Eq. 2-2]

$$CO_2 + H_2 \leftrightarrow CO + H_2O$$ *(reverse water gas shift reaction)* [Eq. 2-3]

$$CO_2 + CH_4 \leftrightarrow 2CO + 2H_2$$ *(dry reforming of methane)* [Eq. 2-4]

$$\left\{\begin{matrix} CO_2 + H_2O \leftrightarrow CO + 3H_2 \\ CH_4 + {}^1/_2\, O_2 \leftrightarrow CO + 2H_2 \\ CH_4 + 2O_2 \leftrightarrow CO_2 + 2H_2O \end{matrix}\right\}$$ *(tri-reforming of methane)* [Eq. 2-5]

$$\left\{\begin{matrix} CO_2 + H_2 \leftrightarrow CO + H_2O \\ CO + 2H_2 \leftrightarrow CH_3OH \end{matrix}\right\}$$ *(methanol synthesis from syngas)* [Eq. 2-6]

$$CO_2 + 3H_2 + CH_3OH \leftrightarrow 2CH_3OH + H_2O$$

*(tri-catalyst cascading methanol synthesis, Huff and Sanford 2011)* [Eq. 2-7]

All of these reactions are well established in industrial processes with the exception of electrochemical and photoelectrochemical routes of $CO_2$ conversion.

### 2.2. $CO_2$ Electrochemical Reduction

Electrochemical conversion of $CO_2$ to liquid fuels and chemical feed stocks is an attractive candidate process in the over-all portfolio of existing $CO_2$ conversion technologies being developed to provide a sustainable form of energy (Whipple et al. 2010). Hydrogen remains the most mature chemical form of energy storage. Nonetheless, we will continue to deal with its unfavorable characteristics such as low volumetric density and low tolerance towards ignition (Centri et al. 2013). Moreover, use of hydrogen would require addition of new energy infrastructures to existing ones. (Roy et al. 2003, Whipple et al. 2010). On this note, chemical storage of energy from hydrocarbons and oxygenates would be more advantageous. These products of $CO_2$ reduction have higher energy density than $H_2$ as well as NiMH, NaS, and Li-ion batteries as shown in Figure 2.1 (Det Norske Veritas 2011). In particular, the liquid phase products of $CO_2$ are more convenient to handle and store. As such, this technology easily adapts to existing energy infrastructures (Centri et al. 2013).

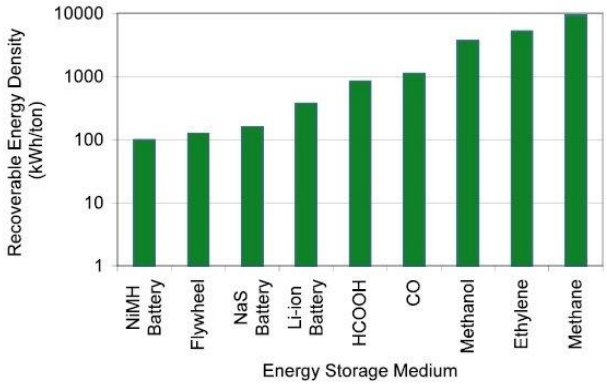


Figure 2.1. Recoverable energy density of products created from electrochemical $CO_2$ conversion processes compared to selected batteries (Det Norske Veritas 2011).

### 2.3. Thermodynamics of $CO_2$ Reduction

$CO_2$ electrochemical reduction involves electrolysis of a conductive solution saturated with $CO_2$ between two immersed electrodes at a sufficiently negative potential, larger than the thermodynamic requirement. In aqueous media, products of $CO_2$ reduction that have been reported in literature include $H_2$, CO, formate, methanol, $CH_4$, $C_2H_4$, ethanol and n-propanol. The stoichiometry of these reactions with their SHE standard reduction potential can be written in the order of electron requirement as follows (Hori 2008, Bard et al. 2001, Varcoe et al. 2004):

| | | |
|---|---|---|
| $CO_2 + H_2O + 2e^- \leftrightarrow CO + 2OH^-$ | -0.52V | [Eq. 2-8] |
| $CO_2 + H_2O + 2e^- \leftrightarrow HCOO^- + OH^-$ | -0.43V | [Eq. 2-9] |
| $CO_2 + 5H_2O + 6e^- \leftrightarrow CH_3OH + 6OH^-$ | -0.81V | [Eq. 2-10] |
| $CO_2 + 6H_2O + 8e^- \leftrightarrow CH_4 + 8OH^-$ | -0.25V | [Eq. 2-11] |
| $2CO_2 + 8H_2O + 12e^- \leftrightarrow C_2H_4 + 12OH^-$ | -0.34V | [Eq. 2-12] |
| $2CO_2 + 9H_2O + 12e^- \leftrightarrow CH_3CH_2OH + 12OH^-$ | -0.33V | [Eq. 2-13] |
| $3CO_2 + 13H_2O + 18e^- \leftrightarrow CH_3CH_2CH_2OH + 18OH^-$ | -0.32V | [Eq. 2-14] |

When operating at these negative potentials using $Cu_2O$ electrodes, the SHE standard reduction potential of Cu(I) and Cu(II) to Cu must also be taken into consideration (Bard et al. 1985):

| | | |
|---|---|---|
| $2CuO + H_2O + 2e^- \leftrightarrow Cu_2O + 2OH^-$ | -0.220V | [Eq. 2-15] |
| $Cu_2O + H_2O + 2e^- \leftrightarrow 2Cu + 2OH^-$ | -0.365V | [Eq. 2-16] |
| $CuO + H_2O + 2e^- \leftrightarrow Cu + 2OH^-$ | -0.290V | [Eq. 2-17] |

Buffer solutions formed by hydrogen bicarbonates are the most commonly used electrolyte. The thermodynamic equilibria of $CO_2$ in aqueous bicarbonate solution are given below (Hori 2008):

$CO_2 + H_2O \leftrightarrow HCO_3^- + H^+$ $pK_{a1} = 6.35$ at 25°C [Eq. 2-18]

$HCO_3^- \leftrightarrow CO_3^{2-} + H^+$ $pK_{a2} = 10.33$ at 25°C [Eq. 2-19]

Since hydrogen activity is dominant in acidic conditions and $CO_2$ molecules do not exist in basic conditions, $CO_2$ reduction is conducted in neutral pH environment (Hori 2008).

## 2.4. Electrode Materials

Several electrode materials have been considered for $CO_2$ electrochemical reduction. The simplest of these are metals. They are conveniently classified as being either HCOO-forming or CO-forming. The HCOO-forming metals include Pb, Hg, In, Sn, Cd, and Tl. The CO-forming metals are further divided into groups based on CO adsorption. They either strongly adsorb CO onto their surface (Ni and Pt) and produce mainly $H_2$ or weakly adsorb CO (Au, Ag, Zn, Pd, and Ga) and produce mainly CO. (Hori 2008) A unique metal in this group is Cu, which moderately adsorbs CO and as a result produces a wide range of products including hydrocarbons and alcohols (Kuhl et al. 2012, Gattrell et al. 2006, Peterson et al. 2010, Roy et al. 2010). For this reason, Cu is the electrode of interest in this study.

## 2.5. $CO_2$ Reduction on Copper Catalysts

### *2.5.1. Studies on Polycrystalline Cu Electrodes*

#### 2.5.1.1. Major Products of Copper

Various forms of Cu electrode have been studied, including single crystal Cu, polycrystalline Cu and alloys of Cu (Hori 2008). Pioneering works by Hori et al. (1989) reported faradaic efficiency of hydrocarbons and alcohols using electrodeposited Cu and are shown in Table 2.1.

Table 2.1. $CO_2$ products on electrodeposited Cu, -1.65V (SCE) (Hori et al. 1989)[*]

| **$CO_2$ Products** | **Faradaic Efficiency, %** |
|---|---|
| $CH_4$ | 29.4 |
| $C_2H_4$ | 30.1 |
| Ethanol | 6.9 |
| n-Propanol | 3.0 |
| CO | 2.0 |
| $HCOO^-$ | 9.7 |
| $H_2$ | 10.9 |

[*Note: Reproduced with permission from The Royal Society of Chemistry.]

Faradaic efficiency is the fraction of total current consumed to reduce $CO_2$ to a specific product. As such, it gives insight into the selectivity of the catalyst. High faradaic efficiency indicates that a specific product is selectively formed. From Table 2.1, we see that Cu was most selective to $CH_4$ and $C_2H_4$ at the applied potential.

Hori's group also demonstrated variations in faradaic efficiencies of $CO_2$ products with applied potential (see Figure 2.2). The plot shows that CO formation was the first step in $CO_2$ reduction occurring at an onset potential of about $-0.8V_{NHE}$. The CO selectivity rose to about 20% near $-1.25V_{NHE}$ and then fell to about 2% near $-1.45V_{NHE}$. The onset formation of CO was closely followed by $HCOO^-$ which showed a similar selectivity pattern with that of CO. Ethylene was the next compound produced from $CO_2$ reduction with an onset potential near $-1.1V_{NHE}$. The ethylene efficiency appeared to peak at $-1.45V_{NHE}$ with a measured selectivity of 23.4%. Finally, methane was the last product detected with an onset potential of $-1.2V_{NHE}$. The $CH_4$ selectivity rose rapidly and became the more favorable product than $C_2H_4$ at potentials more negative than $-1.32V_{NHE}$.

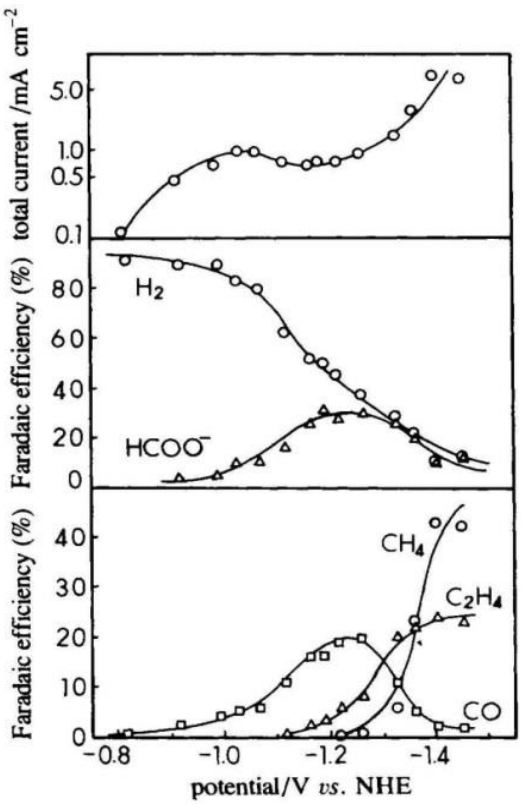


Figure 2.2. Variation of the faradaic efficiencies of the products in electrochemical reduction of $CO_2$ obtained in controlled potential electrolysis, 0.1 mol/dm$^3$ $KHCO_3$ at 19 $^0$C (Hori et al. 1989). [Reproduced with permission from The Royal Society of Chemistry.]

The $CH_4/C_2H_4$ selectivity reached a high of 1.9 near -1.45$V_{NHE}$. The increase in hydrocarbon formation with potential was coupled with a decline in hydrogen formation which initially dominated the process at a high selectivity of 92% near -0.8$V_{NHE}$. The $H_2$ selectivity fell continuously with potential reaching a low of 12% at near -1.45$V_{NHE}$. Figure 2.2 also showed the total current profile which had a characteristic shoulder near -1.1$V_{NHE}$. Hori attributed this shoulder to adsorption of CO which reduced the activity for $H_2$ formation. The current density was in the range of 0.1 to 5.0 mA/cm$^2$.

In another early study, Noda et al. (1989) also examined the $CO_2$ product distribution on Cu as a function of applied potential. They used electrochemical reduction conditions that were similar to that of Hori except that they operated the process at 25 $^o$C

instead of 19 $^{o}$C. They also used polycrystalline Cu instead of electrodeposited polycrystalline Cu. The potential range they considered was between -1.35$V_{Ag/AgCl}$ to -1.75$V_{Ag/AgCl}$ (equivalent to -1.15$V_{NHE}$ to -1.55$V_{NHE}$) compared to the -0.80$V_{NHE}$ to -1.45$V_{NHE}$ range that Hori's group considered.

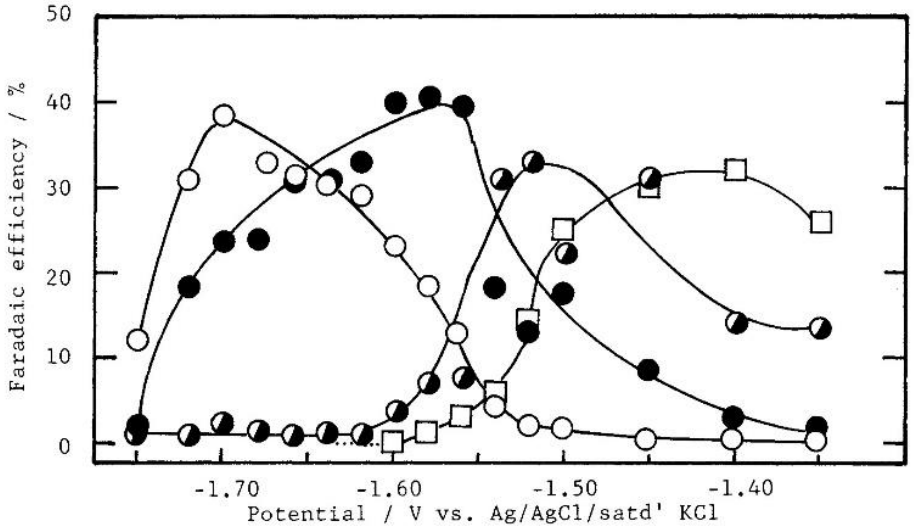


Fig. 1. The faradaic efficiency - potential curves for formations of $HCOO^-$ (□), CO (◑), $C_2H_4$ (●), and $CH_4$ (○) in 0.1 mol $dm^{-3}$ $KHCO_3$ aq. solution at 298 K.

Figure 2.3. The faradaic efficiency-potential curves for formations of $HCOO^-$, CO, $C_2H_4$ and $CH_4$ in 0.1 mol/$dm^3$ $KHCO_3$ aq. solution at 298K. [Reproduced with permission from the Chemical Society of Japan.]

The $CO_2$ product distribution plotted in Figure 2.3 are shown in reverse order of potential. They arrived at a similar product distribution. They were able to show that $CH_4$ faradaic efficiency peaked near -1.5$V_{NHE}$ while ethylene faradaic efficiency peaked near -1.37$V_{NHE}$. They also achieved higher ethylene faradaic efficiency of 41% at the peak potential. Besides gas-phase products, they also observed intermediate amounts of solution-phase products such as acetaldehyde (a.k.a. ethanal) and propionaldehyde (a.k.a. propanal) that were not observed by Hori's group during that time.

2.5.1.2. Trace Products of Copper

Kuhl et al. (2012) also conducted $CO_2$ electrochemical reduction on polycrystalline Cu at different potentials. They measured products using GC and NMR in which they classified them as major, intermediate or minor products (see Figure 2.4).

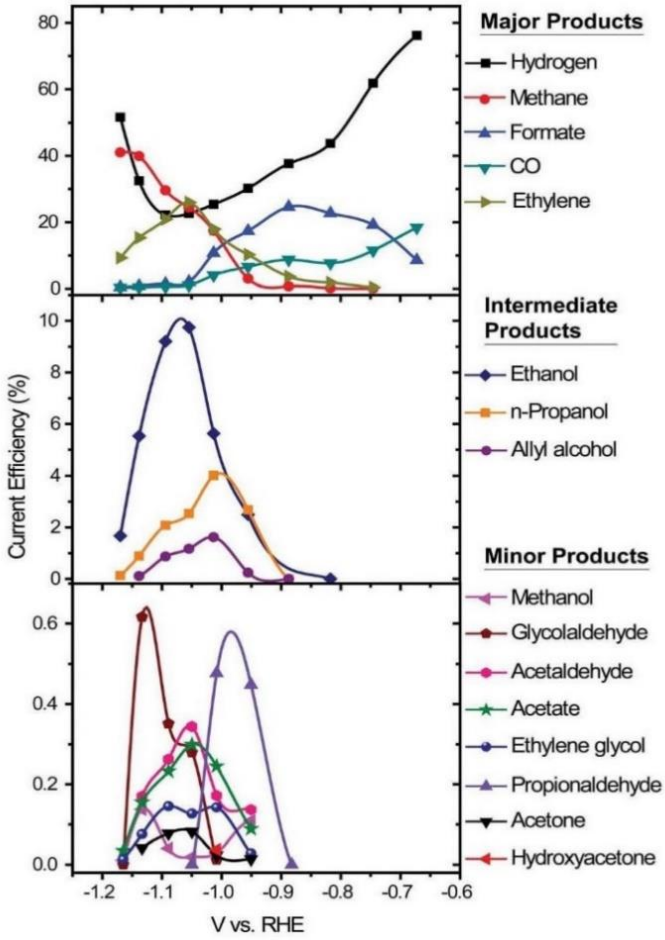


Figure 2.4. Major, intermediate and minor products of $CO_2$ reduction on polycrystalline Cu (Kuhl et al. 2012). [Reproduced with permission from the Royal Society of Chemistry.]

The important part of their results was the observation of new liquid products that were not previously reported by using NMR. These products include methanol ($H_3C$-OH), the $C_2$ oxygenates glycolaldehyde (HO-$CH_2$-CH=O), ethylene glycol (HO-$CH_2$-$CH_2$-OH) and acetone (($H_3C)_2$-C=O) and the $C_3$ oxygenate hydroxyacetone ($H_3C$-CO-$CH_2$-OH).

However, these additional products were only measured in trace amounts (Kuhl et al. 2012).

*2.5.2. Effect of Crystal Orientation on Selectivity of Cu*

Going back to Hori's group, they also studied and compared a series of different orientations of single crystal Cu and showed that Cu(111) surfaces preferably promote $CH_4$ over $C_2H_4$ while Cu(100) surfaces preferably promote $C_2H_4$ over $CH_4$. When Cu(111) steps were incorporated to Cu(100) base, $C_2H_4$ formation was also enhanced. $C_2H_4$ formation was strongest at Cu(911) and Cu(711) surfaces. Cu(711) surface exhibited the highest $C_2H_4/CH_4$ faradaic efficiency ratio, at 13.6 (refer to Figure 2.5).

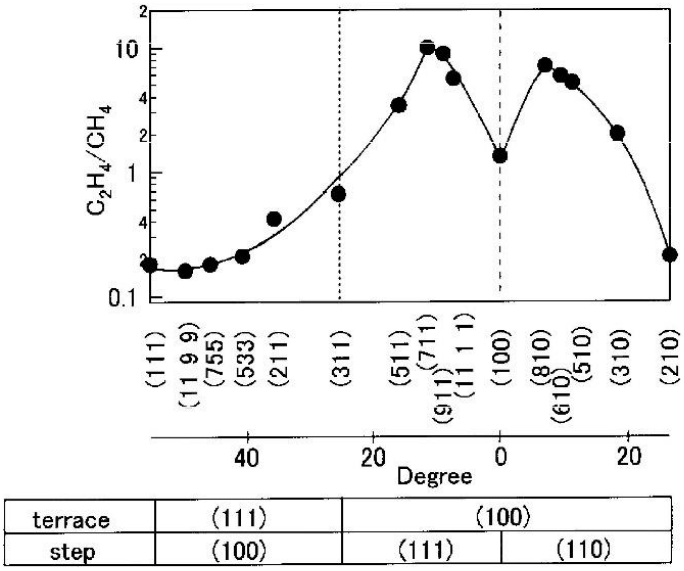


Figure 2.5. Ethylene to methane selectivity at different Cu single crystal planes (Hori et al. 2003). [Reproduced with permission from Elsevier B.V.]

Frese observed a similar trend between $CH_4$ and $C_2H_4$ on Cu(100), Cu(110) and Cu(111) (Hori et al. 2002). Hori extended studies on the effect of crystal orientations and have

additionally observed acetic acid as a major product on Cu (110), along with trace amounts of allyl alcohol, acetaldehyde and propionaldehyde.

Tang et al. (2012) examined surface morphological effect of different polycrystalline Cu on $CO_2$ products by comparing an electropolished Cu (smooth surface) with Cu that was overlaid with Cu nanoparticles (rough surface). With their results, they observed that roughened Cu surfaces improve hydrocarbon selectivity, particularly ethylene, which they attributed to increased number of lowly coordinated edges, defects and steps. Whereas with smooth surface, Cu becomes more $H_2$ selective due to higher number of low index planes such as Cu (100) and Cu (111).

*2.5.3. Other Factors Affecting Selectivity on Cu*

Hori's group also studied the effect of temperature and type of salt used in the electrolyte. The electrocatalytic activity of copper towards $CH_4$, $C_2H_4$, CO and $H_2$ was found to be very sensitive to temperature but not towards $HCOO^-$. In particular, $CH_4$ is favorably produced at 0 $^oC$ at a faradaic efficiency of 65%. The $CH_4$ selectivity then drops steeply to 5% at 40$^oC$. Meanwhile, the effect of temperature on $C_2H_4$ selectivity is opposite to that of $CH_4$, with only 3.5% efficiency at 0 $^oC$ but rising to 20% at 40$^oC$. Meanwhile, the increase in CO selectivity with temperature is less pronounce, rising only from 1% to 5% between 0-40$^oC$ temperature range (Hori et al. 1986). This dramatic temperature effect on selectivity between $CH_4$ and $C_2H_4$ was similarly observed by Cook et al. in 1988 using glassy carbon supported $Cu_2O$ electrodeposit.

The selectivity of Cu is also influenced by the type of electrolyte used. For example, the $CO_2$ product distribution on 0.1M $KC10_4$ at 5 $mA/cm^2$ is 10.2% $CH_4$, 48.1% $C_2H_4$, 15.5% ethanol, 4.2% n-propanol, 2.4% CO, 8.9% $HCOO^-$ and 6.7% $H_2$. Whereas in 0.1M

$K_2HP0_4$ at 5 mA/cm$^2$ the $CO_2$ product distribution is significantly different; 17.0% $CH_4$, 1.8% $C_2H_4$, 0.7% ethanol, 1.3% n-propanol, 5.3% CO and 72.4% $H_2$. Differences in selectivity were most notable on $C_2H_4$ and $H_2$ (Hori et al. 1988).

*2.5.4. Mechanisms of $CO_2$ Product Formation*

2.5.4.1. Experimentally Suggested Pathways

All these results highlight the sensitivity of copper surfaces to different surface and electrochemical conditions which adds to the complexity of its unique attribute. Currently, there is no reaction pathway that completely and accurately describes the reduction of $CO_2$ on copper to at least 17 different C-containing products ($H_2$ not included). However, there are several pieces of experimental evidence on Cu and other metals which suggest that the first step in the reduction of $CO_2$ to hydrocarbons and oxygenates is the formation of adsorbed $CO_2^-$ radical ($O=C-O^-_{ads}$) which is subsequently reduced to adsorbed CO ($C\equiv O_{ads}$) (Hori et al. 1989, Beden et al. 1982, Aylmer-Kelly et al. 1973, McQuillan et al. 1975, Aurian-Blajeni et al. 1983, Chandrasekaran and Bockris 1987, Oda et al. 1996). $CO_2$ can also be reduced to $HCOO^-$. However, it is thought that this pathway no longer undergo any succeeding reduction steps (Hori et al. 1989).

Two pathways have been suggested for the formation of adsorbed CO from $CO_2^-$. The first one is protonation followed by reduction;

$$O=C-O^-_{ads} + H^+ \leftrightarrow O=C-OH_{ads} \qquad \text{[Eq. 2-20]}$$

$$O=C-OH_{ads} + e^- \rightarrow C\equiv O_{ads} + OH^- \qquad \text{[Eq. 2-21]}$$

The second one involves reaction with adsorbed H atom.

$$O=C-O^-_{ads} + H_{ads} \rightarrow C\equiv O_{ads} + OH^- \qquad \text{[Eq. 2-22]}$$

In both of these pathways, $H_2$ formation reactions play an essential role as well. Since the pH condition of most $CO_2$ reduction process occurs below pH = 11, the $H_2$ evolution commence as follows, with the first step being the adsorption of $H^+$ ion.

$$H^+ + e^- \rightarrow H_{ads} \qquad \text{[Eq. 2-23]}$$

This is followed by H-H coupling or by an electrochemical desorption (Bockris and Pentland, 1952),

$$2H_{ads} \rightarrow H_2 \qquad \text{[Eq. 2-24]}$$

$$H_{ads} + H^+ + e^- \rightarrow H_2 \qquad \text{[Eq. 2-25]}$$

Several optical and spectroscopic studies have observed adsorbed CO at sufficient cathodic potential (Hori et al. 1998, Oda et al. 1996, Smith et al. 1997) Likewise, reduction of CO also resulted in similar product distribution (Hori et al. 1987, Hori et al. 1997, DeWulf et al. 1989) which suggests that all hydrocarbons and oxygenates descend from a CO intermediate. From adsorbed CO, the possible routes become wide open and more difficult to confirm, with each pathway dependent upon kinetic barriers (Nie et al. 2013) and local rate determining step (Taniguchi 1989, Frese et al. 1993, Hori 2003).

Hori's group presented a reaction pathway for the formation of $CH_4$, $C_2H_4$, ethanol and n-propanol which closely resembles with the reaction pathways in the Fischer-Tropsch reactions involving CO and $H_2$. Accordingly, he proposed that all these compounds are formed through a CHOH (hydroxymethylene) then $CH_2$ (methylene) intermediate. Additionally, he proposed that ethanol and n-propanol would proceed through a $CH_2$=C=O (ketene) then $CH_2$=CH-OH (ethenol) intermediate (refer to Figure 2.6). Subsequently, Hori in 1997 further proposed that COH is also an intermediate to $CH_4$.

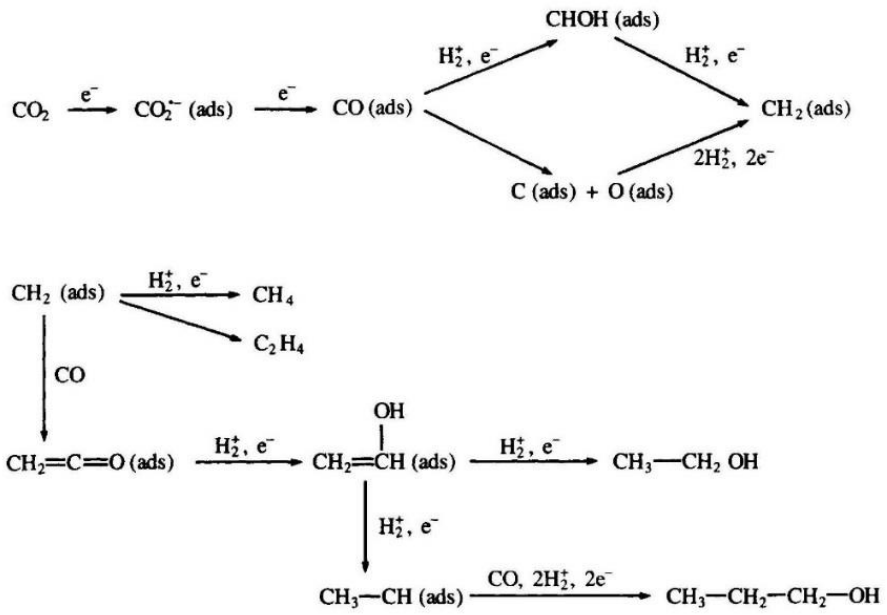


Figure 2.6. Reaction pathways of $CO_2$ reduction to different hydrocarbons and alcohols proposed by Hori et al. in 1989. [Reproduced with permission from The Royal Society of Chemistry.]

Meanwhile, the group of Kuhl suggested that the precursor to different $C_{2+}$ oxygenates is the formation of an enol-like intermediate (with a representative enol form of glyoxal, HO-$CH_2$=C-$(OH)_2$). Due to the presence of hydroxyl and/or carbonyl functional group in these $C_{2+}$ oxygenates, Kuhl further proposed that there is a C-C coupling step and that it takes place before the breaking of at least one of the two bonds in $CO_2$. However, the steps between the adsorbed CO and the enol-like intermediate for both the $C_2$ and $C_3$ pathways remain unclear. Additionally, as to which $C_1$ and $C_2$ intermediates participate in C-C coupling could not be identified at this point. Nonetheless, the group presented different options for $C_1$ intermediates derived from computational studies on Cu(211) (Peterson et al. 2010), Cu(111) (Zhao et al. 2011) and experimental studies on Ag surface by Kostecki and Augustynski (1994). These include CO, COOH (carboxyl), CHO (carbonyl), C-$(OH)_2$ (dihydroxycarbene or dihydroxymethylene), COH

(hydroxymethylidyne) and formaldehyde ($CH_2O$). As seen from Figure 2.7, ethylene, ethanol and n-propanol were considered the most reduced form of $CO_2$ while glyoxal and hydroxyacetone were the least reduced form of $CO_2$ among the $C_{2+}$ oxygenates and that reactions proceed through a series of $2e^- + 2H^+$ additions.

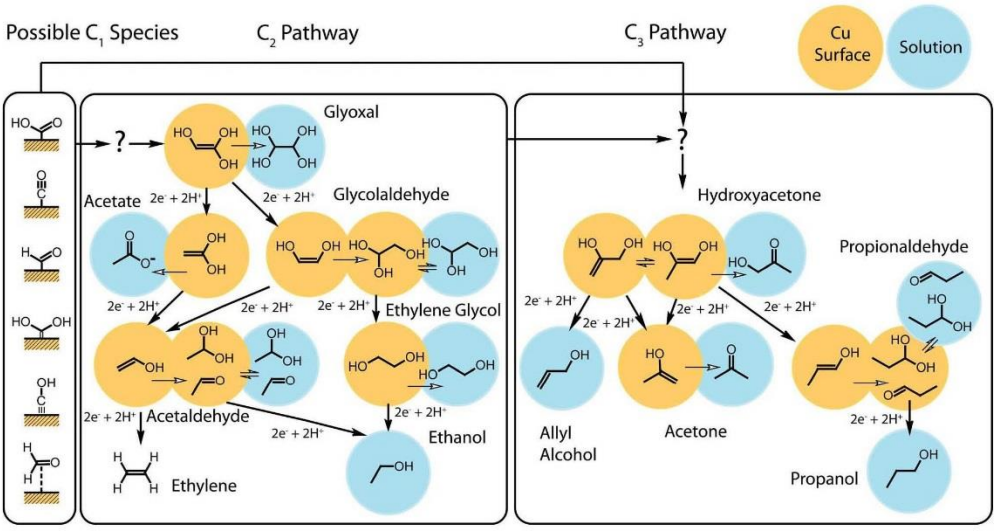


Figure 2.7. Experimentally derived reaction pathways of $CO_2$ reduction to different hydrocarbons and oxygenates proposed by Kuhl et al. in 2012. [Reproduced with permission from The Royal Society of Chemistry.]

The reaction pathways proposed by Schouten's group in 2011 so far provides the most consistent information for methane and ethylene formation based on a realistic electrochemical environment (see Figure 2.8). In order to verify the reaction intermediates of $CO_2$ reduction, they considered the reduction of formaldehyde ($CH_2O$), methanol (methoxy at high pH, $CH_3O$), glyoxal (OHC-CHO), glycoaldehyde (HO-$CH_2$-CHO), ethylene glycol (HO-$H_2C$-$CH_2$-OH) and ethylene oxide ($H_2COCH_2$) and monitored products using mass spectrophotometer.

Reduction of formaldehyde ($CH_2O$) produced methanol ($CH_3OH$) but not formic acid (HCOOH). However, with long term electrolysis, $CH_4$ was also formed. Meanwhile,

reduction of methanol/methoxy did not produce methane. As such, they suggested that $CH_4$ is formed through a closely related intermediate to formaldehyde which is formyl ($CHO_{ads}$) and that $CHO_{ads}$ occurs by hydrogen activated dissociation of $CO_{ads}$ (Ciobica and van Santen 2003, Inderwildi et al. 2008, Shetty et al. 2010, Shetty and van Santen 2010). On the other hand, methanol is formed through the other closely related intermediate to fomaldehyde which is hydroxymethyl ($CH_2OH_{ads}$). This is in contrast to $Cu/ZnO/Al_2O_3$ catalyzed gas phase methanol synthesis where sequentially formate and formaldehyde are the intermediates to that product (Bowker et al. 1988, Nakatsuji and Hu, 2000).

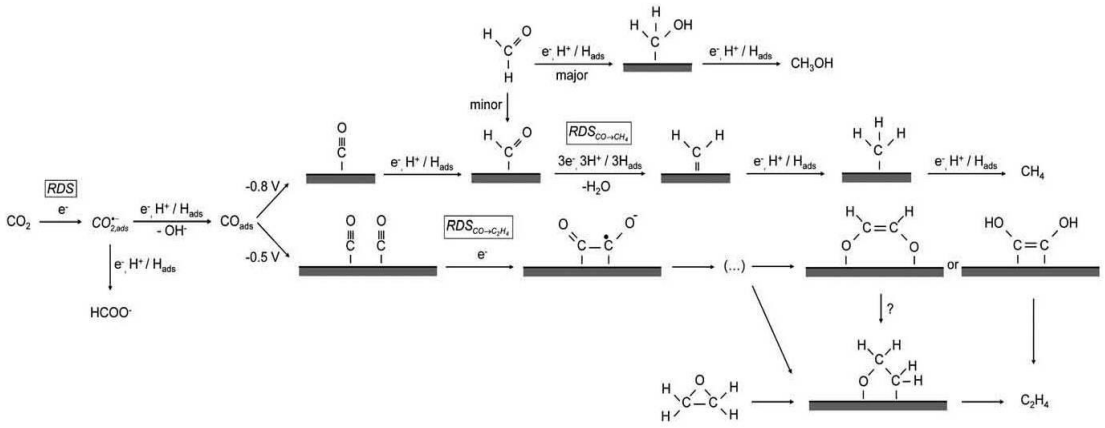


Figure 2.8. Experimentally derived reaction pathways of $CO_2$ reduction to $CH_4$, $CH_3OH$ and $C_2H_4$ proposed by Schouten et al. in 2011. [Reproduced with permission from The Royal Society of Chemistry.]

Reduction of ethylene oxide produced ethylene and no other alcohols and aldehydes. From this result, Schouten's group suggested epoxide in the form of an oxametallacycles as a possible pre-requisite to ethylene. Additionally, they postulated that adsorbed CO dimer ($O=C-C-O^-$) is the first intermediate to the ethylene pathway, similar to that suggested by Gatrell et al. (2006). However, their experimental results are not

sufficient at this point to elucidate the steps proceeding the CO dimer including the epoxide step.

Other experimentally derived reaction pathways include the works of Friebe et al. (1997), DeWulf et al. (1989) and Cook et al. (1988).

2.5.4.2. Computationally Derived Pathways

Computational tools have also been employed to construct the complex reaction pathways of $CO_2$ conversion to hydrocarbons. To date, calculations using density functional theories have hypothesized $CO_2$ pathways to CO, HCOO, $CH_4$, $C_2H_4$, and $CH_3OH$ using data from reaction free energies and activation barriers (Peterson et al. 2010, Nie et al. 2013). There is a general agreement that CO is an important intermediate to hydrocarbon formation (Kuhl et al. 2012). Peterson et al. (2010) hypothesized that the rate determining step in the formation of $CH_4$ and $C_2H_4$ is the hydrogenation of adsorbed CO to form $CHO_{ads}$. With $CH_4$, the sequential intermediates involved are adsorbed formaldehyde ($CH_2O_{ads}$) and adsorbed methoxy ($CH_3O_{ads}$) through addition of a proton-electron pair. With $C_2H_4$, Peterson listed possible intermediate pairings, (a) $CH_2O_{ads}$ + $CH_2O_{ads}$ (formaldehyde), (b) $CH_2O_{ads}$ (formaldehyde) + $CHO_{ads}$ (carbonyl), (c) $CHO_{ads}$ + $CHO_{ads}$ (carbonyl), (d) $CHO_{ads}$ (carbonyl) + $OCH_{3ads}$ (methoxy).

On the other hand, Nie et al. (2013) proposed a major branching point for $CH_4$, $C_2H_4$ and $CH_3OH$ from the CO intermediate based on DFT calculation that incorporate reaction free energies and reaction kinetics of elementary steps. As shown in Figure 2.9, CO will branch out to either $COH_{ads}$ or $CHO_{ads}$ intermediate. $CH_3OH$ is preferably formed through the $CHO_{ads}$ branch point that involves the formation of detached formaldehyde ($CH_2O$) followed by an adsorbed methoxy ($OCH_3$). $CH_4$ and $C_2H_4$ are preferably formed

through the $COH_{ads}$ branch point that involves dissociation of OH followed by a series of H addition.

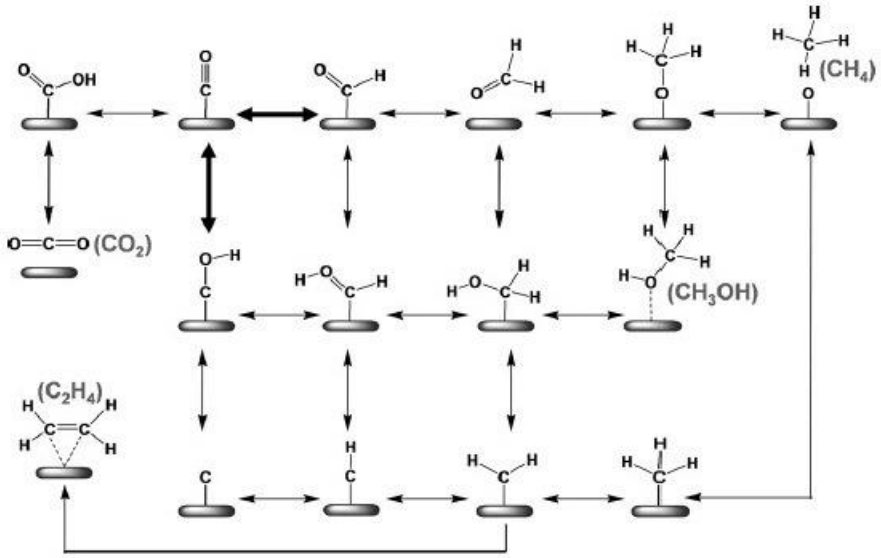


Figure 2.9. Reaction pathways derived from DFT calculations involving reaction free energies and kinetics of elementary steps (Nie et al. 2013). [Reproduced with permission from Wiley-VCH Verlag GmbH & Co.]

This is contrary to the suggestion of Schouten's group wherein $CHO_{ads}$ is the precursor to $CH_4$ and CO dimer formation early in the reduction steps is the precursor to $C_2H_4$. $CH_4$ and $C_2H_4$ pathways then split at the $CH_2$ intermediate with $CH_4$ formed by two additional proton-electron pair and $C_2H_4$ formed by C-C coupling. Cook et al. (1988) also suggest $CH_2$ as the final common intermediate of $CH_4$ and $C_2H_4$. Details on $C_2H_4$ formation however are not given.

Meanwhile, Durand et al. (2011) focused on computational studies to determine the effect of crystal orientation of Cu(100), Cu(111) and Cu(211). Their group showed that Cu(211) has the strongest adsorbing sites for $CO_2$ intermediates while Cu(111) generally has the weakest adsorbing sites.

## 2.6. $CO_2$ Reduction on Copper Oxide Catalysts

### *2.6.1. Properties of $Cu_2O$ and their Synthesis*

Cuprous oxide ($Cu_2O$) is one of the three stable oxide forms of Cu having an oxidation state of +1. The unit cell which consists of 4 Cu atoms and 2 O atoms has a lattice constant of 4.2696 Å. Cu atoms are arranged in a face-centered manner while O atoms are arranged in a body-centered manner. Cu atoms are linearly coordinated to two O atoms while O atoms are tetrahedrally coordinated to four Cu atoms (see Figure 2.10). $Cu_2O$ usually crystallizes into cubes with size ranging from 10 nm to 10,000 nm. It physically exhibits a reddish orange color (Chen and Xue 2013, Meyer et al. 2013).

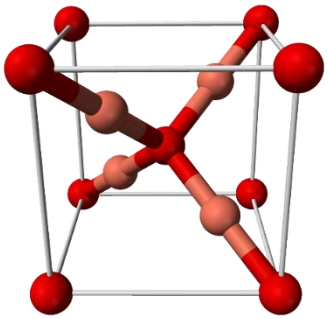

Figure 2.10. Unit cell of $Cu_2O$. (Image was taken from http://en.academic.ru/dic.nsf/enwiki/282750)

$Cu_2O$ nanowires and polyhedrons can also be obtained by tailoring the synthesis condition. Several review articles summarized the different techniques applied to fabricate $Cu_2O$ particles and are listed in Figure 2.11. The reader is referred to these materials for more details (Zoolfakar et al. 2014, Filipic and Cvelbar 2012).

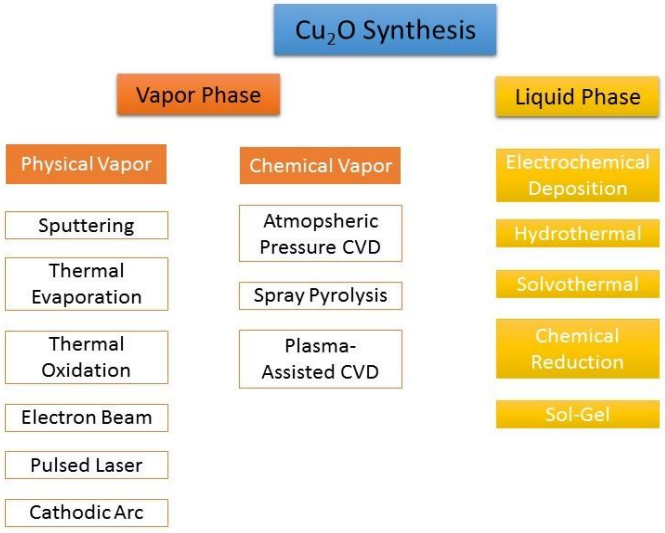


Figure 2.11. Classification of different $Cu_2O$ synthesis methods (Zoolfakar et al. 2014, Filipic and Cvelbar 2012).

In this work, we focus on liquid phase $Cu_2O$ synthesis, particularly wet chemical reduction and electrochemical deposition. In wet chemical reduction, $Cu_2O$ particles are chemically formed by mixing $Cu^{2+}$ precursor salts with reducing agents and other additives e.g. surfactants and precipitators. NaOH is typically used to precipitate $Cu^{2+}$ into $Cu(OH)_2$ before adding the reducing agent to convert $Cu(OH)_2$ to $Cu_2O$. The size and morphology of $Cu_2O$ is sensitive to the composition of reagents used which influence the relative growth of (100) and (111) planes.

In electrochemical reduction, electric current is supplied to simultaneously convert $Cu^{2+}$ precursor salts and grow $Cu_2O$ on a conducting support substrate. The electroplating bath typically consists of the $Cu^{2+}$ precursor salt and chelating agent such as lactic acid. The pH of the bath is adjusted to alkaline condition by addition of NaOH. Morphology is

controlled by the applied potential, pH and the nature of the growth substrate. (Zoolfakar et al. 2014, Filipic and Cvelbar 2012, Chen and Xue 2013)

*2.6.2. Catalyst Work on $Cu_2O$*

A small number of groups have studied $Cu_2O$ as electrocatalyst for $CO_2$ conversion. These reports are interesting because they observed methanol as a major $CO_2$ product. Frese (1991) was the first to study $Cu_2O$ when he demonstrated direct $CO_2$ reduction to methanol. He compared anodized Cu foil, thermally air-oxidized Cu, and air-oxidized Cu on oxidized Ti at different potentials. Highest methanol rates were observed from anodized Cu. The authors suggested that the stronger binding energy of $CO_2$ and CO on $Cu_2O$ and other Cu(I) sites may have facilitated hydrogenation of CO to $CH_3OH$.

Le et al. (2011) also studied different oxidized copper ($Cu_2O$) and similarly reported methanol as the major $CO_2$ product with trace amounts of CO. They compared anodized Cu, thermally air-oxidized Cu, and electrodeposited $Cu_2O$ and showed highest methanol rates and faradaic efficiencies with electrodeposited $Cu_2O$. Potential-dependent methanol formation from $CO_2$ was evaluated between -1.0V and -2.0V (SCE) and rates reportedly decreased at electrolysis time greater than 30 minutes which was accompanied by a rise in $CH_4$ formation. $Cu_2O$ was simultaneously reduced and may have been the reason for the loss in activity. Though they reported high methanol rate on electrodeposited $Cu_2O$, reproducibility of sample preparation and long term stability was a major problem. Nonetheless, Cu(I) sites were believed to be key to high $CH_3OH$ generation.

Chang et al. (2009) prepared $Cu_2O$ nanoparticles by a chemical reduction synthesis and used carbon cloth as support substrate. They qualitatively observed methanol and demonstrated electrochemically stable $Cu_2O$ based on data from cyclic voltammetry.

Li et al. (2012) on the other hand worked on thermally oxidized copper with different thickness prepared by annealing Cu in air. They observed that oxide-derived Cu reduces $CO_2$ to CO at lower onset potential at a significantly higher rate and 20 times better selectivity compared to Hori's copper samples at $-0.9V_{NHE}$. Additionally, they reportedly observed ethanol, propanol and ethane but not methanol and methane on completely reduced $Cu_2O$. The increased CO selectivity at less negative potential may be due to high concentration of grain boundaries with unstable atomic coordination resulting from the reduction of thick $Cu_2O$. Rough copper surfaces consist of high number of low coordinated sites and is believed to enhance the formation of hydrocarbons, particularly ethylene and methane (Tang et al. 2012).

# CHAPTER 3
# GENERAL METHODOLOGY

## 3.1. Synthesis of $Cu_2O$ Particles

$Cu_2O$ particles were synthesized using two methods; namely, (1) electrochemical reduction and (2) wet chemical reduction. With electrochemical reduction, $Cu_2O$ particles were synthesized and simultaneously electroplated to the support substrate without a separate additional mounting step. With wet chemical reduction, $Cu_2O$ particles were formed from dissolved copper salts into powder form as the end product. With this method, we developed various techniques to mount these particles onto the support substrate.

### *3.1.1. Electrochemical Deposition*

$Cu_2O$ particles were synthesized by electrochemical reduction following the procedure described by Golden et al. (1996). The 15 mL electroplating bath consisted of 0.4M copper sulfate pentahydrate solution ($CuSO_4 \cdot 5H_2O$, Sigma-Aldrich, ≥ 98% metals basis) and 3.0M lactic acid solution ($CH_3CH(OH)COOH$, Sigma-Aldrich, ≥ 85% metals basis). The pH of the solution was adjusted to 9.0 while heated at $65^0$C by the addition of 1.0M sodium hydroxide (NaOH) solution (Mallinckrodt Chemicals). $Cu_2O$ was electrochemically deposited on to the support substrate at $65^0$C and at $-0.51V_{Ag/AgCl}$ using a Pt counter electrode (2 cm x 1 cm x 0.015 cm, ESPI Metals, 99.99% metals basis).

### *3.1.2. Wet Chemical Reduction*

With this method, we adopted two sets of procedure which produced $Cu_2O$ particles with distinct particle size range in the micro scale and nanoscale level. The first one followed the procedure described by Chang et al. (2009). First, 0.005M aqueous solution of copper (II) chloride ($CuCl_2$, Sigma-Aldrich, 99.999% trace metals) was mixed with 0.002M polyethylene glycol ($H(OCH_2CH_2)_nOH$ or PEG, Sigma-Aldrich, BioUltra,

MW = 200) surfactant, followed by addition of 0.2M sodium hydroxide solution (NaOH, Sigma-Aldrich, ≥98%, pellets (anhydrous)) and 0.05M (+)-Sodium L-ascorbate ($C_6H_7NaO_6$, LAAS, Sigma-Aldrich, ≥99%) at 1:1:1:1 volumetric ratio. The solution was aged for 6 hours to allow sufficient time for $Cu_2O$ nucleation, growth and sedimentation. The colloidal $Cu_2O$ mixture is shown is Figure 3.1.

Figure 3.1. Colloidal $Cu_2O$ mixture after wet chemical reduction.

Upon completion, the $Cu_2O$ precipitates were collected and rinsed with deionized water to remove excess amount of PEG, NaOH and LAAS.

The second one followed the procedure described by Li et al. (2013). Twelve mL of 0.001M copper (II) acetate ($Cu(CH_3COO)_2$) (ACS Reagent, Acros) was added to 108 mL deionized $H_2O$. This was followed by the addition of 6.0g of polyethylene glycol pellets ($H-(O-CH2-CH2)_n-OH$, MW = 10,000, Sigma). The mixture was allowed to homogenize. This was then followed by the addition of 6.0 mL of 0.6M sodium hydroxide (NaOH, ≥ 98%, Aldrich). The mixture was allowed to precipitate for 10 minutes. This was then followed by the addition of 24 mL of 0.1M L-Ascorbic Acid ($C_6H_8O_6$, AA, 99% ACS Reagent, Acros). The mixture was allowed to reduce for 30 minutes.

$$Cu\ (CH_3COO)_2 \leftrightarrow Cu^{2+} + 2CH_3COO^- \quad \text{[Eq. 3-1]}$$

$$Cu^{2+} + 2OH^- \leftrightarrow Cu(OH)_2 \quad \text{[Eq. 3-2]}$$

$$2Cu(OH)_2 + C_6H_8O_6 \leftrightarrow Cu_2O + C_6H_6O_6 + 3H_2O \quad \text{[Eq. 3-3]}$$

The $Cu_2O$ nanoparticles were then collected by centrifugation at 19,000 rpm for 10 minutes using Jouan MR 22i Centrifuge located at the LSU Department of Chemical Engineering under the supervision of Professor Michael Benton. The particles were washed with deionized $H_2O$ three times and air dried in open container.

### 3.2. Characterization of $Cu_2O$ Particles

The $Cu_2O$ electrocatalysts were characterized using different analytical tools. The FEI Quanta 3D FEG dual beam SEM/FIB system was used to examine the morphology of the supported $Cu_2O$ particles. We used the SEM to measure particle size, determine surface coverage and distribution of particles in the support substrate. The Rigaku MiniFlex X-ray Diffractometer was used to determine the oxidation state of Cu and their crystal orientation. We used the XRD to qualitatively identify the bulk composition of different crystal orientations present. Finally, the Kratos AXIS-165 XPS/Auger surface analysis system was used to determine the surface composition of the electrocatalyst. These tools helped us understand the electrocatalytic activity of $Cu_2O$ towards conversion of $CO_2$ macroscopically. The SEM/FIB and XPS equipment are located at the LSU Materials Characterization Center Shared Instrumentation Facility of the Department of Chemistry. The XRD tool is located at the MCC Lab of the Department of Mechanical Engineering. These equipment are under the supervision of Dr. Congmei Cao.

### 3.3. Development of Support Electrode Assembly

The support electrode assembly was constructed and used in some of the electrochemical studies on $Cu_2O$. To provide a suitable intermediary connection to the

potentiostat, a 4N Cu wire was attached to the sleeve of the support substrate using a silver epoxy paste (EJ-2189, Epoxy Technology). This was followed by a second coating of an insulating epoxy paste (DP-270, 3M) to cover the conducting epoxy as well as the backside of the support substrate and the Cu wire (see Figure 3.2). Other $Cu_2O$ electrodes were not mounted on these support electrode assembly but instead were directly clamped to a stainless steel alligator clip.

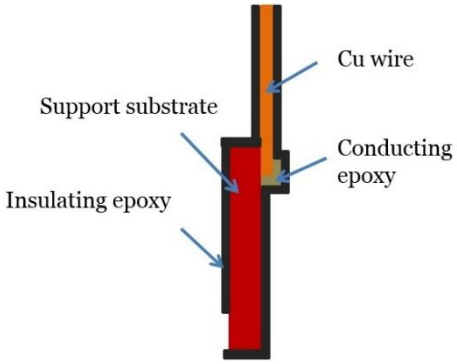


Figure 3.2. Diagram of the support electrode assembly.

### 3.4. $CO_2$ Electrochemical Reduction

$CO_2$ electrochemical reduction was performed in a custom H-type electrochemical cell assembly made of borosilicate glass (see Figure 3.3). The two compartments of the cell were clamped and sealed with a Viton O-ring. The catholyte and anolyte were separated by Nafion PFSA Membrane 117 (DuPont). The reactor had outlets for connection to the potentiostat (Princeton Applied Research (PAR) Model 263A), the gas chromatography equipment (Shimadzu GC-2014) and the $CO_2$ mass flow controller (Omega Engineering Inc). The $Cu_2O$ electrode was assembled on the catholyte compartment immersed in a 15-20 mL solution of 0.5M potassium bicarbonate ($KHCO_3$, Sigma-Aldrich, 99.7% metals basis) pre-saturated with $CO_2$ (99.9999%, Airgas) for 30 minutes. The pH of the electrolyte was 7.6-7.7. Meanwhile, the anolyte compartment was

equipped with a Pt counter electrode. Electrolysis was conducted at different potentials from -1.0$V_{NHE}$ to -2.1$V_{NHE}$.

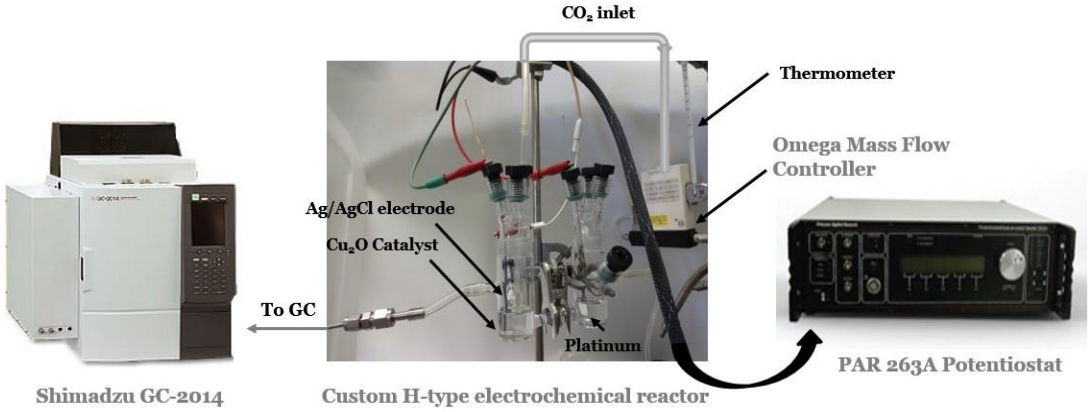


Figure 3.3. Process flow equipment for $CO_2$ electrochemical reduction.

## 3.5. Electrochemical Measurements

### *3.5.1. Uncompensated Resistance Determination*

The uncompensated resistance ($R_u$) determination was performed using the PowerSuite software that controlled the Princeton Applied Research potentiostat. The baseline potential was set at 0.0V and the pulse height at 1.0mV. The software automatically generated the value of the solution resistance after the run. From this value, the potential drop was calculated using the equation derived from Ohm's Law,

$$V_{drop} = I * R_u \qquad \text{[Eq. 3-4]}$$

Finally, the actual potential at the electrode surface was determined,

$$V_{actual} = V_{applied} - V_{drop} \qquad \text{[Eq. 3-5]}$$

### *3.5.2. Cyclic Voltammetry*

Cyclic voltammetry (CV) was performed to evaluate the electrochemical property of $Cu_2O$ particles pertaining to their reduction-oxidation reactions to Cu and CuO states

and identify the potential at which these transitions occur. The potential sweep was between -1.2$V_{Ag/AgCl}$ and 0.6$V_{Ag/AgCl}$ done at four cycles with a sweep rate of 50 mV/s. Cyclic voltammetry was performed under the same electrochemical set-up as $CO_2$ electrochemical reduction. CV was also used as a post synthesis step to prepare a modified $Cu_2O$ surface for testing as a different and separate $Cu_2O$ electrocatalyst.

### 3.6. Gas Chromatography

We used a Shimadzu GC-2014 gas chromatography (GC) system to separate, identify and quantify gas and liquid phase products of $CO_2$ electrochemical reduction. It was an integral unit in the over-all process equipment design that also consisted of the H-type electrochemical reactor, the potentiostat and mass flow controller. The components were separated by differences in their boiling point, polarity and/or intermolecular force of attraction. Given the same molecular characteristics, those with lower boiling points will move faster than those with higher boiling points. The sample gas (or vaporized liquid) along with the carrier gas e.g. He constituted the moving phase while the packing materials along the lining of the column constituted the stationary phase. The columns had adequate length to allow for complete separation of the components.

The GC was equipped with the following features: (a) thermal conductivity detector (TCD), (b) dual flame ionization detector (dual-FID), (c) methanizer, (d) HP plot-u column and (e) multiple gas columns (MS5A, Hayesep Q (H-Q) and T (H-T) and Shimalite Q). The TCD was used to detect and quantify concentrated gas products of $CO_2$, ethylene, $H_2$, methane and CO. The TCD could also detect any $N_2$ and $O_2$ from the air mixture. There were two FID's. The first FID was used to detect and quantify CO and $CH_4$ while offering better sensitivity towards trace amounts. The second FID was used to detect and quantify

ethanol and n-propanol. The methanizer was installed to quantify $CO_2$ and CO by first converting them into methane.

The gas flow chart for the GC installed in the lab is given in Figure 3.4. Gas sampling was done by automated injection through inlet valve 2 and inlet valve 3. Liquid samples could be alternatively introduced through inlet valve 1 but was not used in our experiment. Gas samples entered both analysis valve 2 (10-port configuration) and analysis valve 3 (10-port configuration) at 1 mL loop for each valve switching cycle.

Multiple gas columns were installed in order to sufficiently separate a wide range of gas products. Two MS5A columns were used to separate $O_2$, $N_2$, $CH_4$ and CO. One of them routed the products to the TCD from inlet valve 3 and the other routed the products to the FID-R from inlet valve 2. Two Hayesep Q columns were also used to separate $CO_2$, $CH_4$ and $C_2H_4$. One was linked to the TCD while the other was linked to the FID-R. One Hayesep T column was also installed along the lines between the analysis valve 3 and TCD. Finally, Shimalite Q was also added to separate $H_2$, $O_2$, $N_2$, $CO_2$, CO, and $CH_4$ and restrict flow of $H_2O$ to TCD. Two columns were present for the TCD line. Gas samples that entered analysis valve 2 also entered through analysis valve 3. Any CO and $CO_2$ molecules present were first reduced to $CH_4$ when they passed through the methanizer before they could be identified by the FID-R as $CH_4$ signals. Other gas species passed through the methanizer unreacted before they were oxidized by flame and air in the FID-R. Separation of gas products therefore involved a simultaneous two path process, one for the TCD and the other for the FID-R.

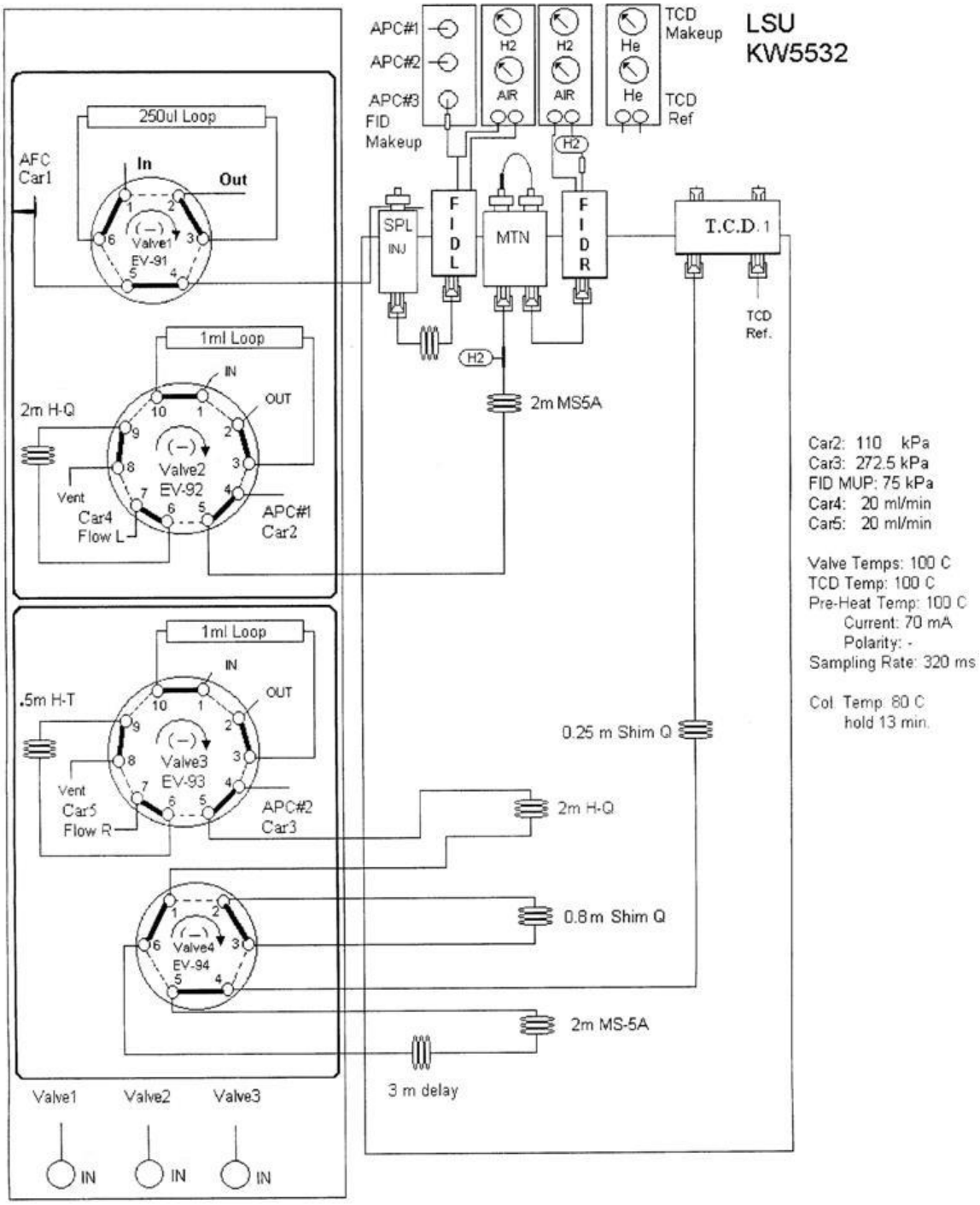


Figure 3.4. Gas-liquid flow diagram of Shimadzu GC-2014 Gas Chromatograph (illustration provided by Shimadzu Corp).

An actual picture inside the oven of the GC is shown in Figure 3.5.

Figure 3.5. Photo of actual column oven of Shimadzu GC-2014 gas chromatograph installed in the lab.

The gas separation was operated under the following temperature setting: Methanizer - 380 $^{o}$C, Column Oven - 80 $^{o}$C, TCD - 100 $^{o}$C and FID-R - 316$^{o}$C. The carrier gases were He and Ar. The program time was 13 minutes per sampling. The derived calibrated peaks of different gases on TCD is given in Figure 3.6.

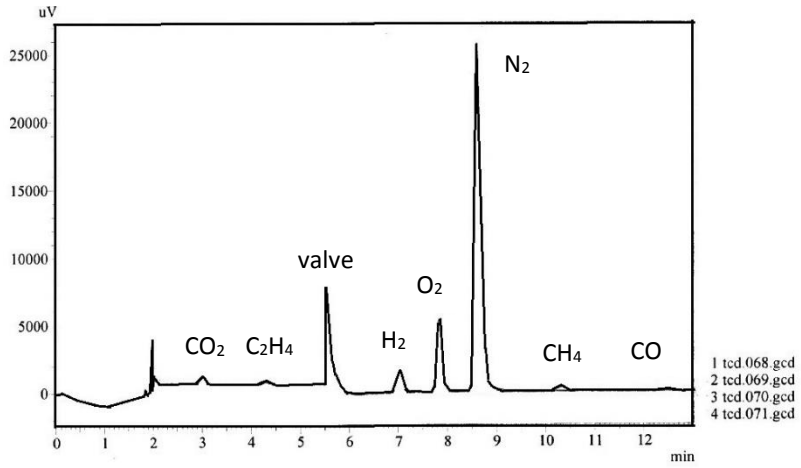


Figure 3.6. TCD peaks of gas products.

Meanwhile, the derived calibrated peaks of different gases on FID is given in Figure 3.7.

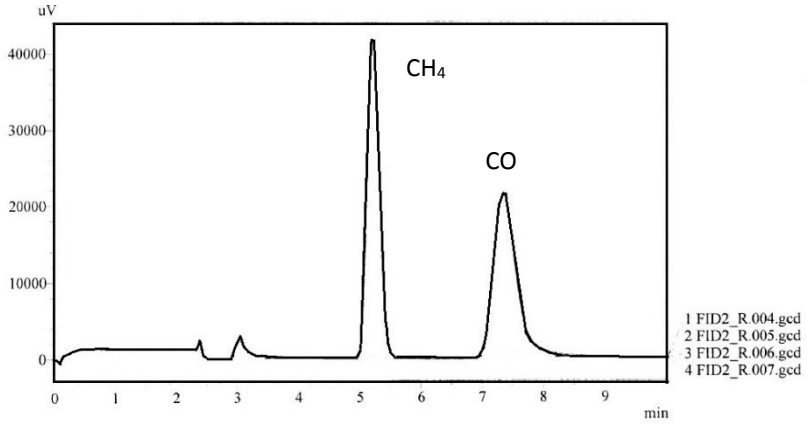


Figure 3.7. FID peaks of gas products.

The GC was initially equipped with Stabilwax column (Agilent) which was later replaced by an HP plot-U column (Agilent). The latter column provided better separation of ethanol and n-propanol. The column consisted of divinylbenzene/ethylene glycol dimethacrylate as stationary phase which has the ability to separate $C_1$ to $C_7$ hydrocarbons,

$CO_2$, methane, air/CO, water, oxygenates, amines, solvents, alcohols, ketones and aldehydes. Liquid products were manually injected to the GC from the injection port where they were quickly vaporized. The injection port featured a split-split less configuration.

I developed the GC method for HP plot-U column, optimized the separation after multiple trials and arrived at the following recipe. The split ratio at the injection port was set at 40 with a fixed temperature of 125 $^{o}$C. The FID-L temperature was set at 150 $^{o}$C. The carrier gas was He (99.9999%). The temperature of the column oven was programmed as follows: (step 1) fixed temperature of 130 $^{o}$C for the first 5 minutes, (step 2) ramped temperature from 130 $^{o}$C to 150 $^{o}$C for the next 2 minutes at 100 $^{o}$C/min and (step 3) fixed temperature of 150 $^{o}$C for the last 4.5 minutes. The total program time was 11.5 min per sampling and trial. I obtained the following peak separation for methanol, ethanol, 1-propanol and 2-propanol.

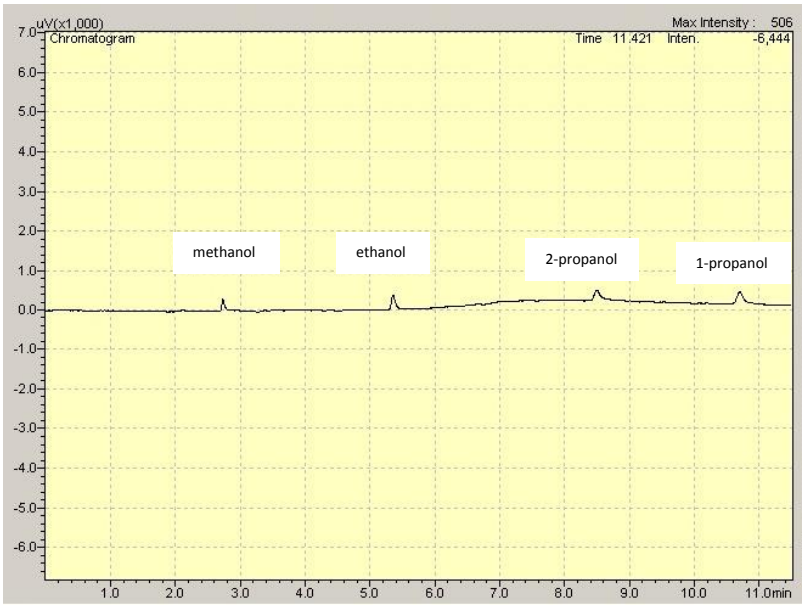


Figure 3.8. FID peaks of different alcohols considered.

## 3.7. Data Processing

### *3.7.1. Oxide Thickness and Mass of $Cu_2O$ Reduced*

Data from current versus time profile could be used to estimate the oxide thickness and the mass of $Cu_2O$ reduced. The trapezoidal rule was used to estimate the area under the curve. The area under the curve gave a unit of Coloumb. From the charge obtained, the oxide thickness and mass of $Cu_2O$ reduced can be computed as follows.

$$l = \frac{Q*M}{f*e*\rho*A} \qquad \text{[Eq. 3-6]}$$

$$m = \frac{Q*M}{f*e} \qquad \text{[Eq. 3-7]}$$

*where,*

$l = oxide\ thickness, cm$
$m = mass\ of\ Cu_2O\ reduced$
$Q = charge, C$
$M = molecular\ weight\ of\ Cu_2O, 143\ g/mol$
$f = faraday\ constant, 96{,}485 \frac{C}{mol\ e}$
$e = electron\ required, 2\ mol\ e$
$\rho = density\ of\ Cu_2O, 6\ g/cm^3$
$A = electrode\ area, cm^2$

We used the following redox reaction as the basis for the electron requirement.

$$Cu_2O + 2H^+ + 2e^- \rightarrow 2Cu + H_2O \qquad \text{[Eq. 3-8]}$$

### *3.7.2. Formation Rate and Faradaic Efficiency*

The electrocatalytic activity of $Cu_2O$ was measured on two metrics, formation rate and faradaic efficiency. Formation rate measured the amount of product generated per given time and electrode area. Faradaic efficiency measured the percentage of total charge used to reduce $CO_2$ to a particular product. Faradaic efficiency determined the $CO_2$ product distribution and selectivity of the catalyst. The equation used for liquid products were

slightly different from gas products because gas measurements were instantaneous while liquid measurements were compounded. The formation rate and faradaic efficiency were computed using the following formulae,

$$G_R = [G] * \frac{r}{T*A*g} \qquad \text{[Eq. 3-9]}$$

$$L_R = [L] * \frac{V}{t*A*M} \qquad \text{[Eq. 3-10]}$$

$$G_E = G_R * \frac{f*e*A}{I} \qquad \text{[Eq. 3-11]}$$

$$L_E = L_R * \frac{f*e*A*t}{Q} \qquad \text{[Eq. 3-12]}$$

*where,*

$G_R = gas\ formation\ rate, \frac{\mu mol}{cm^2*hr}$
$G_E = gas\ faradaic\ efficiency, \%$
$[G] = gas\ concentration, mL/L$
$L_R = liquid\ formation\ rate, \frac{\mu mol}{cm^2*hr}$
$L_E = liquid\ faradaic\ efficiency, \%$
$[L] = liquid\ concentration, mg/L$
$r = carrier\ gas\ flow\ rate, 40\ mL/min$
$T = temperature, K$
$A = electrode\ area, cm^2$
$g = ideal\ gas\ constant, 0.0821\ \frac{L*atm}{mol*K}$
$V = volume, L$
$t = time, hr$
$M = molecular\ weight, \frac{g}{mol}$
$f = faraday\ constant, 96485\ \frac{C}{mol\ e}$
$e = electron\ required, mol$
$Q = charge\ transfer, C$
$I = instantaneous\ curent, \frac{C}{s}$

The electron requirement needed in the equations above were based on the reaction stoichiometry given in [Eq. 2-8] to [Eq. 2-14].

# CHAPTER 4
# $CO_2$ ELECTROCHEMICAL REDUCTION ON POLYCRYSTALLINE COPPER

## 4.1. Introduction

In this chapter, we present our results on polycrystalline copper (Cu). We studied the kinetics and potential dependence of $CO_2$ products selectivity on Cu foil in order to obtain results derived from the same reactor design and process condition as those applied on the $Cu_2O$ samples. We then compared these results to our $Cu_2O$ samples in Chapter 5 and 6.

## 4.2. Materials and Methods

We used two pieces of 99.999% Cu foil (1cm x 2cm x 0.0254 cm). For the kinetic study, the first Cu foil was dipped in 1.0M HCl and sonicated sequentially in 2-propanol, acetone and deionized $H_2O$. $CO_2$ electrochemical reduction was conducted at a fix potential of $-1.5V_{NHE}$ for 110 minutes. For the potential step experiment, the second Cu foil was prepared differently. The electrode was mechanically polished with fine grit pad and sonicated in deionized $H_2O$. $CO_2$ electrochemical reduction was conducted sequentially from $-1.0V_{NHE}$ to $-1.8V_{NHE}$ with 30 minute electrolysis at each potential.

## 4.3. Results and Discussion

### *4.3.1. Kinetics of $CO_2$ Product Formation*

In this section, we studied the kinetics of $CO_2$ reduction on Cu at a fix potential of $-1.5V_{NHE}$ for 110 minutes. We examined the product distribution in terms of formation rate and faradaic efficiency.

4.3.1.1. Characterization of Copper Electrode

SEM Analysis. The SEM images of Cu before and after $CO_2$ reduction are shown in Figure 4.1 and 4.2. The notable change in surface feature was the appearance of nanoparticles. Visually, we also observed blackish discoloration on the surface of Cu after $CO_2$ reduction. DeWulf et al. (1989) and Wasmus et al. (1990) similarly observed black film on the Cu surface after $CO_2$ reduction. Different groups have identified these surface contaminants as carbonaceous or organic species (Kyriacou and Anagnostopoulos 1993, Jermann and Augustynski 1994, Friebe et al. 1997, Wasmus et al. 1990).

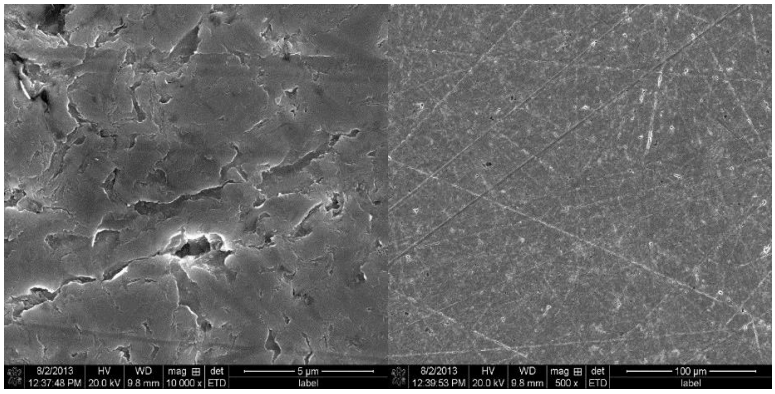

Figure 4.1. SEM of polycrystalline Cu before $CO_2$ reduction.

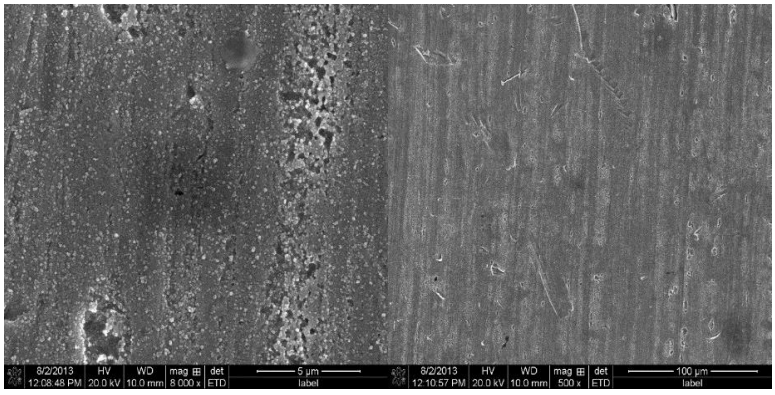

Figure 4.2. SEM of polycrystalline Cu after $CO_2$ reduction.

XRD Analysis. Figure 4.3 shows the XRD peaks of different Cu crystals. The electrode consisted mainly of Cu(200) particles followed by Cu(220), Cu(311) and Cu(111) crystal planes. The XRD scan of Cu before and after $CO_2$ reduction were the same which indicates no change in crystal structure. No crystalline carbon peaks were observed. Therefore, the black deposits on the Cu electrode were amorphous.

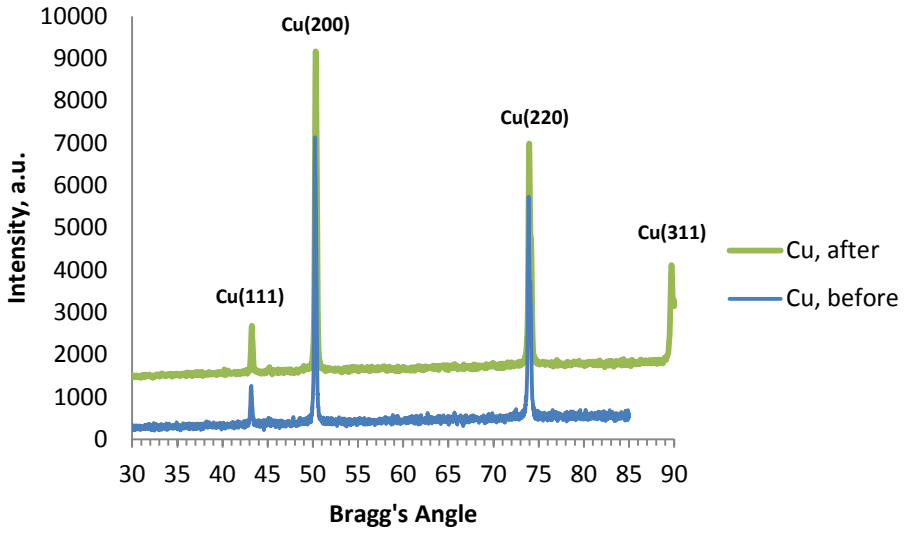


Figure 4.3. XRD profile of polycrystalline Cu before and after $CO_2$ reduction.

XPS Analysis. We also examined the surface composition of Cu before and after $CO_2$ reduction using XPS and the data is given in Table 4.1. The surface of copper consisted of Cu, C and O atoms. The surface of Cu had an unusually high atomic percentage of carbon. The Cu electrode may have been contaminated with carbon impurities during XPS analysis. Nevertheless, we observed a 4% increase in atomic C and 6% increase in atomic O coverage after $CO_2$ electrolysis. The increase in C atomic percentage supports the visual

observation of a black film. On the other hand, the increase in O atomic concentration was a result of surface oxidation during aqueous electrolysis of $CO_2$ (Frese 1991).

Table 4.1. Surface composition of polycrystalline Cu before and after $CO_2$ reduction.

| **Element** | **Before ECR** | | **After ECR** | |
|---|---|---|---|---|
| | [Atomic] % | [Mass] % | [Atomic] % | [Mass] % |
| Cu, 2p | 23.5 | 59.9 | 13.8 | 43.3 |
| C, 1s | 55.6 | 26.7 | 59.5 | 35.5 |
| O, 1s | 20.9 | 13.4 | 26.7 | 21.3 |

4.3.1.2. $CO_2$ Electrochemical Reduction

Current Profile. We monitored the current during $CO_2$ reduction on Cu electrode at -1.5$V_{NHE}$. The electrolysis of $CO_2$ on copper generated a current versus time profile given in Figure 4.4. The process registered an initial current density of 13.3 mA/cm$^2$ which decreased to 7.7 mA/cm$^2$ for an average of 9.2 mA/cm$^2$. The measured current density at the end of electrolysis was comparable to that obtained by Hori et al. (1989). The loss in current activity was a result of the adsorption of carbon deposits on the surface of Cu (Hori 2008).

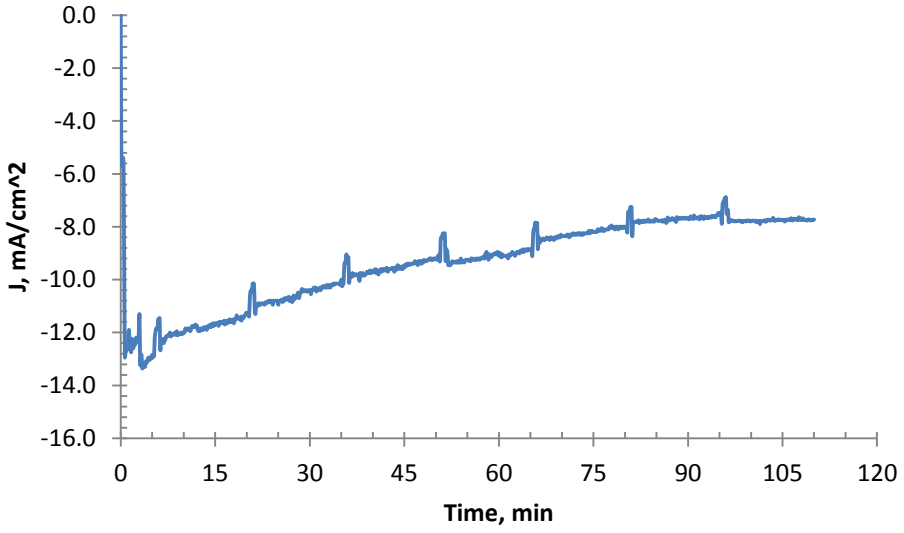


Figure 4.4. Current profile of polycrystalline Cu during $CO_2$ reduction at -1.5$V_{NHE}$.

Product Formation Rates. Figure 4.5 shows the formation rates of methane, ethylene, CO and $H_2$ between 60 minutes and 110 minutes. We computed the time average rates and obtained mean measurements of 2.8, 0.3, 8.3 and 176 µmol/cm$^2$*hr respectively. We saw a 27% decrease in the total formation rates. Individually, the values of $H_2$, $CH_4$ and $C_2H_4$ formation rates decreased by 28%, 18% and 27% respectively while CO formation rate was unchanged. We did not observe any detectable methanol, ethanol and n-propanol products. Moderate to trace amount of these products have been observed on Cu from the work of Hori's group and Kuhl's group under similar reaction conditions.

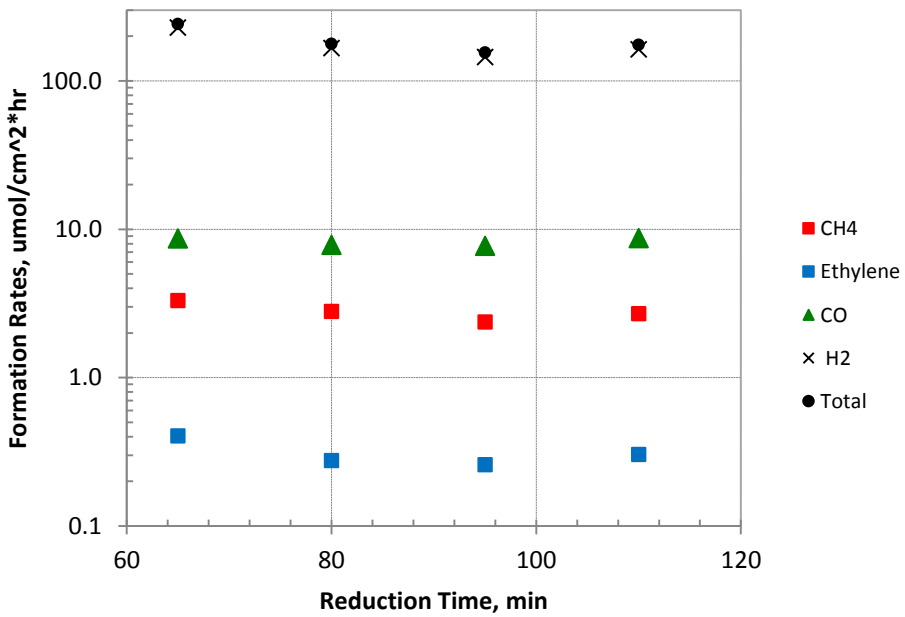


Figure 4.5. Formation rate of products on polycrystalline Cu during $CO_2$ reduction at -1.5$V_{NHE}$.

Product Faradaic Efficiencies. Figure 4.6 shows the faradaic efficiencies of methane, ethylene, CO and $H_2$ between 60 minutes and 110 minutes. We classified the products of $CO_2$ reduction into three groups based on faradaic efficiency. Major products

would have >10% faradaic efficiency. Intermediate products would have 1%-10% faradaic efficiency. Minor products would have <1% faradaic efficiency. Based on this classification; methane, ethylene and CO were intermediate products with average faradaic efficiencies of 7.5%, 1.2% and 5.5% respectively.

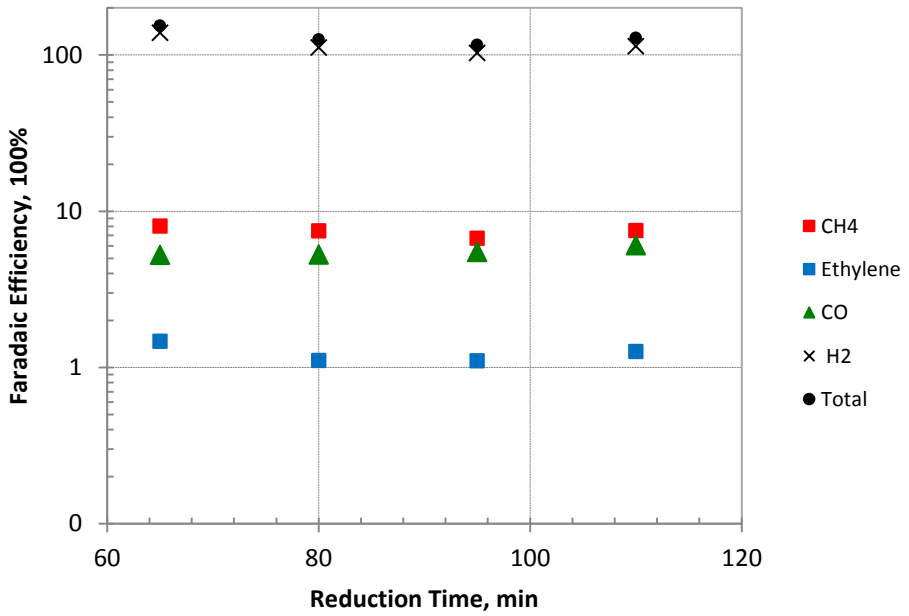


Figure 4.6. Faradaic efficiency of products on polycrystalline Cu during $CO_2$ reduction at $-1.5V_{NHE}$.

We computed the $C_2H_4/CH_4$ and $(C_2H_4+CH_4)/CO$ selectivity ratios and obtained values of 0.2 and 1.6 respectively. In comparison, Hori's group obtained a $C_2H_4/CH_4$ selectivity ratio of 0.5-0.9 which is in the same range as ours. Meanwhile, their $(C_2H_4+CH_4)/CO$ selectivity ratio was 8.9-32.3 at $-1.5V_{NHE}$. The difference in the ratio of the latter is due to the larger difference in faradaic efficiency between CO and the two hydrocarbons.

We observed higher $H_2$ faradaic efficiency compared to those obtained by Hori's group. One source of difference in selectivity ratios could come from using 0.5M instead

of 0.1M $KHCO_3$ solution. According to Hori (2008), with more concentrated $KHCO_3$ solution, a greater number of $HCO_3^-$ ions are available to react with $OH^-$ ions that are released during $CO_2$ reduction. Consequently, the pH at the electrode-electrolyte interface will be less basic promoting $H_2$ evolution. The presence of carbonaceous species could have also contributed to this high $H_2$ activity. In Chapter 6, we show that carbon electrodes mainly produce $H_2$.

*4.3.2. Effect of Potential on Product Distribution*

4.3.2.1. Current Profile

The current profile generated during $CO_2$ reduction at different potentials is presented in two ways. Figure 4.7a shows the current profile at all potentials. Meanwhile, Figure 4.7b shows the current profile between -1.0$V_{NHE}$ and -1.5$V_{NHE}$ to magnify the features at this potential range. As seen in Figure 4.7a, current density increased exponentially with potential between -1.3$V_{NHE}$ and -1.8$V_{NHE}$.

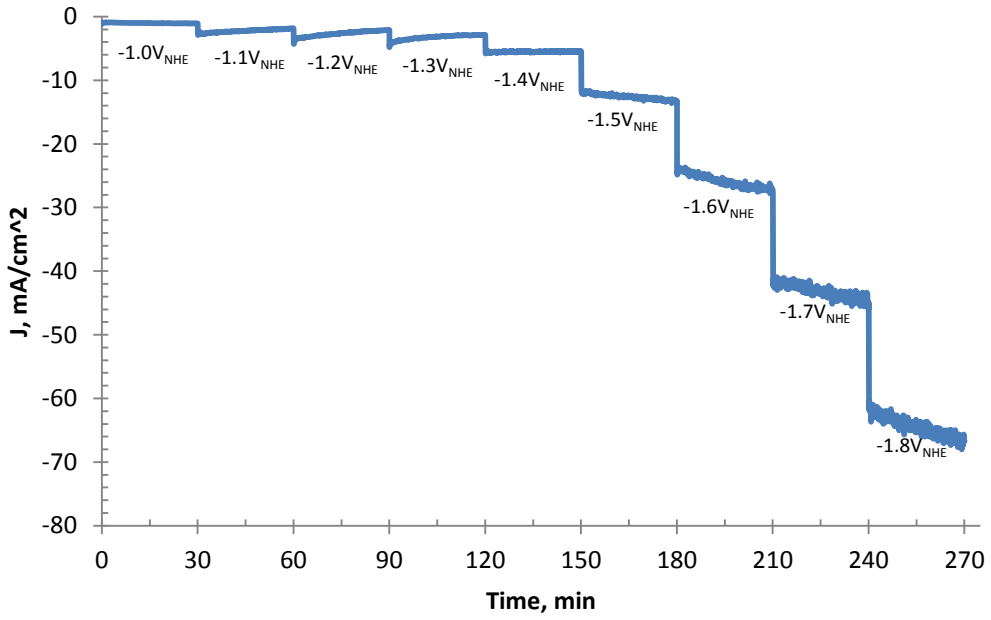


Figure 4.7a. Current profile of polycrystalline Cu during $CO_2$ reduction at different potentials.

In Figure 4.7b, we observed a decrease in current density with time at -1.1$V_{NHE}$, -1.2$V_{NHE}$ and -1.3$V_{NHE}$. Current density was steady at -1.4$V_{NHE}$. While at potential more negative than -1.4$V_{NHE}$, current density increased with time. These results indicate that Cu electrode is more susceptible to deactivation at less negative potential.

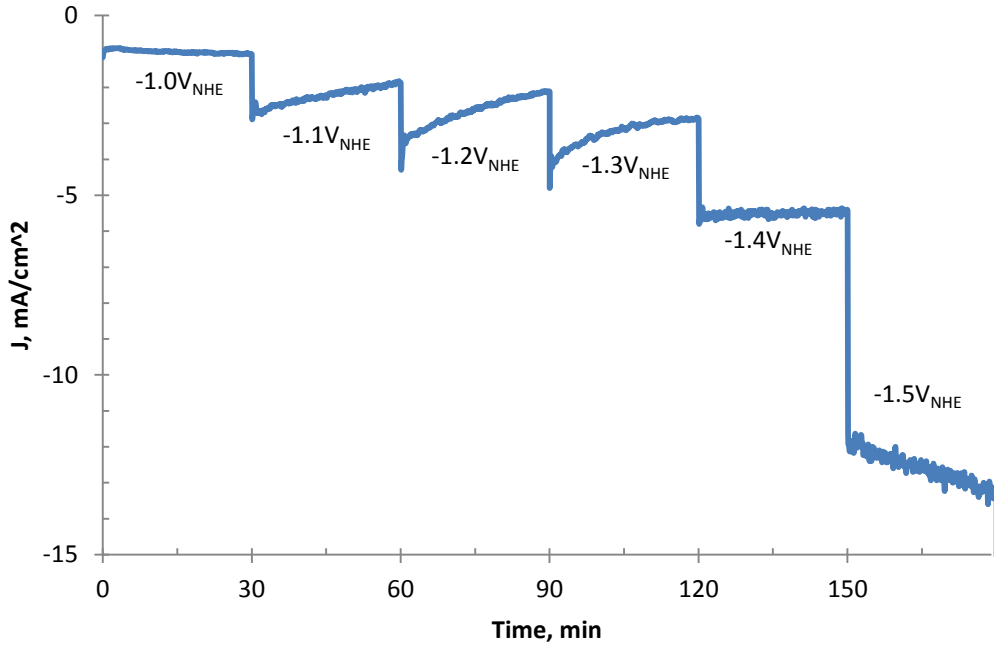


Figure 4.7b. Magnified current density versus time profile of poly-Cu at potentials between -1.0$V_{NHE}$ and -1.5$V_{NHE}$.

We then used the data in Figure 4.7a to obtain the total current versus potential (I-V) curve shown in Figure 4.8. The plot shows presence of shoulder which indicates formation of adsorbed intermediates that temporarily slowed the reduction steps (Hori et al. 1989). The adsorption and reduction of adsorbed species then accelerated at potentials more negative than -1.3$V_{NHE}$ which indicate increased turnover frequency.

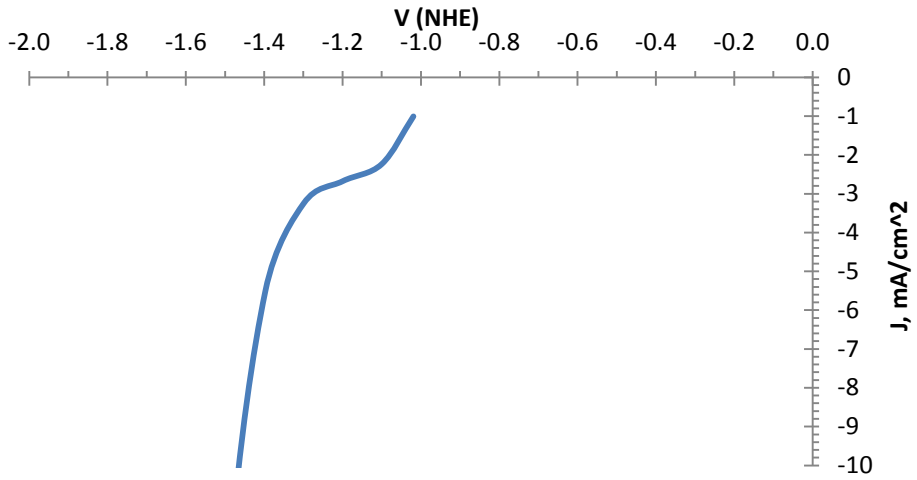


Figure 4.8. Equivalent voltammogram of polycrystalline Cu resulting from the potential step electrolysis of $CO_2$.

We also calculated the total current density used to make hydrocarbons and plotted them versus potential in Figure 4.9. The total hydrocarbon current density was computed by multiplying total hydrocarbon faradaic efficiency with total current density.

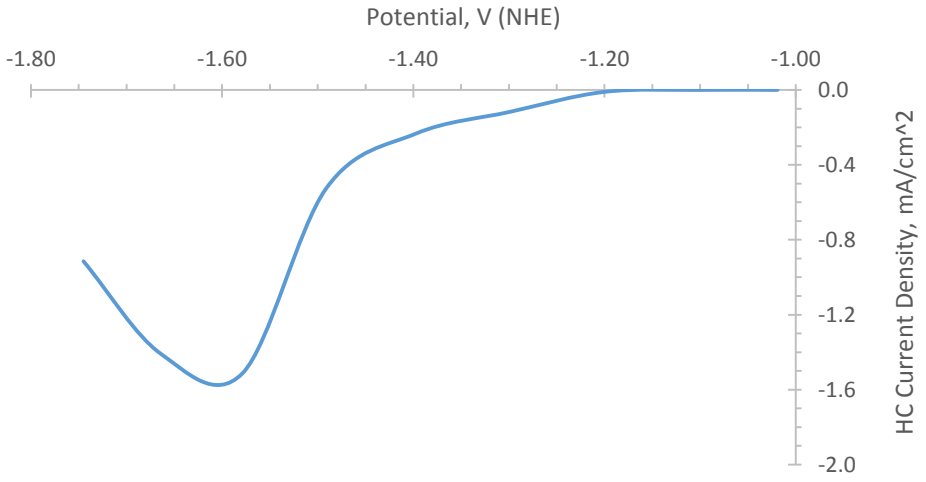


Figure 4.9. Current density versus potential of total hydrocarbon formation on polycrystalline Cu.

The graph showed a reverse in the hydrocarbon current at -1.6$V_{NHE}$, while the total current in Figure 4.8 continued to increase. This shows that the electrochemical activity towards hydrocarbon formation reached a peak at -1.66$V_{NHE}$ and decreased from there onwards. On the other hand, $H_2$ activity continued to increase exponentially.

4.3.2.2. $CO_2$ Product Formation Rates

Figure 4.10 shows the formation rates of methane, ethylene, CO and $H_2$. Reduction of $H_2O$ to $H_2$ dominated the process at all potentials and was the only detectable product at -1.0$V_{NHE}$ and -1.1$V_{NHE}$. $H_2$ formation rates accelerated beyond -1.4$V_{NHE}$ and was responsible for the majority of the charge transfer activity. $H_2$ formation is a kinetically favorable process on this copper electrode under the electrochemical conditions applied due to the abundance of $H_2O$ species and lower kinetic barrier for hydrogen adsorption and coupling (Frese, 1991).

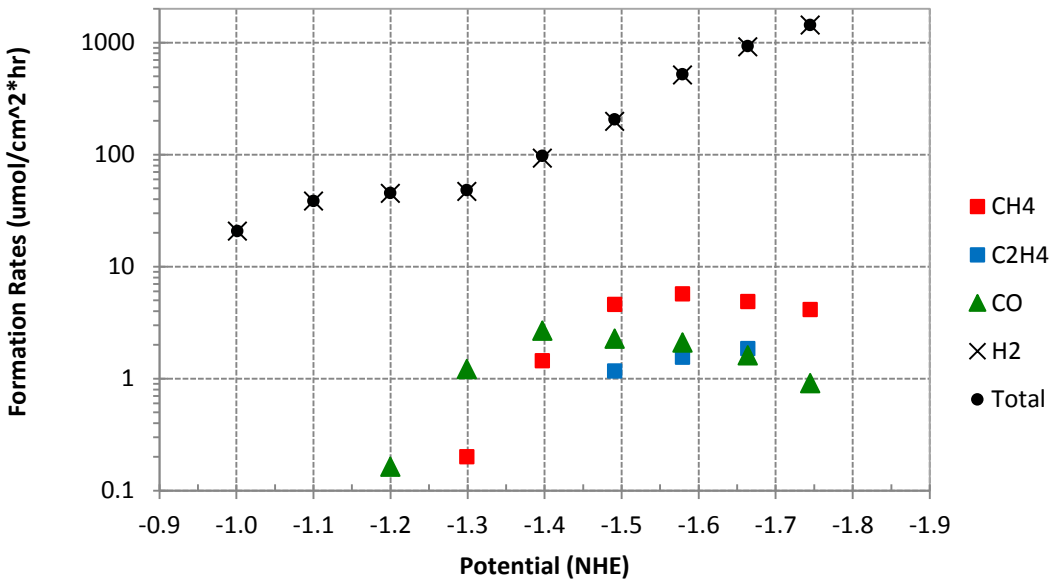


Figure 4.10. Formation rate of products on polycrystalline Cu during $CO_2$ reduction at different potentials.

Meanwhile, among the reduction products arising from $CO_2$, CO was the first product detected, at -1.20 $V_{NHE}$, followed by $CH_4$ at -1.30 $V_{NHE}$ and $C_2H_4$ at -1.49 $V_{NHE}$. The CO formation rate peaked at -1.40 $V_{NHE}$ with a rate of 2.7 µmol/cm$^2$*hr. The $CH_4$ formation rate peaked at -1.58 $V_{NHE}$ with a rate of 5.7 µmol/cm$^2$*hr. The $C_2H_4$ formation rate peaked at -1.66 $V_{NHE}$ with a rate of 1.6 µmol/cm$^2$*hr.

4.3.2.3. $CO_2$ Product Faradaic Efficiencies

Figure 4.11 shows the faradaic efficiency of methane, ethylene, CO and $H_2$ in logarithmic scale. Over-all, $H_2$ production showed highest faradaic efficiency. Between -1.0$V_{NHE}$ and -1.5$V_{NHE}$, we observed a decrease in $H_2$ faradaic efficiency. During this period, we simultaneously observed an increase in total hydrocarbon faradaic efficiency.

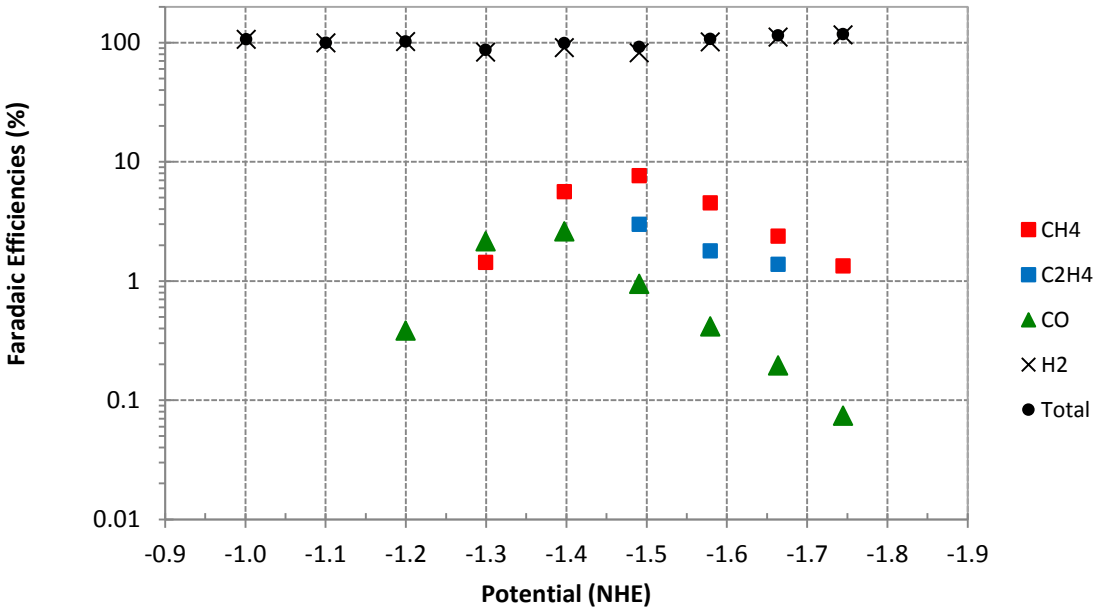


Figure 4.11. Faradaic efficiency of products on polycrystalline Cu during $CO_2$ reduction at different potentials.

Our product distribution on Cu was similar to those obtained by Hori and Kuhl's groups but with minor differences. CO was the only detectable product derived from $CO_2$ at -1.20 $V_{NHE}$. $CH_4$ was the next $CO_2$ product detected at -1.30 $V_{NHE}$ followed by $C_2H_4$ at -1.49 $V_{NHE}$. In Hori's experiment, ethylene was first detected before methane. In Kuhl's work, ethylene and methane were first observed at the same potential. The CO selectivity peaked at -1.40 $V_{NHE}$ with a faradaic efficiency of 2.6%. The $CH_4$ selectivity peaked at -1.49 $V_{NHE}$ with a faradaic efficiency of 7.7%. The $C_2H_4$ selectivity peaked at -1.49 $V_{NHE}$ with a faradaic efficiency of 3.0%.

Additionally, we did not observe an intersection of the faradaic efficiency curves between methane and ethylene. In the potential step studies done by Hori's group in 1989, Cu showed higher ethylene selectivity than methane selectivity at potentials less negative than -1.36$V_{NHE}$ and lower ethylene selectivity than methane selectivity at potentials more negative than -1.36$V_{NHE}$ (see Figure 2.2). Noda's group in 1989 similarly observed a switch point in ethylene and methane selectivity at -1.45$V_{NHE}$ (see Figure 2.3). In our case, methane selectivity was higher than ethylene selectivity at all potentials between -1.3$V_{NHE}$ and -1.7$V_{NHE}$.

The faradaic efficiencies of CO and $CH_4$ formation in this mechanically polished electrode at -1.5$V_{NHE}$ were lower than in the HCl treated Cu electrode, but do not adequately suggest that HCl treatment would offer better pre-cleaning step. Although both pre-cleaning steps remove native oxides on the Cu surface, Cu surfaces are known to re-oxidize immediately when re-exposed to air (Frese 1991). Frese reported that HCl treatment leads to formation of CuCl but did not examine its effect on Cu selectivity. Use of chloride ions to Cu surface were reported to improve hydrocarbon formation in Cu

(Kyriacou and Anagnostopoulos 1992). On the other hand, mechanically polishing with micro-sized grit pad are expected to roughen the Cu surface. Roughened Cu surfaces were observed to enhance ethylene formation (Tang et al. 2012). However, we did not observe comparable ethylene formation with that of Tang's group as a result of mechanical polishing.

This dynamic product distribution indicate a changing surface coverage of intermediate species with applied potential. The catalyst surface was initially covered with $H_{ads}$ species that were subsequently reduced to $H_2$. With additional overpotential, $CO_{ads}$ intermediates begin to form and replace some of the $H_{ads}$ species. At more negative potential, some of the $CO_{ads}$ intermediate were also further reduced to $COH_{ads}$ and $CHO_{ads}$ intermediate while the momentum of $H_2$ formation was regained.

These results also suggest that Cu surfaces has a potential window favorable for hydrocarbon formation in the vicinity of $-1.5V_{NHE}$. Outside this potential range, Cu becomes strongly selective towards $H_2$.

Additionally, these results also show evidence that there are fewer catalytic sites in Cu that reduces $CO_2$ to $CO_{ads}$ intermediates. More sites on the Cu surface produce $H_2$ regardless of the electrode potential applied and these sites likely include C-terminated surfaces from carbonaceous impurities. $H_2O$ molecules are also more readily accessible at the surface than $CO_2$ and do not suffer from transport limitation that $CO_2$ molecules experience (see Figure 4.9). Li et al. (2014) reported that the decline in hydrocarbon formation at more negative potential is due to onset of mass-transfer limitation of CO molecules.

We did not observe detectable amounts of methanol, ethanol, n-propanol and other oxygenates which have been reported in related literature because the sensitivity of the GC limits its detection to about 0.05% faradaic efficiency. Additionally, we do not have an existing calibration method to detect and measure other $C_{2+}$ gas phase products.

4.3.2.4. Comparison of Key Selectivity Ratios

We compare our results with those obtained by Hori et al. (1989), Noda et al. (1989) and Kuhl et al. (2012). Particularly, we looked at comparing selectivity ratios based on key branching points of the $CO_2$ reaction pathway; namely, (1) the desorption of $CO_{ads}$ intermediate versus further reduction of the $CO_{ads}$ intermediate and (2) the C-C coupling step. Based on experimental data, C-C coupling step is thought to occur via the dimerization of $CO_{ads}$ early in the reduction pathway (Schouten et al. 2011). Therefore the selectivity ratios considered were the following, $\frac{C_2H_4}{C_2H_4+CH_4}$ and $\frac{C_2H_4+CH_4}{C_2H_4+CH_4+CO}$ which will have values between 0 and 1. {Note that different selectivity ratio equations were used to compare the electrocatalytic activity of our Cu and $Cu_2O$ electrodes [ $C_2H_4/CH_4$ and $(C_2H_4 + CH_4)/CO$ ] }.

Figure 4.12 shows the selectivity ratio based on the C-C coupling branching step. The data from our copper electrode is marked in yellow color. Between $-1.2V_{NHE}$ and $-1.5V_{NHE}$, the groups have shown that the selectivity of Cu to $C_2H_4$ over $CH_4$ decreased with potential. However, the data points from Hori and our group also indicate the possibility that the selectivity of Cu to $C_2H_4$ over $CH_4$ could alternatively increase at more negative potential.

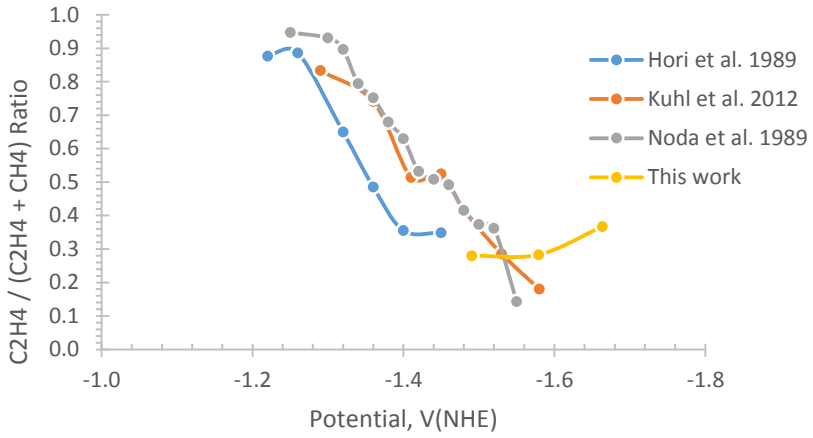


Figure 4.12. Ethylene to (ethylene + methane) ratio of different polycrystalline Cu samples.

Figure 4.13 shows the selectivity ratio based on the branching point of the $CO_{ads}$ intermediate to either CO or hydrocarbon (see reaction mechanism diagrams in Figure 2.8 and 2.9). The data from our copper electrode is marked in yellow color. Between -1.1$V_{NHE}$ and -1.7$V_{NHE}$, there is a general agreement among different groups that the selectivity of Cu to hydrocarbons (particularly $CH_4$ and $C_2H_4$) increases with potential to nearly 1. The rise of hydrocarbon selectivity in our Cu electrode is less steep than that of Hori's group. They also observed the steepest increase in hydrocarbon selectivity with potential. This was followed by the Cu electrode studied by Kuhl's group.

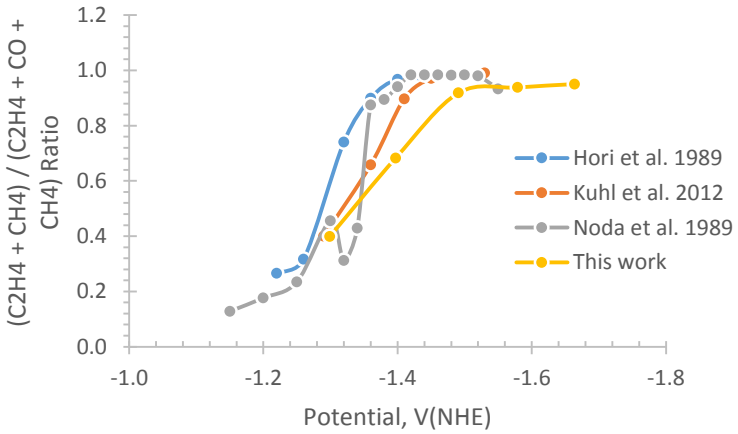


Figure 4.13. (Ethylene + methane) / (ethylene + methane + CO) ratio of different polycrystalline Cu samples.

### 4.4. Summary and Conclusion

We studied the kinetics and potential dependence of $CO_2$ reduction on polycrystalline Cu. Our kinetic study at the fixed potential of $-1.5V_{NHE}$ showed that CO, $CH_4$ and $C_2H_4$ were produced at intermediate levels. We obtained higher selectivity on $CH_4$ than $C_2H_4$ similar to what Hori's group has observed. With our potential step experiments, we detected methane before ethylene, which is different to what Hori and Kuhl's group have observed. Moreover, our $H_2$ faradaic efficiencies were higher. As such, the faradaic efficiency of our CO and hydrocarbon products were lower compared to Hori's numbers. In the next two chapters, we used our results on Cu to compare the electrocatalytic activity of $Cu_2O$, with special focus on $C_2H_4$, $CH_4$ and CO selectivity.

# CHAPTER 5
# $CO_2$ ELECTROCHEMICAL REDUCTION ON ELECTRODEPOSITED $Cu_2O$ FILM

## 5.1. Introduction

In this chapter we studied the electrocatalytic activity of $Cu_2O$ synthesized by electrochemical deposition. In Section 5.3.1, we examined the effect of oxide thickness on CO formation. In Section 5.3.2, we studied the kinetics of $CO_2$ reduction at -1.5$V_{NHE}$ and monitored other products. For these $Cu_2O$ electrodes, we used Cu as the growth substrate. In Section 5.3.3, we studied the effect of Nafion on the stability and product distribution of $Cu_2O$ film. With this experiment, we used Toray as the growth substrate. Finally in Section 5.3.4, we studied the electrocatalytic activity of $Cu_2O$ electrodeposited on CuO sublayer.

## 5.2. Materials and Methods

### *5.2.1. Effect of Oxide Thickness on CO Formation*

To study the effect of oxide thickness, we considered three different deposition times during electroplating of $Cu_2O$; namely, (1) 1 minute, (2) 10 minutes and (3) 60 minutes. We used Cu foils as the growth substrate and they were electropolished in 85% $H_3PO_4$ at 0.4$V_{Ag/AgCl}$ before the electroplating step. $Cu_2O$ films were electrodeposited using procedure described in Chapter 3.1.1.

### *5.2.2. Kinetics of $CO_2$ Reduction*

In this section, we also used Cu electropolished in 85% $H_3PO_4$ at 0.4$V_{Ag/AgCl}$ as the growth substrate. $Cu_2O$ film was electrodeposited for 30 minutes using the standard procedure given in Chapter 3.1.1 for 30 minutes.

*5.2.3. Effect of Nafion*

To study the effect of Nafion, two different Toray supported $Cu_2O$ electrodes were prepared. The first sample consisted of a Toray support base, a first layer of Nafion and a second layer of $Cu_2O$ film. A thick layer of Nafion (5 wt% in perfluorinated resin solution mixed with aliphatic alcohols and water, Sigma-Aldrich) was brush-coated onto the Toray substrate and the solvents were allowed to evaporate completely. This was followed by electrodeposition of the $Cu_2O$ film for 30 minutes. The second sample consisted of a Toray support base with a first layer of Nafion, a second layer of electrochemically deposited $Cu_2O$ and a third layer of Nafion. The same procedure was applied for the first two layers. The third layer of Nafion was then brush-coated onto the $Cu_2O$ covered Toray substrate and the electrode was allowed to dry.

*5.2.4. Kinetic Study on $Cu_2O$ Film Electrodeposited on CuO Layer*

To study the effect of depositing $Cu_2O$ layer to an existing CuO film, we used Cu support substrate dipped in 1.0M HCl. Before the electroplating step, we oxidized the Cu foil by thermal oxidation in the presence of air using a Lindberg/Blue 3 Zone Furnace at 400 $^oC$ for 4 hours with a 25 $^oC$/min heating ramp and a natural cool down. The $Cu_2O$ layer was then electrodeposited for 10 minutes.

**5.3. Results and Discussion**

*5.3.1 Effect of Oxide Thickness on CO Formation*[1]

In this section, we compared the electrocatalytic activity of $Cu_2O$ films with different oxide thicknesses. We only considered the effect of oxide thickness on the first step of $CO_2$ activation which is CO formation. In the succeeding sections, we have also considered the formation of other hydrocarbons and oxygenates.

[1]This section previously appeared on reference: Tsai, C-C., J. Bugayong, G.L. Griffin. 2012. "Role of Surface Oxide Layer during $CO_2$ Reduction at Copper Electrodes." MRS Proceedings 1446: 59-64. [Reproduced with permission from the Cambridge University Press.]

5.3.1.1. Current Profile

Figure 5.1 shows the current profile generated by the three $Cu_2O$ electrodes during $CO_2$ reduction for 20 minutes. Transient currents associated with copper oxide reduction were observed within the first 5 minutes. The 1 minute $Cu_2O$ sample had the smallest shoulder, followed by the 10 minute $Cu_2O$ sample, then the 60 minute $Cu_2O$ sample. When all reducible copper oxide particles were converted to copper (see below), the current then reached a steady-state value of approximately 3.0 mA/cm$^2$.

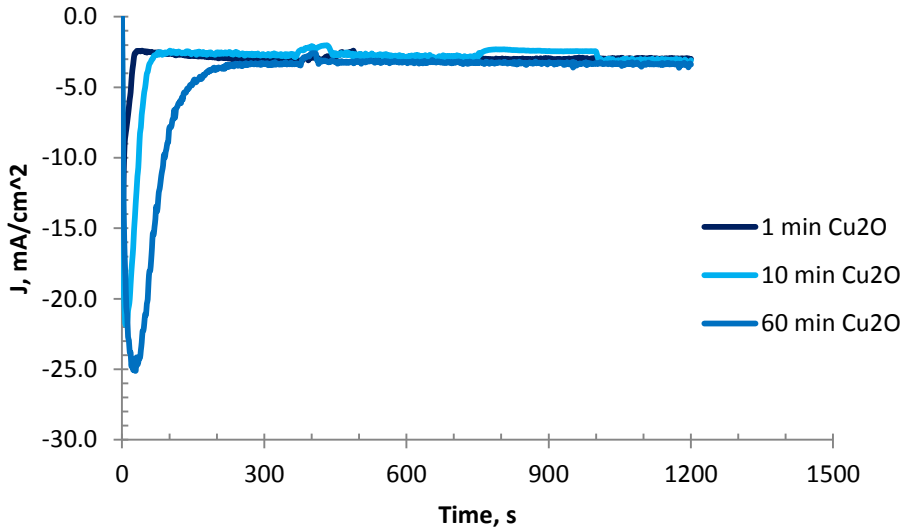


Figure 5.1. Current profile generated during $CO_2$ reduction on $Cu_2O$ film at -1.1$V_{NHE}$.

5.3.1.2. Characteristics of $Cu_2O$ Films and Their Thicknesses

The electrodeposited $Cu_2O$ films produced different colors (see Table 5.1). The 10 minute and 60 minute copper oxide films were purple in color. Meanwhile, the 1 minute $Cu_2O$ film was mainly gold color with green and purple spots. During $CO_2$ reduction at -1.1$V_{NHE}$, color changes were observed at the surface which indicates that the $Cu_2O$ layers were altered. The difference in color of the $Cu_2O$ film is due to the difference in how light travels through the film (Lee et al. 2013). The color has been used to estimate oxide

thickness of thin films such as $SiO_2$ and $Si_3N_4$ in wafer processing (Henrie et al. 2004). However, we used our data on current density versus time curves to estimate the oxide thickness using trapezoidal method. The computed oxide thickness of the $Cu_2O$ films are given in Table 5.1. The oxide thicknesses were between 0.1 and 2.0 µm. As expected, the oxide thickness increased with deposition time.

Table 5.1. Characteristics of $Cu_2O$ Electrodeposited on Cu at 1, 10 and 60 minutes.

| $Cu_2O$ | Film Color | Oxide Thickness, µm |
|---|---|---|
| 1 min | Gold, other color spots | 0.1396 |
| 10 min | Purple, uniform | 0.7144 |
| 60 min | Purple, uniform | 1.9874 |

However, the growth rate of the oxide layer decreased with time. The data points fit a decay function of the form, $y = 0.1453x^{0.6515}$ ($R^2 = 0.9964$), as shown in Figure 5.2. This was due to an increased diffusion distance for oxygen to travel to the Cu layer.

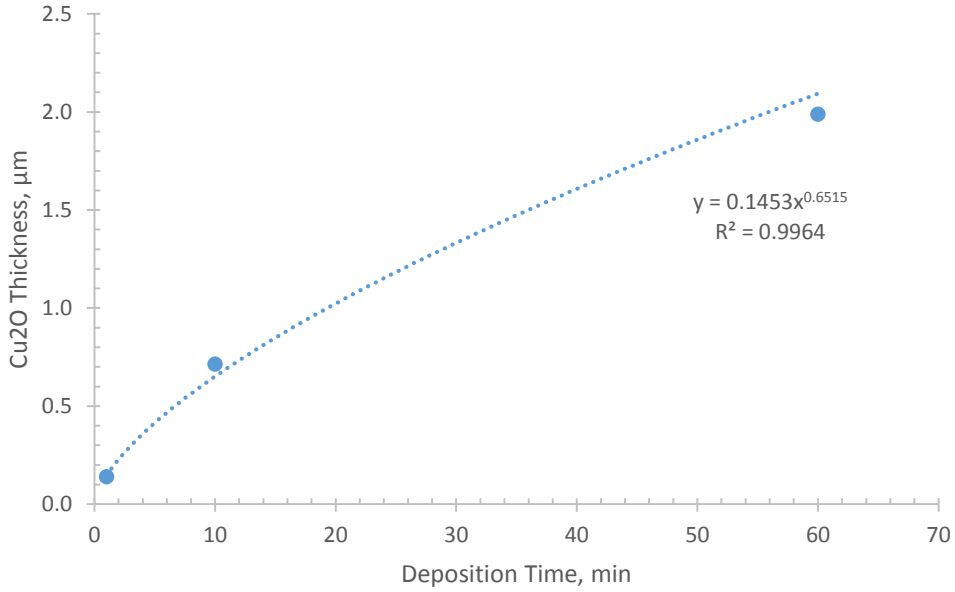


Figure 5.2. Thickness profile of $Cu_2O$ on Cu estimated from the current density versus time plot in Figure 5.1.

Consequently, the time it took to reach steady state current also increased with deposition time as follows: (a) t = 41 s for the 1 minute $Cu_2O$ sample, (b) t = 79 s for the 10 minute $Cu_2O$ sample and (c) t = 270 s for the 60 minute $Cu_2O$ sample. Interestingly, the relationship between the deposition time and the amount of reduction time under transient current condition is highly linear ($R^2$=0.9998) as shown in Figure 5.3. This suggest that the time required to reduce $Cu_2O$ particles are linearly proportional to the amount of time used during electrodeposition. The transient and deposition times were not in a one-to-one correspondence because the deposition and reduction processes were operated at different potentials.

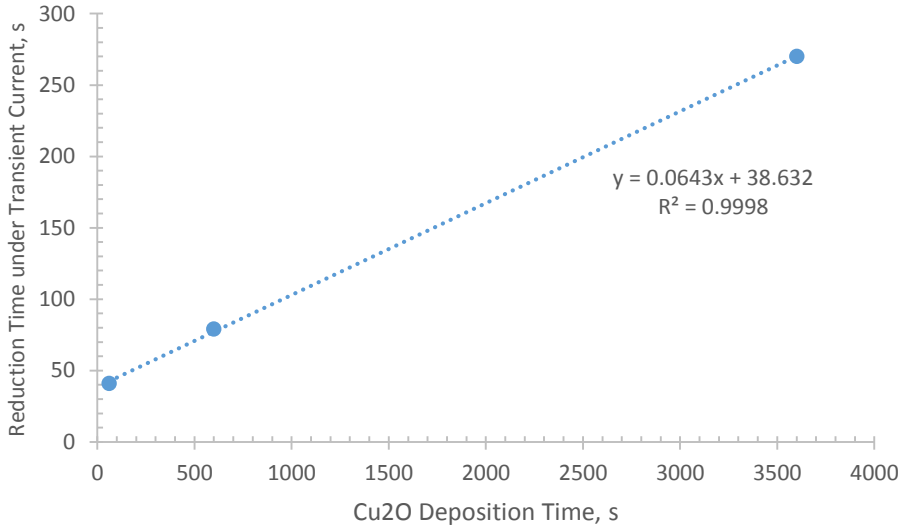


Figure 5.3. Plot of $Cu_2O$ deposition time and transient time needed to convert $Cu_2O$ to Cu.

5.3.1.3. Gas Product Analysis

CO Formation Rate. Figure 5.4 shows the formation rates of CO on these electrocatalysts. CO formation rate increased with oxide thickness. This indicates that copper surfaces derived from the reduction of thicker copper oxide increasingly favor CO

formation, perhaps metastable oxide as suggested by Li et al. in 2012. However, the graph also showed that the increase in CO formation rate decreased with oxide thickness which suggest that activity was mostly confined at the outer layer where mass transfer effect is lower. CO formation rate was higher at 5 minutes than at 20 minutes reduction time. This suggests that between 5 minutes and 20 minutes, the active sites of the catalyst layer have switched preference even though current was mostly steady. The reduction of copper oxide would cause rearrangement of atoms which would lead to about 11% decrease in volume because Cu atoms are smaller than $Cu_2O$ molecules.

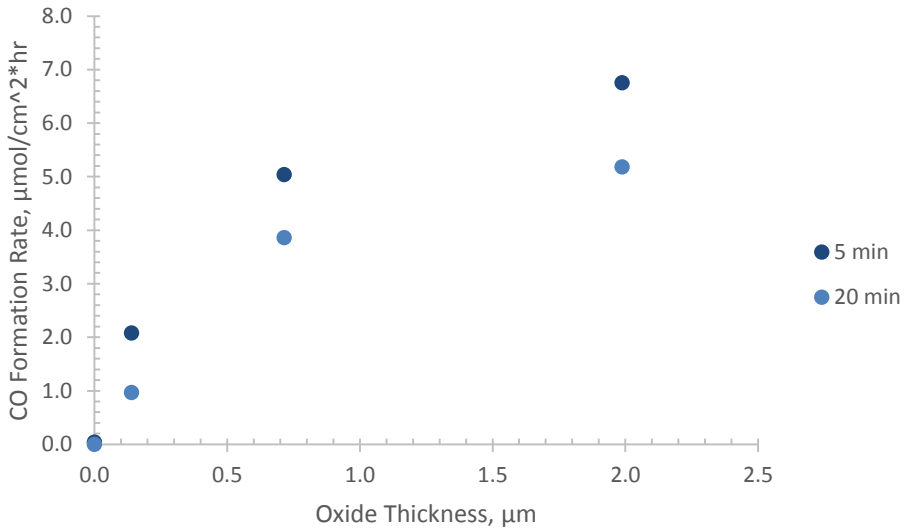


Figure 5.4. CO formation rates on $Cu_2O$ film with different oxide thicknesses.

CO Faradaic Efficiency. Figure 5.5 shows the faradaic efficiency of CO on these electrocatalysts. The faradaic efficiency rose faster than its formation rate between the 1 minute and 10 minute $Cu_2O$ electrodes and rose slower between the 10 minute and 60 minute $Cu_2O$ electrodes. The difference in slope between faradaic efficiencies and formation rates is a result of the relative magnitude of the formation rate of CO and $H_2$ at the surface.

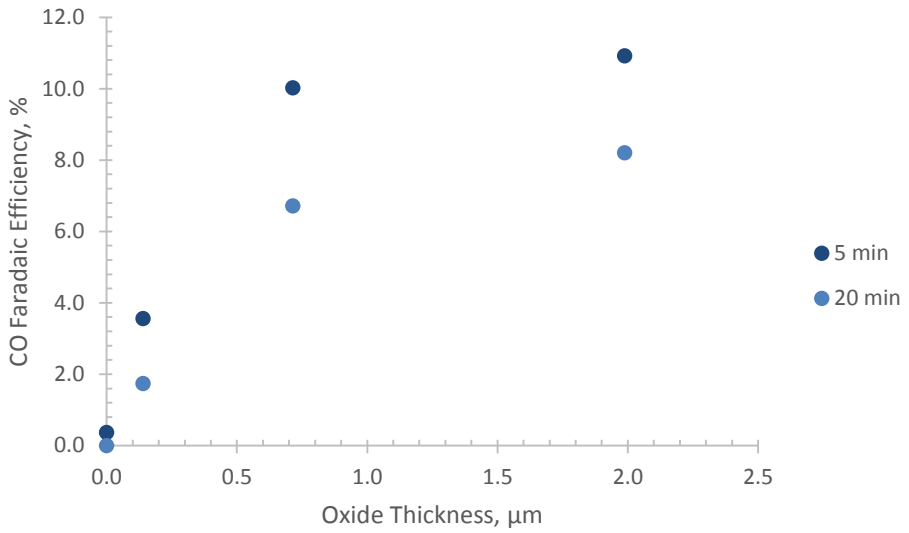


Figure 5.5. CO faradaic efficiencies on $Cu_2O$ film with different oxide thicknesses.

$H_2$ Formation Rate. Figure 5.6 shows the formation rates of $H_2$ production. The $H_2$ rates were one order of magnitude higher than the CO rates, similar to what we have observed on polycrystalline Cu in Chapter 4.

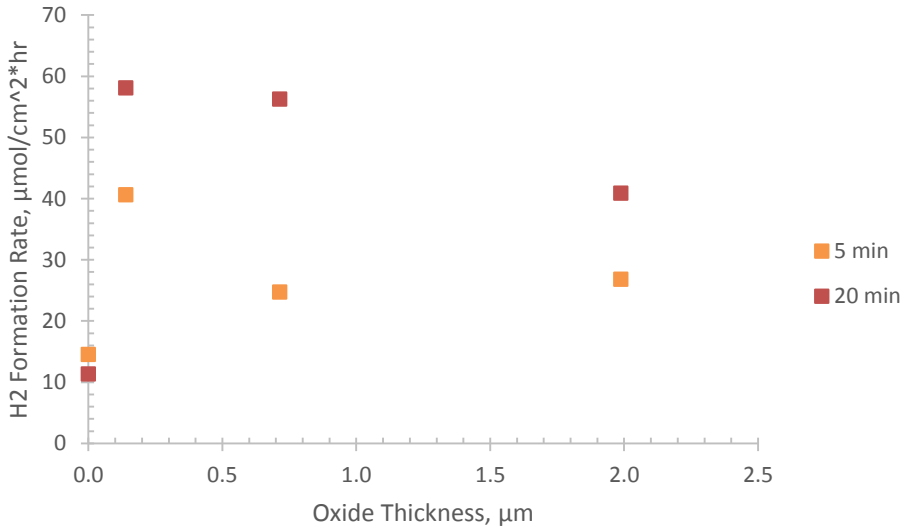


Figure 5.6. $H_2$ formation rates on $Cu_2O$ film with different oxide thicknesses.

The $H_2$ formation rates of the Cu substrate with no initial electrodeposited $Cu_2O$ were lower than that of the oxide-derived Cu electrodes because of surface area difference. As such, the CO formation rates were also lower. The formation rate increased with reduction time for the oxide-derived Cu electrodes and decreased with time in the non-oxidized Cu electrode.

$H_2$ Faradaic Efficiency. Figure 5.7 shows the faradaic efficiency of $H_2$ formation on these electrocatalysts. $H_2$ faradaic efficiency decreased with oxide thickness, which is opposite of what we observed on CO. This indicates that Cu surfaces derived from thicker $Cu_2O$ films suppress $H_2$ formation better. Nevertheless, the present $Cu_2O$ electrodes were still more efficient towards $H_2$ than CO. In Chapter 4, we listed the possible reasons for this observation which included presence of carbon impurities and higher concentration of $H_2O$ molecules on the electrolyte. $H_2O$ molecules compete with sites where $CO_2$ intermediates are adsorbed. The rate of CO and $H_2$ formation is partly controlled by the amount of $CO_{ads}$ intermediate on the surface (Hori et al. 1991).

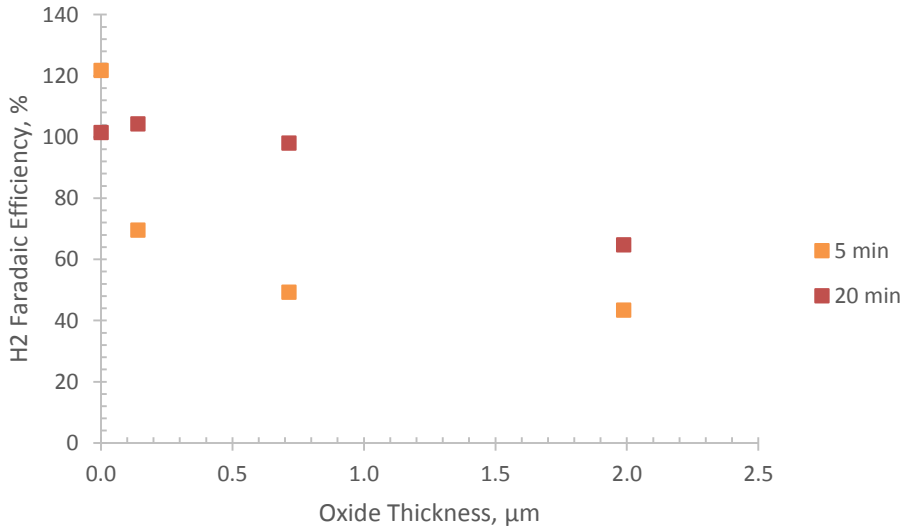


Figure 5.7. $H_2$ faradaic efficiencies on $Cu_2O$ film with different oxide thicknesses.

*5.3.2. Kinetics of $CO_2$ Reduction*

In this section, we studied the electrocatalytic activity of $Cu_2O$ film ($Cu/_{ECD}Cu_2O$) and measured other products of $CO_2$ reduction. We extended the reduction time from 20 minutes to 110 minutes to examine the activity of $Cu_2O$ electrodes at longer time period. We increased the applied potential from $-1.1V_{NHE}$ to $-1.5V_{NHE}$ to determine if we can improve the productivity and selectivity of $Cu_2O$ to CO and hydrocarbons. We characterized the catalysts using SEM and XRD before and after $CO_2$ reduction.

5.3.2.1. Electrode Characterizations

SEM Analysis. Figure 5.8 shows the SEM image of $Cu_2O$ film grown on Cu substrate. The Cu support substrate was completely covered by the $Cu_2O$ layer. The $Cu_2O$ film consisted mainly of cubes and few rectangular pyramids. The particles grew non-uniformly with average length of 800 nm.

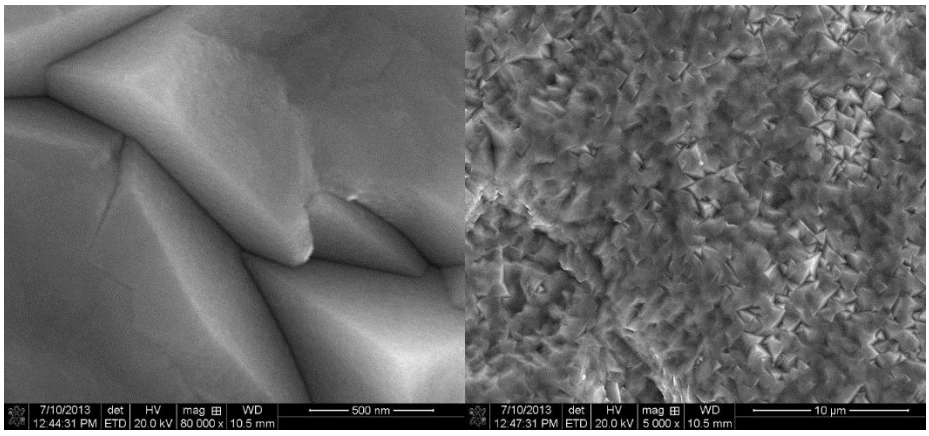


Figure 5.8. SEM of $Cu/_{ECD}Cu_2O$ electrode before $CO_2$ reduction at $-1.5V_{NHE}$ (left) 80,000x and (right) 5,000x magnification.

After $CO_2$ reduction, $Cu_2O$ evolved into smaller particles clustered into their original cubic structure (see Figure 5.9). Canals also formed on the reduced film likely aided by the lattice strain build-up caused by the decrease in particle volume during the

reduction of $Cu_2O$ to Cu. Aggressive $H_2$ evolution likely compounded the breaking of the films too.

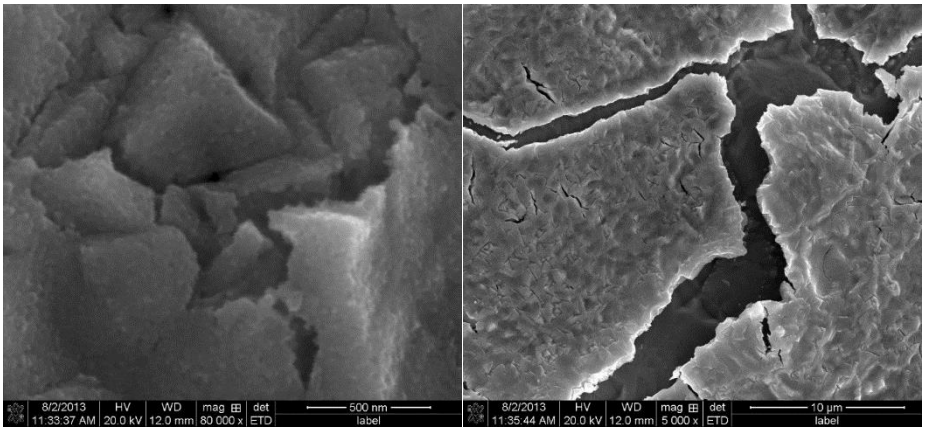


Figure 5.9. SEM of $Cu/_{ECD}Cu_2O$ electrode after $CO_2$ reduction at -1.5$V_{NHE}$ (left) 80,000x magnification and (right) 5,000x magnification.

XRD Analysis. The XRD scan of $Cu/_{ECD}Cu_2O$ electrode before $CO_2$ reduction is given in Figure 5.10. The scan revealed $Cu_2O(111)$ oriented crystal planes. There were also $Cu_2O(222)$, $Cu_2O(202)$ and $Cu_2O(200)$ crystal planes that were present in smaller quantities.

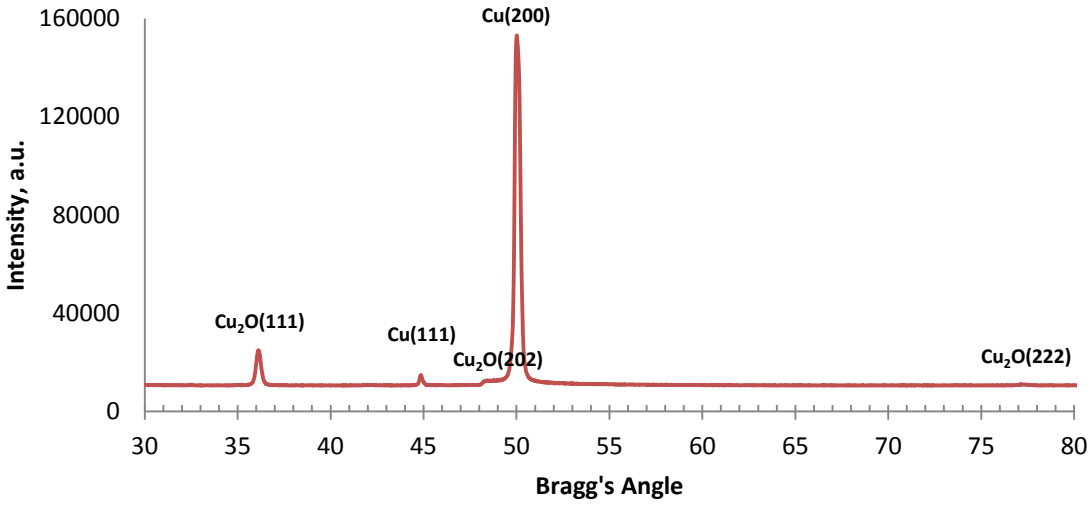


Figure 5.10. XRD scan of $Cu/_{ECD}Cu_2O$ electrode before $CO_2$ reduction.

Meanwhile, the XRD scan after $CO_2$ reduction is given in Figure 5.11. The XRD peaks of $Cu_2O$ particles disappeared, except for $Cu_2O(202)$. The intensity of Cu(200) oriented planes increased. Our XRD and SEM results confirm our earlier observation of color change when the $Cu_2O$ film was simultaneously reduced to Cu. However, we observed residual $Cu_2O$ particles.

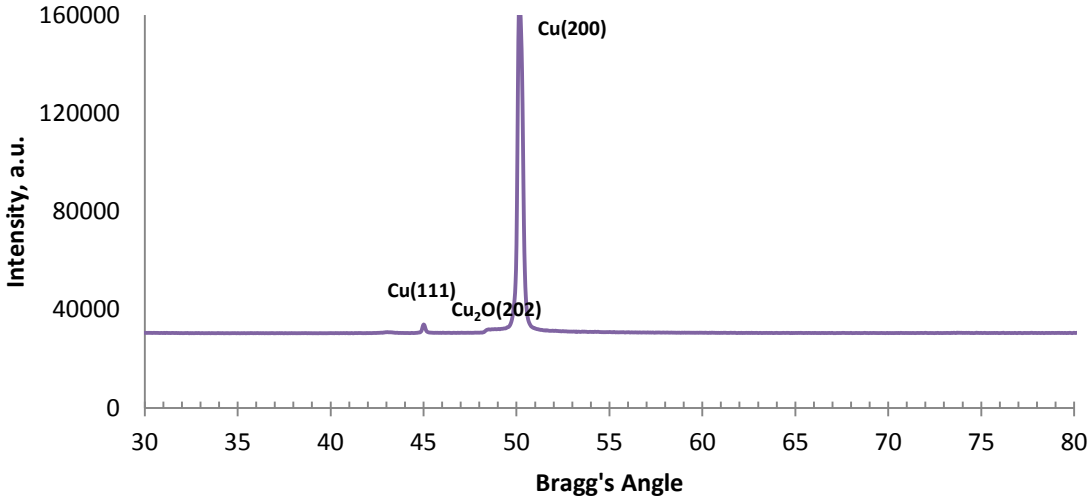


Figure 5.11. XRD scan of $Cu/_{ECD}Cu_2O$ electrode after $CO_2$ reduction.

5.3.2.2. Current Profile

Figure 5.12 shows the current profile of the $Cu/_{ECD}Cu_2O$ electrode during $CO_2$ reduction at $-1.5V_{NHE.}$ The reduction current was constant at 15 $mA/cm^2$ but with oscillation possibly caused by uneven $H_2$ bubble formation. The transient current at the beginning of electrolysis corresponded to approximately 1.29 µm oxide thickness which fits the decay function in Figure 5.2.

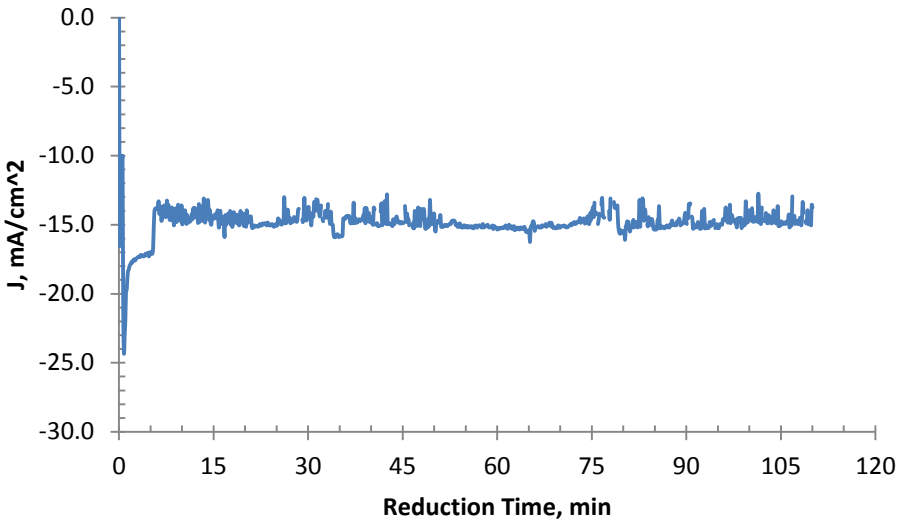


Figure 5.12. Current profile during -1.5$V_{NHE}$ electrolysis on Cu/$_{ECD}Cu_2O$ electrode.

5.3.2.3. GC Product Analysis

Product Formation Rates. Figure 5.13 shows formation rates of different liquid and gas phase products. Hydrogen was the main product with average rates of 411 µmol/$cm^2$*hr.

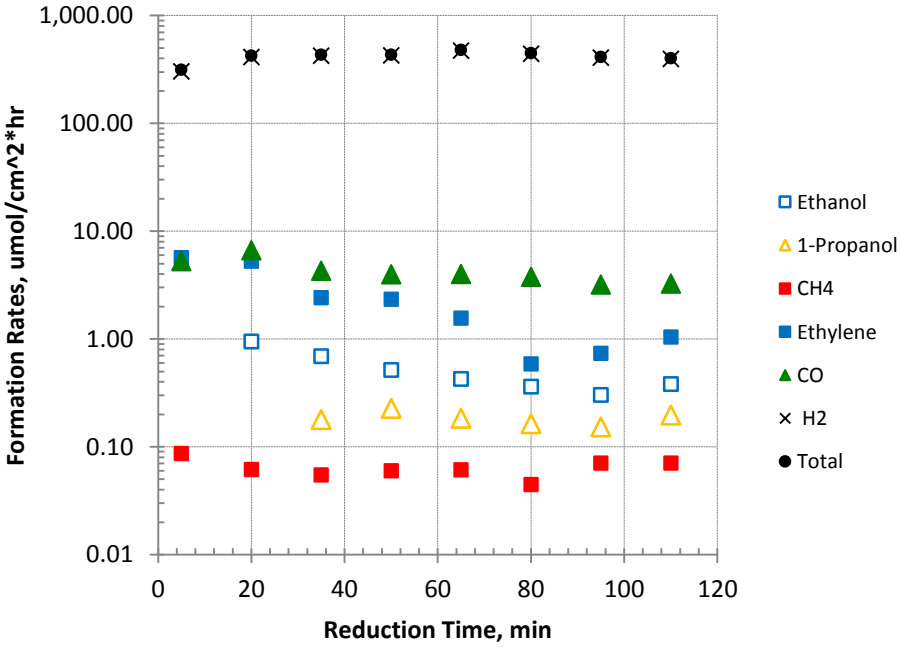


Figure 5.13. Formation rate of products on Cu/$_{ECD}Cu_2O$ electrode during $CO_2$ reduction at -1.5$V_{NHE}$.

CO was produced at a lower rate of 4.3 μmol/cm$^2$*hr followed by ethylene at 2.5 μmol/cm$^2$*hr. Methane was also detected at trace amounts of less than 0.1 μmol/cm$^2$*hr. Liquid products such as ethanol and n-propanol were also produced with rates of 0.52 and 0.18 μmol/cm$^2$*hr respectively.

Product Faradaic Efficiencies. Figure 5.14 shows the corresponding faradaic efficiencies of the $CO_2$ (and $H_2O$) reduction products. The product distribution was dynamic despite a steady current flow. The $CH_4$ selectivity was very low but stable near 0.1%. Ethylene had an initial faradaic efficiency of 11% which decreased to around 2.0% for an average of 5.2%. The decrease in ethylene faradaic efficiency did not lead to an increase in $CH_4$ or CO faradaic efficiency. $H_2$ faradaic efficiency was also relatively flat. The average CO faradaic efficiency was 1.5%.

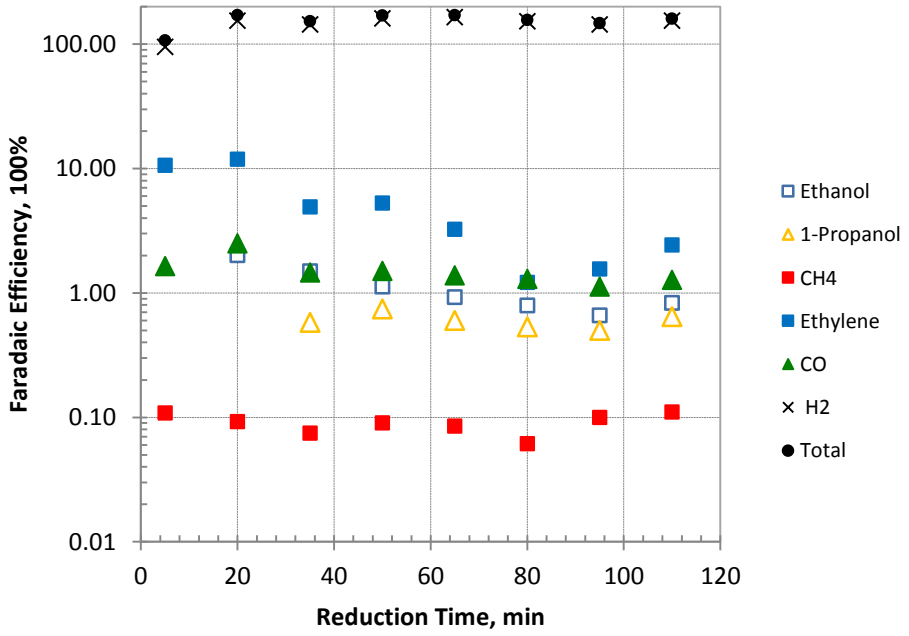


Figure 5.14. Faradaic efficiency of products on $Cu/_{ECD}Cu_2O$ electrode during $CO_2$ reduction at -1.5$V_{NHE}$.

Most likely, there was an increase in formate selectivity which we did not monitor. The pathway to formation of $HCOO^-$ does not pass through the $CO_{ads}$ intermediate unlike the hydrocarbons and oxygenates. The formate route is also considered terminal. Although more Cu particles were (200) oriented than (111), we do not have information on the relative composition at the surface. But ethylene selectivity was better than methane selectivity which is different to what we have observed with polycrystalline Cu.

In comparison to our results at $-1.1V_{NHE}$ electrolysis (see Section 5.3.1), the CO faradaic efficiency at $-1.5V_{NHE}$ was lower. This is in agreement with Hori's observation on CO. Meanwhile, the $H_2$ faradaic efficiency at $-1.5V_{NHE}$ was higher than at $-1.1V_{NHE}$ which is opposite to Hori's observation on $H_2$.

We also compared the $C_2H_4$ and $CH_4$ selectivity of electrodeposited $Cu_2O$ with that of polycrystalline Cu in Chapter 4. The $C_2H_4/CH_4$ efficiency ratio in the Cu catalyst was 0.2. With electrodeposited $Cu_2O$ catalyst, the $C_2H_4/CH_4$ efficiency ratio increased to 57.2. The enhanced ethylene selectivity in Cu resulting from the reduction of electrodeposited $Cu_2O$ is due to the formation of more low-coordinated active sites (Li et al. 2012; Tang et al. 2012).

*5.3.3. Effect of Nafion*

Nafion is commonly used as both electrolyte and support substrate in proton exchange membrane fuel cells (PEMFCs) and PEM electrolyzers. They are excellent materials in these applications because of their high proton conductivity and low electron conductivity (Yaroslavtsev 2013, Peighambardoust et al. 2010, Ito et al. 2011, DeWulf and Bard 1988). Nafion was also used to improve wettability of carbon nanotubes (CNTs) in the preparation of amperometric biosensors (Wang et al. 2003).

In this section, we studied the effect of Nafion on the selectivity of electrodeposited $Cu_2O$ film. Nafion is incorporated to the electrode in two configurations; namely, (1) Toray/Nafion/$Cu_2O$ and (2) Toray/Nafion/$Cu_2O$/Nafion. Toray was coated with Nafion before $Cu_2O$ was electrodeposited for 30 minutes. Electrolysis of $CO_2$ was performed at $-1.5V_{NHE}$ for 110 minutes. We monitored CO, $CH_4$, $C_2H_4$, ethanol, n-propanol and $H_2$ products with our GC instrument and characterized the electrodes with SEM, XRD and XPS.

5.3.3.1. Electrode Characterizations

SEM of Toray/Nafion/$Cu_2O$. The fresh $Cu_2O$ film electrodeposited on Toray exhibited a microsphere structure of overlapping cubes (see Figure 5.15). As seen in the right image, there were exposed parts of the Toray growth substrate.

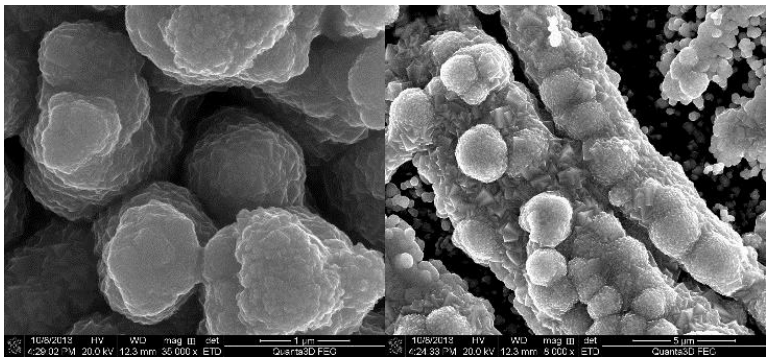

Figure 5.15. SEM of fresh Toray/Nafion/$Cu_2O$ taken at different magnifications, (left) 35,000x and (right) 8,000x.

After $CO_2$ electrolysis, an evolution of morphology was observed (see Figure 5.16). The microspheres became less defined and there was formation of nanoparticles. The formation of nanoclusters appeared to increase the surface area available for $CO_2$ reduction.

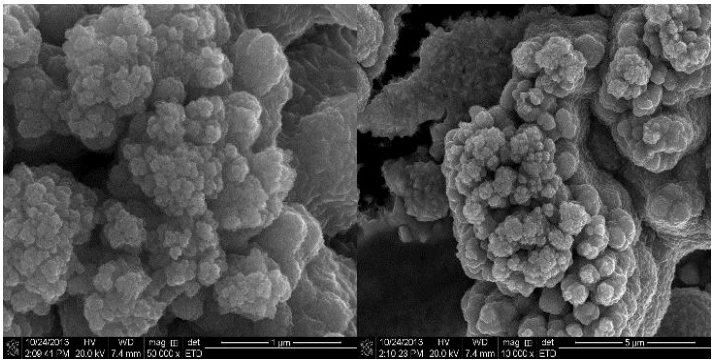

Figure 5.16. SEM of Toray/Nafion/$Cu_2O$ taken at 50,000x (left) and 10,000x (right) magnification.

SEM of Toray/Nafion/$Cu_2O$/Nafion. Figure 5.17 shows the SEM of the fresh $Cu_2O$ electrode with an outer layer of Nafion. The image on the left only shows Nafion because the $Cu_2O$ particles were fully covered in this region of the electrode. Since we did not obtain a good image of the TNEN electrode due to poor surface conductivity, a representative image was taken from the TNE electrode for the image on the right. Note that both $Cu_2O$ electrodes were prepared sequentially on the same plating bath and operating condition. Likewise, as will be shown in the SEM after $CO_2$ reduction (in Figure 5.18), there was evidence of an initial formation of microspheres similar to what we observed with our TNE electrode.

Despite saturating the surface of the $Cu_2O$ film with the Nafion solution, we still observed regions of the electrode surface that were not covered with Nafion. This was because when excess amount of the Nafion solution dried out, the solidified Nafion clumped together to achieve physical equilibrium. We have also observed this event while coating Nafion to the polished glassy carbon plate. Nevertheless, $Cu_2O$-nafion interfaces were present and may offer unique electrocatalytic activity towards $CO_2$ conversion. The SEM in Figure 5.17 shows microspheres of $Cu_2O$ cubes.

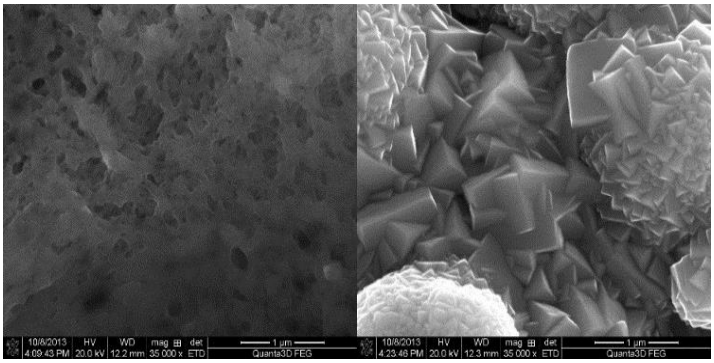

Figure 5.17. SEM of Toray/Nafion/$Cu_2O$/Nafion before $CO_2$ reduction (left) $Cu_2O$ not visible and fully covered in Nafion (right) representative image taken from the TNE sample.* (*Note: Both electrodes were prepared sequentially on the same bath and electrodeposition condition).

After $CO_2$ reduction, the $Cu_2O$ microspheres again evolved into dispersed nanoclusters that did not retain their cubic architecture (see Figure 5.18).

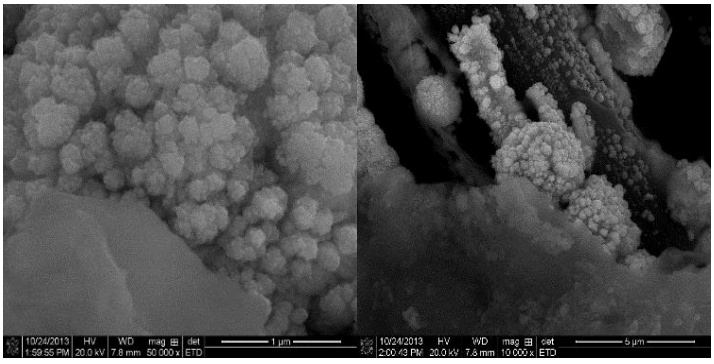

Figure 5.18. SEM of Toray/Nafion/$Cu_2O$/Nafion after $CO_2$ reduction taken at (left) 50,000x and (right) 10,000x magnifications.

XRD Scan of Toray/Nafion/$Cu_2O$. The XRD scan of Toray/Nafion/$Cu_2O$ before $CO_2$ reduction is given in Figure 5.19. The oxide is mostly made up of $Cu_2O$(110) crystal planes with lower number of $Cu_2O$(200) and $Cu_2O$(220) crystal planes. This is different from $Cu_2O$ film electrodeposited on Cu which were mostly oriented in the (111) direction.

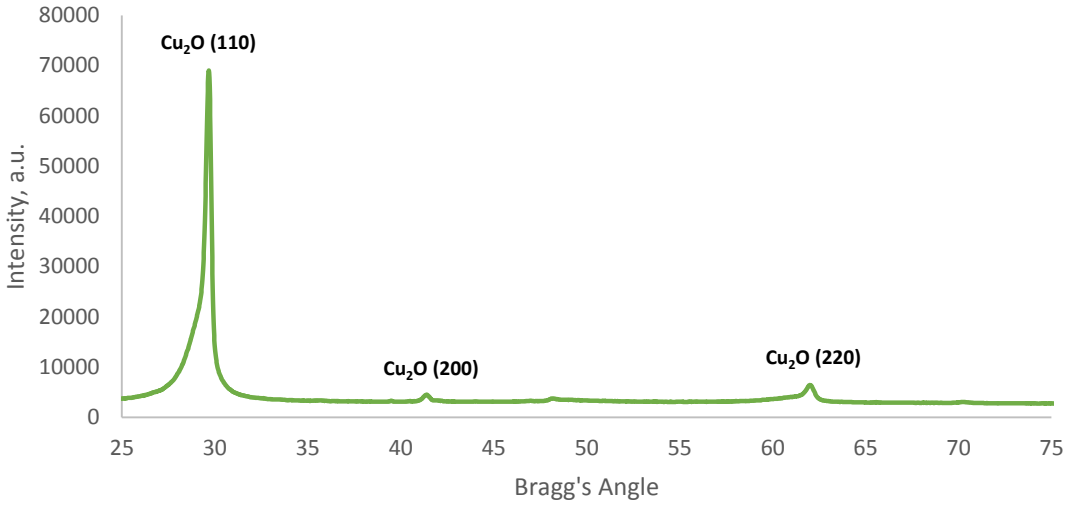


Figure 5.19. XRD scan of Toray/Nafion/$Cu_2O$ electrode.

XRD Scan of Toray/Nafion/$Cu_2O$/Nafion. The XRD scan before $CO_2$ reduction is given in Figure 5.20. The oxide has similar distribution of crystal phases as that of the Toray/Nafion/$Cu_2O$ electrode.

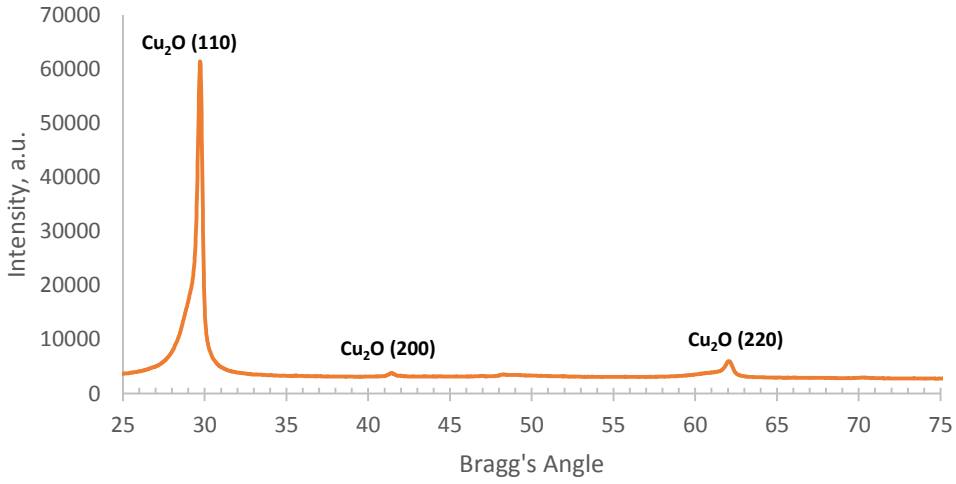


Figure 5.20. XRD scan of Toray/Nafion/$Cu_2O$/Nafion electrode.

XPS Scan of Toray/Nafion/$Cu_2O$. The XPS spectra and elemental composition of Toray/Nafion/$Cu_2O$ electrode were determined. The XPS profile is given in Figure 5.21 and shows the peaks of $Cu^{2p}$, $F^{1s}$, $O^{1s}$, $C^{1s}$ and contaminants typically observed during XPS analysis at their characteristic binding energies.

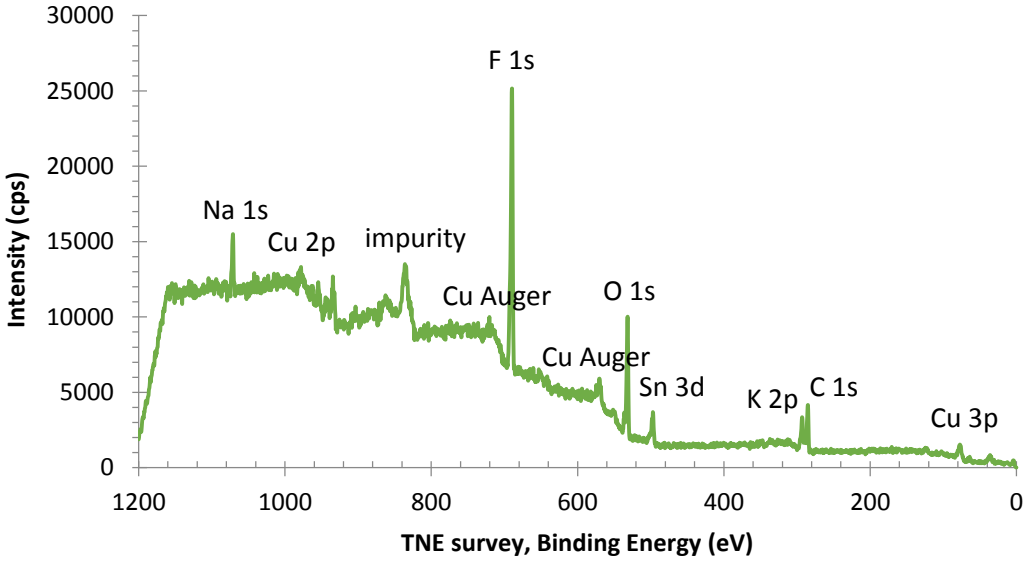


Figure 5.21. XPS spectra of surface elements in Toray/Nafion/$Cu_2O$ electrode.

Meanwhile, the surface composition derived from the elemental peak areas is given in Table 5.2. Flourine made up the bulk of the surface with about 57% atomic and 56% mass concentration. Nafion which has a molecular formula of $C_7HF_{13}O_5S \cdot C_2F_4$ contributed to the high signal of fluorine. Stoichiometrically, the $Cu_2O$ particle would have an atomic Cu/O ratio of 2. However in our sample, the Cu/O ratio was only 0.26. This is because O atoms from Nafion were also accounted.

Table 5.2. Surface composition of Toray/Nafion/$Cu_2O$ electrode.

| Element | [Atomic] % | [Mass] % |
|---|---|---|
| Cu 2p | 5.0 | 16.4 |
| O 1s | 19.3 | 16.0 |
| F 1s | 56.9 | 56.0 |
| C 1s | 18.8 | 11.6 |

XPS Scan of Toray/Nafion/$Cu_2O$/Nafion. The XPS spectra and elemental composition of Toray/Nafion/$Cu_2O$/Nafion electrode were aso determined. The XPS profile is given in Figure 5.22.

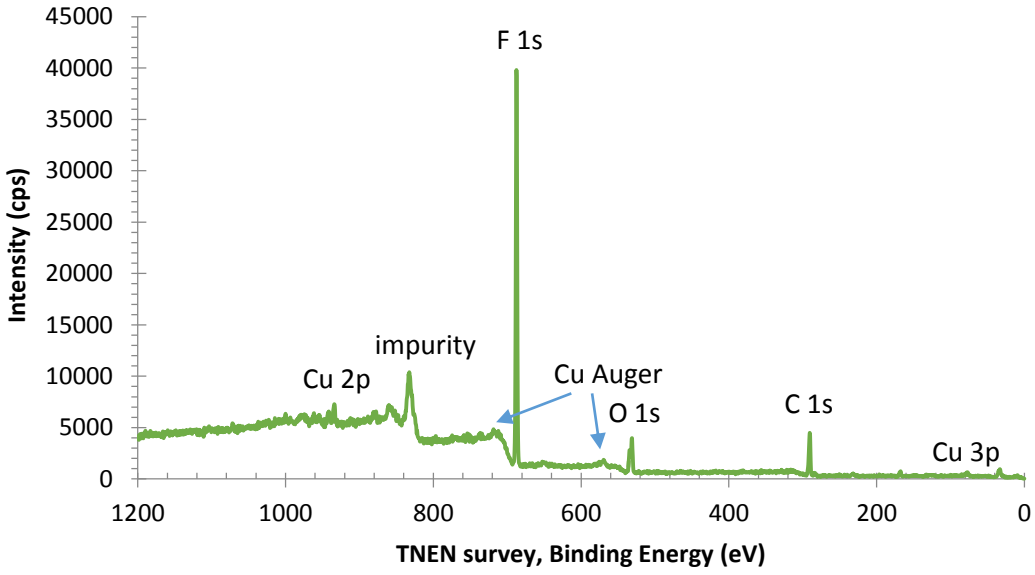


Figure 5.22. XPS spectra of surface elements in Toray/Nafion/$Cu_2O$/Nafion electrode.

Meanwhile, the surface composition derived from the elemental peak areas is given in Table 5.3. Flourine again made up the bulk of the surface with about 81% atomic and 77% mass concentration. The higher F content is due to the additional Nafion layer applied over the $Cu_2O$ film. The Cu/O ratio was 0.30.

Table 5.3. Surface composition of Toray/Nafion/$Cu_2O$/Nafion electrode.

| Element | [Atomic] % | [Mass] % |
|---|---|---|
| Cu 2p | 3.7 | 11.8 |
| O 1s | 12.4 | 9.9 |
| F 1s | 80.8 | 76.5 |
| C 1s | 3.0 | 1.8 |

5.3.3.2. Current Profile

Figure 5.23 compares the amount of current that flowed on both electrodes during $CO_2$ reduction. In the Toray/Nafion/$Cu_2O$ (TNE) electrode, the reduction process achieved steady-state current of -18 mA after 20 minutes.

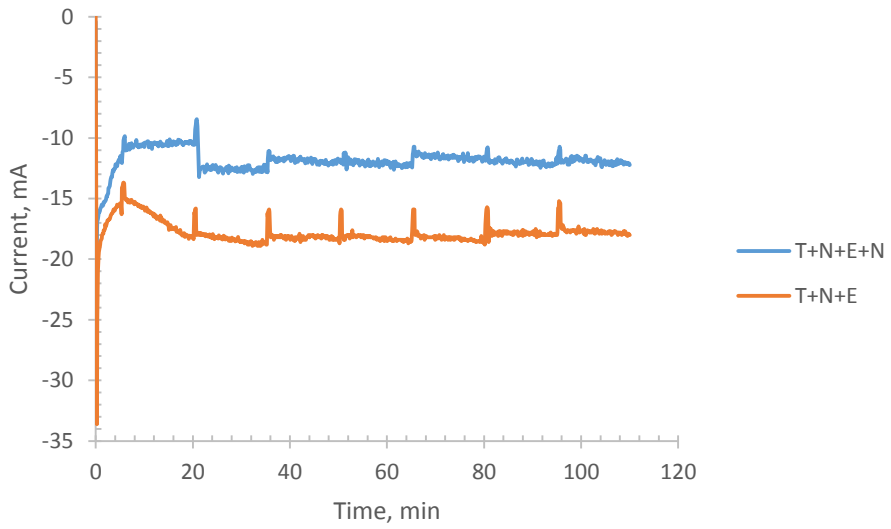


Figure 5.23. Current profile of TNEN and TNE electrodes during $CO_2$ electrolysis at -1.5$V_{NHE}$.

In the Toray/Nafion/$Cu_2O$/Nafion (TNEN) electrode, the reduction process achieved steady-state current of -12 mA after 20 minutes. The lower current in TNEN electrode suggests that the Nafion coating may be inhibiting current flow to the $Cu_2O$ surfaces.

5.3.3.3. GC Product Analysis

Comparison of Product Formation Rates. We then compared the electrocatalytic activity of the two electrodes by looking at their product formation rates. Figure 5.24 shows the product formation rates in the TNE electrode. The initial production rate of CO and $C_2H_4$ were 7.3 and 4.2 µmol/cm$^2$*hr respectively. However, the rates decreased to 1.6 and 0.8 µmol/cm$^2$*hr at the end of the process for an average of 3.1 and 1.8 µmol/cm$^2$*hr.

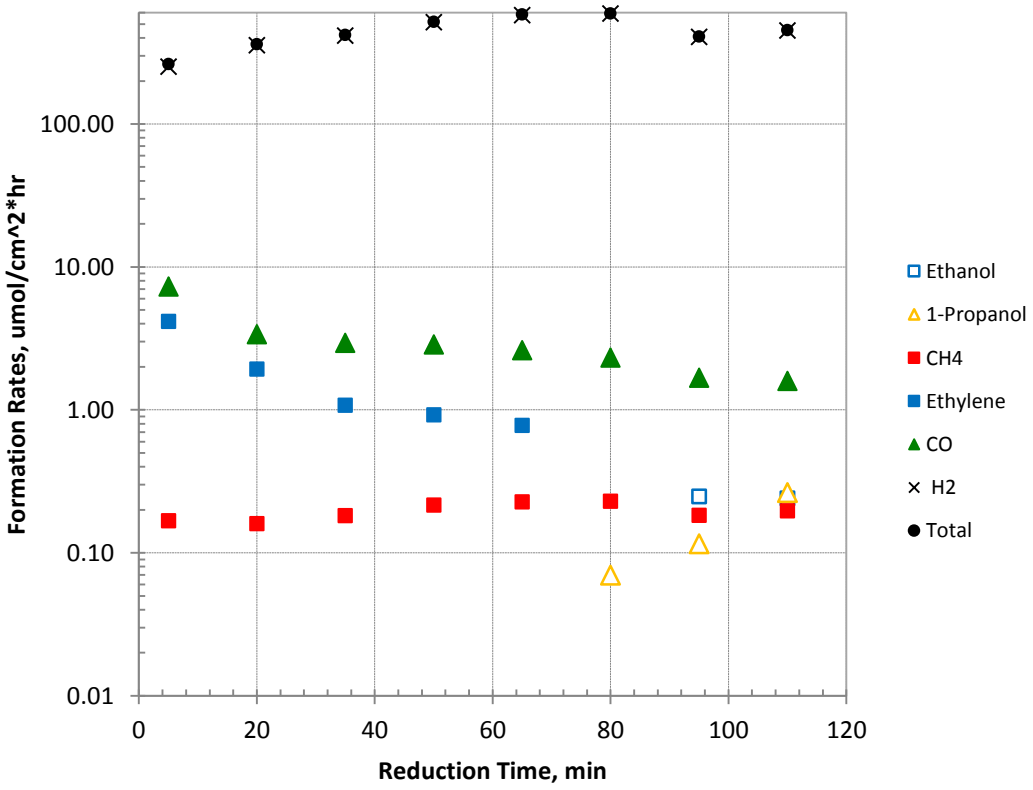


Figure 5.24. Formation rate of products on TNE electrode during $CO_2$ reduction at -1.5$V_{NHE}$.

Meanwhile, Figure 5.25 shows the product formation rates in the TNEN electrode where the production rate of CO and $C_2H_4$ were more stable with mean measured values of 5.3 and 3.2 µmol/cm$^2$*hr respectively. The liquid products ethanol and n-propanol

increased then stabilized with time for an average rate of 0.6 and 0.2 μmol/cm$^2$*hr respectively. We did not observe trace amount of $CH_4$ in the TNEN electrode.

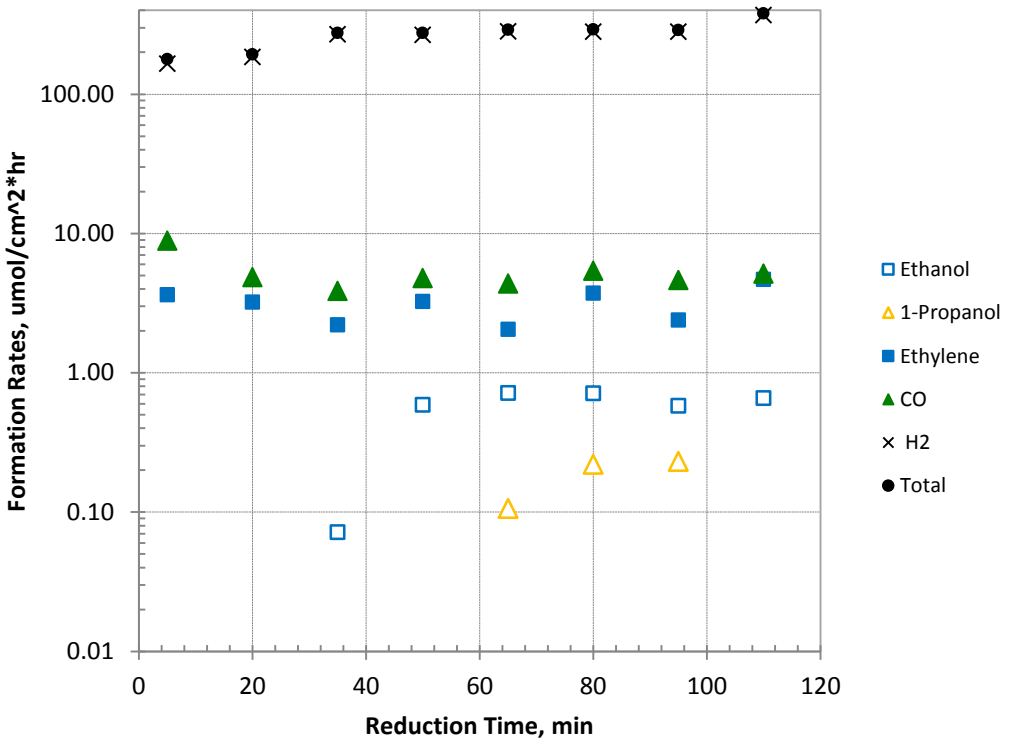


Figure 5.25. Formation rate of products on TNEN electrode during $CO_2$ reduction at -1.5$V_{NHE}$.

The mean total product formation rate was 450 μmol/cm$^2$*hr in the TNE electrode and 272 μmol/cm$^2$*hr in the TNEN electrode. The difference in the total product formation rate was in agreement with the difference in their steady state current. The bulk of production came from the reduction of $H_2O$ to $H_2$.

Comparison of Product Faradaic Efficiencies. Figure 5.26 shows the product distribution on the TNE electrode. CO selectivity decreased from the faradaic efficiency of 3.0% to 0.6%. Ethylene selectivity also decreased from the faradaic efficiency of 10.0% to

1.6% at 65 minutes before it became undetectable. The average faradaic efficiency of ethylene and CO were 4.0% and 1.1% respectively. Both ethanol and n-propanol were detected later into the process at average faradaic efficiencies of less than 1.0%.

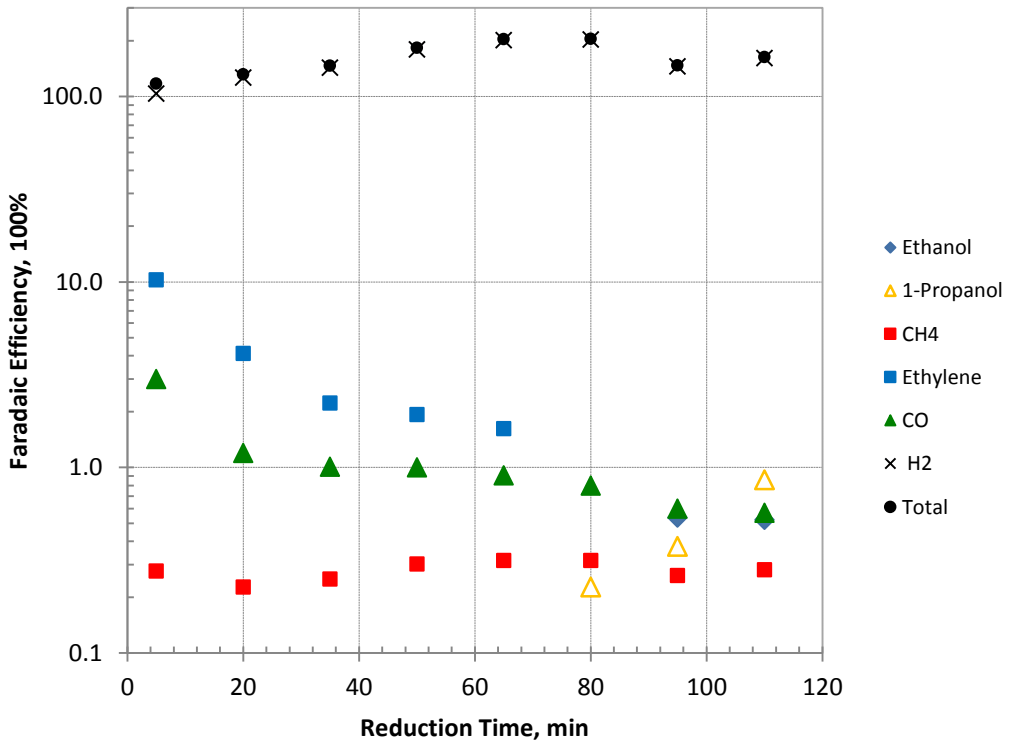


Figure 5.26. Faradaic efficiency of products on TNE electrode during $CO_2$ reduction at $-1.5V_{NHE}$.

For the TNEN electrode, we observed a better maintained selectivity towards CO and $C_2H_4$ (see Figure 5.27). Meanwhile, ethanol selectivity increased with reduction time then stabilized between 50 and 110 minute reduction time. However, we did not detect any methane in the TNEN sample. The average faradaic efficiency of ethylene, CO, ethanol and n-propanol products were 8.6%, 2.4%, 1.5% and 0.8% respectively.

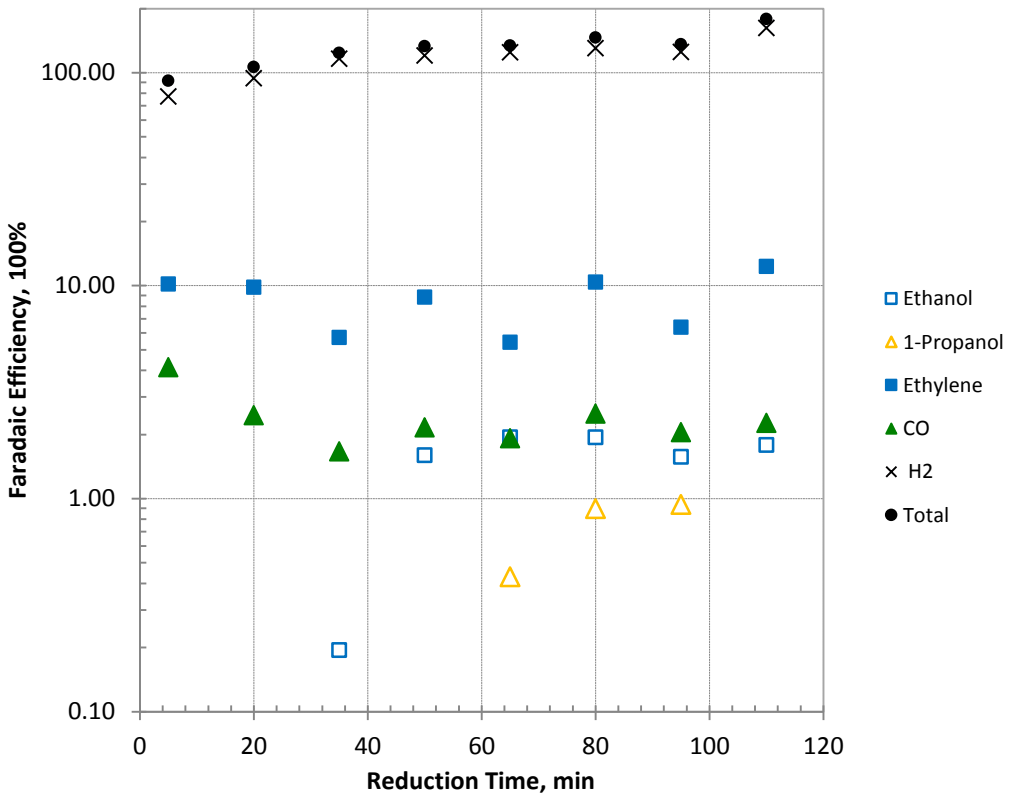


Figure 5.27. Faradaic efficiency of products on TNEN electrode during $CO_2$ reduction at -1.5$V_{NHE}$.

These results suggest that Nafion may be stabilizing the formation of CO and $C_2H_4$. The reduced Cu-nafion interface may be active site in the formation of CO and $C_2H_4$ while being more selective to $C_2H_4$ than to $CH_4$. The Nafion overlayer may be inhibiting a key intermediate in the formation of $CH_4$ while promoting the C-C coupling step. Hori suggested that $CH_4$ formation is enhanced by $H_2$ formation, however we did not consistently observe that with our results.

*5.3.4. Kinetic Study on $Cu_2O$ Film Electrodeposited on CuO Layer*

We also studied the electrocatalytic activity of $Cu_2O$ film deposited on a thermally grown CuO. This catalyst was examined by Ghadimkhani's group using

photoelectrochemical reduction of $CO_2$. In their experiment, the photoelectrode was irradiated with visible light and simultaneously electrolyzed at -0.2$V_{NHE}$ for 90 minutes. They obtained 85 μM methanol at 95% selectivity. In this section, we substituted photogenerated current with application of a more negative potential (-1.5$V_{NHE}$) and examined the product distribution.

5.3.4.1. Electrode Characterizations

SEM Analysis. SEM images were taken at different stages of the fabrication of Cu/$_{TH}$CuO/$_{ECD}$$Cu_2O$ electrocatalyst. We denote $_{TH}$CuO as the thermal oxide and $_{ECD}$$Cu_2O$ as the electrodeposited $Cu_2O$. The Cu electrode was thermally oxidized and the SEM of the resulting surface is shown in Figure 5.28. The Cu/$_{TH}$CuO surface consisted of irregularly shaped CuO particles and few overgrowth of nanorods.

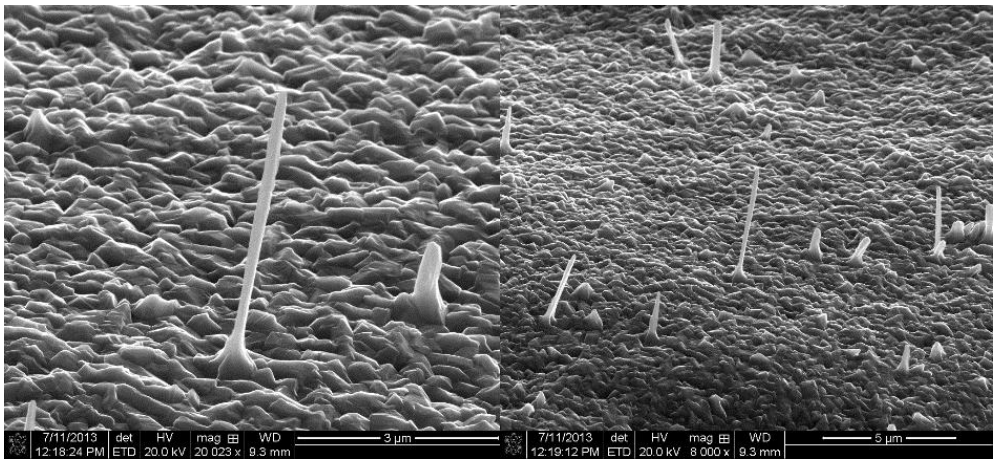


Figure 5.28. SEM of Cu/$_{TH}$CuO electrode.

$Cu_2O$ was then electrodeposited to the CuO layer and nanorods. The resulting SEM is shown in Figure 5.29. The surface of Cu/$_{TH}$CuO/$_{ECD}$$Cu_2O$ consisted of triangular pyramidal $Cu_2O$ particles overlayering the CuO film and nanorod overgrowths.

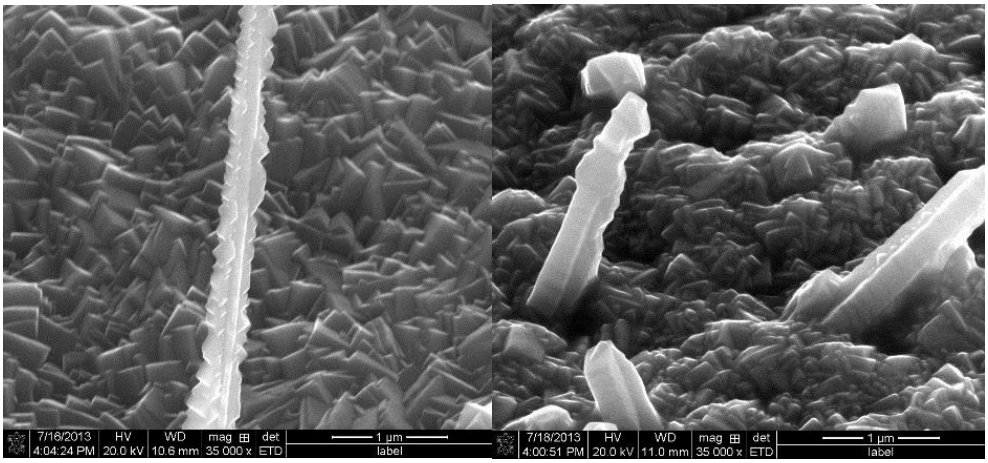


Figure 5.29. SEM of Cu/$_{TH}$CuO/$_{ECD}$Cu$_2$O electrode before $CO_2$ reduction.

Finally, after $CO_2$ reduction, the electrode surface was again monitored by SEM. Figure 5.30 shows that nanowires disappeared and $Cu_2O$ micro pyramids were broken down into nanoparticles.

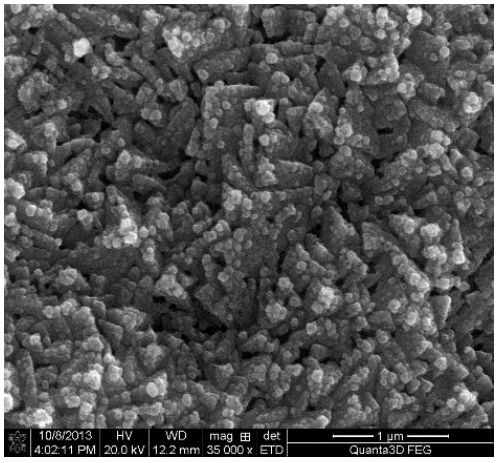


Figure 5.30. SEM of Cu/$_{TH}$CuO/$_{ECD}$Cu$_2$O electrode after $CO_2$ reduction at -1.5$V_{NHE}$ for 110 minutes.

XRD of Cu/$_{TH}$CuO/$_{ECD}$Cu$_2$O. The Cu/$_{TH}$CuO/$_{ECD}$Cu$_2$O electrode was then analyzed by XRD. The XRD profile given in Figure 5.31 shows different crystal phases of Cu, CuO and $Cu_2O$. The Cu crystals consisted of a mixture of Cu(111), Cu(200) and Cu(220)

oriented particles. Meanwhile the CuO particles consisted of a mixture of CuO(002) and CuO(111) crystal phases. Lastly, the $Cu_2O$ film consisted of $Cu_2O$(111), $Cu_2O$(200) and $Cu_2O$(222) crystal orientations.

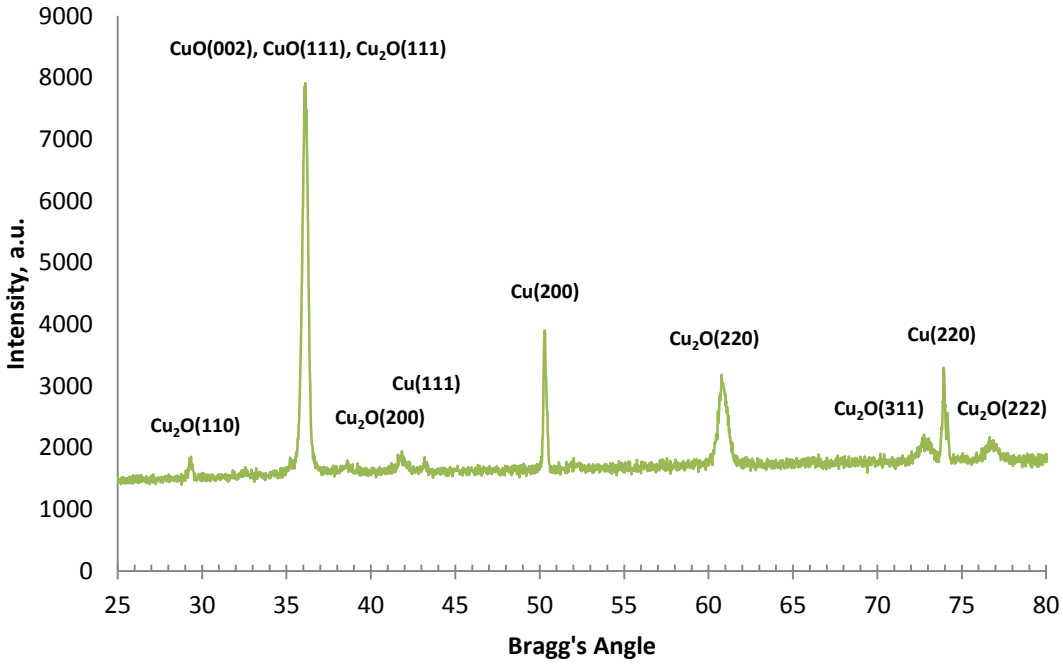


Figure 5.31. XRD scan of $Cu/_{TH}CuO/_{ECD}Cu_2O$ electrode before $CO_2$ reduction.

Additionally, there were new $Cu_2O$ crystal planes that were not present in other $Cu_2O$ electrodes. They included $Cu_2O$(110), $Cu_2O$(220) and $Cu_2O$(311) oriented particles. These additional crystal orientations likely resulted from growth on the CuO sublayer.

The XRD of the $Cu/_{TH}CuO/_{ECD}Cu_2O$ electrode after $CO_2$ reduction at $-1.5V_{NHE}$ was also determined. As seen in Figure 5.32, the original CuO and $Cu_2O$ crystal planes disappeared except for presence of residual $Cu_2O$(200) planes in very small number. Interestingly, we also observed formation of CuO(202) particles that were not previously

present before $CO_2$ reduction. This observation suggest that the electrode maintained its oxidized state despite the application of high negative potential. However, the particles still underwent an electrochemical transformation, but they were not completely reduced to Cu. We have not previously observed this phenomenon with our electrodeposited $Cu_2O$ particles.

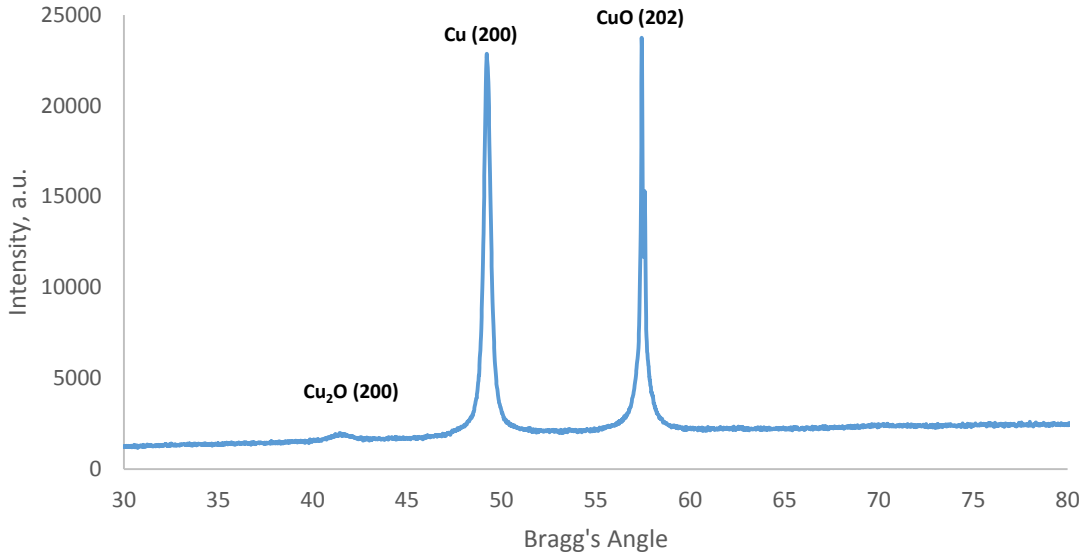


Figure 5.32. XRD scan of $Cu/_{TH}CuO/_{ECD}Cu_2O$ electrode after $CO_2$ reduction.

XPS of $Cu/_{TH}CuO/_{ECD}Cu_2O$**.** The XPS profile before $CO_2$ reduction is given in Figure 5.33. The XPS scan revealed Na 1s, Cu 2p, O 1s and C 1s elemental species at the surface of the electrode. The Na contaminants may have risen either during the fabrication of the electrode or during preparation for XPS analysis. They may only be physically lodged. The XPS shows large O 1s and C 1s peak relative to Cu 2p peak.

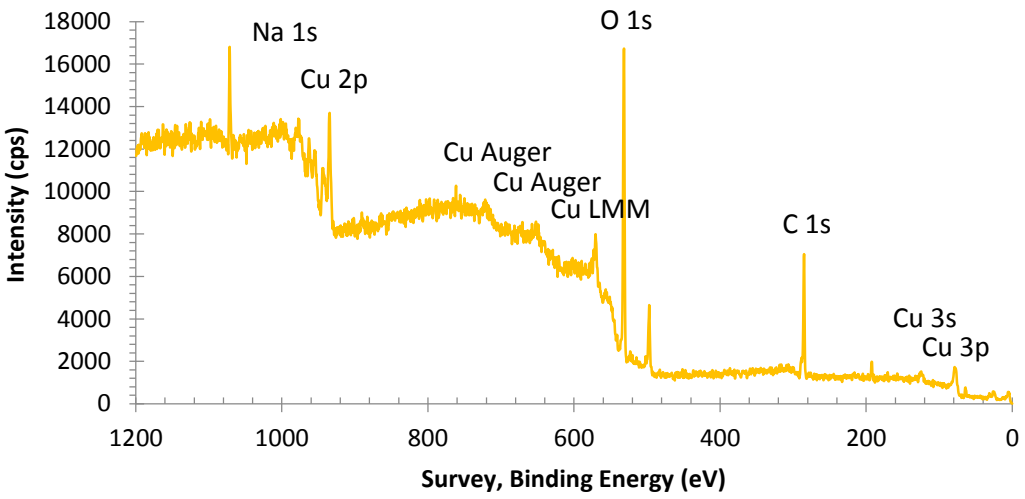


Figure 5.33. XPS survey of $Cu/_{TH}CuO/_{ECD}Cu_2O$ electrode before $CO_2$ reduction.

The XPS profile after $CO_2$ reduction is given in Figure 5.34. The Na 1s peak has disappeared which indicate that these species where only physically lodged at the surface. The O 1s and C 1s peaks diminished while the Cu 2p peak intensified.

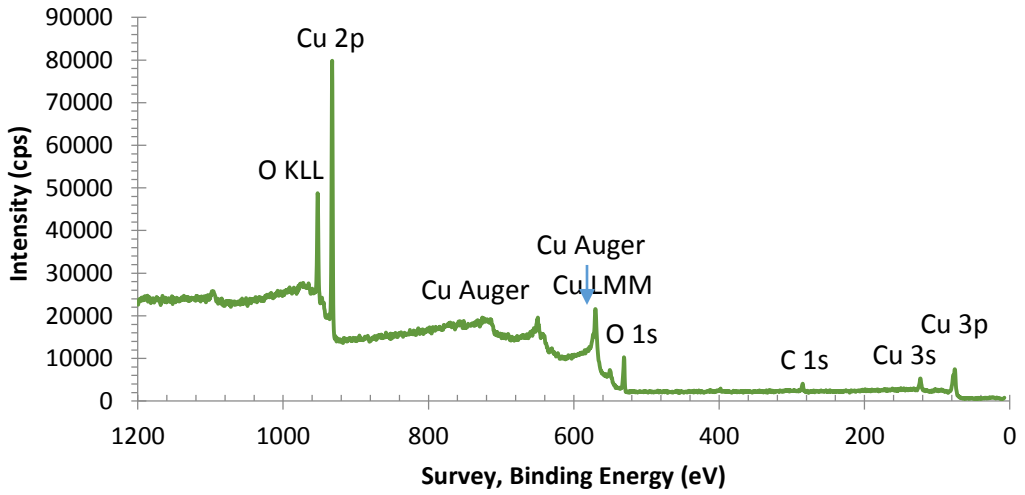


Figure 5.34. XPS survey of $Cu/_{TH}CuO/_{ECD}Cu_2O$ electrode after $CO_2$ reduction.

We then determined the composition of the electrode using peak areas obtained from the XPS plot and it is listed in Table 5.4. The atomic Cu/O ratio before $CO_2$ reduction

was 0.2 which increased to 2.4 after $CO_2$ reduction. The increase in Cu/O ratio was a result of the reduction of CuO and $Cu_2O$ to Cu. We also observed an initially high carbon content which decreased significantly after $CO_2$ reduction. While carbon contamination is common with XPS instrumentation, the reason for the decrease in the carbon content is not clear. Cu electrodes has been observed to lose activity due to the formation of carbonaceous compounds during electrolysis with bicarbonate solution. However, in this particular experiment, the XPS is suggesting that the initial carbon impurities were stripped off during electrolysis.

Table 5.4. Surface composition of $Cu/_{TH}CuO/_{ECD}Cu_2O$ electrode.

| Element | Before $CO_2$ ECR | | After $CO_2$ ECR | |
|---|---|---|---|---|
| | [Atomic] % | [Mass] % | [Atomic] % | [Mass] % |
| Cu, 2p | 10.4 | 34.3 | 57.4 | 85.7 |
| O, 1s | 47.8 | 39.8 | 23.7 | 8.9 |
| C, 1s | 41.5 | 26.0 | 18.9 | 5.3 |

5.3.4.2. Current Profile

The current profile is given in Figure 5.35. The plot shows a gradual increase in current between 0 and 65 minutes. The rise in current could have resulted from the increase in conductivity of the surface as $Cu_2O$ crystals became Cu crystals.

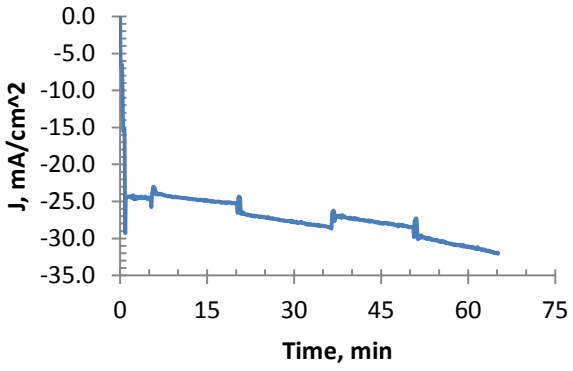


Figure 5.35. Current density versus time profile of $Cu/_{TH}CuO/_{ECD}Cu_2O$ electrode during $CO_2$ reduction at $-1.5V_{NHE}$.

5.3.4.3. GC Product Analysis

Product Formation Rates. Finally, we used GC to identify and quantify the different products of $CO_2$ reduction. The formation rates are given in Figure 5.36. CO had the highest average formation rate of 16 µmol/cm$^2$*hr, followed by ethylene at 9.1 µmol/cm$^2$*hr. We observed very low rates of methane formation, at 0.04 µmol/cm$^2$*hr. With this electrode, we observed a relatively stable production rates for CO and $C_2H_4$. The kinetic pattern of $H_2$, CO, $C_2H_4$ and $CH_4$ formation were alike.

We also observed ethanol and n-propanol products at 3.7 µmol/cm$^2$*hr and 1.8 µmol/cm$^2$*hr respectively. The ethanol and n-propanol rates were dynamic with relatively high initial rates that slowed towards the end of the process.

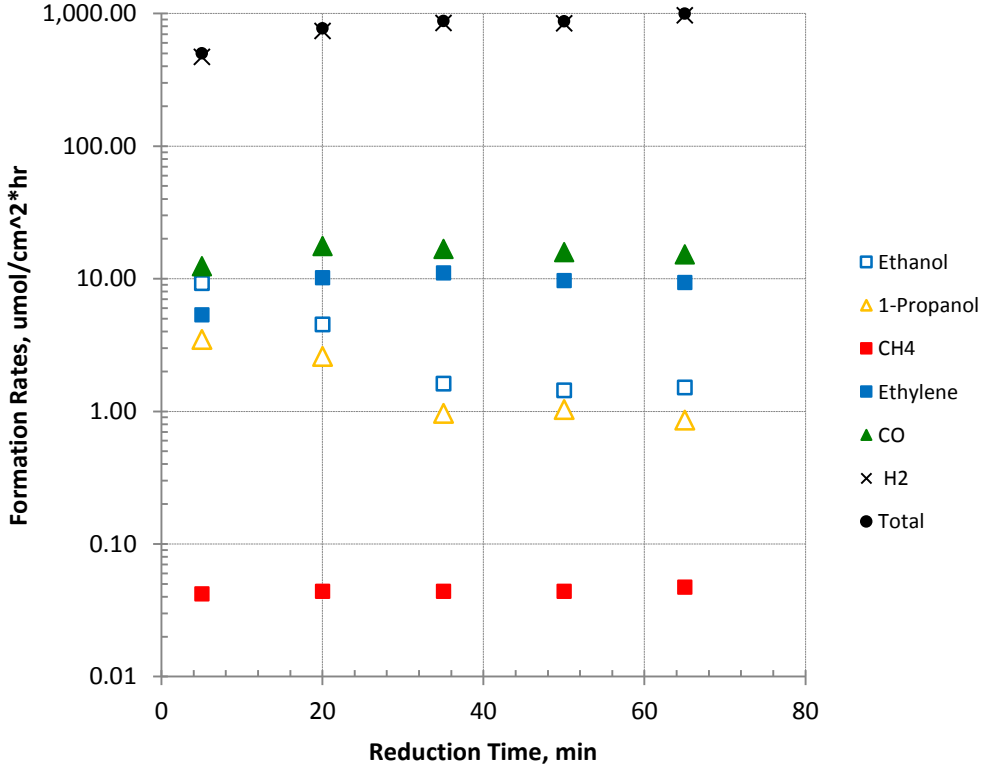


Figure 5.36. Formation rate of products on Cu/$_{TH}$CuO/$_{ECD}$Cu$_2$O electrode during $CO_2$ reduction at -1.5V$_{NHE}$.

Product Faradaic Efficiencies. The faradaic efficiency of ethanol, n-propanol, methane, ethylene, CO and $H_2$ are given in Figure 5.37. The electrocatalyst had an initially high selectivity for alcohol compared to the $Cu/_{ECD}Cu_2O$ catalyst with 13.2% ethanol and 7.5% n-propanol respectively versus 2% ethanol and 0.7% n-propanol in the latter. We observed formation of these alcohols instead of methanol. The $Cu/_{TH}CuO/_{ECD}Cu_2O$ electrode also showed higher mean selectivity for alcohol compared to the $Cu/_{ECD}Cu_2O$ electrode with 5.0% ethanol and 3.6% n-propanol versus 1.1% ethanol and 0.6% n-propanol in the latter.

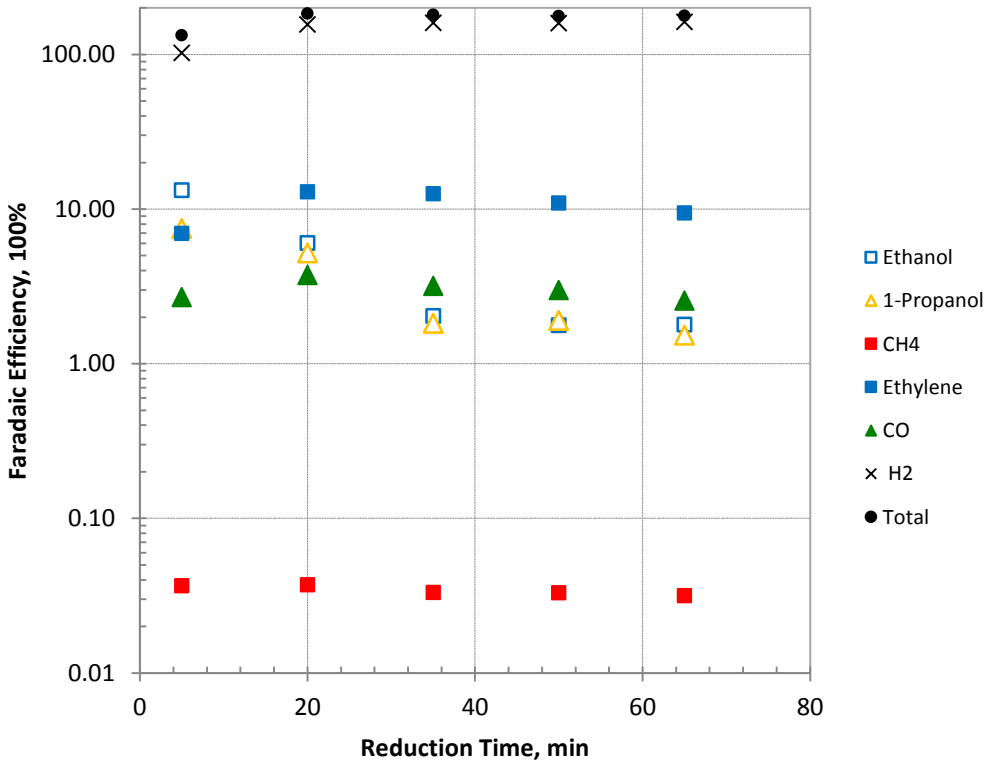


Figure 5.37. Faradaic efficiency of products on $Cu/_{TH}CuO/_{ECD}Cu_2O$ electrode during $CO_2$ reduction at $-1.5V_{NHE}$.

We also observed better selectivity for ethylene and CO in the $Cu/_{TH}CuO/_{ECD}Cu_2O$ electrode with 11% ethylene and 3.0% CO efficiency versus 5.2% ethylene and 1.5% CO efficiency in $Cu/_{ECD}Cu_2O$.

The presence of CuO as nucleation and growth precursor to electrodeposited $Cu_2O$ may have promoted the formation of more low-coordinated sites during subsequent reduction of $Cu_2O$ to Cu which enhanced selectivity of hydrocarbons and oxygenates. The XRD result also indicated that the CuO layer was stable although phase transformation occurred. The XRD of Cu-$Cu_2O$ after $CO_2$ reduction consisted of Cu(200) > Cu(220) > $Cu_2O$(202) > Cu(111). The XRD of $Cu/_{TH}CuO/_{ECD}Cu_2O$ electrode after $CO_2$ reduction consisted of Cu(200) > CuO(202) > $Cu_2O$(200).

With Ghadimkhani's electrode, the $Cu_2O$ catalyst was photoelectrochemically stable. The formation of methanol may be associated with presence of a stable $Cu_2O$ catalyst while the formation of ethanol and n-propanol may be associated with reduced $Cu_2O$ particles.

**5.4. Summary and Conclusion**

In this Chapter, we studied the electrocatalytic activity of $Cu_2O$ film electrochemically deposited on Cu foil and Toray carbon fiber paper. The $Cu_2O$ film had a cubic architecture. $Cu_2O$ film electrodeposited on Cu were mostly oriented in the (111) direction while those electrodeposited on Toray were mostly oriented in the (110) direction.

In the first section, we have determined that thicker oxide improves CO formation while suppressing $H_2$ formation.

In the second part, we looked at the kinetics of $CO_2$ reduction on $Cu/_{ECD}Cu_2O$. We observed more products with this electrode than in polycrystalline Cu of Chapter 4 with

the detection of ethanol and n-propanol. The order of preference also changed, particularly at -1.5$V_{NHE}$. In Cu, selectivity was in the order of $CH_4$ > CO > $C_2H_4$. In Cu/$_{ECD}Cu_2O$, selectivity was in the order of $C_2H_4$ > CO > $CH_4$. After $CO_2$ reduction, majority of $Cu_2O$ crystal planes disappeared.

These results indicate that Cu derived from $Cu_2O$ film is different from polycrystalline Cu. With Cu, $CO_{ads}$ were more reducible to $CH_4$ than $C_2H_4$. With Cu/$_{ECD}Cu_2O$, $CO_{ads}$ were more reducible to $C_2H_4$ than $CH_4$ despite having more Cu(200) particles present after the reduction of $Cu_2O$.

In the third section, we observed that Nafion stabilized the selectivity of $C_2H_4$ and CO and also inhibited the formation of $CH_4$.

Finally in the last section, we observed additional $Cu_2O$ crystal planes as a result of using CuO as growth template. The use of a CuO layer as growth substrate for electrodeposited $Cu_2O$ particles appeared to improve the selectivity of $Cu_2O$ to hydrocarbons, especially ethylene, ethanol and n-propanol.

# CHAPTER 6
# $CO_2$ ELECTROCHEMICAL REDUCTION ON SUPPORTED $Cu_2O$ PARTICLES

## 6.1. Introduction

In this Chapter, we studied the electrocatalytic activity of colloidal $Cu_2O$ particles supported on three different substrates; namely, (1) Toray, (2) glassy carbon and (3) copper. In Section 6.3.2, we examined the kinetics of $CO_2$ reduction on Toray supported $Cu_2O$ particles. First, we looked at the reproducibility of product distribution on $Cu_2O$ particles by applying two sets of $CO_2$ reduction on the same electrode 12 days apart. Then we studied the effect of different catalyst preparation conditions; namely (1) effect of aging time during $Cu_2O$ synthesis, (2) effect of Nafion, (3) effect of reagent composition during $Cu_2O$ synthesis, particularly on the amount of NaOH and (4) effect of $Cu_2O$ polarization. Finally, we examined the product distribution at different potentials. We compared two sets of $Cu_2O$ particles, the larger $Cu_2O$ MP and the smaller $Cu_2O$ particles. We also compared these results to polycrystalline Cu.

We then studied the effect of using two other support substrates. In Section 6.3.3, we deposited $Cu_2O$ particles on glassy carbon and studied both the kinetics and the potential dependence of $CO_2$ reduction on this electrode. In Section 6.3.4, we deposited $Cu_2O$ particles on Cu and studied the kinetics at $-1.5V_{NHE}$.

## 6.2. Materials and Methods

### *6.2.1. Preparation of Toray, Glassy Carbon and Copper Support Substrates*

Several pieces of 1 cm x 2 cm x 0.019 cm Toray carbon fiber paper (Toray, TGP-H-060, Fuel Cell Store), 1 cm x 2 cm x 0.0254 cm Cu sheet (ESPI Metals) and 1 cm x 2 cm x 0.1 cm Glassy Carbon plate (Alfa Aesar) were cut from source materials.

Cu sheets and GL plates were first cleaned in 1.0M HCl (35.5-38% reagent bottle, Aristar) for 10 minutes, then sonicated in 2-propanol (99.5%, Mallinckrodt), acetone (99.5%, Mallinckrodt) and deionized $H_2O$, sequentially for 10 minutes. Toray was used without any additional pre-treatments.

*6.2.2. Synthesis of Colloidal $Cu_2O$ Particles*

$Cu_2O$ particles were synthesized by two different but similar procedures, the first followed the steps described by Chang et al. in 2009 while the second followed the steps described by Li et al. in 2013. The details are given in Section 3.1.2. After collecting dried powders of $Cu_2O$ particles, they were deposited to three different support substrates.

*6.2.3. Application to Support Substrate*

With Toray, the substrate was immersed in a 10 mL ethanol solution consisting of defined amount of $Cu_2O$ particles, Nafion (perfluorinated ion-exchange resin, 5 wt% solution in lower aliphatic alcohols/$H_2O$ mix, Sigma-Aldrich) and ethanol ($CH_3CH_2OH$, Sigma-Aldrich, ≥99.5%). The solvent was allowed to evaporate in open container which allowed $Cu_2O$ particles to settle on the surface.

With GL, a $Cu_2O$-nafion ink was prepared instead of $Cu_2O$-nafion mixture. In this case, 1 mL of ethanol was used as solvent to $Cu_2O$ and Nafion blend. The ink was composed of 17 wt% $Cu_2O$ and 83 wt% Nafion. The ink was brush-coated on the front and back side of GL and allowed to dry in open air. The $Cu_2O$ and Nafion loading was 0.83 $mg/cm^2$ and 3.99 $mg/cm^2$ respectively.

With Cu, a hole was drilled on the sleeve part of the Cu sheet for attachment to the 4N Cu wire. The $Cu_2O$-nafion ink was brush-coated to the Cu surface. The ink mixture

contained 17 wt% $Cu_2O$ and 83 wt% Nafion. The $Cu_2O$ and Nafion loading were 0.9 $mg/cm^2$ and 4.3 $mg/cm^2$ respectively.

*6.2.4. $CO_2$ Reduction on Control Electrodes (Support Substrates)*

$CO_2$ electrochemical reduction was applied on (1) Toray without Nafion pre-treatment, (2) Toray with Nafion pre-treatment and (3) Glassy carbon plate (GL) at $-1.5V_{NHE}$ for 110 minutes.

*6.2.5. $CO_2$ Reduction on Toray Supported $Cu_2O$ Particles*

6.2.5.1. Effect of Electrode Preparation Condition

We made several modifications to the standard procedure on $Cu_2O$ electrocatalysts preparation and investigated their effects on the electrocatalytic activity of $Cu_2O$. We considered three factors; namely, (1) composition of reagent ingredients during the synthesis of $Cu_2O$ particles (2) aging time during post $Cu_2O$ synthesis and (3) Nafion/$Cu_2O$ ratio. $CO_2$ reduction was performed on these electrodes at $-1.5V_{NHE}$ for 110 minutes.

The standard chemical reduction synthesis of $Cu_2O$ involved mixing 4 different reagents with the following composition, (1) 0.005M $CuCl_2$, (2) 0.002M PEG, (3) 0.2M NaOH, (4) 0.05M LAAS. For the effect of reagent concentration, we examined +/- concentrations of PEG, NaOH, and LAAS from standard values; (1) 0.03M and 0.07M L-AAS, (2) 0.1M and 0.3M NaOH and (3) 0.001M and 0.003M PEG.

To study the effect of aging time, we aged the $Cu_2O$ particles for 0, 30 min and 360 minutes. To examine the effect of Nafion, we considered Nafion/$Cu_2O$ mass ratio of 0, 1.2 and 2.4.

6.2.5.2. Effect of Cyclic Voltammetry

In this section, we subjected two $Cu_2O$ electrodes to four cycles of voltammetry before $CO_2$ reduction, the first one was without Nafion and the second one was with Nafion. The cyclic voltammetry was conducted between -1.2$V_{Ag/AgCl}$ and +0.6$V_{Ag/AgCl}$ at a sweep rate of 50 mV/s under $CO_2$ electrolysis condition.

6.2.5.3. Effect of Particle Size on Product Distribution

In this section, we compared two sets of $Cu_2O$ electrocatalysts with distinct particle size; namely, (1) $Cu_2O$ MP and (2) $Cu_2O$ NP. $Cu_2O$ MP and $Cu_2O$ NP were synthesized by wet chemical reduction method as described by Chang et al. (2009) and Li et al. (2013) respectively. We examined the product distribution of these particles at different potentials by performing $CO_2$ reduction between -1.0$V_{NHE}$ and -1.7$V_{NHE}$, with 30 minute electrolysis at each potential.

*6.2.6. $CO_2$ Reduction on Glassy Carbon Supported $Cu_2O$ Particles*

In this section, we performed two batches of $CO_2$ reduction on a single GL/$Cu_2O$ electrode. The first batch was conducted at -1.5$V_{NHE}$ for 110 minutes. The second batch was conducted at a series of potential step from -1.1$V_{NHE}$ to -1.7$V_{NHE}$ for 60 minutes on each potential.

*6.2.7. $CO_2$ Reduction on Copper Supported $Cu_2O$ Particles*

In this section, we performed $CO_2$ reduction at -1.5$V_{NHE}$ for 110 minutes.

**6.3. Results and Discussion**

*6.3.1. $CO_2$ Reduction on Control Electrodes (Support Substrates)*

Before we examined the electrocatalytic activity of $Cu_2O$ particles, we first determined the electrocatalytic activity of the support substrates. Both carbon fiber paper

(Bidault et al. 2009, Huanga and Wang 2014, Sharma and Pollet, 2012, de Jongh 2012) and glassy carbon (Van Der Linden and Dieker 1980) are materials commonly used as electrodes or support substrates in fuel cells and other electrochemical applications due to their excellent mechanical and thermal properties. They do not decompose under high potential electrolysis, although they catalyze the reduction of $H_2O$ molecules. Additionally, Toray offers high surface area and accessibility to gaseous species while GL has the rigidity that makes it flexible to a wide variety of reactor configuration.

6.3.1.1. Toray and Toray/Nafion

Current Profile. Figure 6.1 shows the current profile generated by Toray and Toray/Nafion electrodes. With Toray, electrolysis started with a low current of 1 mA but gradually increased to 28 mA towards the end of the reduction period. The Toray sample obtained from Fuel Cell Store was pre-coated with Teflon in order to suppress liquid wetting and promote gas phase reactions on the surface and is likely the reason for the initially low current.

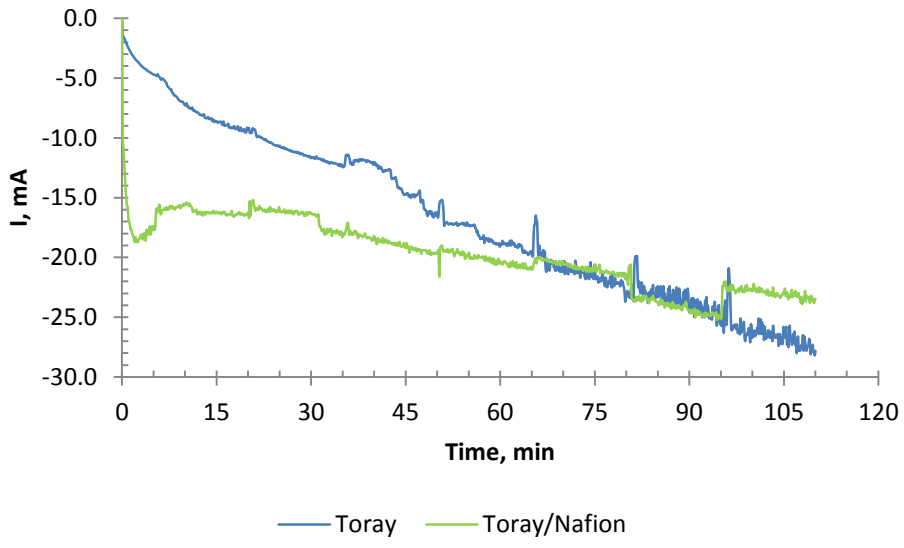


Figure 6.1. Current profile of Toray and Toray/Nafion electrodes at -1.5$V_{NHE}$ $CO_2$ reduction.

With Toray/Nafion electrode, $CO_2$ reduction immediately produced high current near its high of 24 mA. The presence of Nafion allowed for the immediate onset of electrochemical reactions which where otherwise restrained on the purely Toray electrode. Near the end of the process, the two electrodes exhibited fairly identical current flow.

Product Distribution on Toray. The graphs in Figure 6.2 and 6.3 show the formation rates and faradaic efficiencies of $H_2$, CO and $CH_4$ on Toray electrode respectively.

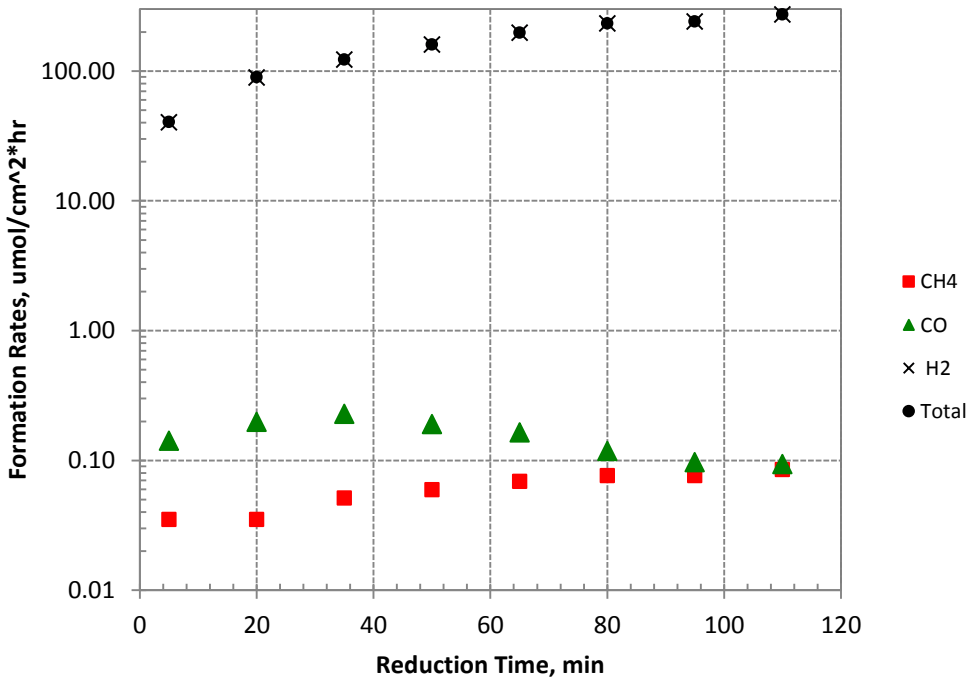


Figure 6.2. Product formation rates during $CO_2$ reduction on Toray at -1.5$V_{NHE}$.

Toray mainly produced $H_2$ with an initial, final and average production rates of 40, 273 and 170 µmol/$cm^2$*hr. Toray also produced trace amounts of CO and $CH_4$ products at less than 0.3 µmol/$cm^2$*hr.

Faradaic efficiency plot in Figure 6.3 expectedly showed high $H_2$ faradaic efficiency that was close to or slightly exceeding 100%. We also observed CO and $CH_4$

but at faradaic efficiencies of less than 0.5%. Majority of measured current was therefore used to reduce $H_2O$ to $H_2$.

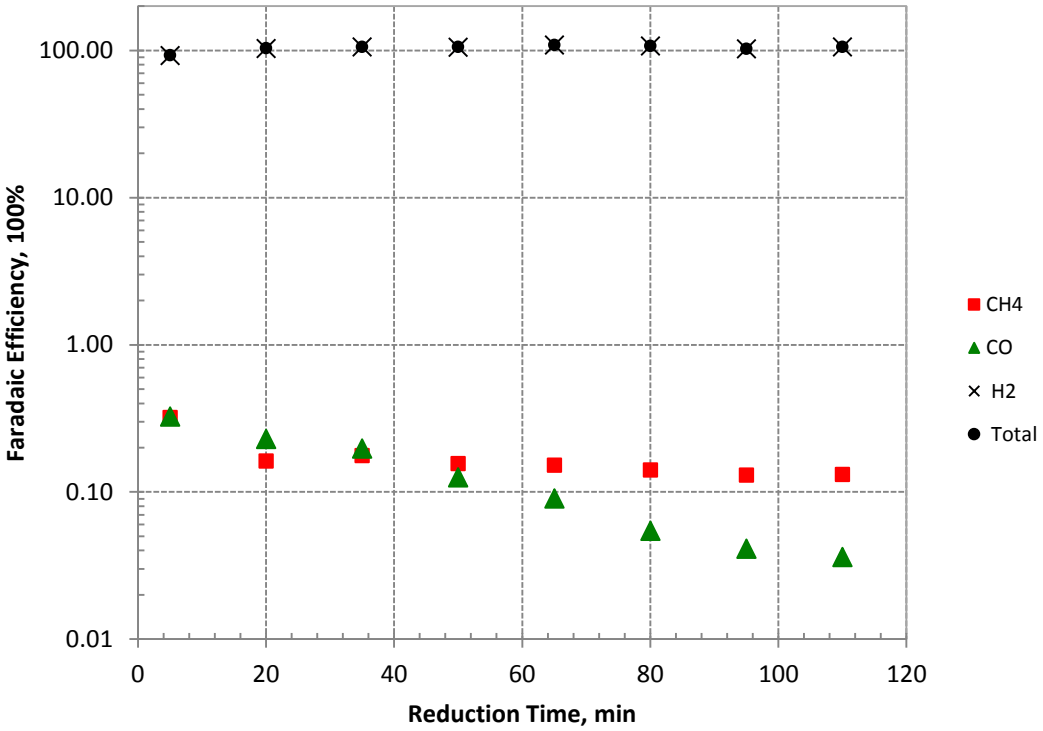


Figure 6.3. Faradaic efficiency of products during $CO_2$ reduction on Toray at -1.5$V_{NHE}$.

Product Distribution on Toray/Nafion. Meanwhile, the graph in Figure 6.4 shows the formation rates and faradaic efficiencies of $H_2$, CO and $CH_4$ on Toray/Nafion electrode. Again, the electrode mainly produced $H_2$ with an initial, final and average production rates of 163, 236 and 198 μmol/$cm^2$*hr. The measured initial $H_2$ rate was higher in Toray/Nafion than in Toray which was expected from the current profile in Figure 6.1, while the average $H_2$ rate was close to that of Toray. The electrode also produced trace amounts of CO and $CH_4$ products at less than 0.1 μmol/$cm^2$*hr.

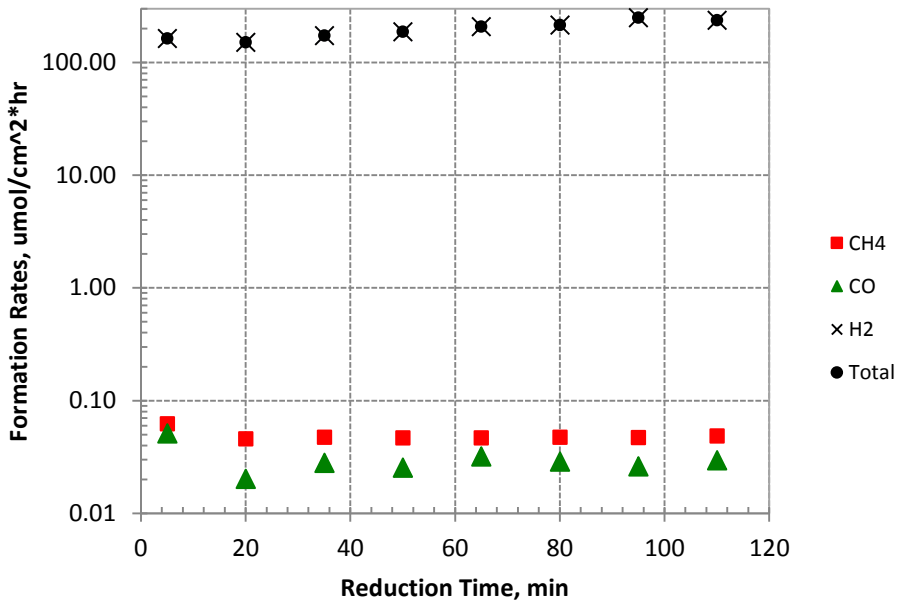


Figure 6.4. Product formation rates during $CO_2$ reduction on Toray/Nafion at -1.5$V_{NHE}$.

Faradaic efficiency plot in Figure 6.5 also showed high $H_2$ faradaic efficiency that was close to or slightly exceeding 100%.

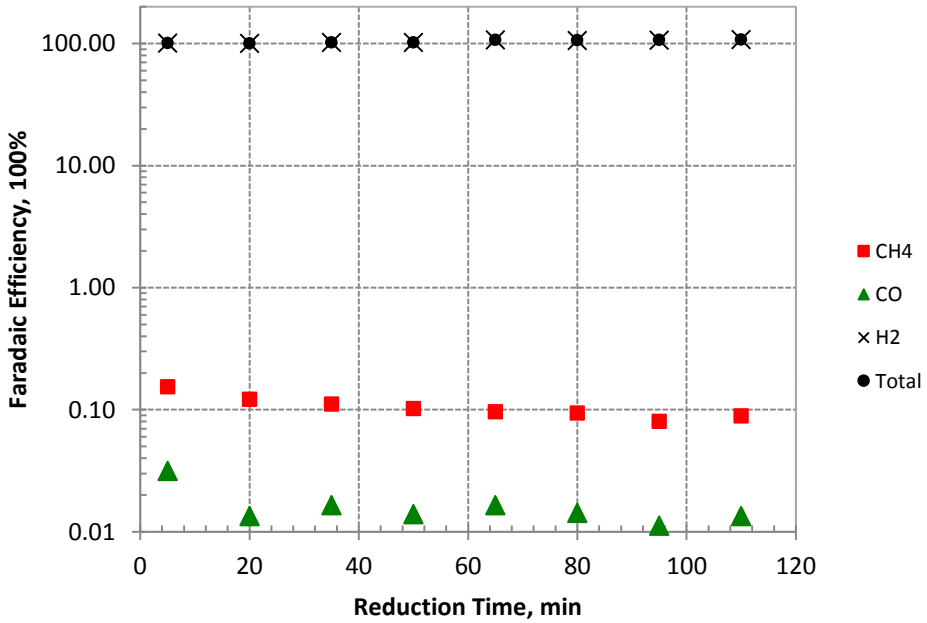


Figure 6.5. Faradaic efficiency of products during $CO_2$ reduction on Toray/Nafion at -1.5$V_{NHE}$.

We also observed CO and $CH_4$ but at faradaic efficiencies of less than 0.2%. Majority of measured current was therefore used to reduce $H_2O$ to $H_2$.

6.3.1.2. Glassy Carbon

Current Profile. $CO_2$ reduction on GL generated a mean current of 7.6 mA (electrode area of 1.9 $cm^2$) as shown in Figure 6.6 which was lower than in Toray. This is because GL has lower surface area per square length than Toray. The current profile was similar to that of Toray electrode.

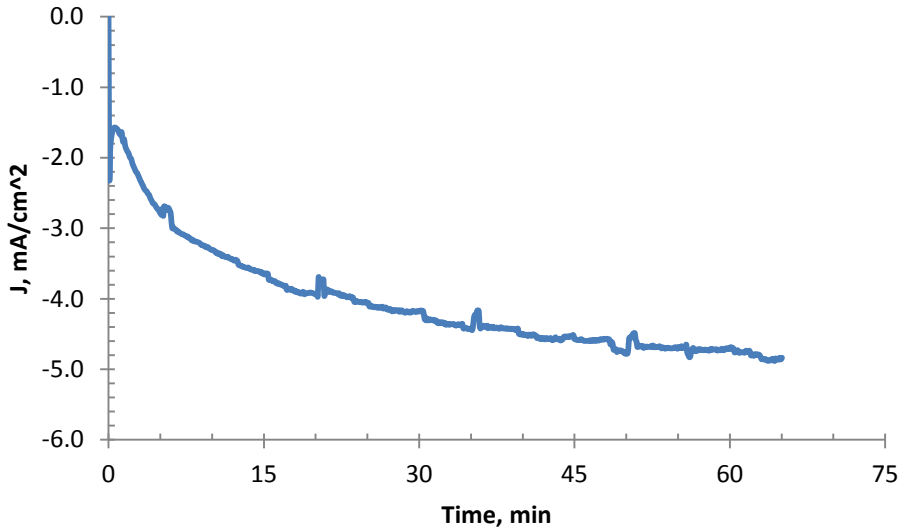


Figure 6.6. Current profile of glassy carbon at -1.5$V_{NHE}$ $CO_2$ reduction.

Product Distribution. The graphs in Figure 6.7 and 6.8 show the formation rates and faradaic efficiencies of $H_2$, CO and $CH_4$ on glassy carbon electrode. The electrode mainly produced $H_2$ with an initial, final and average production rates of 32, 96 and 73 µmol/$cm^2$*hr. These values were less than what were generated on Toray electrodes. GL also produced trace amounts of CO and $CH_4$ products at less than 0.6 µmol/$cm^2$*hr.

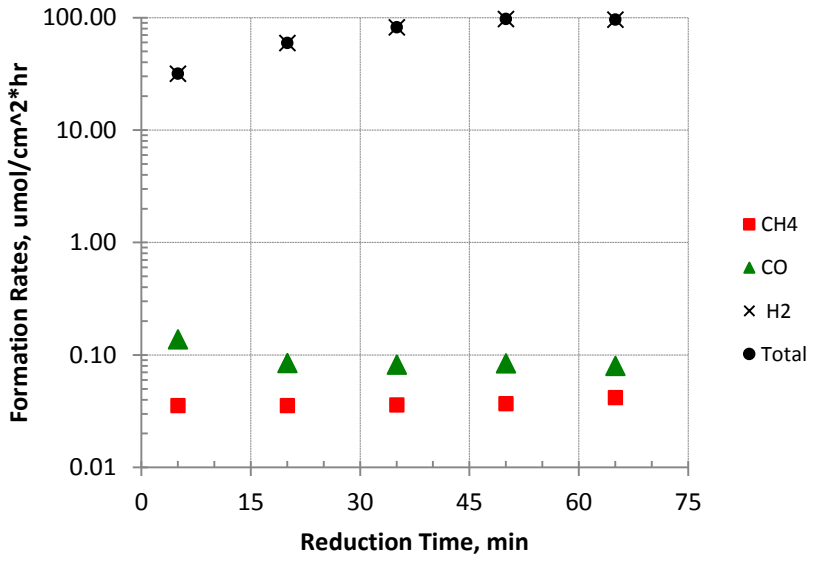


Figure 6.7. Product formation rates during $CO_2$ reduction on glassy carbon electrode at $-1.5V_{NHE}$.

Like Toray, GL showed very high selectivity towards $H_2$ and the product was responsible for most of the current activity. CO and $CH_4$ current efficiencies were limited to less than 0.7%.

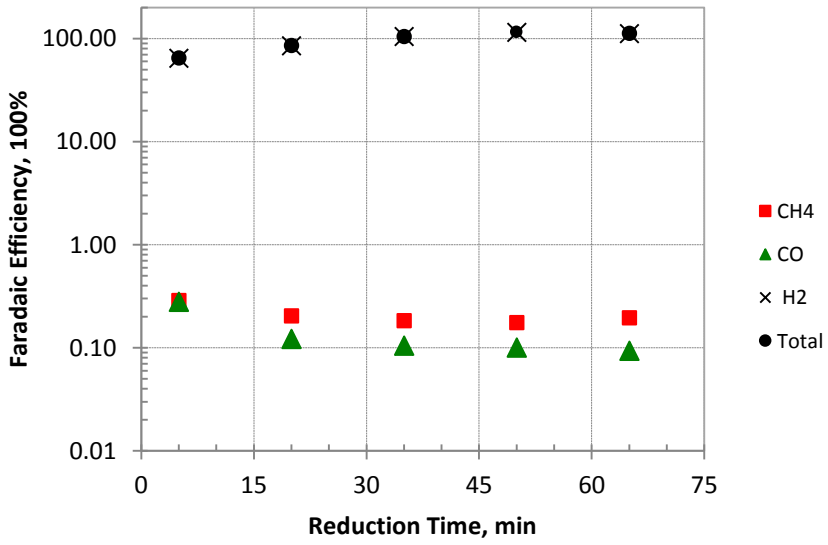


Figure 6.8. Faradaic efficiency of products during $CO_2$ reduction on glassy carbon electrode at $-1.5V_{NHE}$.

These results suggest that any hydrocarbon formation from $CO_2$ will only occur on $Cu_2O$ particles. Nevertheless, $H_2$ formation would also be expected to occur and compete with $CO_2$ on these $Cu_2O$ surfaces.

### *6.3.2. $CO_2$ Reduction on Toray Supported $Cu_2O$ Particles*[2]

We now examine the electrocatalytic $CO_2$ activity on Toray supported $Cu_2O$ particles. In this section, we looked at the effect of different synthesis conditions and reaction conditions on the formation rate and selectivity of $Cu_2O$ particles towards ethanol, n-propanol, methane, ethylene and CO. We have also considered $H_2$ formation, although they are not derived from $CO_2$ reduction. While $H_2O$ is reduced to $H_2$, some H atoms from $H_2O$ species are also utilized in the hydrogenation of CO intermediates.

#### 6.3.2.1. Reproducibility Test[3]

We started this section by examining the reproducibility of product distribution on Toray/Nafion/$Cu_2O$ electrode which represents our baseline sample. The electrode consisted of 26.5 mg $Cu_2O$ and 21.1 mg Nafion. We conducted two separate batches of $CO_2$ reduction with a time difference of 12 days.

SEM Analysis. Figure 6.9 shows an SEM image of colloidal $Cu_2O$ particles with Nafion binder before and after the first $CO_2$ reduction. The $Cu_2O$ particles were cubic with a set of 80 nm particles and 400 nm particles. Thermodynamically and kinetically, $Cu_2O$ particles are expected to get reduced to Cu particles at the applied potential of $-1.5V_{NHE}$. However, in this particular image scan area, the SEM image does not show physical evidence of a change in the cubic structure or decoration of particles. Nafion, which can be seen here like a transparent paste may have prevented the reduction of $Cu_2O$ that it is in

[2]This section previously appeared in the reference: Bugayong, J. and G.L. Griffin. 2013. "Electrochemical Reduction of CO2 using Supported Cu2O Nanoparticles." Electrochemical Synthesis of Fuels 2, Electrochemical Society Transactions: 58 (2), 81-89. [Reproduced with permission from The Electrochemical Society.]

contact with. The smaller $Cu_2O$ particles also appeared to agglomerate into larger $Cu_2O$ particles.

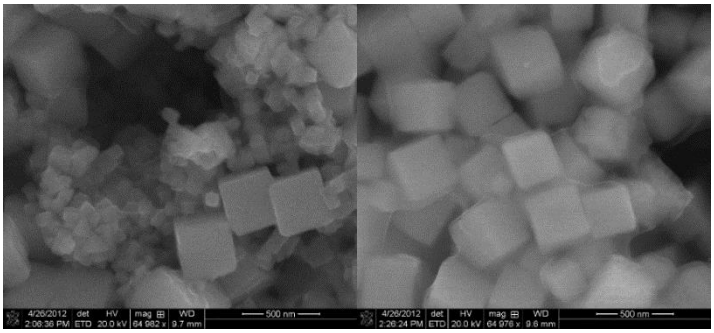

Figure 6.9. SEM of fresh $Cu_2O$ (left) and $Cu_2O$ after $CO_2$ reduction at -1.5$V_{NHE}$ (right).

Current Profile. Figure 6.10 shows current profile on the two batches of $CO_2$ reduction applied on the electrode. The first run had an average current of 24 mA while the second run had an average current of 18 mA. The second process therefore showed about 25% less current than the first process which would indicate a lower total formation rate. The brief spikes in the plot at regular interval was caused by liquid sampling taken every 15 minutes. In both runs, the total current steadily decreased with time.

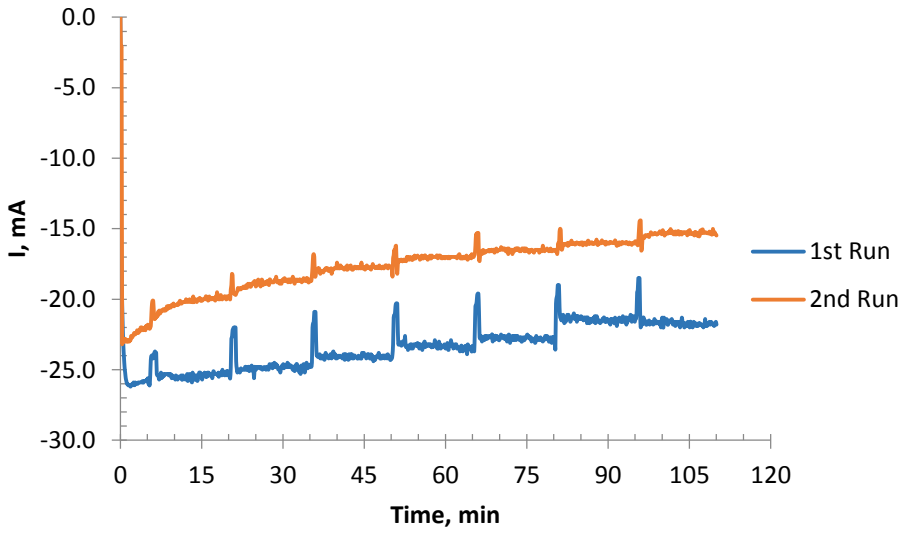


Figure 6.10. Current profile of the first and second $CO_2$ reduction on the baseline Toray/Nafion/$Cu_2O$ electrode at -1.5$V_{NHE}$.

[3]This section previously appeared in reference: 3.Bugayong, J. and G.L. Griffin. 2013. "Electrochemical Reduction of CO2 using Supported Cu2O Catalysts." MRS Proceedings 1542. [Reproduced with permission from the Cambridge University Press.]

Product Formation Rates. Figure 6.11 shows the formation rates of ethanol, methane, ethylene, CO and $H_2$ during the first $CO_2$ reduction. CO showed the highest formation rates, with a mean production rate of 41 µmol/cm$^2$*hr. This was followed by ethylene with 13 µmol/cm$^2$*hr. On the other hand, we observed a low methane production rate of only 0.3 µmol/cm$^2$*hr. We also observed ethanol with a stable formation rate of 2.3 µmol/cm$^2$*hr. The kinetics of CO, $CH_4$ and $C_2H_4$ formation agrees with the branch point identified by Hori's reaction pathway, desorption of $CO_{ads}$ intermediate versus hydrogenation of $CO_{ads}$ intermediate to hydrocarbon. Additionally, CO formation appeared to be more favorable during the early stage of the process whereas hydrocarbon formation are more favorable during the later part of the reduction process.

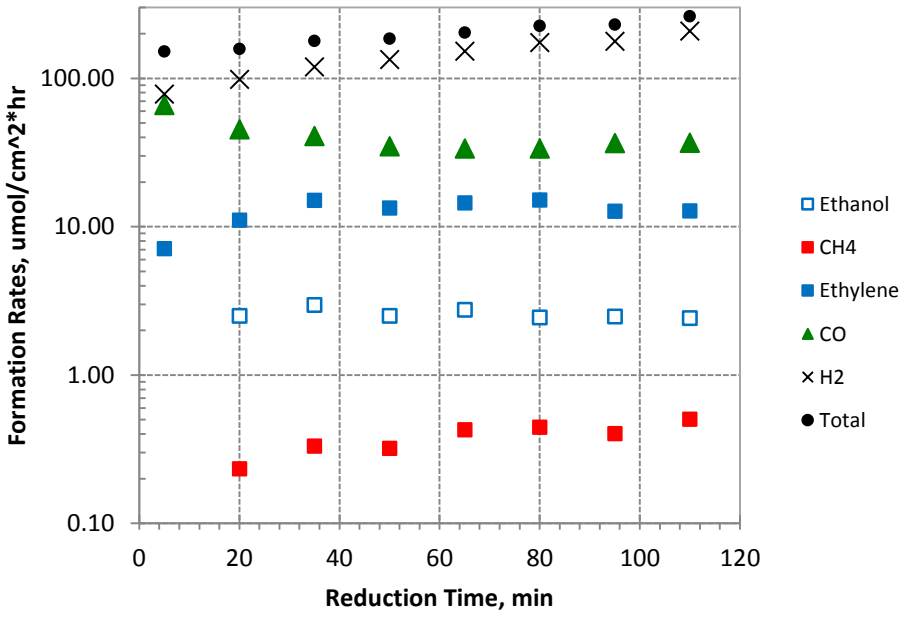


Figure 6.11. Formation rate of products during the first $CO_2$ reduction on the baseline Toray/Nafion/$Cu_2O$ electrode at -1.5$V_{NHE}$.

The total formation rate increased despite a decrease in the total current. This may suggest slow process of $Cu_2O$ reduction that occur throughout the process.

Meanwhile, Figure 6.12 shows the formation rates of ethanol, methane, ethylene, CO and $H_2$ during the second $CO_2$ reduction. The kinetics of CO, $CH_4$ and $C_2H_4$ formations are identical to that of the first $CO_2$ reduction. Again, CO registered the highest formation rate, at 45 µmol/cm$^2$*hr. This was followed by ethylene and ethanol, at 9.5 and 1.2 µmol/cm$^2$*hr respectively. Methane formation was again low, at only 0.6 µmol/cm$^2$*hr. The total formation rate decreased in the first half then increased in the second half of the process.

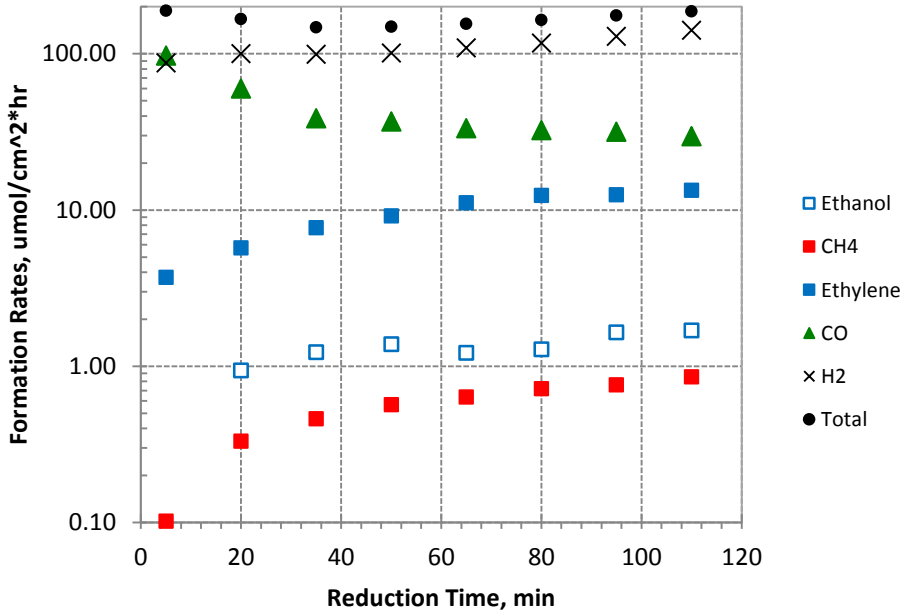


Figure 6.12. Formation rate of products during the second $CO_2$ reduction on the baseline Toray/Nafion/$Cu_2O$ electrode at -1.5$V_{NHE}$.

Product Faradaic Efficiencies. Figure 6.13 shows the product distribution of ethanol, methane, ethylene, CO and $H_2$ during the first $CO_2$ reduction. The catalyst had an average 49% selectivity towards hydrocarbon formation. CO and $C_2H_4$ were the major hydrocarbon products with 16% and 28% faradaic efficiencies respectively. Intermediate amount of ethanol was produced at 4.8% faradaic efficiency with minor levels of $CH_4$ at

0.5% faradaic efficiency. The faradaic efficiency of $C_2H_4$ and $CH_4$ increased while the CO faradaic efficiency decreased.

The average $C_2H_4/CH_4$ selectivity ratio from this sample was 58.7 compared to a ratio of 0.2 from our Cu electrode and to a ratio of 14 on single crystal Cu(711) obtained by Hori's group. Additionally, the average $(C_2H_4 + CH_4)/CO$ selectivity ratio was 1.85 which is only slightly higher than 1.3 with our Cu electrode. This suggests that $Cu_2O$ catalysts exhibit a different mechanism of $CO_2$ conversion compared to Cu.

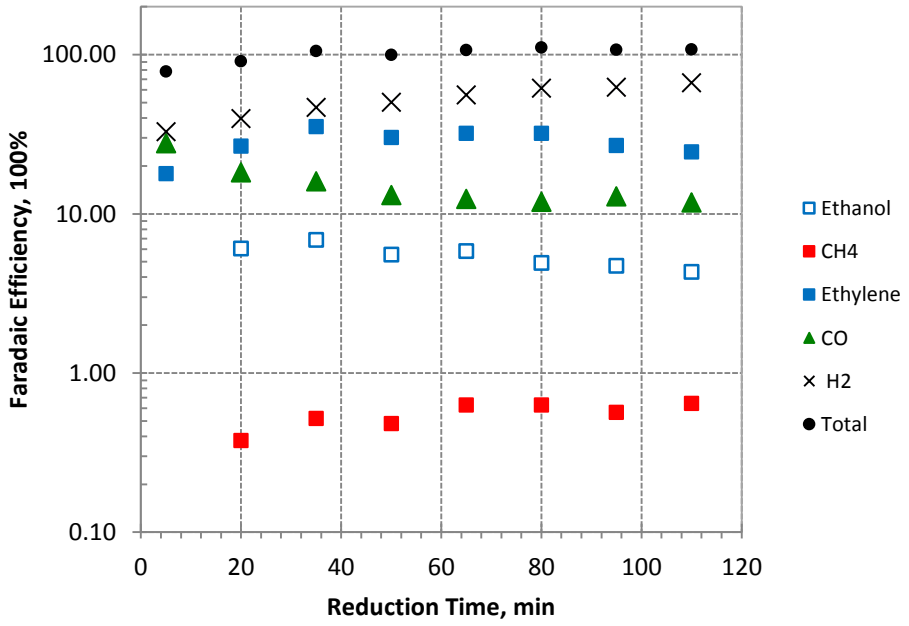


Figure 6.13. Faradaic efficiency of products during the first $CO_2$ reduction on the baseline Toray/Nafion/$Cu_2O$ electrode at -1.5$V_{NHE}$.

At this point in our results, we don't have SEM images to show that $Cu_2O$ particles were reduced to Cu although related studies on $Cu_2O$ have shown that these particles will be reduced under these potential condition (Le et al. 2011, Li and Kanan 2012). With our other experiments on $Cu_2O$, which will be presented in the succeeding sections, we have simultaneously observed considerable morphological change in the $Cu_2O$ particles and formation of Cu XRD peaks. As such, in the event of $Cu_2O$ particle reduction, there would

be formation of dispersed Cu clusters. These surfaces have higher number of low coordinated sites were $C_{2+}$ hydrocarbons are formed. Li (2012) suggested that the reduction of thick thermal copper oxide produced denser Cu grain boundaries that are abundant in sites that enhance CO selectivity and lower its kinetic potential requirement.

The selectivity of ethanol changed proportionately with ethylene which suggests these two products may proceed through a parallel reaction pathway. It is not clear which intermediates participate in the coupling reaction. Likely candidates include $CO_{ads}$, $CH_{2ads}$, $COH_{ads}$ and $CHO_{ads}$ intermediates. Kuhl suggested that glyoxal ($HO\text{-}CH{=}C\text{-}(OH)_2$) and/or acetaldehyde ($H_3C\text{-}CH{=}O$) maybe a common intermediate and branch point towards ethanol and ethylene.

During the second $CO_2$ reduction, the catalyst had a slightly better over-all hydrocarbon selectivity at 54% (see Figure 6.14).

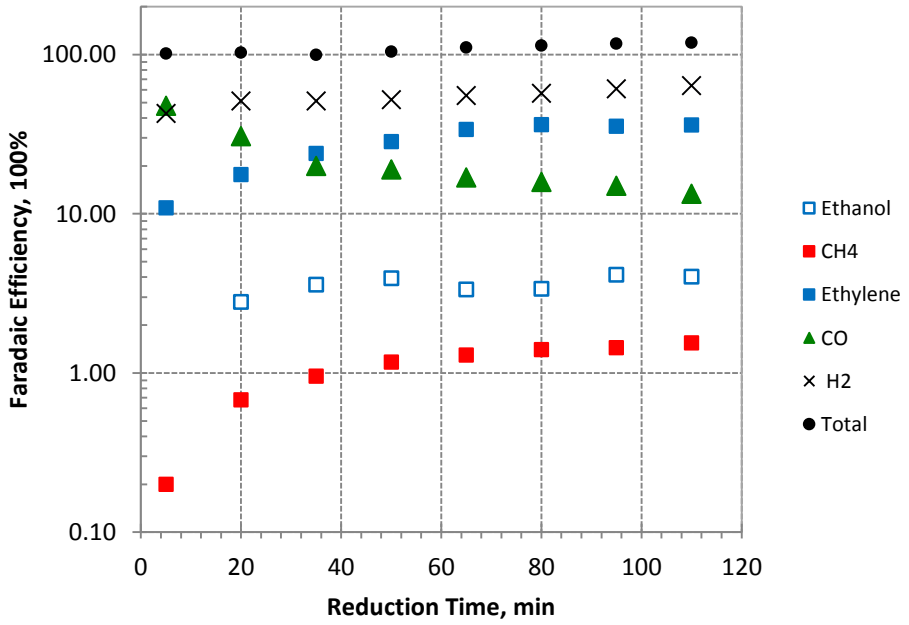


Figure 6.14. Faradaic efficiency of products during the second $CO_2$ reduction on the baseline Toray/Nafion/$Cu_2O$ electrode at -1.5$V_{NHE}$.

The kinetic variation in selectivity is similar to the first run, except that the CO selectivity was higher while ethanol selectivity was slightly lower. The average faradaic efficiencies were 28% ethylene, 22% CO, 3.2% ethanol and 0.5% methane. These results show that $CO_2$ reduction on colloidal $Cu_2O$ electrocatalyst is reproducible.

6.3.2.2. Effect of NaOH Concentration During $Cu_2O$ Synthesis

SEM Analysis. We have examined the electrocatalytic activity of colloidal $Cu_2O$ particles that were prepared by wet chemical reduction using 0.2M NaOH added to 0.005M $Cu^{2+}$ ions. Stoichiometrically, the amount of NaOH added to the mixture is sufficient to precipitate all available $Cu^{2+}$ ions to $Cu(OH)_2$ while leaving excess NaOH in the mixture (0.19M). However, we observed that by further increasing the amount of NaOH, it started to cause formation of other morphologies (see Figure 6.15). The reduction of $Cu_2O$ particles during $CO_2$ reduction also resulted in the evolution of more highly differentiated architecture of particles.

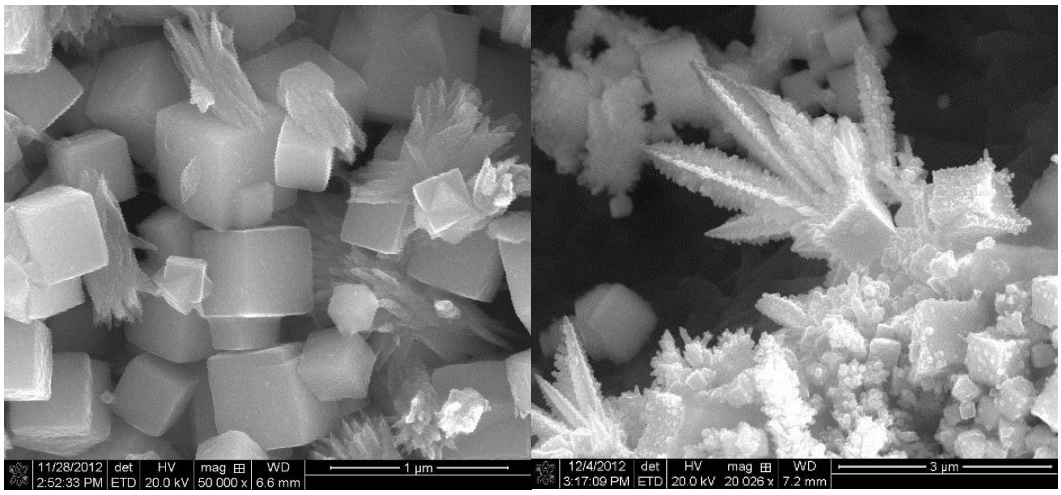


Figure 6.15. SEM of $Cu_2O$ particles prepared using 0.3M NaOH (left) before $CO_2$ reduction and (right) after $CO_2$ reduction at -1.5$V_{NHE}$ for 110 minutes.

Current Profile. The current profile at -1.5$V_{NHE}$ $CO_2$ reduction was compared with that obtained from the baseline $Cu_2O$ electrode (refer to Figure 6.16). Higher total current was observed, with an average of 37 mA, compared to 24 mA from the baseline $Cu_2O$ electrode.

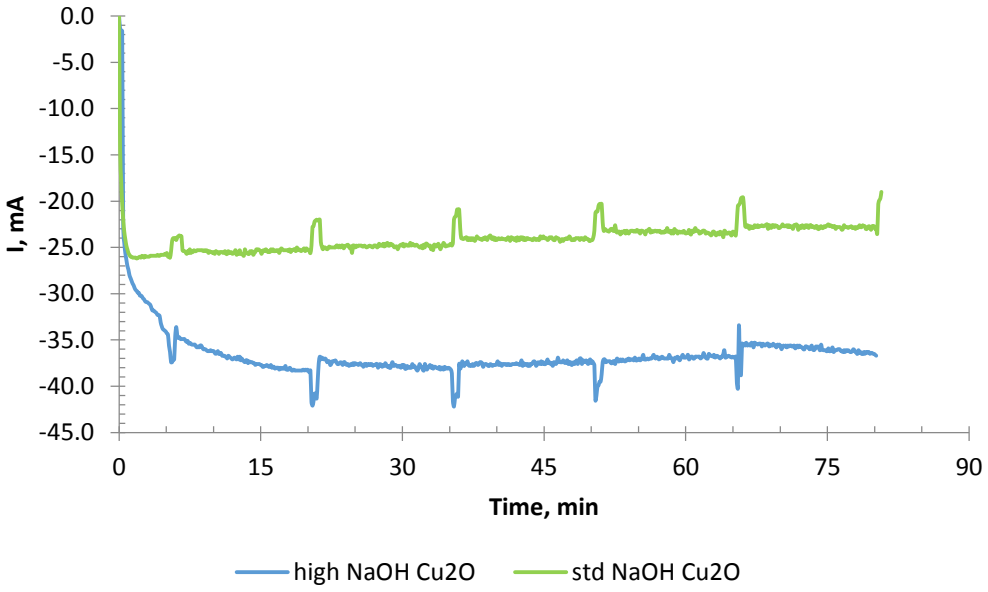


Figure 6.16. Current profile of the high NaOH $Cu_2O$ and baseline $Cu_2O$ electrodes.

Product Distribution. We then examined the product distribution on this catalyst by comparing the formation rate and faradaic efficiencies of ethanol, $CH_4$, ethylene, CO and $H_2$ with that of the baseline Toray/Nafion/$Cu_2O$ sample ($Cu_2O$-360B). We observed the same sequence with formation rates (see Figure 6.17). The electrode showed highest activity towards CO formation, at 37 µmol/$cm^2$*hr which is comparable to the baseline $Cu_2O$ electrode. This was followed by ethylene at 9.6 µmol/$cm^2$*hr and ethanol at 1.1 µmol/$cm^2$*hr. Methane was only produced at trace level of 0.2 µmol/$cm^2$*hr.

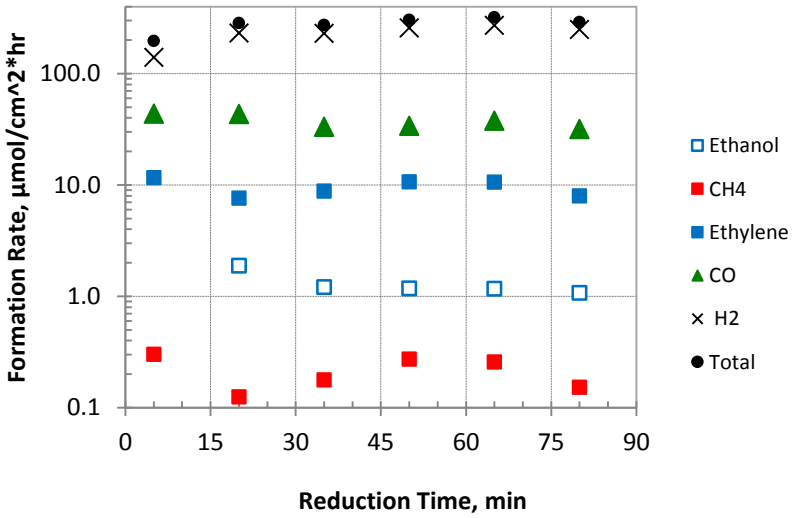


Figure 6.17. Formation rate of products during $CO_2$ reduction on $Cu_2O$ prepared with high NaOH concentration at -1.5$V_{NHE}$.

In terms of selectivity, we saw a 36% decrease in ethylene faradaic efficiency, 33% decrease in CO faradaic efficiency and 42% increase in $H_2$ faradaic efficiency (see Figure 6.18). There was also a decrease in ethanol and methane products. These results suggest that the more homogeneous $Cu_2O$ particles exhibited better selectivity towards ethylene, CO and ethanol than $Cu_2O$ particles with mixed structures.

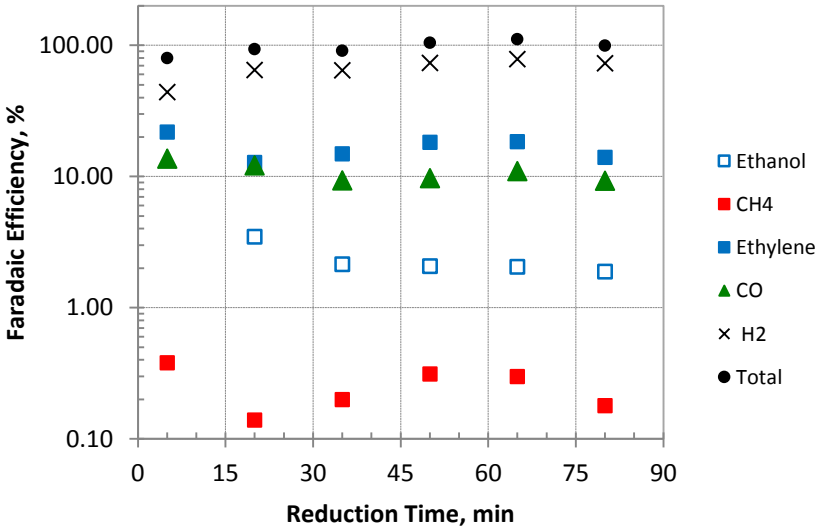


Figure 6.18. Faradaic efficiency of products during $CO_2$ reduction on $Cu_2O$ prepared with high NaOH concentration at -1.5$V_{NHE}$.

6.3.2.3. Effect of $Cu_2O$ Synthesis Aging Time

Next, we studied the effect of aging time during nucleation step of $Cu_2O$ synthesis on the initial particle size and on the product distribution. We confirmed any variation in the size of the particle using SEM. In the electrocatalyst that we studied in the previous section, the particles were aged for 6 hours. In here, we attempted to vary the particle size by lowering the aging times to 0 and 30 minutes.

We considered comparing 4 different electrodes; (1) zero minute $Cu_2O$ ($Cu_2O$-0), (2) 30 minute $Cu_2O$ ($Cu_2O$-30), (3) 360 minute $Cu_2O$ ($Cu_2O$-360A, with comparable $Cu_2O$ loading as the first two samples and pre-characterized by cyclic voltammetry) and (4) $Cu_2O$ electrode from the previous section ($Cu_2O$-360B, aged for 360 minutes and had a high $Cu_2O$ loading). The data in Table 6.1 shows the $Cu_2O$ loading of the different electrodes but with the same Nafion/$Cu_2O$ mass ratio.

Table 6.1. Composition of $Cu_2O$ electrode with different aging time and loading.

| Electrode | $Cu_2O$ Loading, mg | Nafion/$Cu_2O$ Mass Ratio |
|---|---|---|
| $Cu_2O$-0 | 0.9 | 0.8 |
| $Cu_2O$-30 | 1.9 | 0.8 |
| $Cu_2O$-360A | 1.1 | 0.8 |
| $Cu_2O$-360B | 26.5 | 0.8 |

SEM Analysis. The SEM image of the $Cu_2O$-0 electrode before and after $CO_2$ reduction is given in Figure 6.19. The approximate size of the $Cu_2O$-0 particles were 200 nm with variations in the range of 100 – 300 nm. After $CO_2$ reduction, we observed nanoparticle decorations on the surface of the cubes.

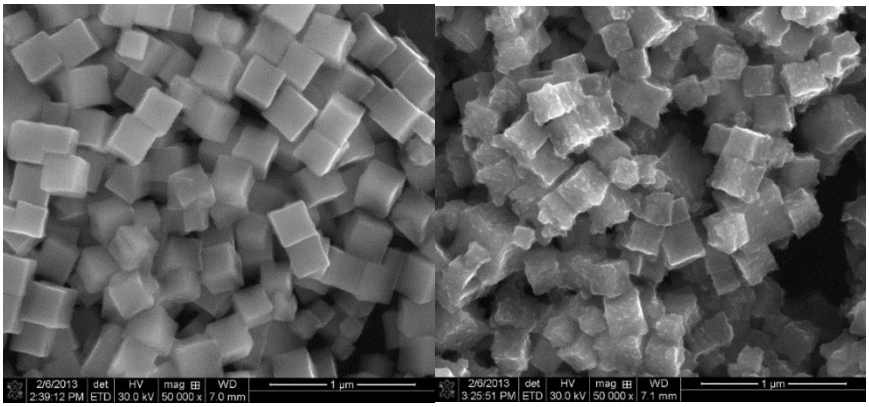

Figure 6.19. SEM of $Cu_2O$-0 sample (left) before $CO_2$ reduction and (right) after 110 minute $CO_2$ reduction at -1.5$V_{NHE}$.

Meanwhile, the SEM image of the $Cu_2O$-30 electrode before and after $CO_2$ reduction is given in Figure 6.20. The approximate size of the $Cu_2O$-30 particles were slightly larger, at 250 nm with variations in the range of 150 – 350 nm. After $CO_2$ reduction, we also observed nanoparticle decorations on the surface of the cubes.

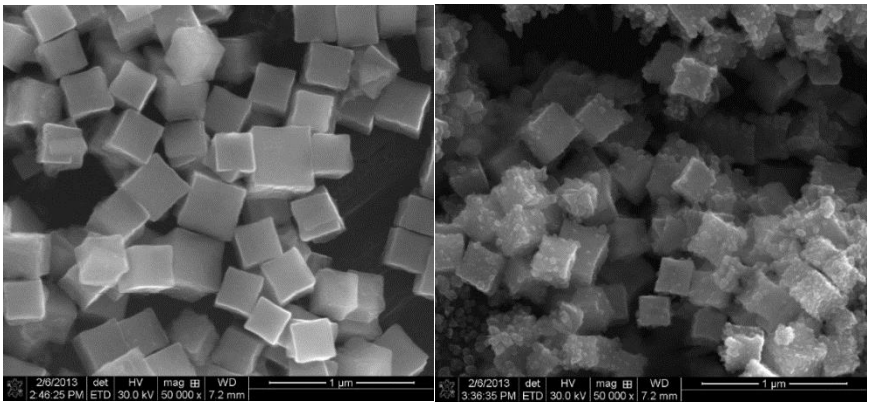

Figure 6.20. SEM of $Cu_2O$-30 sample (left) before $CO_2$ reduction and (right) after 110 minute $CO_2$ reduction at -1.5$V_{NHE}$.

Lastly, the SEM image of the $Cu_2O$-360B electrode is given in Figure 6.21. The electrode generated a mixture of distinct 400 nm and 80 nm sized particles. After $CO_2$

reduction, we did not observe formation of nanoparticle decorations on the surface of the cubes. A thin layer of Nafion could also be seen coated on these particles.

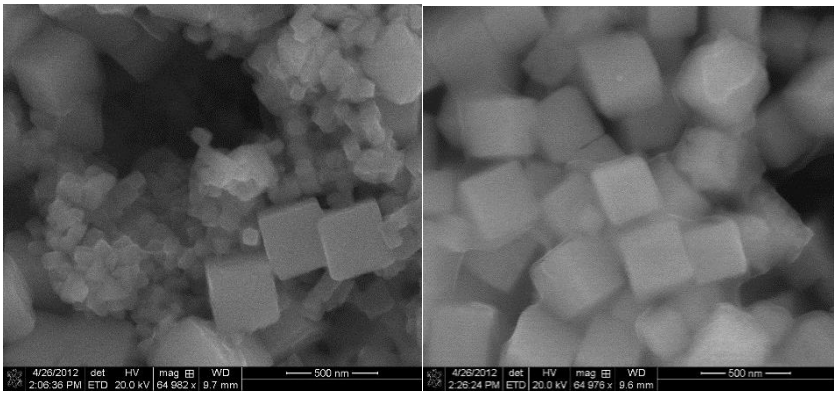

Figure 6.21. SEM of baseline $Cu_2O$-360B sample (left) before $CO_2$ reduction and (right) after 110 minute $CO_2$ reduction at -1.5$V_{NHE}$.

Controlling the particle size by changing the aging time during $Cu_2O$ nucleation stage appeared to be not sufficient. The bulk of particle growth may have taken place immediately after the reducing agent (ascorbate) was added.

Additionally, these images suggest that Nafion was stabilizing the surface morphology of the $Cu_2O$ particles. Although Nafion was present in all these electrodes by the same Nafion/$Cu_2O$ ratio, the Nafion and $Cu_2O$ mixture did not achieve even distribution during the evaporation of the Nafion solvent. In the regions of the electrode where Nafion were not effectively coating the $Cu_2O$ particles, these particles were reduced to Cu.

Current Profile. We also compared the current flow in these electrodes and have included the result from the control electrodes, Toray (T) and Toray/Nafion (T/N) (see Figure 6.22). The graph from the $Cu_2O$-0 sample showed a current flow ($I_{ave}$ = -30 mA) that increased with electrolysis time, exhibiting high noise level that was more pronounce than the one in the Toray sample. The graph of the $Cu_2O$-30 sample showed a stable current

flow that gradually increased with electrolysis time. The graph of the $Cu_2O$-360A sample showed a stable and steady-state current flow. This sample underwent four cycles of voltammetry prior to electrolysis which may have helped equilibrate the surface of the electrode. The graph of the $Cu_2O$-360B minute growth sample showed a stable current flow that gradually decreased with electrolysis time.

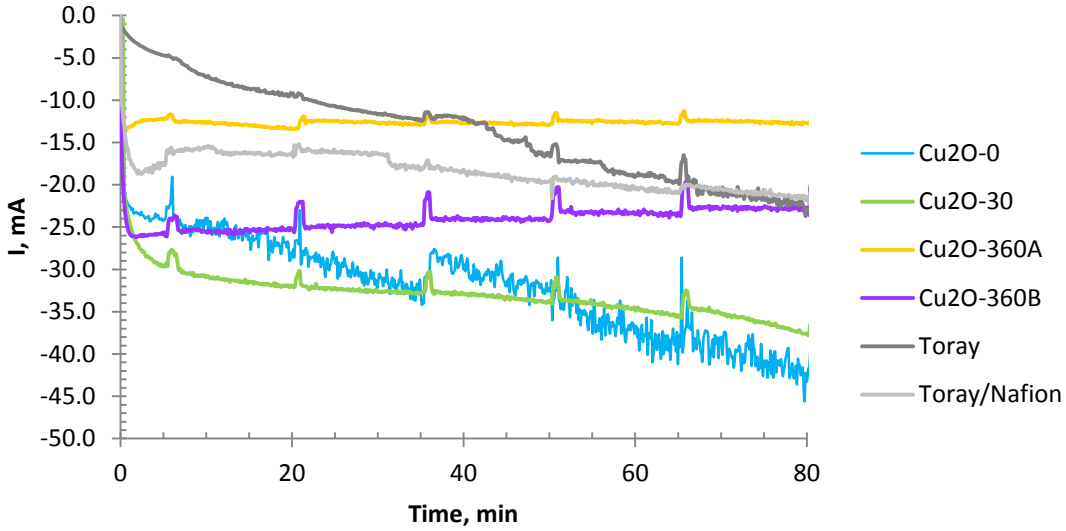


Figure 6.22. Current profile of $Cu_2O$ particles with different synthesis aging time generated during $CO_2$ reduction at -1.5$V_{NHE}$.

Comparison of Product Distribution. Finally, we compared the product distribution of these electrodes. Different from the previous sections and Chapters, we present our comparison here by grouping the data based on the individual products of $CO_2$ (and $H_2O$) reduction rather than by electrode. The electrodes were compared in this manner because of the number of products and electrodes being compared.

*$H_2$ Formation*. First, we compared the electrodes based on $H_2$ formation, which is formed solely from $H_2O$ reduction on exposed Toray surfaces. Foremost, the $H_2$ formation rate increased with time for all the electrodes as seen in Figure 6.23. The $Cu_2O$-0 electrode showed the highest average $H_2$ formation rate and fastest increase in product generation

from 118 to 402 µmol/cm$^2$*hr. Meanwhile, the $Cu_2O$-360A electrode showed the lowest average $H_2$ formation rate and slowest increase in product generation from 31 to 130 µmol/cm$^2$*hr.

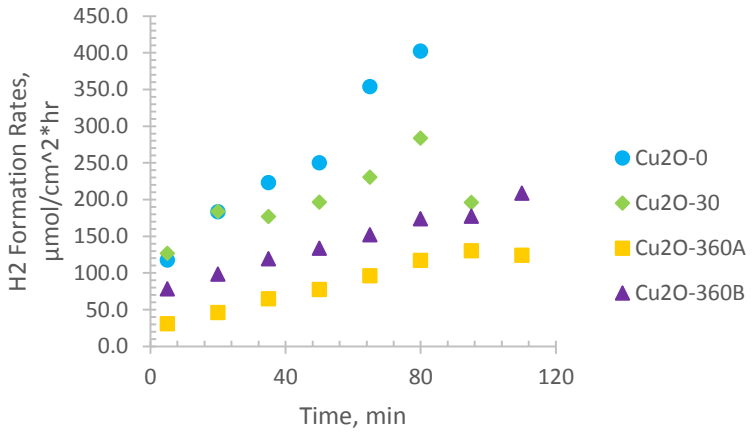


Figure 6.23. Formation rate of $H_2$ on $Cu_2O$ particles with different synthesis aging time during $CO_2$ reduction at -1.5$V_{NHE}$.

In terms of faradaic efficiency shown in Figure 6.24, the $Cu_2O$-0 electrode still showed the highest faradaic efficiency although the rate of increase in value is now more identical to that of the other electrodes. Meanwhile, the two $Cu_2O$-360 electrodes showed identical faradaic efficiencies especially in the first half of the process.

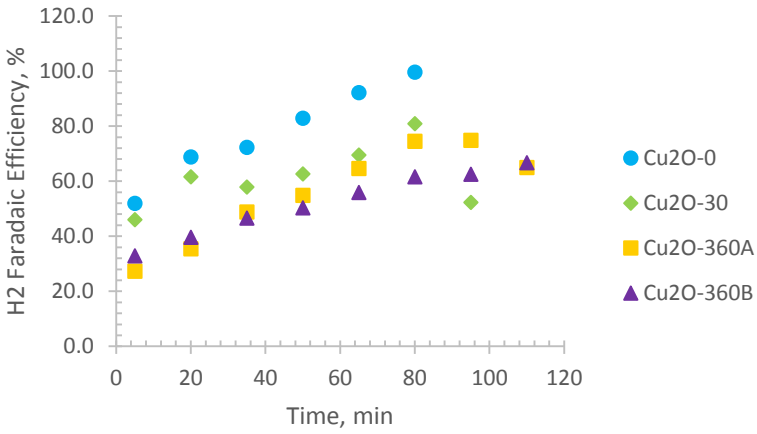


Figure 6.24. Faradaic efficiency of $H_2$ on $Cu_2O$ particles with different synthesis aging time during $CO_2$ reduction at -1.5$V_{NHE}$.

*CO Formation*. Next, we compared the electrodes based on their selectivity to CO which is the second reduced form of $CO_2$ after $HCOO^-$ (see Figure 6.25).

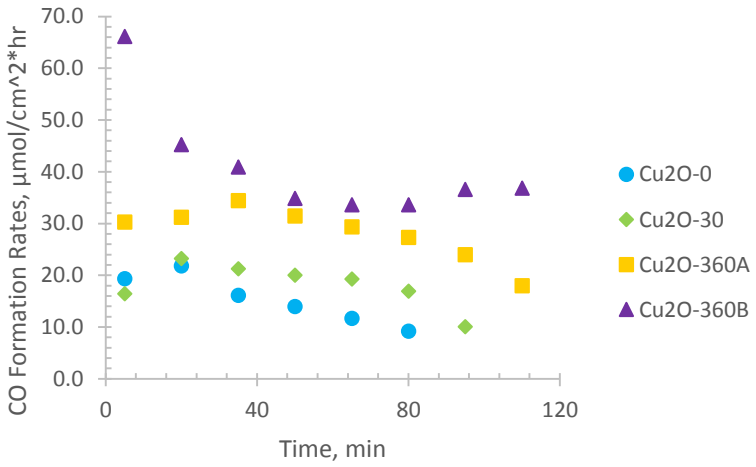


Figure 6.25. Formation rate of CO on $Cu_2O$ particles with different synthesis aging time during $CO_2$ reduction at -1.5$V_{NHE}$.

The $Cu_2O$-360B electrode showed the highest initial CO formation rate of 66 µmol/$cm^2$*hr measured at the 5 minute sampling time and the highest over-all average rate of 41 µmol/$cm^2$*hr. This was followed by the $Cu_2O$-360A electrode at an average rate of 28 µmol/$cm^2$*hr. Meanwhile, the $Cu_2O$-0 electrode showed the lowest average CO formation rate of 15 µmol/$cm^2$*hr.

In terms of faradaic efficiency, the graph in Figure 6.26 shows that the CO faradaic efficiency decreased with time for all the electrodes. Despite producing CO at a lower rate, the $Cu_2O$-360A electrode showed better over-all CO faradaic efficiency of 20% compared to the $Cu_2O$-360B electrode which had 16% faradaic efficiency. The $Cu_2O$-0 electrode still registered the lowest average faradaic efficiency of 5.3%.

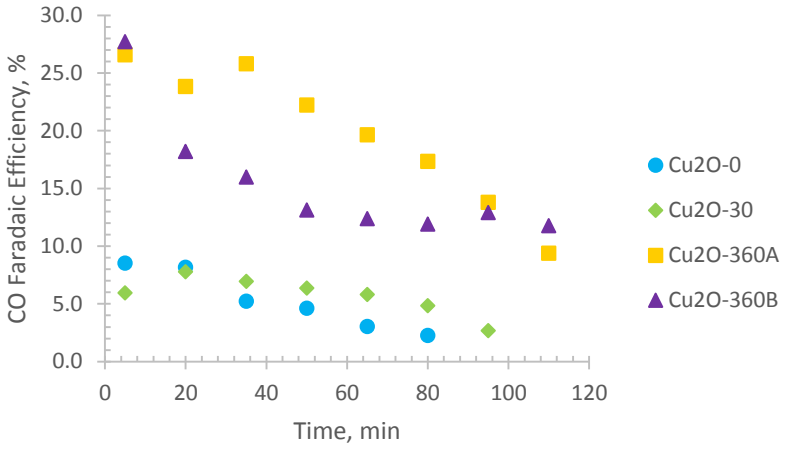


Figure 6.26. Faradaic efficiency of CO on $Cu_2O$ particles with different synthesis aging time during $CO_2$ reduction at -1.5$V_{NHE}$.

*Methane Formation*. Next, we compared the electrodes based on their productivity and selectivity to methane. The methane formation rates decreased with time for all samples except in the $Cu_2O$-360B electrode where the rates were already the lowest but slightly increased with time (see Figure 6.27). The $Cu_2O$-0 electrode exhibited an initially high methane formation rate of 4.4 µmol/cm$^2$*hr but the rate also dropped steeply for an average of 1.6 µmol/cm$^2$*hr. This was followed closely by the $Cu_2O$-30 electrode with an average $CH_4$ formation rate of 1.3 µmol/cm$^2$*hr.

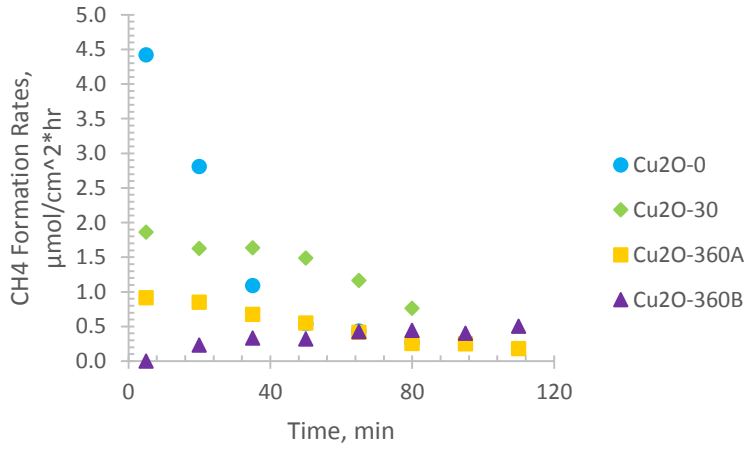


Figure 6.27. Formation rate of methane on $Cu_2O$ particles with different synthesis aging time during $CO_2$ reduction at -1.5$V_{NHE}$.

The graph in Figure 6.28 still showed that the $CH_4$ faradaic efficiency decreased with time for all the electrodes. Again, the $Cu_2O$-0 electrode exhibited an initially high methane faradaic efficiency of 8% relative to the other samples. This level represents the second highest methane faradaic efficiency achieved among the $Cu_2O$ particles studied and was about the same with our Cu electrode. The $Cu_2O$-30 and $Cu_2O$-360A electrodes this time had about the same faradaic efficiencies even though their formation rates were different. The $CH_4$ faradaic efficiencies of the four electrodes approached to an identical value of about 0.6% at the end of the process.

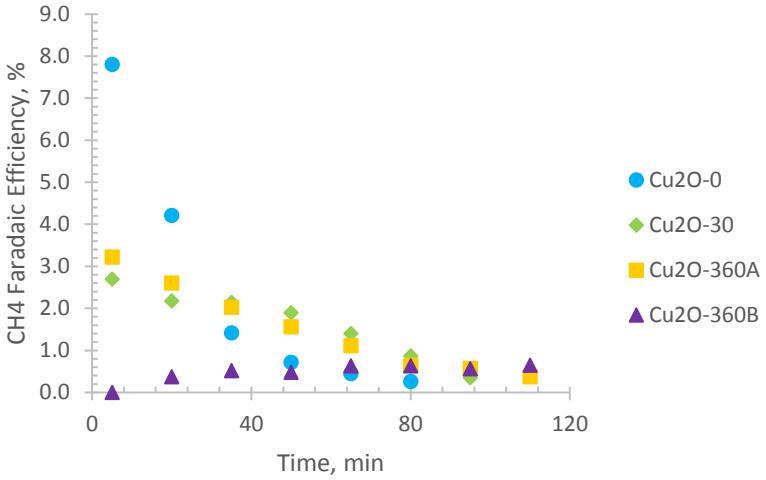


Figure 6.28. Faradaic efficiency of methane on $Cu_2O$ particles with different synthesis aging time during $CO_2$ reduction at -1.5$V_{NHE}$.

*Ethylene Formation*. Next, we compared the electrodes based on their electrocatalytic activity towards ethylene formation. The graph in Figure 6.29 shows the catalysts were more dynamic with their activity towards ethylene compared to their activity towards CO and $CH_4$. Over-all, the $Cu_2O$-360B electrode showed the highest average $C_2H_4$ formation rate of 13 µmol/$cm^2$*hr. Meanwhile, the other $Cu_2O$-360A electrode showed the lowest $C_2H_4$ formation rate of 2.6 µmol/$cm^2$*hr. At 20 minutes, the $Cu_2O$-30 electrode produced

the highest ethylene formation rate at 16 μmol/cm$^2$*hr. However, the production rate decreased rapidly after that.

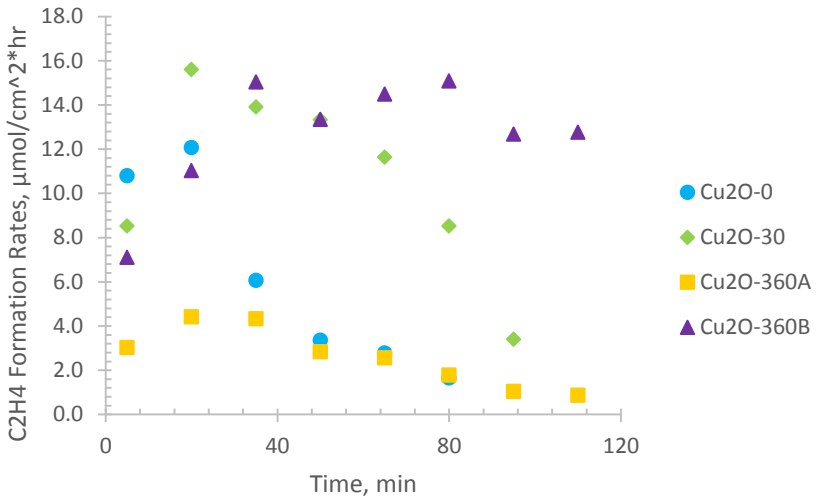


Figure 6.29. Formation rate of ethylene on $Cu_2O$ particles with different synthesis aging time during $CO_2$ reduction at -1.5$V_{NHE}$.

In terms of faradaic efficiency (refer to Figure 6.30), the $Cu_2O$-360B electrode still showed the highest $C_2H_4$ faradaic efficiency, followed by the $Cu_2O$-30, $Cu_2O$-360A and $Cu_2O$-0 electrode.

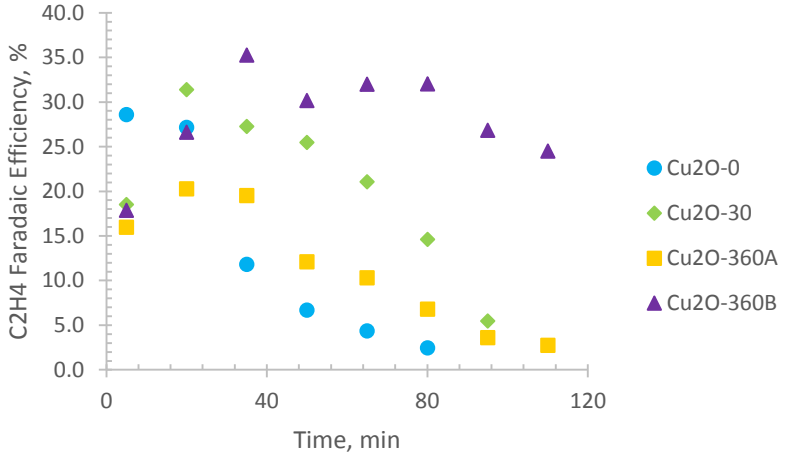


Figure 6.30. Faradaic efficiency of ethylene on $Cu_2O$ particles with different synthesis aging time during $CO_2$ reduction at -1.5$V_{NHE}$.

*Ethanol Formation*. Finally, we compared the activity of these electrodes toward ethanol formation (see Figure 6.31). The ethanol formation rates decreased with time in all samples except for the $Cu_2O$-360B electrode where the rates were relatively more flat than the rest and also showed the highest average ethanol formation rate of 2.3 µmol/cm$^2$*hr. This was followed by the $Cu_2O$-30 electrode with ethanol formation rate of 1.9 µmol/cm$^2$*hr.

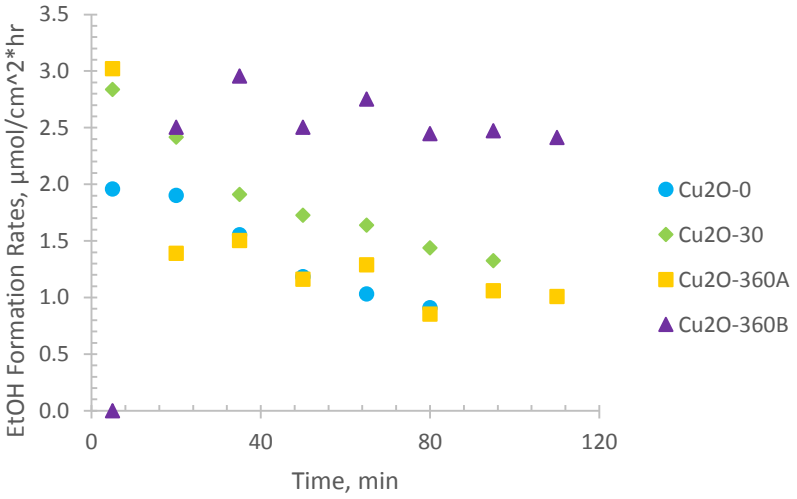


Figure 6.31. Formation rate of ethanol on $Cu_2O$ particles with different synthesis aging time during $CO_2$ reduction at -1.5$V_{NHE}$.

In terms of faradaic efficiency, the $Cu_2O$-360A electrode showed an initially high selectivity towards ethanol at about 16% (see Figure 6.32). The selectivity of these electrodes toward ethanol did not differ by more than an order of magnitude and ranged between 2-8 %.

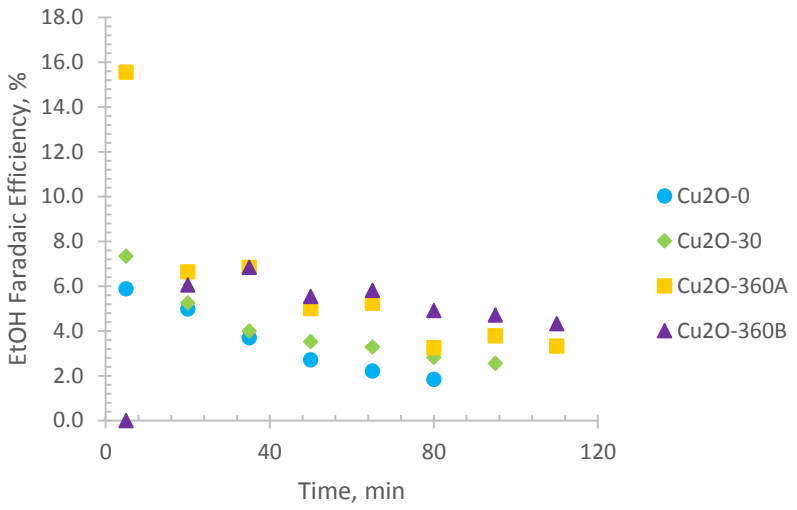


Figure 6.32. Faradaic efficiency of ethanol on $Cu_2O$ particles with different synthesis aging time during $CO_2$ reduction at -1.5$V_{NHE}$.

To summarize, the main result was the high CO and ethylene selectivity on the $Cu_2O$-360B electrode and the high CO selectivity on the $Cu_2O$-360A electrode compared to the other two electrodes. The reduction of larger $Cu_2O$ particles may result in more kinks, steps and defects than the smaller $Cu_2O$ particles. We also observed a copper-like behavior on the $Cu_2O$-0 electrode which showed a relatively high initial methane faradaic efficiency.

The reduction of larger $Cu_2O$ particles may have produced more dispersed Cu clusters that stabilize the high rate of ethylene formation and its selectivity. Li et al. (2012) observed that thicker $Cu_2O$ films grown by thermal oxidation exhibited higher CO faradaic efficiency because the resulting Cu have higher concentration of unstable grain boundaries than polycrystalline Cu. They also suggested that grain boundary is a key design feature to improving selectivity towards $C_{2+}$ hydrocarbons (Li et al. 2014).

The amount of $Cu_2O$ particles present on the surface of Toray also affected the product formation rates, particularly CO, ethylene and ethanol. The $Cu_2O$-360B electrode

which had a $Cu_2O$ loading of 26.5 mg showed higher CO, ethylene and ethanol formation rates than the $Cu_2O$-360A electrode which had a $Cu_2O$ loading of only 1.1 mg. However, whereas the $Cu_2O$ loading increased by a factor of 24, the CO, ethylene and ethanol formation rates only increased by a factor of 1.5, 5 and 1.6. This suggest that only the particles in the outermost layer were the most active in the electrochemical reduction of $CO_2$.Those particles located in the inner region of the electrode did not encounter as many $CO_2$ molecules as those on the surface due to mass transfer limitation.

6.3.2.4. Effect of Nafion

After studying the effect of NaOH composition and particle aging time during nucleation stage of the $Cu_2O$ synthesis, we then looked at the effect Nafion on the electrocatalytic activity of colloidal $Cu_2O$ particles. Nafion was added during the electrode assembly primarily to provide a binding support to foreign $Cu_2O$ particles on Toray.

In Section 6.3.2.3, we observed that $Cu_2O$ particles encapsulated with Nafion did not undergo a change in structure, whereas those $Cu_2O$ particles without Nafion covering had decorations on the surface of the cubes. In Chapter 5, we also observed that Nafion helped stabilize the formation of CO and $C_2H_4$. In this section we examined the effect of Nafion on colloidal $Cu_2O$ particles by considering three different Nafion/$Cu_2O$ ratios; namely, 0.0, 1.2 and 2.4.

<u>$Cu_2O$ Loading</u>. The three electrodes compared were labelled as follows: (1) TC – Toray + $Cu_2O$, (2) TLC – Toray + Low Nafion + $Cu_2O$ (TLC) and (3) Toray + High Nafion + $Cu_2O$ (THC). Table 6.2 shows the amount of $Cu_2O$ on Toray as well as the mass ratio of Nafion to $Cu_2O$ for each sample. The TLC and THN samples prepared have high $Cu_2O$ loading compared to the TC sample. The low loading in the TC sample relative

to the TLC and THN samples is due to difference in preparation condition, particularly on the amount of reagents used during $Cu_2O$ synthesis.

Table 6.2. Composition of $Cu_2O$ Electrodes with Different Amounts of Nafion.

| Electrode | $Cu_2O$ Loading, mg | Nafion/$Cu_2O$ Mass Ratio |
|---|---|---|
| Toray + $Cu_2O$ (TC) | 3.0 | 0.0 |
| Toray + Low Nafion + $Cu_2O$ (TLC) | 38.0 | 1.2 |
| Toray + High Nafion + $Cu_2O$ (THC) | 30.6 | 2.4 |

Current Profile. We monitored the current profile generated by these electrodes during $CO_2$ reduction at -1.5$V_{NHE}$ (refer to Figure 6.33). The TC samples showed a stable and steady state current flow of about 20 mA. The TLC sample registered the highest amount of current among the three samples, with a mean value of 40 mA which was twice that of TC. Meanwhile the THC sample had a mean current of 24 mA. We observed transient current in all three samples which indicate reduction of $Cu_2O$ particles.

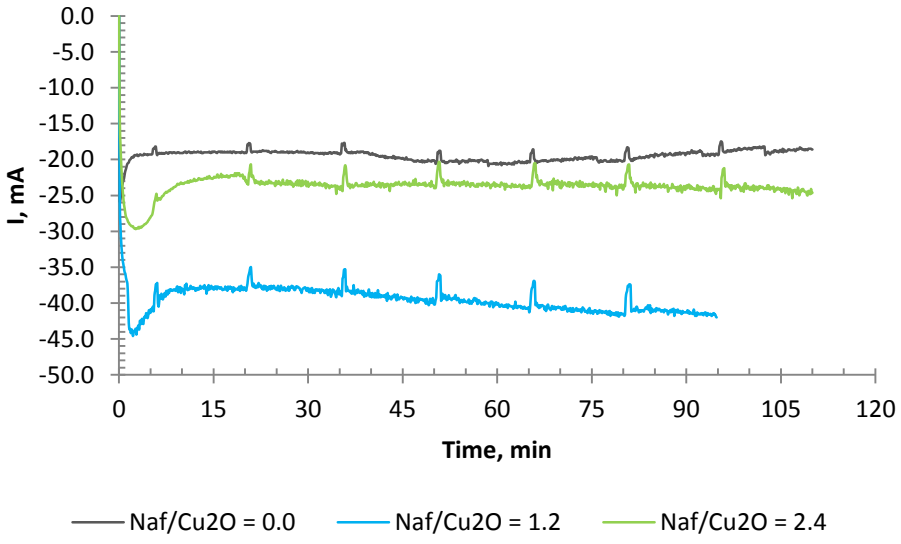


Figure 6.33. Current profile generated by $CO_2$ reduction on $Cu_2O$ particles with different amounts of Nafion at -1.5$V_{NHE}$.

$H_2$ Formation. First, we compared $H_2$ formation of these electrocatalysts. Figure 6.34 shows the $H_2$ formation rates where the TLC electrode showed highest $H_2$ activity which increased with time from an initial rate of 143 µmol/cm$^2$*hr to the final rate of 325 µmol/cm$^2$*hr for an average of 270 µmol/cm$^2$*hr. This was followed by the THC electrode with initial, final and average rates of 120, 187 and 162 µmol/cm$^2$*hr. The TLC electrode showed the least $H_2$ rates at initial, final and average rates of 97, 103 and 116 µmol/cm$^2$*hr. $H_2$ formation rate generally increased with time similar to what we have observed on Toray. However, the TC electrode showed a peak in $H_2$ rates halfway through the process.

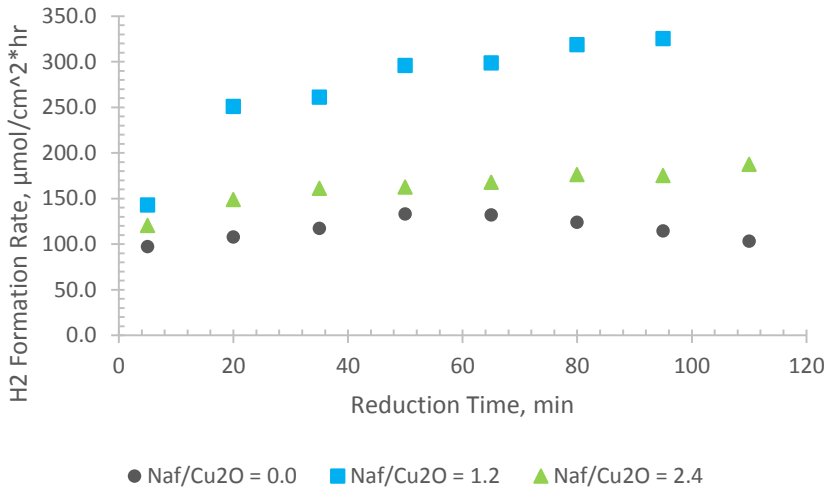


Figure 6.34. $H_2$ formation rates on $Cu_2O$ particles with different amounts of Nafion during $CO_2$ reduction at -1.5$V_{NHE}$.

The three electrodes showed closer faradaic efficiency values as seen in Figure 6.35. The $H_2$ selectivity for all three samples increased with time at a decreasing rate. Additionally, the TC electrode showed a maximum $H_2$ faradaic efficiency around 50 minutes.

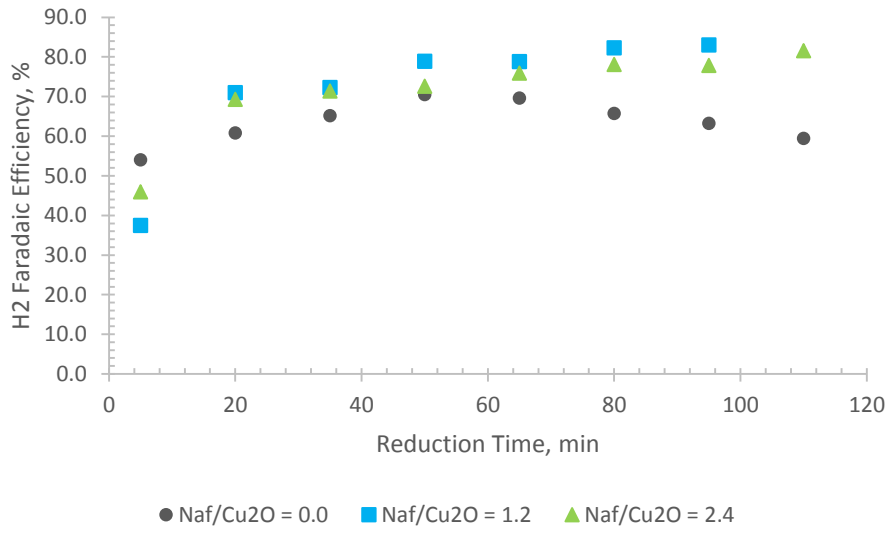


Figure 6.35. Faradaic efficiency of $H_2$ formation on $Cu_2O$ particles with different amounts of Nafion during $CO_2$ reduction at -1.5$V_{NHE}$.

CO Formation. Next, we look at CO formation in Figure 6.36. The TC electrode showed highest CO activity but decreased with time from an initial rate of 21 µmol/cm$^2$*hr to the final rate of 14 µmol/cm$^2$*hr for an average of 16 µmol/cm$^2$*hr. This was followed closely by the TLC electrode which showed a steadier CO formation rate.

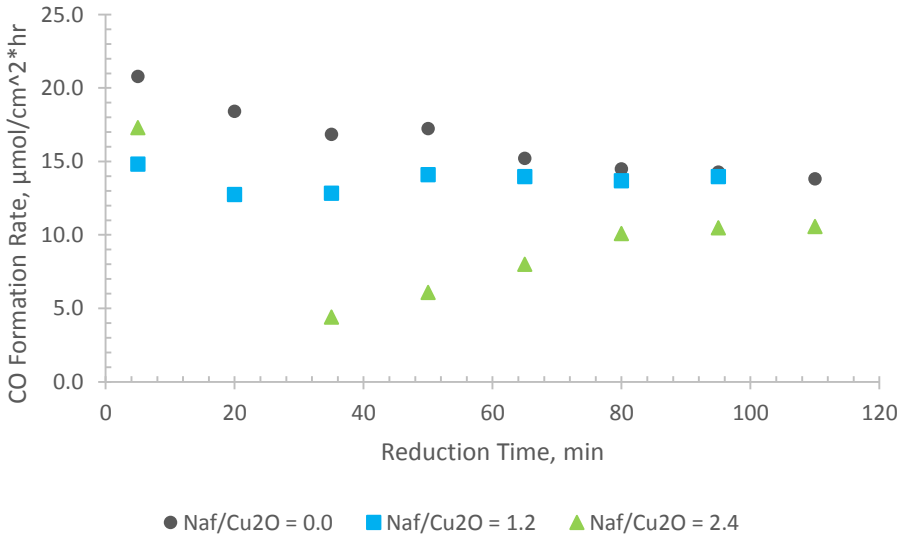


Figure 6.36. CO formation rates on $Cu_2O$ particles with different amounts of Nafion during $CO_2$ reduction at -1.5$V_{NHE}$.

The initial, final and average rates were 15, 14 and 14 µmol/cm$^2$*hr. The THC electrode showed the least CO rates at initial, final and average rates of 17, 11 and 8 µmol/cm$^2$*hr and the kinetics was also very dynamic.

In terms of faradaic efficiency, The TC electrode showed the highest average CO selectivity of 9% faradaic efficiency with a high of 12% near the start of reduction and gradually decreased to 8% by the end of the process. The TLC and THC electrodes had about the same average faradaic efficiency of 4%. The CO selectivity on the TLC electrode was kinetically stable (refer to Figure 6.37).

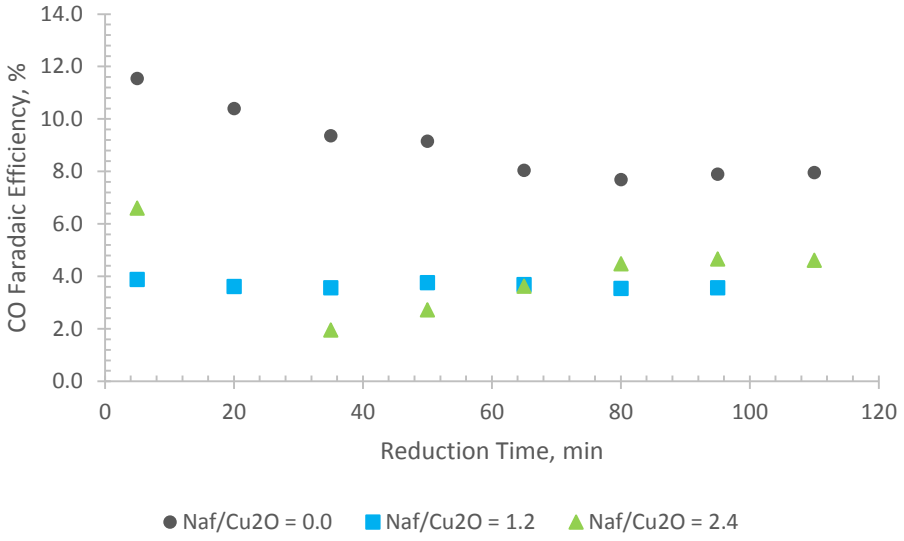


Figure 6.37. Faradaic efficiency of CO formation on $Cu_2O$ particles with different amounts of Nafion during $CO_2$ reduction at -1.5$V_{NHE}$.

Methane Formation. Next, we look at methane where all the samples exhibited less than 0.3 µmol/cm$^2$*hr formation rate (see Figure 6.38) and one order of magnitude lower than CO. The TLC electrode showed the highest average methane formation rate of 0.2 µmol/cm$^2$*hr.

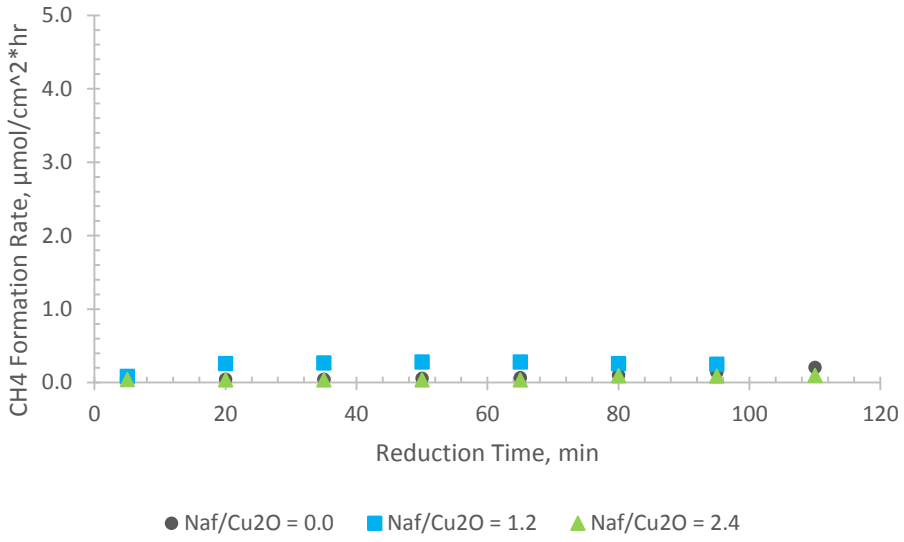


Figure 6.38. Methane formation rates on $Cu_2O$ particles with different amounts of Nafion during $CO_2$ reduction at -1.5$V_{NHE}$.

Meanwhile, the faradaic efficiency of the three electrodes were less than 0.5% (see Figure 6.39). In Section 6.3.2.3, we observed $CH_4$ efficiencies between 0.5-3.0% on $Cu_2O$ particles with different aging times. In those samples, the Nafion/$Cu_2O$ ratio was 0.8. $CH_4$ selectivity may be constrained with increased Nafion content.

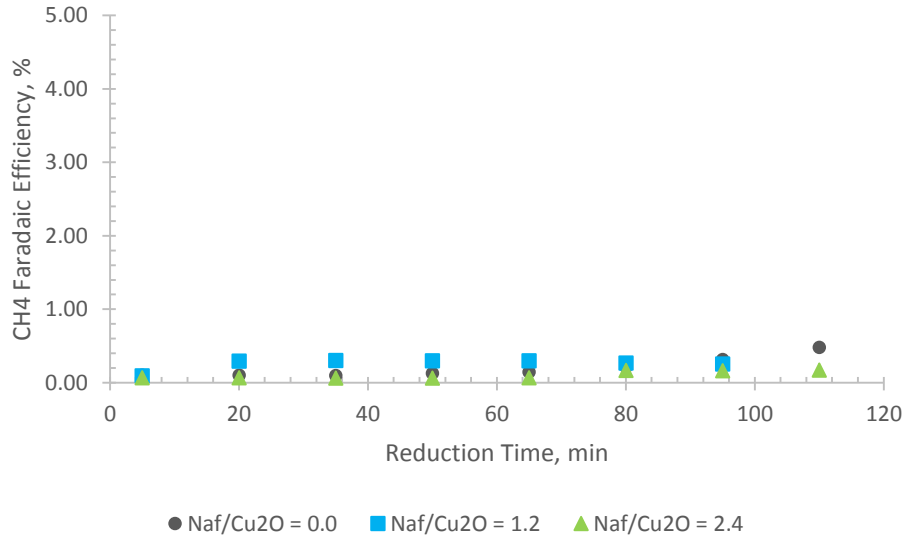


Figure 6.39. Faradaic efficiency of methane formation on $Cu_2O$ particles with different amounts of Nafion during $CO_2$ reduction at -1.5$V_{NHE}$.

Ethylene Formation. Next, we look at ethylene formation in Figure 6.40. The TC electrode showed the lowest ethylene rates at initial, final and average rates of 2.4, 2.2 and 1.2 µmol/cm$^2$*hr. On the other hand, the TLC electrode showed the highest ethylene activity with an initial, final and average rates of 8, 11 and 12 µmol/cm$^2$*hr. This was followed by the THC electrode with an initial, final and average rates of 2.2, 5.4 and 5.3 µmol/cm$^2$*hr.

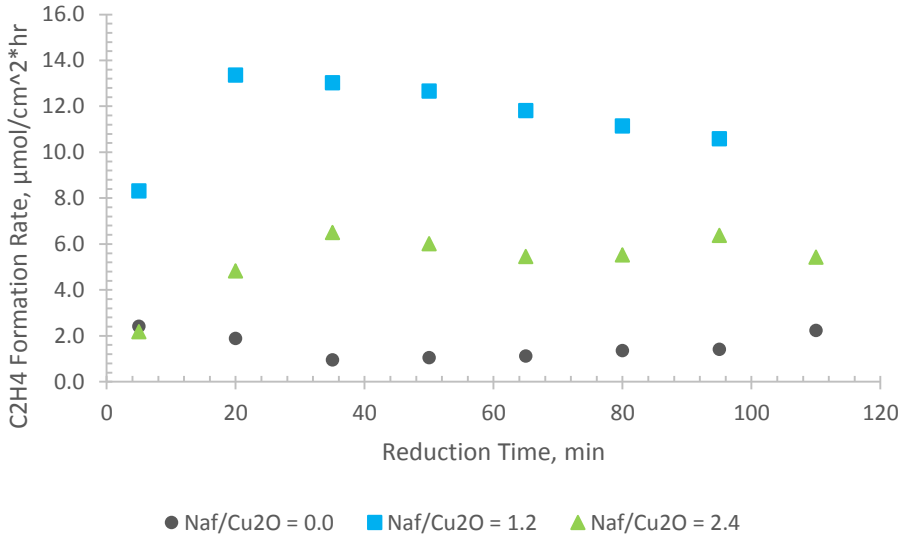


Figure 6.40. Ethylene formation rates on $Cu_2O$ particles with different amounts of Nafion during $CO_2$ reduction at -1.5$V_{NHE}$.

In terms of faradaic efficiency shown in Figure 6.41, the TLC electrode again showed the highest ethylene selectivity with an initial, final and average percentage of 13%, 16% and 19%. This was followed by the THC electrode with an initial, final and average percentages of 5%, 14% and 14%. The TC electrode showed the lowest ethylene selectivity at initial, final and average percentages of 2.4%, 2.2% and 1.2%.

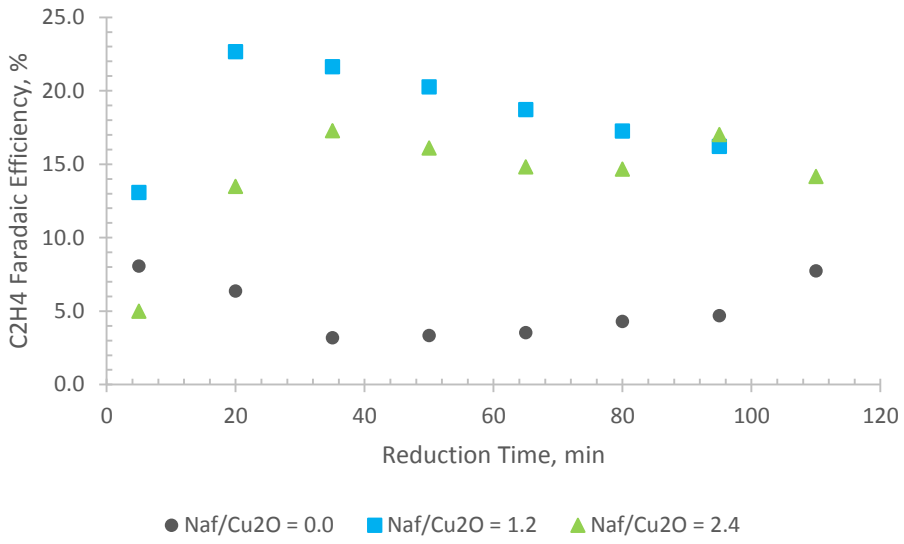


Figure 6.41. Faradaic efficiency of ethylene formation on $Cu_2O$ particles with different amounts of Nafion during $CO_2$ reduction at -1.5$V_{NHE}$.

Ethanol Formation. Finally, we look at the ethanol product distribution of the three electrodes. As seen in Figure 6.42, the TC electrode showed the lowest average ethanol rate of 0.2 µmol/cm$^2$*hr. Meanwhile, the TLC electrode showed the highest ethanol activity with a 20 minute, final and average rates of 3.6, 2.6 and 2.7 µmol/cm$^2$*hr.

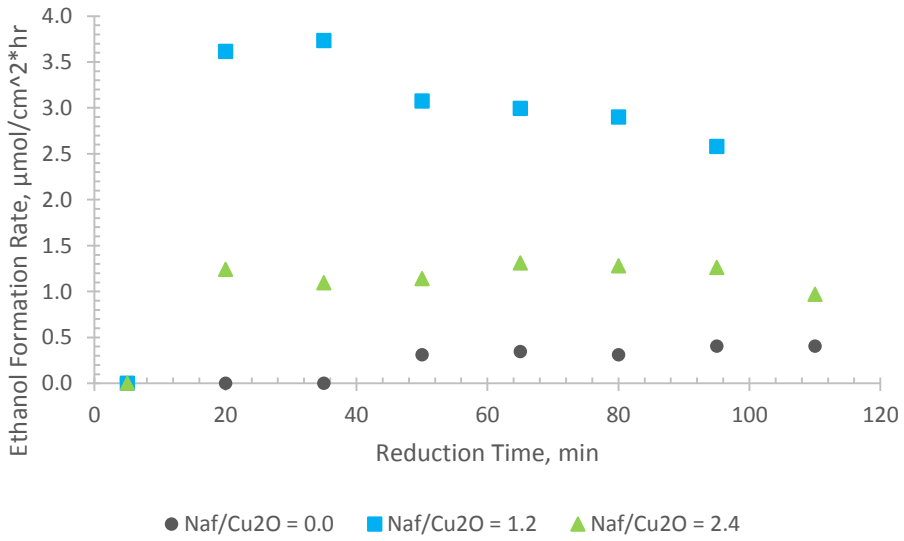


Figure 6.42. Ethanol formation rates on $Cu_2O$ particles with different amounts of Nafion during $CO_2$ reduction at -1.5$V_{NHE}$.

This was followed by the THC electrode with a 20 minute, final and average rates of 1.2, 1.0 and 1.0 µmol/cm$^2$*hr. We noticed that there were no measurable ethanol products early in the reduction process. This suggest that ethanol is kinetically slower to develop compared to ethylene.

In terms of faradaic efficiency shown in Figure 6.43, the TLC electrode again showed the highest ethanol selectivity with a 20 minute, final and average percentage of 6.0%, 4.2% and 4.5%. This was followed by the THC electrode with a 20 minute, final and average percentages of 3.3%, 2.6% and 2.8%. The TC electrode showed the lowest average ethanol faradaic efficiency of 0.7%.

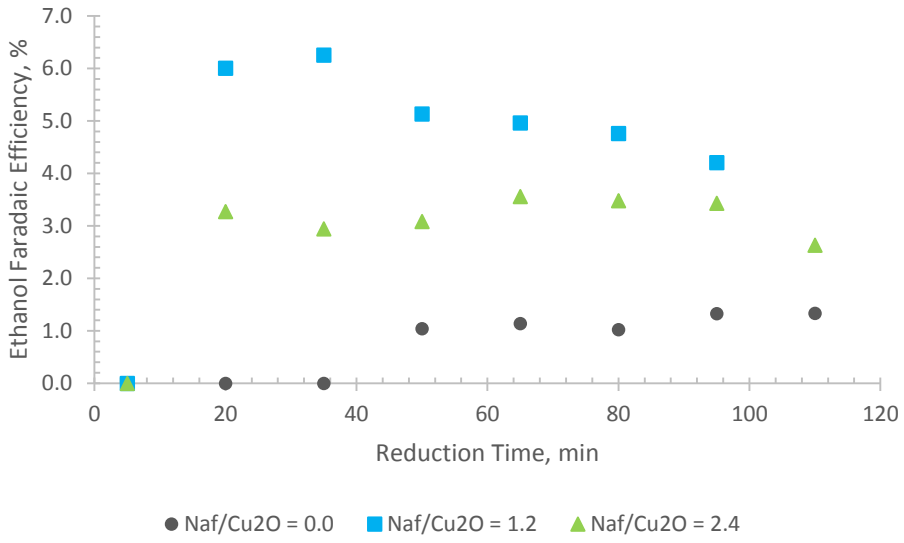


Figure 6.43. Faradaic efficiency of ethanol formation on $Cu_2O$ particles with different amounts of Nafion during $CO_2$ reduction at -1.5$V_{NHE}$.

Over-all, the results suggest that moderate amounts of Nafion help improve the selectivity of $Cu_2O$ particles to ethylene and ethanol. However, excessive amounts of Nafion also lowers their selectivity to these products.

6.3.2.5. Effect of Cyclic Voltammetry

In the previous sections, we studied the effect of different electrode preparation conditions on the electrocatalytic activity of $Cu_2O$ particles towards $CO_2$ reduction. In this section, we examined the product distribution on $Cu_2O$ particles after they were characterized by cyclic voltammetry. Cyclic voltammetry was conducted on two different electrodes, (1) Toray/$Cu_2O$ (CV) and (2) Toray/Nafion/$Cu_2O$ (CV).

Toray/$Cu_2O$ (CV) Electrode

*Cyclic Voltammetry*. As shown in Figure 6.44, there was no visible peak associated with the reduction of $Cu_2O$ to Cu in the first cathodic sweep, although we observed a minor shoulder in the blue line between -0.35V and -0.6V.

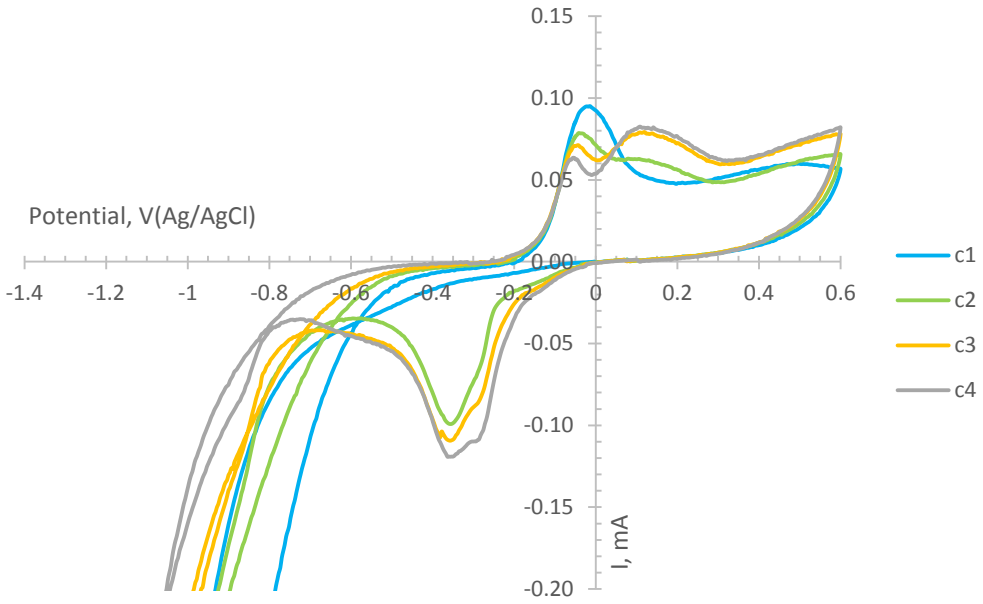


Figure 6.44. Four cycle voltammetry of Toray/$Cu_2O$ (CV) electrode (50 mV/s).

$Cu_2O$ may not have become readily reduced during the first cathodization at the expected potential and may have occurred at more negative potential. In the first anodic sweep, peak due to Cu oxidation appeared. The anodized Cu was reduced more easily compared to the colloidal $Cu_2O$ as seen by the appearance of cathodic peaks.

*Current Profile of the First Reduction*. We then performed $CO_2$ reduction after cyclic voltammetry. The current versus time profile is shown in Figure 6.45. The mean total current was 12.5 mA. We note that the reduction between 20 and 35 minutes occurred without a $CO_2$ carrier bubbling. As such, the current became flat during this period.

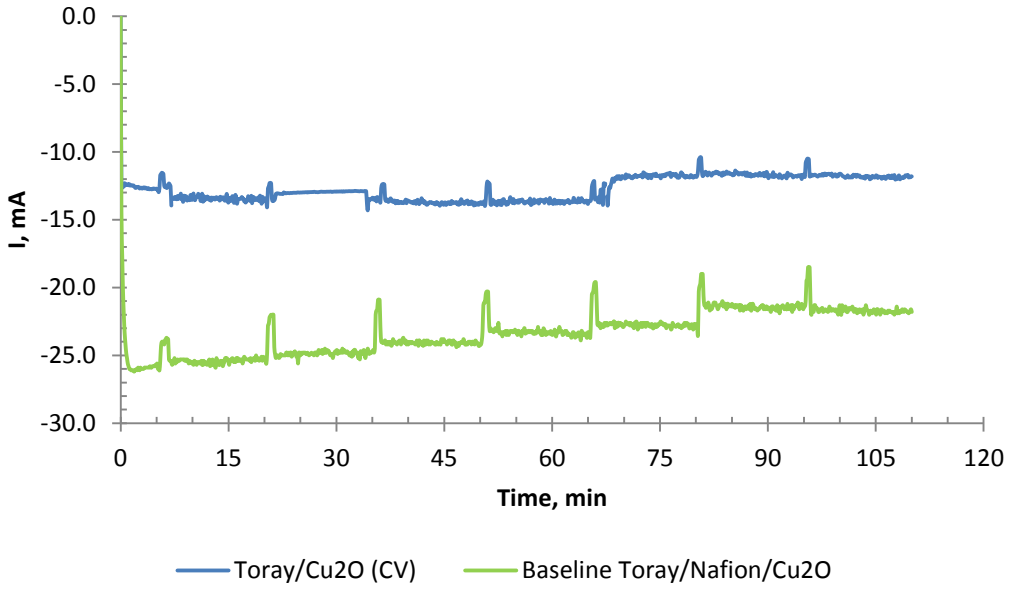


Figure 6.45. Current profile of Toray/$Cu_2O$ (CV) and baseline Toray/Nafion/$Cu_2O$ electrodes.

*Product Distribution During the First Reduction*. The graph in Figure 6.46 shows the formation rate of different $CO_2$ products. The production rates at 35 minute sampling were not included because their values were unusually high as a result of interrupted $CO_2$ bubbling. Over-all, we observed a decrease in the formation rates of $CO_2$ products with

concurrent increase in $H_2$ production. CO formation had the highest productivity averaging 6.8 µmol/cm$^{2*}$hr (ranging between 3.6 – 10.2 µmol/cm$^{2*}$hr). This was followed by ethylene at 2.5 µmol/cm$^{2*}$hr (ranging between 0.1 – 7.0 µmol/cm$^{2*}$hr), methane at 1.0 µmol/cm$^{2*}$hr (ranging between 0.2 – 2.3 µmol/cm$^{2*}$hr) and ethanol at 0.5 µmol/cm$^{2*}$hr (ranging between 0.3 – 0.8 µmol/cm$^{2*}$hr).

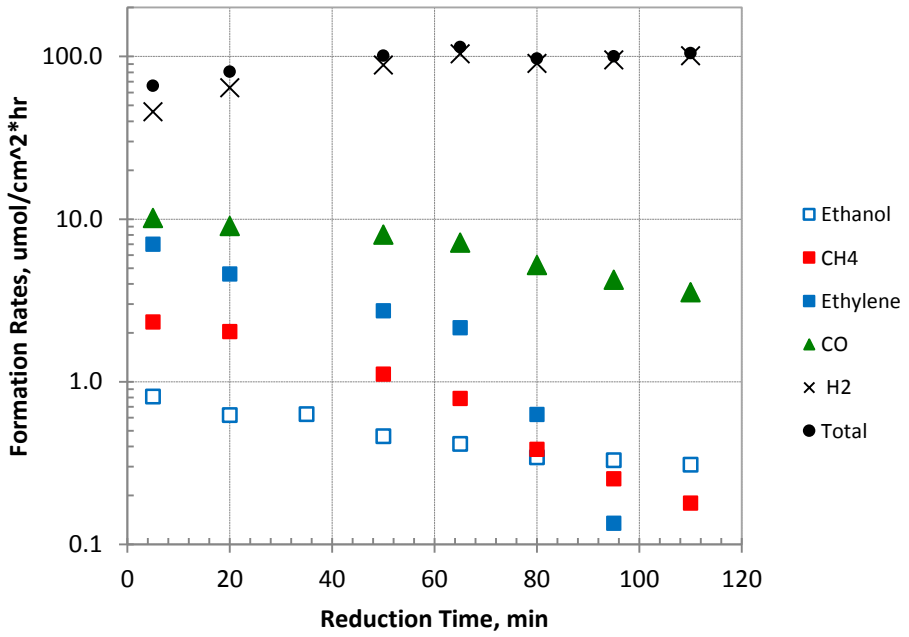


Figure 6.46. Product formation rates during $CO_2$ reduction on Toray/$Cu_2O$ (CV) at -1.5$V_{NHE}$.

In terms of faradaic efficiency (refer to Figure 6.47), the electrode showed higher selectivity towards ethylene versus CO due to difference in electron requirements between the two products. Ethylene was a major product only during the first half of the process. Ethylene showed an initial faradaic efficiency of 39% which decreased by 3 orders of magnitude to 0.7% for an average of 12%. CO was produce at intermediate faradaic efficiency with an initial and final selectivity of 8.6% and 3.2% respectively for an average of 5.6%.

The other $CO_2$ products were produced at intermediate efficiencies. Methane had an initial faradaic efficiency of 7.9% which decreased by two orders of magnitude to 0.7% for an average of 3.3%. Finally, ethanol had an initial faradaic efficiency of 4.2% which decreased to 1.6% for an average of 2.4%.

The decrease in $CO_2$ product efficiency occurred despite a relatively steady state current. The decline was offsetted by rising $H_2$ production. The decrease in ethylene faradaic efficiency was the most severe, followed by methane then ethanol. These results indicate that the cathodized $Cu_2O$ particles without a Nafion binder experienced surface deactivation likely from formation of carbon deposits which lowered the number of active sites that generate hydrocarbons. $H_2$ productivity increased from 46 to 101 μmol/cm$^2$*hr while it selectivity increased from 39% to 92%.

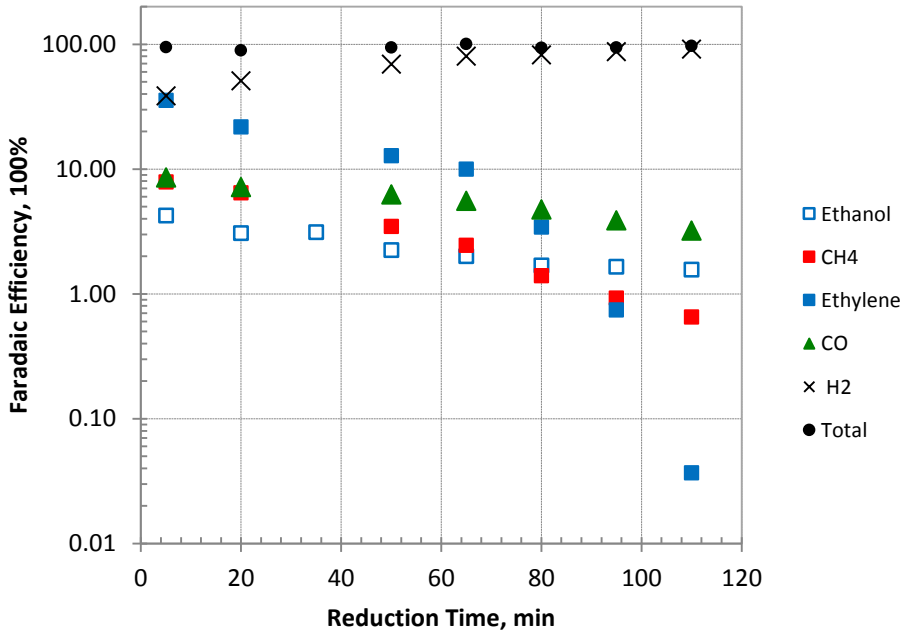


Figure 6.47. Faradaic efficiency of products during $CO_2$ reduction on Toray/$Cu_2O$ (CV) at -1.5$V_{NHE}$.

*Current Profile of the Second Reduction*. We also performed a second electrolysis on the characterized $Cu_2O$ sample and unintentionally generated a pulsating current flow (see Figure 6.48). The current which averaged at 26 mA fluctuated by approximately 17 mA. This was likely a result of a mechanically unstable connection on the electrode which subjected the particles to a very dynamic current at the interface to maintain a fix applied potential.

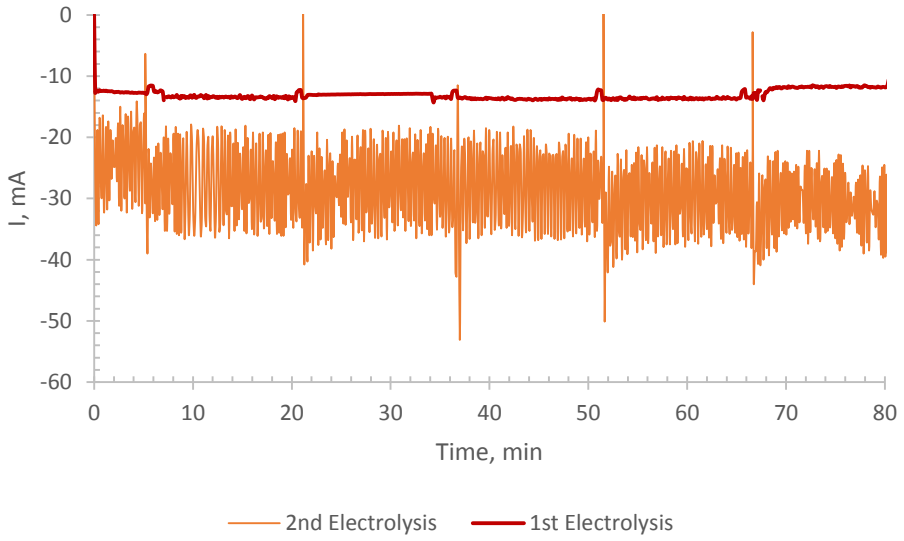


Figure 6.48. Current profile of the Toray/$Cu_2O$ (CV) electrode during the two $CO_2$ reductions at -1.5$V_{NHE}$.

*Product Distribution During the Second Reduction*. We then examined the $CO_2$ product distribution on the electrode after generating this type of behavior. The catalyst showed an over-all improvement in the product formation rates that were also kinetically more stable compared to the first $CO_2$ reduction (see Figure 6.49). For example, the average ethylene formation rate was 16 µmol/$cm^2$*hr, which was up from 2.5 µmol/$cm^2$*hr. The average CO formation rate was 13 µmol/$cm^2$*hr which was higher than 6.8 µmol/$cm^2$*hr. The average methane formation rate was 5.4 µmol/$cm^2$*hr which was better than 1.0

μmol/cm$^2$*hr. Finally, the average ethanol formation rate was 0.6 μmol/cm$^2$*hr but was only slightly higher than 0.5 μmol/cm$^2$*hr.

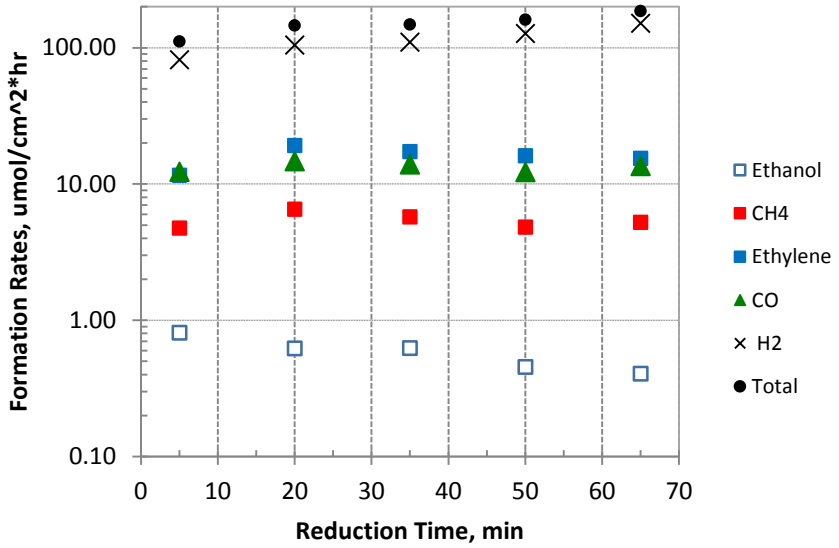


Figure 6.49. Product formation rates during the second $CO_2$ reduction on Toray/$Cu_2O$ (CV) electrode at -1.5$V_{NHE}$.

In terms of faradaic efficiency, the catalyst again showed an over-all improvement in the hydrocarbon faradaic efficiency and stability (see Figure 6.50).

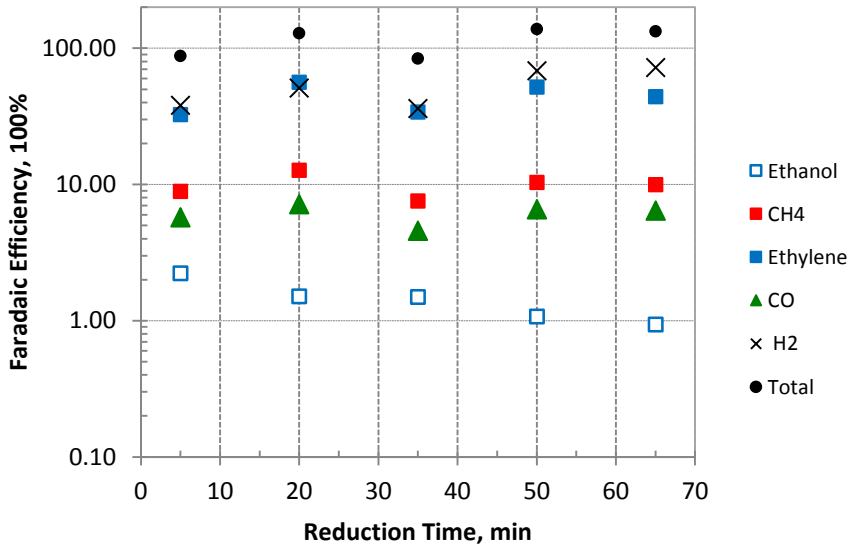


Figure 6.50. Faradaic efficiency of products during the second $CO_2$ reduction on Toray/$Cu_2O$ (CV) electrode at -1.5$V_{NHE}$.

The over-all $CO_2$ product faradaic efficiency increased from 23% to 61%. Individually, the average ethylene faradaic efficiency went up from 12% to 44%. The average CO faradaic efficiency was 6.1%, almost unchanged from 5.6%. The average methane faradaic efficiency was 9.9% versus 3.3%. This value represents the highest $CH_4$ efficiency obtained from our $Cu_2O$ samples. On the other hand, the average ethanol faradaic efficiency slightly decreased from 2.4% to 1.4%.

The constantly shifting current experienced by the catalyst enhanced and stabilized hydrocarbon selectivity and particularly promoted $CH_4$ formation. Modulated/pulsed potential experiment during $CO_2$ reduction was shown to improve the performance of $Cu_2O$ (Shiratsuchi et al. 1993, Nogami et al. 1994).

Toray/Nafion/$Cu_2O$ Electrode

*Cyclic Voltammogram*. The plot in Figure 6.51 showed that during the first

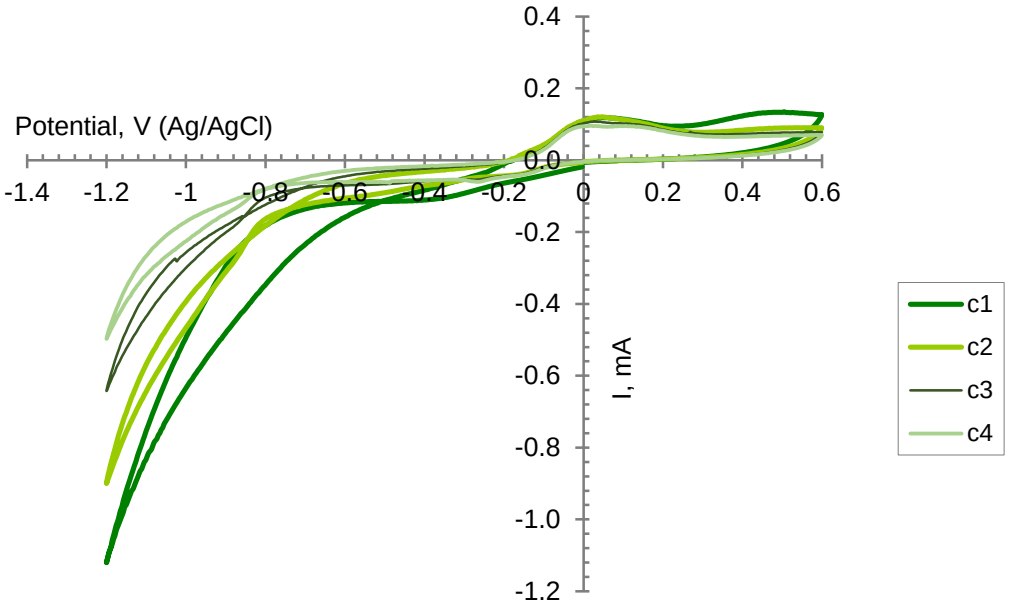


Figure 6.51. Cyclic voltammetry of Toray/Nafion/$Cu_2O$ (CV) electrode on $CO_2$ saturated 0.5M $KHCO_3$ solution at 50 mV/s.

cathodic sweep, a reduction peak was already observed which indicate a small number $Cu_2O$ particles were converted to Cu. During the first anodic sweep, higher current flowed than during the first cathodic sweep and produced an oxidation peak attributed to conversion of Cu to $Cu_2O$ and CuO. The succeeding sweeps continued to show peaks attributed to Cu redox reactions.

*Current Profile*. After conducting cyclic voltammetry, $CO_2$ electrochemical reduction was performed which generated current profile that is shown in Figure 6.52. The graph also includes data from the baseline Toray/Nafion/$Cu_2O$ electrode. We observed a more flat current at around 13 mA, which represent 45% less current than in the baseline Toray/Nafion/$Cu_2O$ sample.

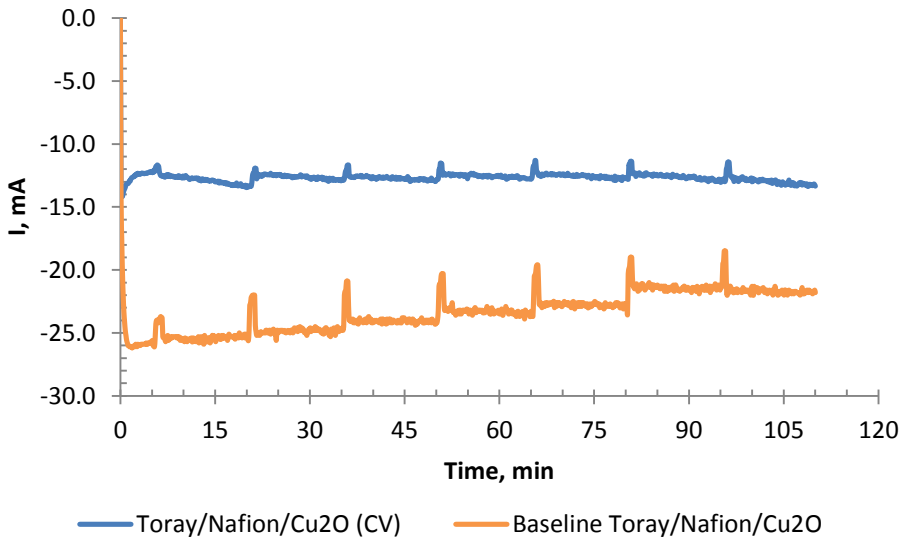


Figure 6.52. Current profile on Toray/Nafion/$Cu_2O$ (CV) generated during $CO_2$ reduction at -1.5$V_{NHE}$.

*Product Distribution*. We then obtained the product distribution of ethanol, methane, ethylene, CO and $H_2$. Figure 6.53 shows the product formation rates. The

electrode had the highest productivity towards CO, at an average of 28 µmol/cm$^2$*hr. This was followed by ethylene and ethanol at 2.6 and 1.4 µmol/cm$^2$*hr respectively. Methane was again the least produced product of $Cu_2O$ at 0.5 µmol/cm$^2$*hr. Meanwhile, the average $H_2$ formation rate was 86 µmol/cm$^2$*hr.

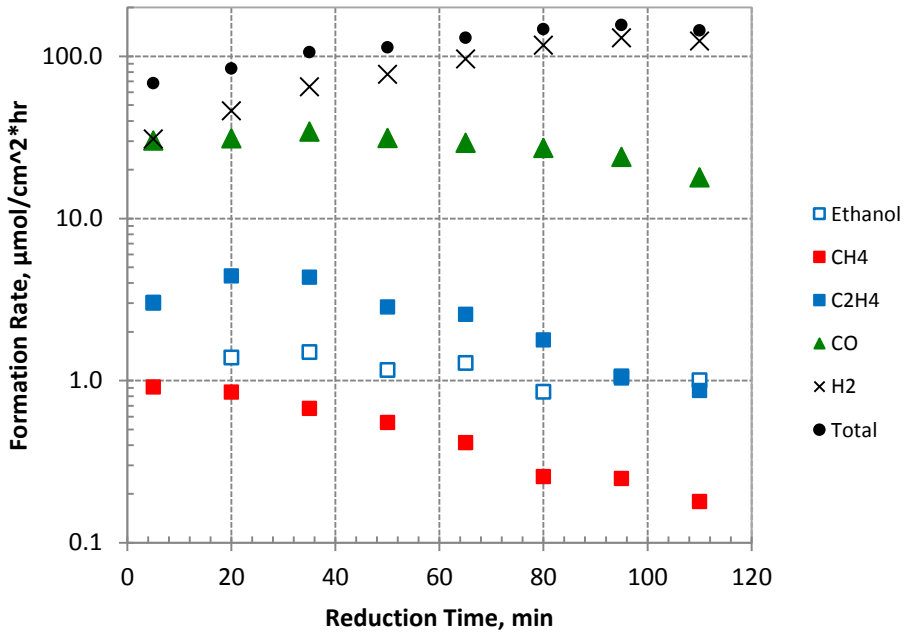


Figure 6.53. Product formation rates during $CO_2$ reduction on Toray/Nafion/$Cu_2O$ (CV) electrode at -1.5$V_{NHE}$.

Compared to our baseline Toray/Nafion/$Cu_2O$ electrode, the pre-anodized Toray/Nafion/$Cu_2O$ (CV) electrode showed lower $H_2$, CO and hydrocarbon formation. The order of productivity was CO > ethylene > ethanol > methane which was the same with the baseline electrode. The over-all lower formation rates were likely due to lower $Cu_2O$ loading of 1.1 mg compared to 26.5 mg.

Meanwhile, Figure 6.54 shows the product distribution in terms of faradaic efficiency. We observed an over-all decrease in the faradaic efficiency of $CO_2$ products

similar to the pre-anodized Toray/$Cu_2O$ (CV) electrode. CO was a major product at 20% average faradaic efficiency. This was followed by ethylene and ethanol at 11% and 6.2% average faradaic efficiencies, respectively. This electrode showed the highest initial ethanol faradaic efficiency of 16%. $CH_4$ was an intermediate product at 1.5% average faradaic efficiency. Meanwhile, the average $H_2$ faradaic efficiency was 56%.

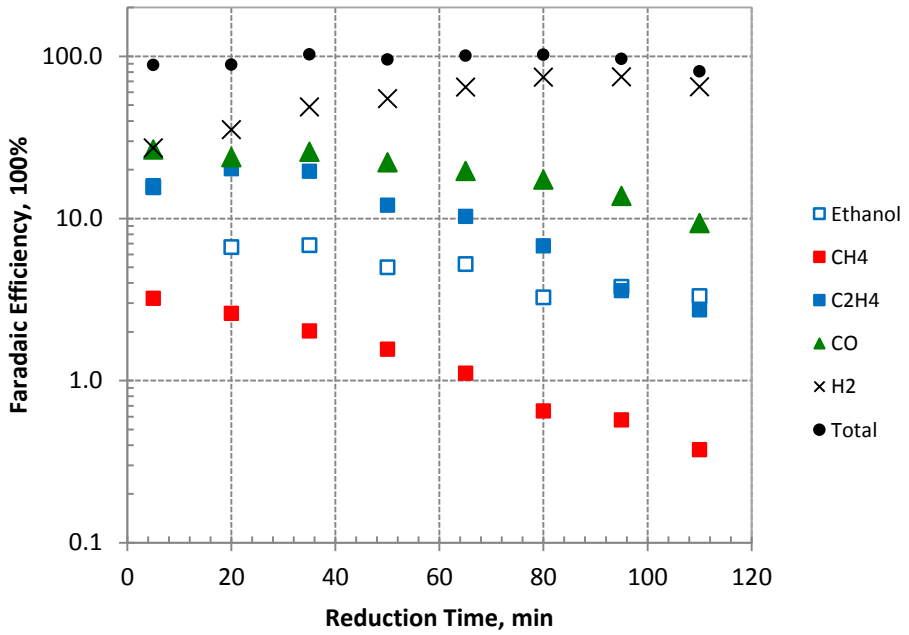


Figure 6.54. Faradaic efficiency of products during the $CO_2$ reduction on Toray/Nafion/$Cu_2O$ (CV) at -1.5$V_{NHE}$.

Compared to our baseline Toray/Nafion/$Cu_2O$ electrode, the pre-anodized Toray/Nafion/$Cu_2O$ (CV) electrode showed higher $H_2$, CO, methane and ethanol selectivity but lower ethylene selectivity. As such, there was a minor change in the order of selectivity, particularly on CO and ethylene, as follows, CO > ethylene > ethanol > methane. The pre-anodization step did not significantly alter the productivity and selectivity of the electrode.

For this electrode, the Nafion/$Cu_2O$ ratio was 0.8. With our study on the effect of Nafion, we have shown that the electrode with the Nafion/$Cu_2O$ ratio of 1.2 showed the best productivity and selectivity to ethylene. Meanwhile, the electrode with the Nafion/$Cu_2O$ ratio of 0.0 showed the best productivity and selectivity to CO.

6.3.2.6. Effect of Particle Size on Product Distribution

In this section, we compared the electrocatalytic activity of two sets of $Cu_2O$ catalyst having distinct particle size. The first one was synthesized based on a wet chemical reduction method described by Chang et al. (2009). These $Cu_2O$ particles ($Cu_2O$ MP) typically have an average size of 200-400 nm. The second one was synthesized based on the wet chemical reduction method described by Li et al. (2013). These $Cu_2O$ particles ($Cu_2O$ NP) typically have an average size of 40-50 nm. The difference in particle size was derived from the difference in the relative concentration of reagents added to make these particles. Table 6.3 summarizes their compositions.

Table 6.3. Composition of reagents used for the two $Cu_2O$ synthesis methods.

| Reagent, in M | Chang et al. (2009) | Li et al. (2013) |
|---|---|---|
| $Cu^{2+}$ | 0.005 *(in acetate)* | 0.001 (*in chloride)* |
| PEG | 0.002 *(in PEG 200)* | 0.05 (*in PEG 10,000)* |
| NaOH | 0.2 | 0.3 |
| Ascorbate | 0.05 | 0.2 |

The first reason for the difference in particle size was the use of different amount of $Cu^{2+}$ in the starting mixture. The Li method used 5x less amount of $Cu^{2+}$ than the Chang method. The second reason was the difference in the amount of capping agent added to the mixture. With Chang's method, we used 1.3 g PEG / g $Cu^{2+}$, whereas with the Li method, we used 606.8 g PEG / g $Cu^{2+}$. The combination of lower amount of $Cu^{2+}$ and higher amount of ion dispersing agent (PEG) led to an over-all decrease in the $Cu_2O$ particle size.

The $Cu_2O$ loading on both samples were 1.2 mg. Nafion was added to both set of $Cu_2O$ particles at the same proportion of 1.1 mg Nafion / mg $Cu_2O$ before they were brush-coated to the support electrode assembly.

These two $Cu_2O$ particles were then compared by examining their morphologies and their electrocatalytic activity towards conversion of $CO_2$ to hydrocarbons and oxygenates at different potentials between $-1.0V_{NHE}$ and $-1.7V_{NHE}$. Selectivity was compared among these electrodes and against polycrystalline Cu.

SEM Analysis. First we checked on the structure of both sets of $Cu_2O$ particles on the SEM before and after $CO_2$ reduction (refer to Figures 6.55 and 6.56). The $Cu_2O$ MP catalyst was made up mainly of cubes with a small number of dual cubes and other irregularly-shaped structures. The average particle size of these $Cu_2O$ MP particles was 200 nm. On the other hand, the $Cu_2O$ NP particles were also cubes but the average particle size was 50 nm. The $Cu_2O$ NP particles were only 4x smaller than the $Cu_2O$ MP particles despite using 50x more capping agent per $Cu^{2+}$ ion with the Li method.

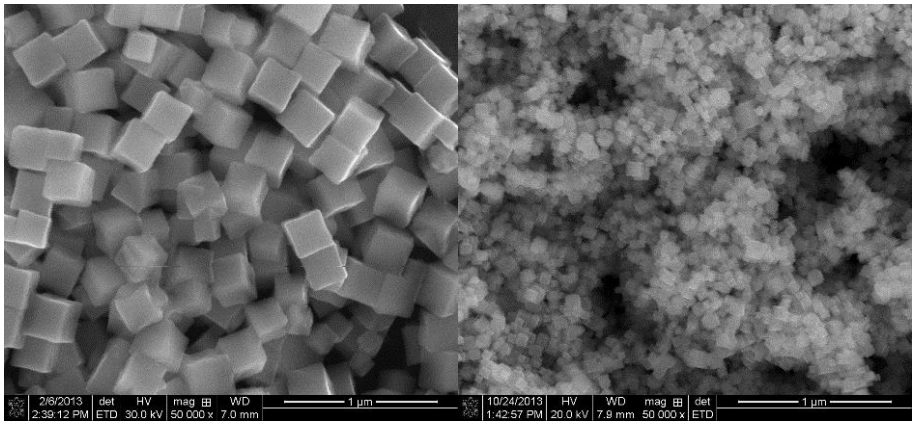


Figure 6.55. SEM of $Cu_2O$ MP (left) $Cu_2O$ NP (right) before $CO_2$ reduction.

After nearly 4 hours of $CO_2$ electrolysis, the SEM indicated that both set of particles evolved to about the same size and feature. The $Cu_2O$ MP disintegrated into smaller multi-faceted nanoparticles while the $Cu_2O$ NP particles agglomerated into multi-faceted nanoparticles. This results suggest that with sufficient electrolytic time, particles having initially different particle size will evolve into identical structure and size. Both set of $Cu_2O$ particles lost their original cubic architecture.

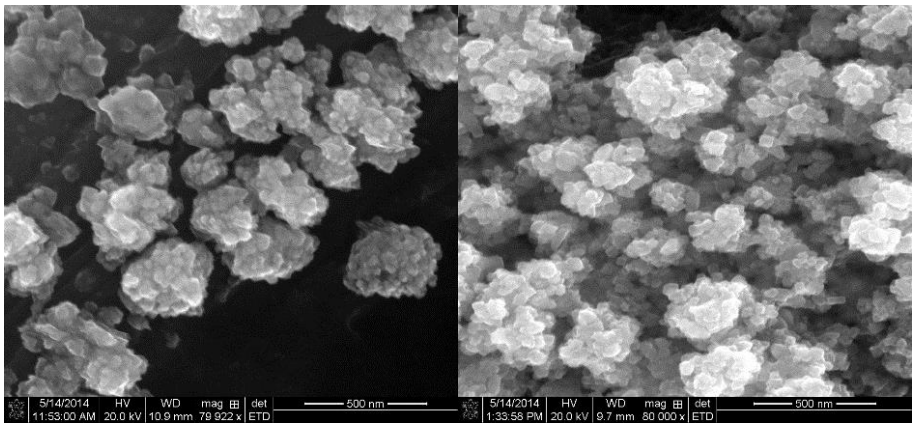


Figure 6.56. SEM of $Cu_2O$ MP (left) and $Cu_2O$ NP (right) after 4 hours of potential step $CO_2$ reduction.

Current Profile. We monitored the current flow on both samples during the 4 hour electrolysis. As seen in the Figure 6.57, both electrodes showed comparable amount of current between -1.0$V_{NHE}$ and -1.5$V_{NHE}$. We would expect to obtain similar total formation rates from the two sample at this range. Meanwhile at -1.6$V_{NHE}$ onwards, the current flow on the $Cu_2O$ MP increased with potential more strongly than on the $Cu_2O$ NP and also increased with time. This unsteady rise in current was likely due to expanding $H_2$ evolution on the electrode surface which we have also observed previously with fixed potential experiment.

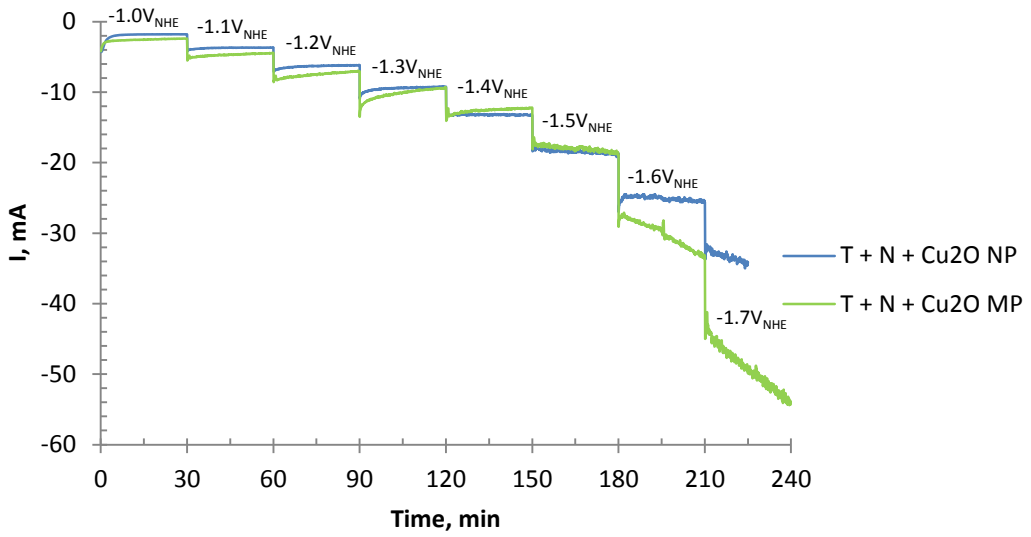


Figure 6.57. Current profile of $Cu_2O$ MP and $Cu_2O$ NP during 4 hours of potential step $CO_2$ electrolysis.

We also plotted the IR-corrected potential versus average current on both samples in Figure 6.58 and showed that the electrolysis was operating in a kinetically limited potential region characterized by high $H_2$ activity.

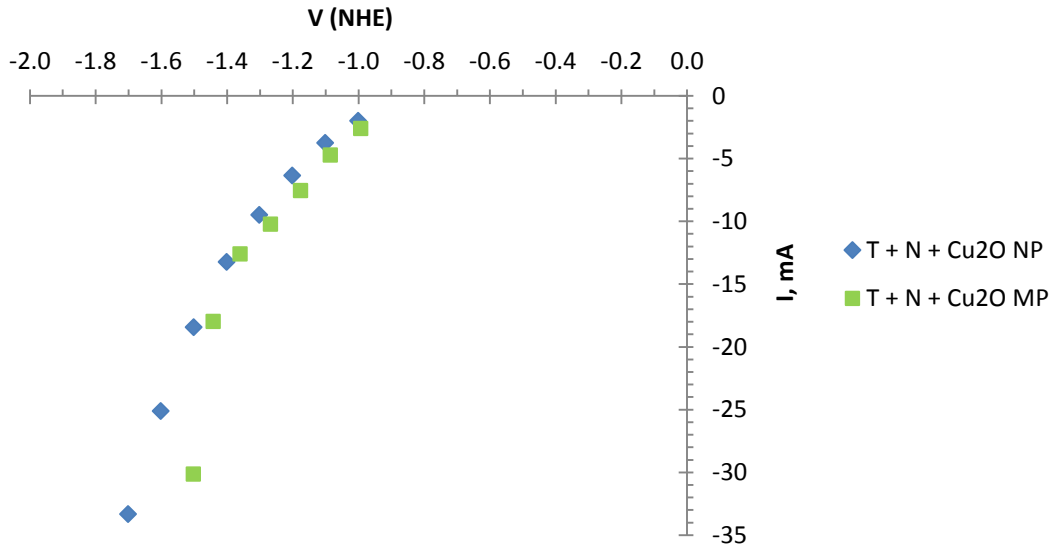


Figure 6.58. Equivalent voltammogram of the potential step electrolysis of $CO_2$ on $Cu_2O$ MP and $Cu_2O$ NP electrodes.

Product Distribution on $Cu_2O$ MP Electrode. We then analyzed the $CO_2$ product distribution on $Cu_2O$ MP and $Cu_2O$ NP particles. First we looked at composite formation rate on the $Cu_2O$ MP electrode (refer to Figure 6.59). We observed an increase in $H_2$ formation rate from 55 µmol/cm$^2$*hr at -0.99$V_{NHE}$ to 1,066 µmol/cm$^2$*hr at -1.54$V_{NHE}$. Meanwhile, the total CO + hydrocarbon formation rate increased from 1.6 µmol/cm$^2$*hr at -1.09$V_{NHE}$ to 25 µmol/cm$^2$*hr at -1.44$V_{NHE}$ then decreased to 21 µmol/cm$^2$*hr at -1.54$V_{NHE}$. CO and ethylene productivity peaked at -1.44$V_{NHE}$ to 8.2 and 13 µmol/cm$^2$*hr respectively. Methane productivity peaked at -1.50$V_{NHE}$ to 1.7 µmol/cm$^2$*hr.

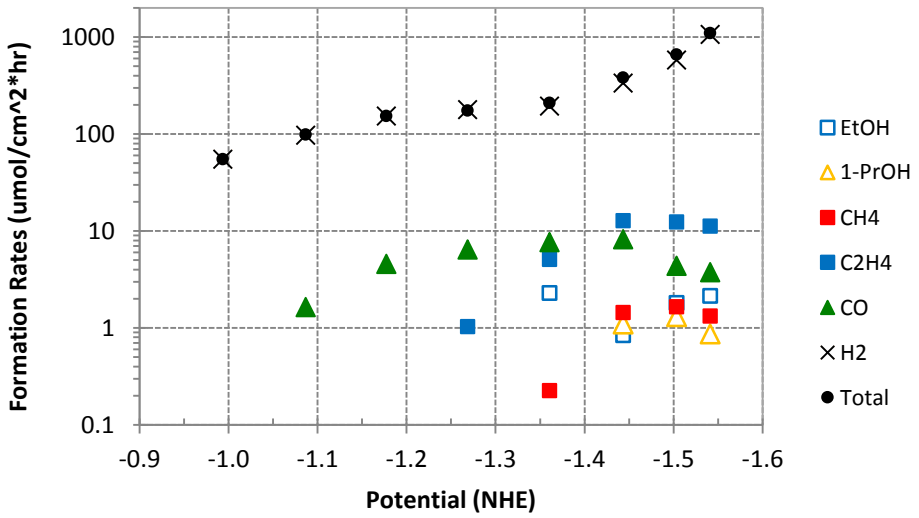


Figure 6.59. Product formation rates during $CO_2$ reduction on $Cu_2O$ MP electrode at different potentials.

Now we looked at faradaic efficiency data in Figure 6.60. At potentials less negative than -1.27$V_{NHE}$, we only detected CO and $H_2$. The CO selectivity increased incrementally before reaching a maximum of 3.6% at -1.27$V_{NHE}$. From its peaks value, the selectivity declined to a low of 0.4% at -1.54$V_{NHE}$. $H_2$ selectivity decreased between

-0.99$V_{NHE}$ and -1.36$V_{NHE}$, which coincided with an increase in CO selectivity. $H_2$ selectivity then increased from -1.36$V_{NHE}$ to -1.54$V_{NHE}$.

At -1.27$V_{NHE}$, we started to detect hydrocarbons and oxygenates with ethylene as the first product observed with a selectivity of 3.4%. Its selectivity peaked to 22% at -1.44$V_{NHE}$ then decreased to 6.9% at -1.54$V_{NHE}$. Ethanol was first observed at more negative potential of -1.36$V_{NHE}$ where it achieved its highest peak of 5.9% efficiency before decreasing to 0.9% at -1.54$V_{NHE}$. Methane first formed at the same potential as ethanol with a selectivity of 0.4%. Its selectivity climbed slightly to 1.7% at -1.44$V_{NHE}$ before decreasing to 0.6% at -1.54$V_{NHE}$.

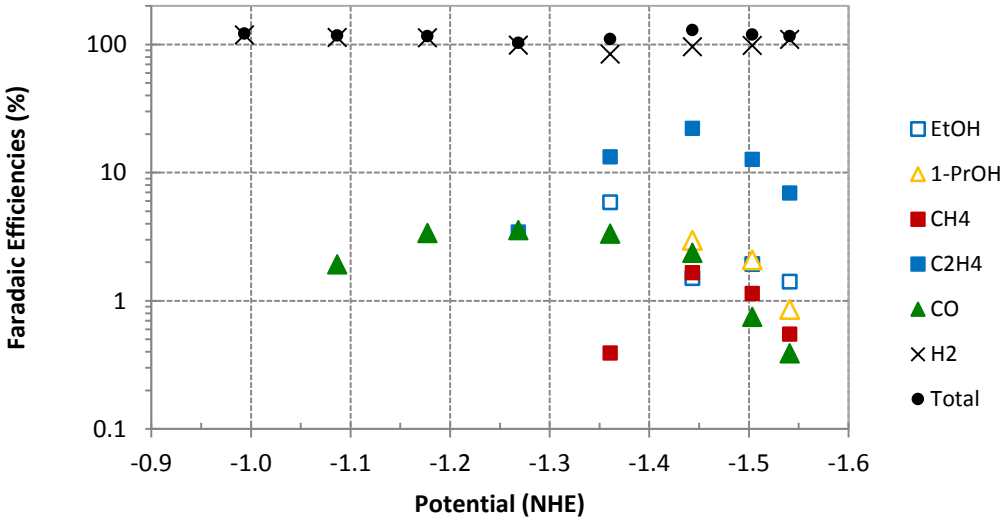


Figure 6.60. Faradaic efficiency of products during $CO_2$ reduction on $Cu_2O$ MP electrode at different potentials.

At the potential window where CO selectivity decreased (between -1.27$V_{NHE}$ and -1.54$V_{NHE}$), hydrocarbon products were formed and their selectivities peaked at -1.44$V_{NHE}$. Between -1.44$V_{NHE}$ and -1.54$V_{NHE}$, the selectivity of CO and hydrocarbons decreased while that of $H_2$ increased. These shifts in product selectivity of the $Cu_2O$ MP electrode demonstrate the different reaction intermediates that prevail during the potential steps. At

low negative potential, only $H_{ads}$ were reduced to $H_2$. At more negative potential, $CO_{ads}$ were also formed then desorbed to CO. Then at sufficiently more negative potential, some of the $CO_{ads}$ intermediates were also reduced further into $CHO_{ads}$ and $COH_{ads}$ intermediates either as monomer or dimer.

We also looked at comparing the selectivity ratio $C_2H_4/CH_4$ and $(C_2H_4 + CH_4)/CO$ with our reduced $Cu_2O$ electrode and those from Hori's results. The $C_2H_4/CH_4$ selectivity ratio of this oxide derived Cu at $-1.5V_{NHE}$ was 11.1 which is significantly higher than 0.9 on Hori's polycrystalline Cu at the same applied potential but lower than 14 on Hori's single crystal high index Cu (711) electrode. Meanwhile, the average $(C_2H_4 + CH_4)/CO$ selectivity ratio was 18.4 compared to 32 (upper limit range of 9-32) on Hori's polycrystalline Cu sample at the same applied potential.

Product Distribution on $Cu_2O$ NP Electrode. Next we looked at the potential dependent product distribution on $Cu_2O$ NP electrode. First we examined the formation rates shown in Figure 6.61.

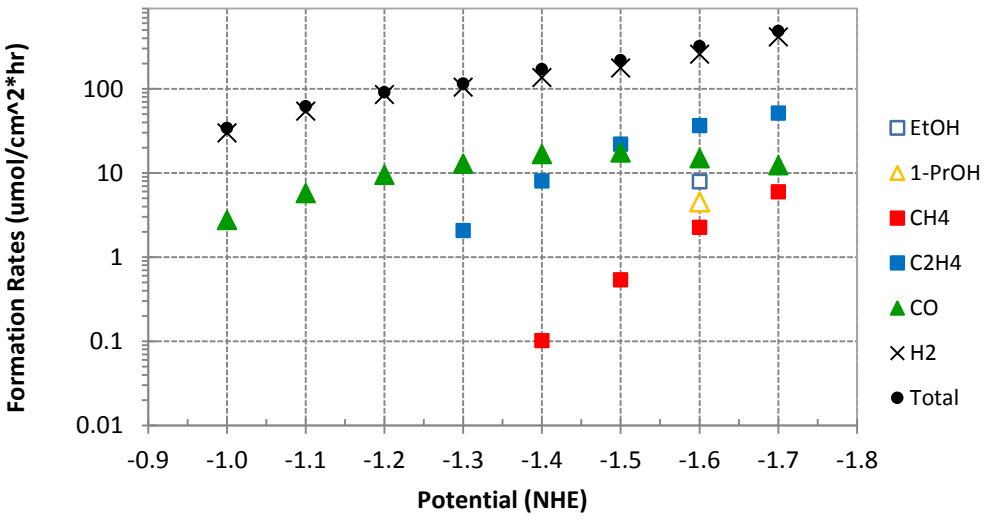


Figure 6.61. Product formation rates during $CO_2$ reduction on $Cu_2O$ NP electrode at different potentials.

We again observed an increase in $H_2$ formation rate from 30 µmol/cm$^2$*hr at -1.0$V_{NHE}$ to 413 µmol/cm$^2$*hr at -1.7$V_{NHE}$. Meanwhile, the total CO + hydrocarbon formation rate increased from 2.8 µmol/cm$^2$*hr at -1.0$V_{NHE}$ to 71 µmol/cm$^2$*hr at -1.6$V_{NHE}$.

CO productivity peaked at -1.5$V_{NHE}$ to 18 µmol/cm$^2$*hr. Ethylene productivity increased from 2.1 µmol/cm$^2$*hr at -1.3$V_{NHE}$ to 51 µmol/cm$^2$*hr at -1.7$V_{NHE}$. Methane productivity increased from 2.1 µmol/cm$^2$*hr at -1.4$V_{NHE}$ to 6.0 µmol/cm$^2$*hr at -1.7$V_{NHE}$.

Then we looked at the faradaic efficiency data in Figure 6.62. At potentials less negative than -1.3$V_{NHE}$, we only detected CO and $H_2$. $H_2$ selectivity decreased between -1.0$V_{NHE}$ and -1.5$V_{NHE}$ and then increased from -1.5$V_{NHE}$ and -1.7$V_{NHE}$. The CO selectivity was steady at 8% between -1.0$V_{NHE}$ and -1.2$V_{NHE}$ before it started to decrease at -1.3$V_{NHE}$ falling to 1.9% at -1.7$V_{NHE}$. At that point (-1.3$V_{NHE}$), hydrocarbons were observed.

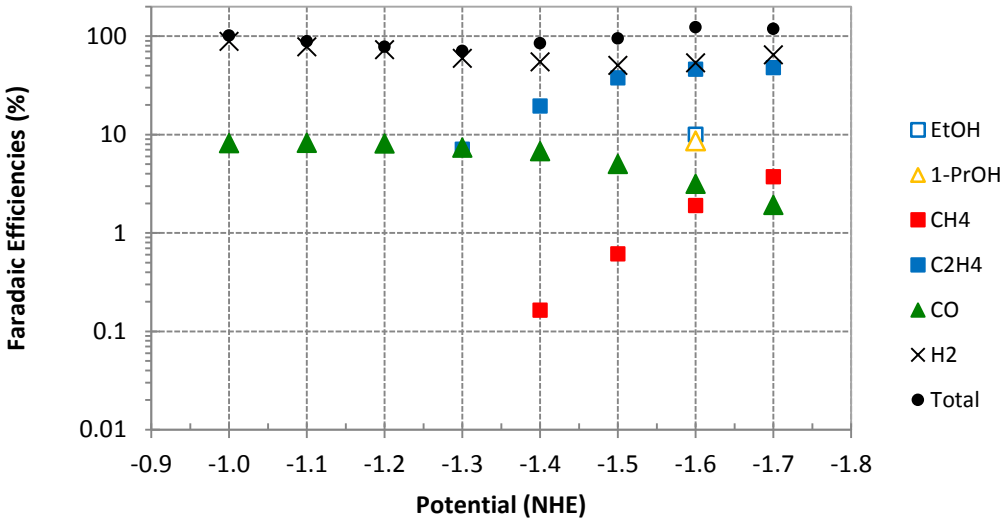


Figure 6.62. Faradaic efficiency of products during $CO_2$ reduction on $Cu_2O$ NP electrode at different potentials.

The first hydrocarbon detected was ethylene at -1.3$V_{NHE}$ with a 7.1% faradaic efficiency. Its selectivity increased to 48% at -1.7$V_{NHE}$ without a maxima. The second hydrocarbon detected was methane at -1.4$V_{NHE}$ with a 0.2% faradaic efficiency. Its selectivity increased to 3.8% faradaic efficiency and also without a maxima. Ethanol and n-propanol products were only observed at -1.6$V_{NHE}$ with faradaic efficiencies of 10.1% and 8.7% respectively.

We also looked at comparing the selectivity ratio $C_2H_4/CH_4$ and $(C_2H_4 + CH_4)/CO$ with our reduced $Cu_2O$ electrode and those from Hori's results. The $C_2H_4/CH_4$ selectivity ratio of this oxide derived Cu at -1.5$V_{NHE}$ was 61.3 which is significantly higher than 0.9 on Hori's polycrystalline Cu sample at the same applied potential and higher than 14 on Hori's single crystal high index Cu (711) electrode. Meanwhile, the average $(C_2H_4 + CH_4)/CO$ selectivity ratio was 7.7 compared to 32 (upper limit range of 9-32) on Hori's polycrystalline Cu sample at the same applied potential.

At the potential range where $H_2$ selectivity decreased (between -1.0$V_{NHE}$ and -1.2$V_{NHE}$), the CO selectivity was constant. This suggests an increasing $CO_{ads}$ coverage on the surface of the electrode. At the potential window where CO selectivity decreased (between -1.2$V_{NHE}$ and -1.7$V_{NHE}$), hydrocarbon products were formed and their total faradaic efficiencies increased to their peak values at -1.6$V_{NHE}$. As explained earlier, these changes in product selectivity on the $Cu_2O$ NP electrode again demonstrate the different reaction intermediates that prevail at different potentials.

Our $CO_2$ product distribution at different potentials supports the mechanisms that have been established on the reaction pathways of $CO_2$ on copper. For example, our results support Hori's theory that $H_{ads}$ and $CO_{ads}$ compete for coverage on the active sites on Cu.

At low and high potentials, $H_2O$ molecules are more favorably adsorbed. At intermediate potentials, $CO_2$ molecules also become favorably adsorbed. Depending on the relative barrier between the kinetics of CO desorption and CO hydrogenation, either CO or hydrocarbons will be produced. We have shown that CO are kinetically favored at low to intermediate potential while hydrocarbons are kinetically favored at higher potential.

Comparison of Individual Products on $Cu_2O$ MP, $Cu_2O$ NP and Cu Electrodes

*$H_2$ Formation*. We then compared the $Cu_2O$ MP, $Cu_2O$ NP and Cu electrodes by the individual $CO_2$ (and $H_2O$) products. First, we looked at data on $H_2$ formation shown in Figure 6.63. We observed an increase in $H_2$ formation rates on all three electrodes. The $Cu_2O$ MP electrode showed higher $H_2$ rates than $Cu_2O$ NP and Cu electrodes. The $Cu_2O$ NP electrode showed lower $H_2$ rates than Cu between -1.5$V_{NHE}$ and -1.7$V_{NHE}$.

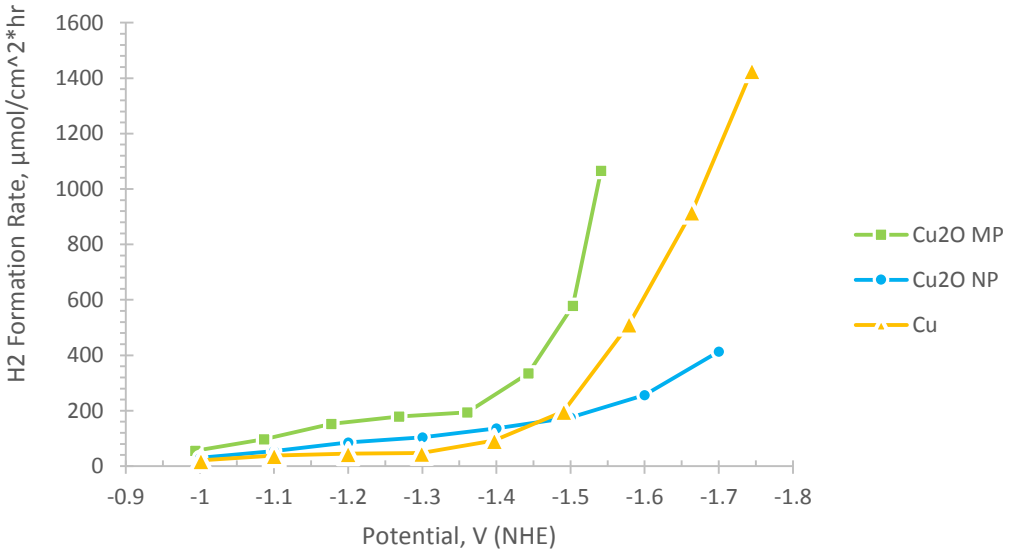


Figure 6.63. Formation rate of $H_2$ on $Cu_2O$ MP, $Cu_2O$ NP and Cu at different potentials.

Next we looked at $H_2$ faradaic efficiency of the three electrodes (see Figure 6.64). The $Cu_2O$ NP electrode showed over-all lowest $H_2$ selectivity in which its faradaic efficiency decreased to 51% at -1.5$V_{NHE}$ from its initial faradaic efficiency of 89% at -1.0$v_{NHE}$. This was followed by Cu electrode whose $H_2$ faradaic efficiency showed two minima, the first one was at -1.3$V_{NHE}$ with 83% faradaic efficiency and the second one was at -1.5$V_{NHE}$ with 82% faradaic efficiency. The $Cu_2O$ MP electrode showed over-all highest $H_2$ selectivity in which its faradaic efficiency reached its lowest value of 84% at -1.36$V_{NHE}$.

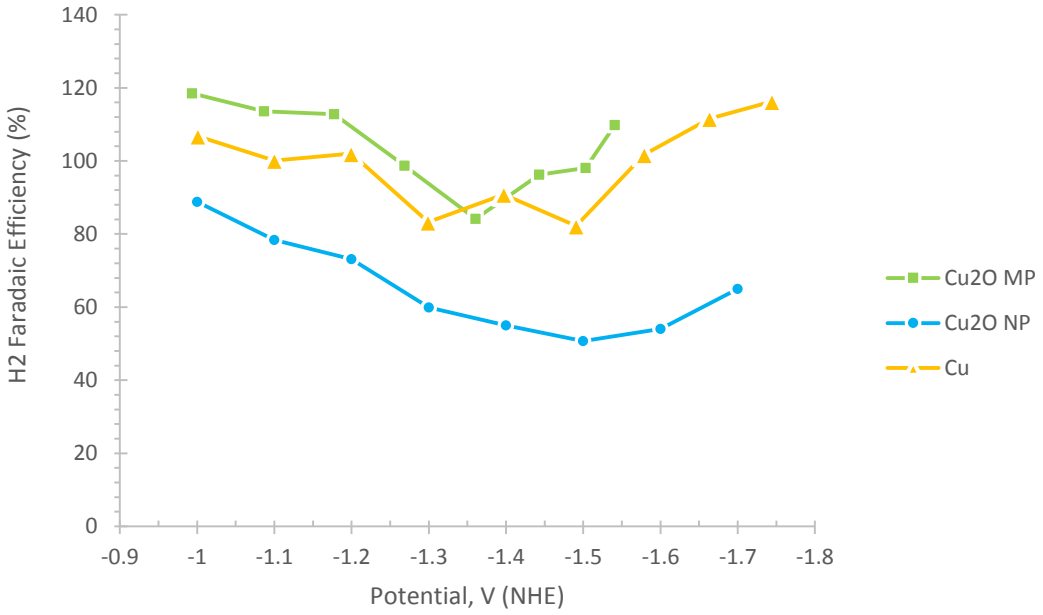


Figure 6.64. Faradaic efficiency of $H_2$ on $Cu_2O$ MP, $Cu_2O$ NP and Cu at different potentials.

*CO Formation*. We then compared CO formation on these electrocatalysts. First, we looked at formation rates shown in Figure 6.65. The $Cu_2O$ NP electrode showed the highest over-all CO formation rate, followed by the $Cu_2O$ MP electrode and the Cu electrode.

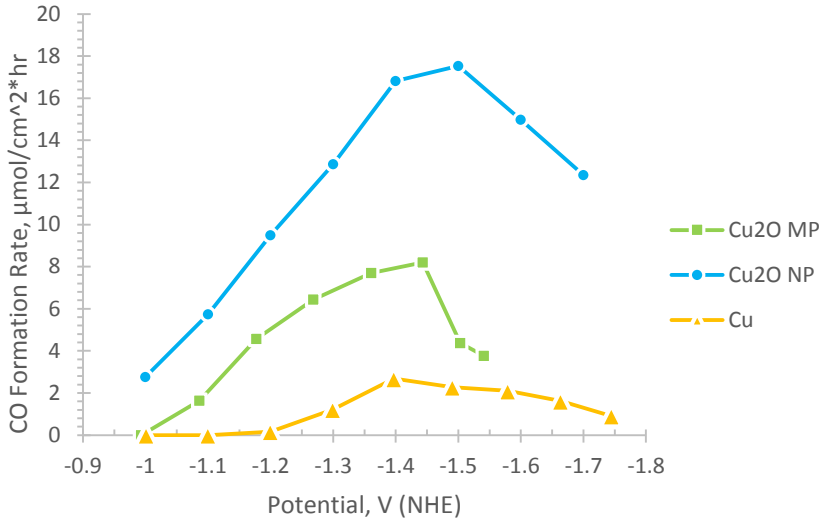


Figure 6.65. Formation rate of CO on $Cu_2O$ MP, $Cu_2O$ NP and Cu at different potentials.

In terms of faradaic efficiencies (see Figure 6.66), the $Cu_2O$ NP electrode again showed the highest over-all CO faradaic efficiency and at lower potential. Meanwhile, the Cu electrode showed the lowest over-all CO faradaic efficiency although it showed identical CO selectivity between -1.40$V_{NHE}$ and -1.54$V_{NHE}$ with that of the $Cu_2O$ MP electrode.

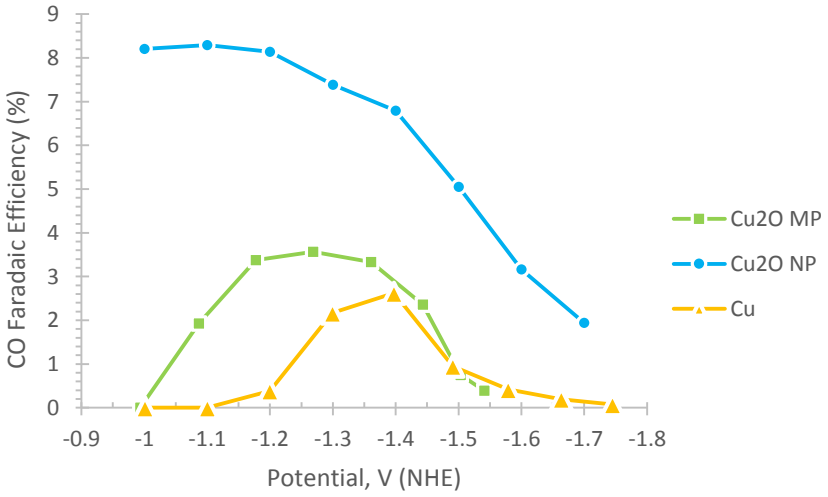


Figure 6.66. Faradaic efficiency of CO on $Cu_2O$ MP, $Cu_2O$ NP and Cu at different potentials.

The CO selectivity on both the Cu and $Cu_2O$ MP electrodes was essentially zero at -1.0$V_{NHE}$ while the $Cu_2O$ NP electrode still showed 8.2% faradaic efficiency. In comparison, Li's thermally oxidized $Cu_2O$ achieved 30% faradaic efficiency at -1.0$V_{NHE}$. These results suggest that Cu clusters derived from wet reduction and thermal oxidation are still different from each other.

*Methane Formation*. Next, we looked at methane formation. First, we compared their formation rates which are shown in Figure 6.67. The Cu electrode showed over-all highest methane productivity than the $Cu_2O$ MP and NP electrodes. However, at more negative potentials (> 1.7$V_{NHE}$), we observed that the methane production began to exceed that of the Cu electrode.

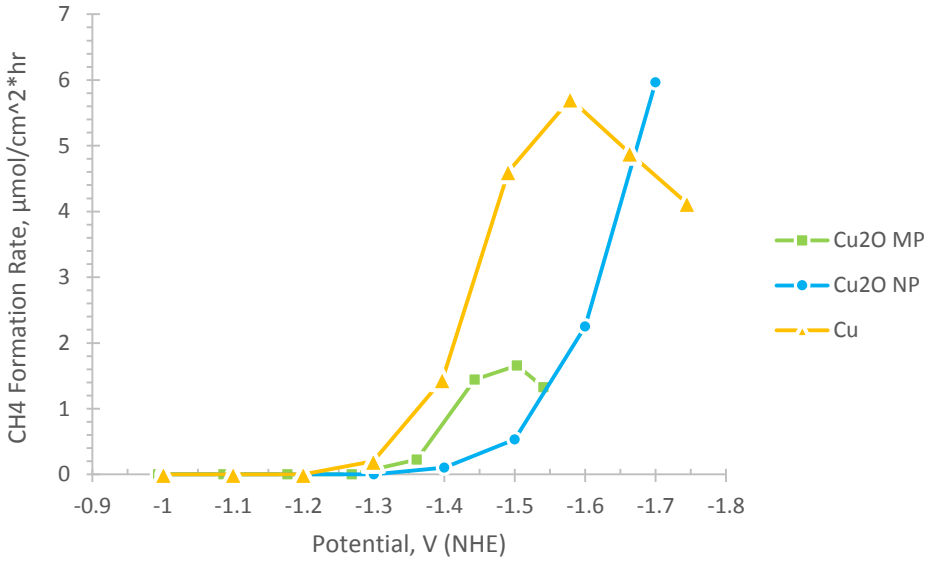


Figure 6.67. Formation rate of methane on $Cu_2O$ MP, $Cu_2O$ NP and Cu at different potentials.

We then compared their selectivity to methane (see Figure 6.68). Again, the Cu electrode showed the highest over-all methane faradaic efficiency at lower potential

relative to the other two electrodes. However at around -1.65$V_{NHE}$, we again observed that the methane selectivity of the $Cu_2O$ NP electrode began to exceed that of the Cu electrode.

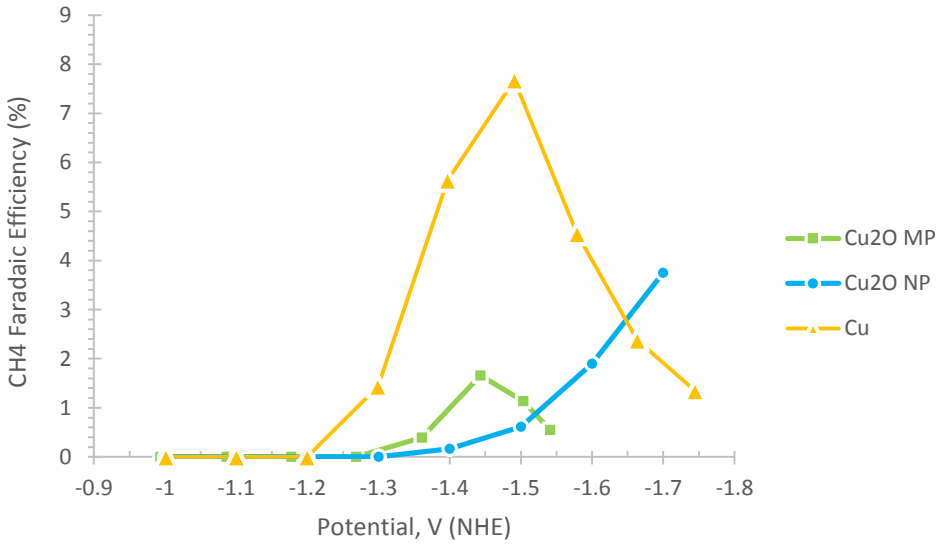


Figure 6.68. Faradaic efficiency of methane on $Cu_2O$ MP, $Cu_2O$ NP and Cu at different potentials.

We note that Li's group did not detect any methane with their oxide derived Cu particles. Instead they observed ethane ($C_2H_6$). This indicate that our oxide derived Cu particles still have Cu-like features that were completely absent from thermally oxidized Cu particles.

Both Hori and Schouten have suggested that methane forms on Cu(111) surfaces. However, we did not detect comparable amounts of $CH_4$ in our sample. Likely these Cu(111) oriented particles were in close proximity to Cu(200) oriented particles.

*Ethylene Formation*. Finally, we compared the three electrodes based on ethylene formation. Again, we looked at their formation rates (refer to Figure 6.69). Both the $Cu_2O$ NP and $Cu_2O$ MP electrodes showed identical ethylene formation rates up to -1.5$V_{NHE}$.

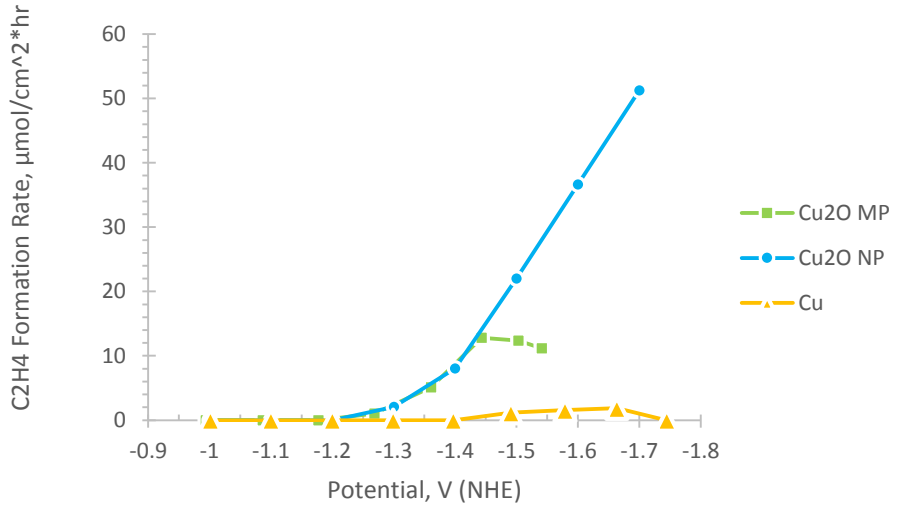


Figure 6.69. Formation rate of ethylene on $Cu_2O$ MP, $Cu_2O$ NP and Cu at different potentials.

Then the ethylene productivity continued to increase on the $Cu_2O$ NP electrode beyond $-1.5V_{NHE}$ while that of the $Cu_2O$ MP electrode declined. Meanwhile, the Cu electrode showed little ethylene productivity.

We then compared their faradaic efficiencies (see Figure 6.70). Both the $Cu_2O$ NP and $Cu_2O$ MP electrodes again showed identical ethylene selectivity up to $-1.5V_{NHE}$. Then the ethylene productivity continued to improve on the $Cu_2O$ NP electrode beyond $-1.5V_{NHE}$ while that of the $Cu_2O$ MP electrode declined. Meanwhile, the Cu electrode showed little ethylene selectivity.

In the previous sections, we have consistently observed higher ethylene and higher ethylene to methane ratio from $Cu_2O$ particles at $-1.5V_{NHE}$. We extended our study to examine ethylene selectivity at other potentials. Our results showed that ethylene selectivity differ between $Cu_2O$ MP and $Cu_2O$ NP at potentials more negative than

-1.45$V_{NHE}$. While the ethylene selectivity on $Cu_2O$ MP fell after -1.45$V_{NHE}$, that of $Cu_2O$ NP continued to increase reaching 48% faradaic efficiency at -1.7$V_{NHE}$, which is the highest ethylene selectivity measured on $Cu_2O$ particles under stable current electrolysis.

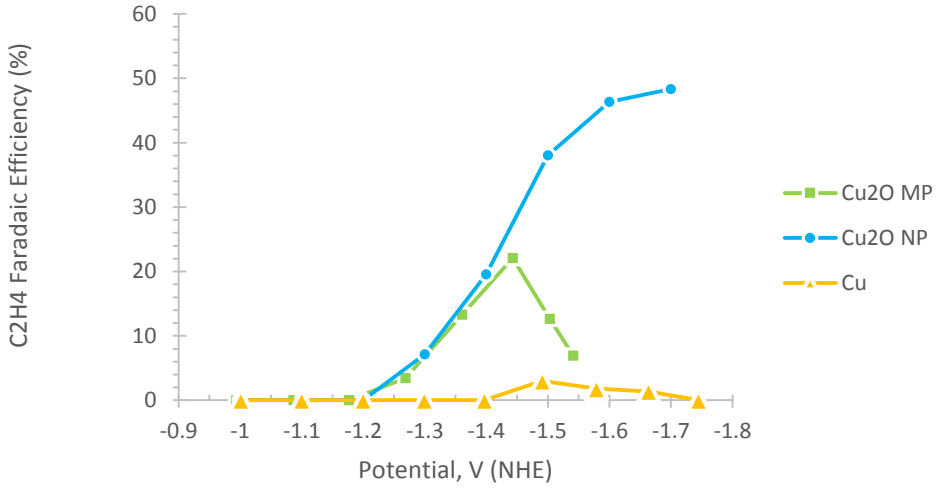


Figure 6.70. Faradaic efficiency of ethylene on $Cu_2O$ MP, $Cu_2O$ NP and Cu at different potentials.

Hori and Schouten have suggested that ethylene preferably forms on Cu(100) and on steps in Cu(111). The XRD scan of our $Cu_2O$ particles showed that the orientation of oxide derived Cu particles were mainly Cu(111), followed by Cu(200) then Cu(222). Although there were no Cu(100) surfaces in our sample, Cu(200) is the same as Cu(100). The reduced $Cu_2O$ particles likely generated a lot of Cu(200) steps on Cu(111) and Cu(222) planes at the surface.

Metallic Cu surfaces generated ethylene efficiency of 22% at -1.3$V_{NHE}$ (Hori et al. 1989). Though $Cu_2O$ surfaces showed very high ethylene selectivity (>22%), they were obtained at more negative potential (greater than -1.4$V_{NHE}$) compared to Cu. However, we

obtained higher ethylene efficiency of 16% at -1.4$V_{NHE}$ compared to just 4% from thermally oxidized Cu sample. This indicate that the resulting surface of our oxide-derived Cu particles have more preference to ethylene than CO.

### *6.3.3. $CO_2$ Reduction on Glassy Carbon Supported $Cu_2O$ Particles*[4]

In this section, we used GL as support substrate to the $Cu_2O$ particles in order to minimize mass transfer effects associated with using porous materials. Glassy carbon is a suitable support material because it is rigid and has low electrical resistance (van der Linden and Dieker 1980). It is also stable under high potential electrolysis. Nevertheless, it is an electrochemically active surface towards $H_2O$ reduction.

$Cu_2O$ samples were prepared by colloidal synthesis, mixed with Nafion, then brush coated to the glassy carbon plate. Due to the mirror like surface of GL, we increased the Nafion to $Cu_2O$ mass ratio to 4.8 to improve the adhesion of the $Cu_2O$ particles. For this particular electrocatalyst, the initial $Cu_2O$ Loading was 5.8 mg while the Nafion loading was 27.6 mg.

Two sets of $CO_2$ electrochemical reduction were performed. The first one involved electrolysis at a constant potential of -1.5$V_{NHE}$ for 125 minutes. The second electrolysis consisted of a sequence of potentials starting from -1.1$V_{NHE}$ to -1.7$V_{NHE}$, with 60 minute electrolysis at each potential, with the exception of -1.3$V_{NHE}$ which ran for 120 minutes.

#### 6.3.3.1. SEM Analysis

The SEM image of $Cu_2O$ particles before the first electrolysis is shown in Figure 6.71. The particles ranged in size from 700 – 900 nm. Majority of the particles were cubes while a few have dual cubic structures. Some particles were fully covered with Nafion while others were only partially covered. Some areas of the glassy carbon plate were not

[4]This section previously appeared in reference: Griffin, G.L. and J. Bugayong. 2014. "Electrochemical Reduction of CO2 Using Copper Oxide Nanoparticles Supported on Glassy Carbon Electrodes." MRS Proceedings 1677. [Reproduced with permission from the Cambridge University Press.]

covered by $Cu_2O$ particles and were therefore exposed to the electrolyte during electrolysis. Nevertheless, the $Cu_2O$ particles were mechanically stable.

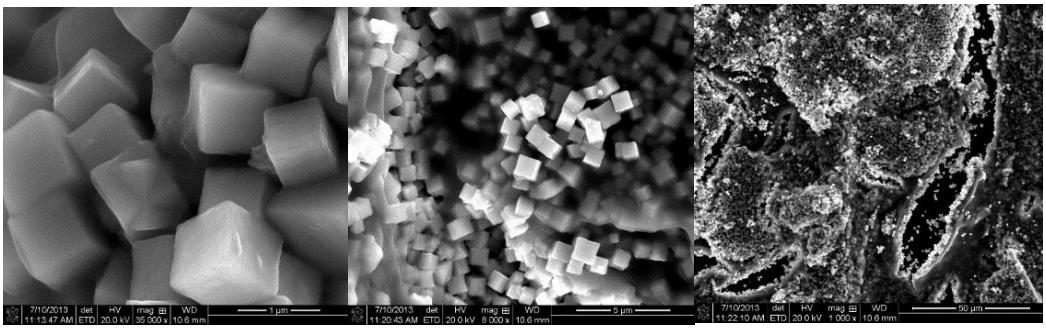

Figure 6.71. SEM images of GL/Nafion/$Cu_2O$ electrode before $CO_2$ reduction at (left) 35,000x (center) 8,000x and (right) 1,000x magnification.

After 7 hours of $CO_2$ electrochemical reduction, the architecture of particles became more diverse as shown in Figure 6.72. A percentage of $Cu_2O$ cubes evolved into particles with multiple structures such as nanoparticles, pyramidal rods and branching fibers. However, some of the cubes remained intact.

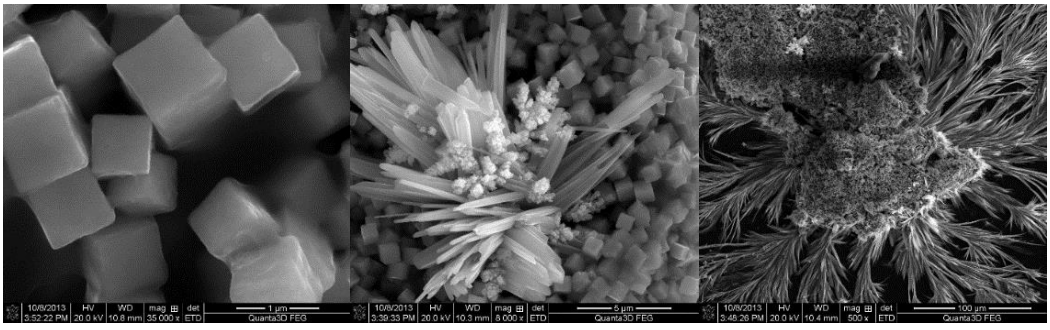

Figure 6.72. SEM images of GL/Nafion/$Cu_2O$ electrode after two batches of $CO_2$ reduction at (left) 35,000x (center) 8,000x and (right) 500x magnification.

6.3.3.2. XRD Analysis

The XRD scan was performed before the first $CO_2$ reduction (ECR) and after the second $CO_2$ reduction. The XRD scans shown in Figure 6.73 revealed different $Cu_2O$

crystal peaks on $Cu_2O$ before $CO_2$ reduction. Based on peak intensity, the electrode consisted of (200) > (111) > (220) > (311) oriented particles. After two batches of $CO_2$ reduction which covered a total time of 7 hours, we observed new peaks that were characteristic of Cu crystals. However, we still observed significant signals from the listed $Cu_2O$ crystal planes. The XRD profile shifted by approximately 0.5°.

This result suggests that the bulk of $Cu_2O$ particle were not reduced to Cu particles. The SEM also showed presence of cubes after $CO_2$ reduction which is indicative of $Cu_2O$ particles. The Nafion that was in contact with the $Cu_2O$ particles may have prevented the particles from reducing to Cu possibly by providing a barrier for electron transfer. It is also possible that these particles experienced significantly lower localized potential gradient.

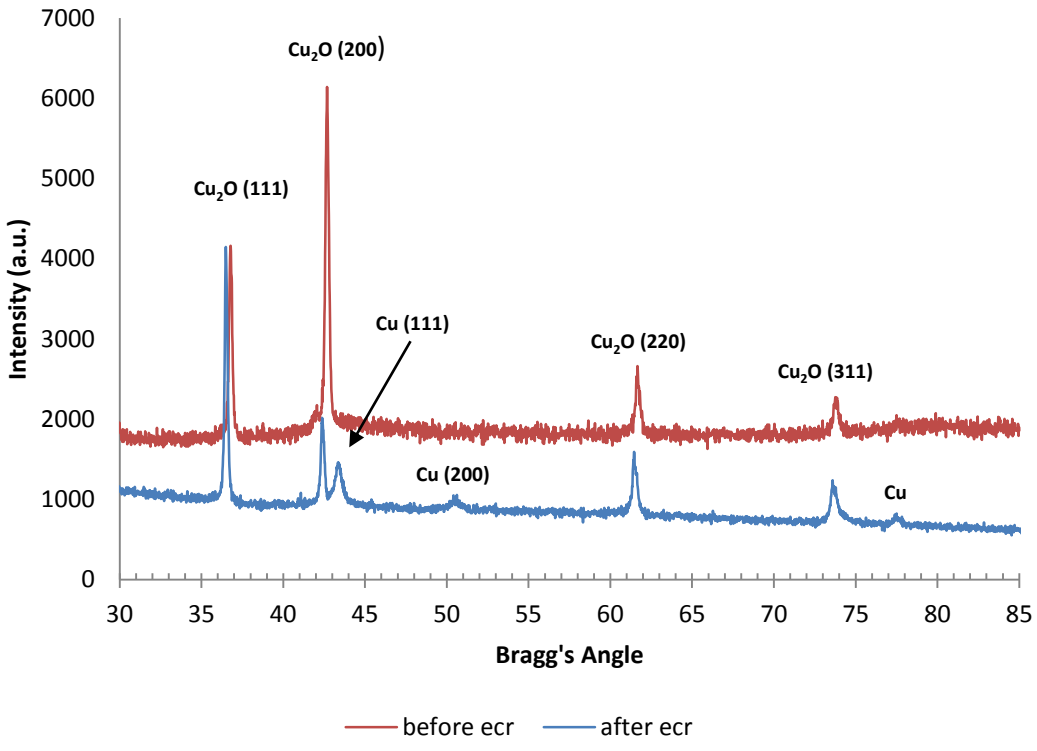


Figure 6.73. XRD profile of GL/Nafion/$Cu_2O$ electrode before and after $CO_2$ reduction.

6.3.3.3. Current Profile of the Fixed Potential Reduction

Figure 6.74 shows the current profile generated by the first $CO_2$ reduction which included the data from the baseline Toray/Nafion/$Cu_2O$ sample. The current slowly increased with time but a plateau was observed between 65 and 80 minutes. During this short period, there was no $CO_2$ fed into the solution. The absence of convection caused by purging of the $CO_2$ carrier gas temporarily lowered the current flow by 2-5 mA. The over-all total current were higher than the one generated by the baseline Toray/Nafion/$Cu_2O$ electrode.

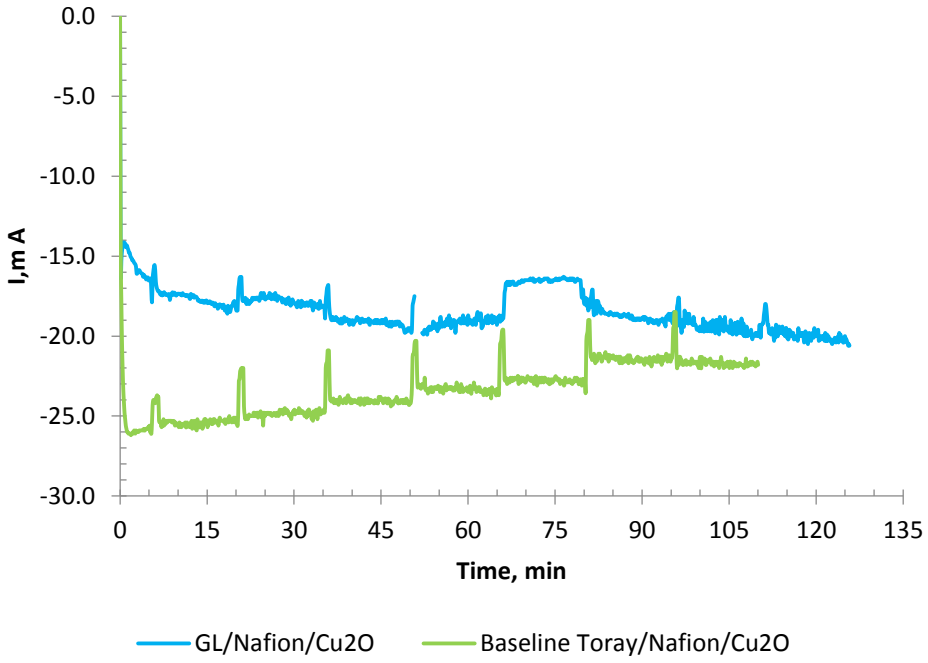


Figure 6.74. Current profile of GL/Nafion/$Cu_2O$ and baseline Toray/Nafion/$Cu_2O$ electrodes during $CO_2$ reduction at -1.5$V_{NHE}$ for 110 minutes.

6.3.3.4. Current Profile of the Potential Step Reduction

Figure 6.75 shows the current profile of the potential step reduction from -1.1$V_{NHE}$ to -1.7$V_{NHE}$. The current was steady at -1.1$V_{NHE}$ and -1.3$V_{NHE}$. At -1.5$V_{NHE}$, we observed

a slow increase in current flow. Finally at -1.7$V_{NHE}$, there was fluctuation of current revolving around -39 mA. The noise was driven by formation of large $H_2$ bubbles.

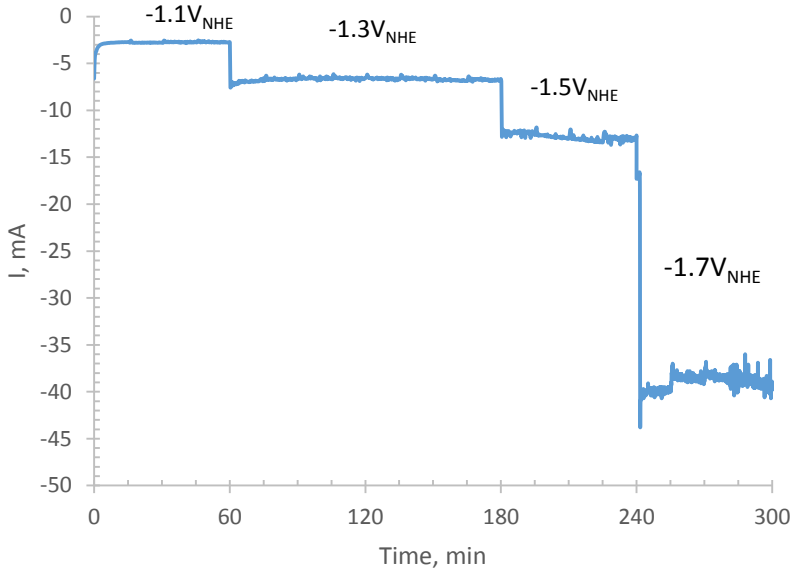


Figure 6.75. Current profile of the GL/Nafion/$Cu_2O$ electrode during potential step electrolysis of $CO_2$.

6.3.3.5. Kinetic Study

We then analyzed the kinetics of first $CO_2$ reduction and the product formation rates are given in Figure 6.76. We observed high $H_2$ formation rates which increased from 99 µmol/$cm^2$*hr to 192 µmol/$cm^2$*hr at 65 minutes into the process and then levelled off around that rate. The CO formation rate meanwhile increased in the first 65 minutes from 5.8 µmol/$cm^2$*hr to 17 µmol/$cm^2$*hr before the process was interrupted by a cut off in $CO_2$ supply. Upon resumption, the CO productivity fell to 9.6 µmol/$cm^2$*hr but increased again to 14 µmol/$cm^2$*hr by the end of the electrolysis.

Meanwhile, the kinetics of ethylene formation followed the same pattern seen in the CO curve. The ethylene formation rate increased in the first 65 minutes from 3.2 µmol/$cm^2$*hr to 10 µmol/$cm^2$*hr before the process was interrupted. Upon resumption, the ethylene productivity fell to 8.2 µmol/$cm^2$*hr before increasing again with time to 10

μmol/cm$^2$*hr by the end of the process. The ethylene productivity from this electrode was slightly on par with the baseline Toray/Nafion/$Cu_2O$ electrode.

Meanwhile, the methane product had an average formation rate at 2.0 μmol/cm$^2$*hr which is higher than in the baseline Toray/Nafion/$Cu_2O$ electrode. The GC also observed ethanol and n-propanol at lower average rates of 0.6 and 0.2 μmol/cm$^2$*hr respectively but were lower than in the baseline Toray/Nafion/$Cu_2O$ electrode.

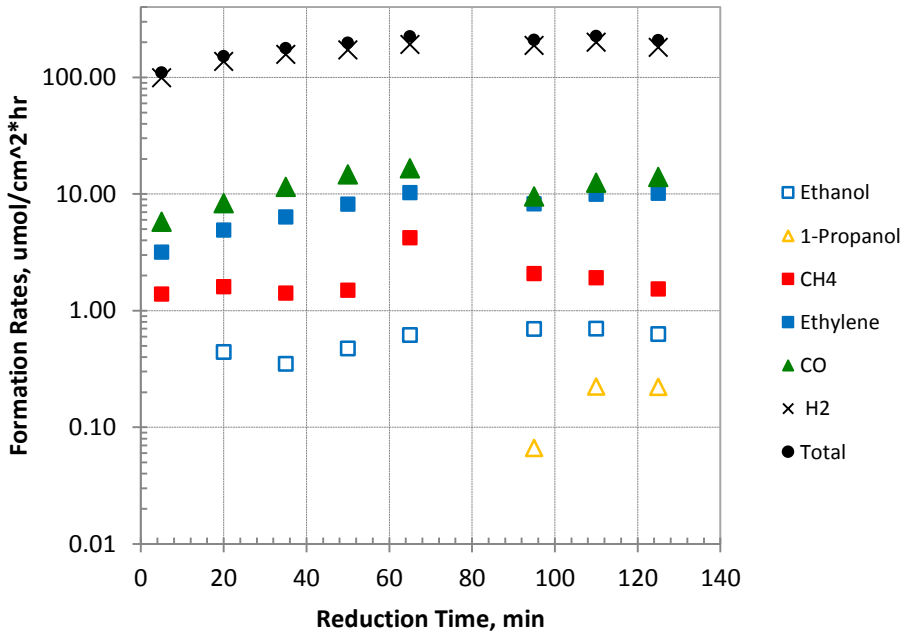


Figure 6.76. Formation rate of products during $CO_2$ reduction on GL/Nafion/$Cu_2O$ electrode at -1.5$V_{NHE}$.

Unique with this sample was that the selectivity of $H_2$, $C_2H_4$ and CO increased with time between 0 and 65 minutes. We did not observe a switch in selectivity between $H_2$ and $CO_2$ products, as well as between CO and the hydrocarbons. This would suggest that either the number of active sites in the electrocatalyst or the turnover frequency increased during this period.

We then looked at the faradaic efficiencies of these products (see Figure 6.77). We observed ethylene as the only major $CO_2$ product with peak faradaic efficiency of 41% and a mean of 31%. This $Cu_2O$ electrocatalyst produced one of the highest ethylene selectivity at -1.5$V_{NHE}$ and is also slightly better than the baseline Toray/Nafion/$Cu_2O$ electrode.

The methane selectivity was also above 1% faradaic efficiency with an average of 5.3% which is also one of the highest we have achieved with our $Cu_2O$ electrode and an order of magnitude better than with our baseline Toray/Nafion/$Cu_2O$ electrode. The rest of the $CO_2$ products were also produced at intermediate selectivity. The electrode showed an average CO, n-propanol and ethanol faradaic efficiency of 7.9%, 2.4% and 1.1% respectively. The enhancement of ethylene and methane formation may be due to lower mass transfer limiting effect.

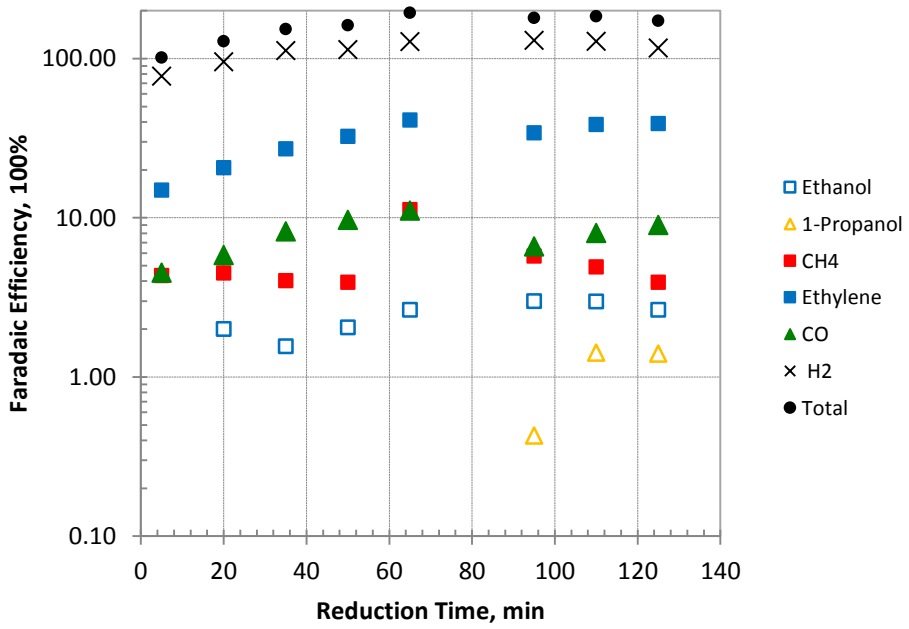


Figure 6.77. Faradaic efficiency of products during $CO_2$ reduction on GL/Nafion/$Cu_2O$ electrode at -1.5$V_{NHE}$.

We then compared the selectivity ratio $C_2H_4/CH_4$ and $(C_2H_4 + CH_4)/CO$ of our $Cu_2O$ electrode with Hori's results. The $C_2H_4/CH_4$ selectivity ratio was 5.8 which was significantly higher than 0.9 on Hori's polycrystalline Cu sample at the same applied potential but lower than 14 on Hori's single crystal high index Cu (711) electrode. Meanwhile, the average $(C_2H_4 + CH_4)/CO$ selectivity ratio was 4.6 compared to 32 (upper limit range of 9-32) on Hori's polycrystalline Cu sample at the same applied potential. This is because the gap in faradaic efficiency between hydrocarbons and CO in the $Cu_2O$ electrode was not as wide as in their Cu electrode.

6.3.3.6. Effect of Potential

We then look at the effect of potential on the formation rates of ethanol, n-propanol, methane, ethylene, CO and $H_2$ shown in Figure 6.78. We observed that the formation rate of these products increased with potential. At $-1.1V_{NHE}$, the GC only detected CO and $H_2$ at average rates of 3.4 and 55 μmol/cm$^2$*hr. At $-1.3V_{NHE}$, ethylene was produced with an initial rate of 0.5 μmol/cm$^2$*hr that increased to 40 μmol/cm$^2$*hr at $-1.7V_{NHE}$.

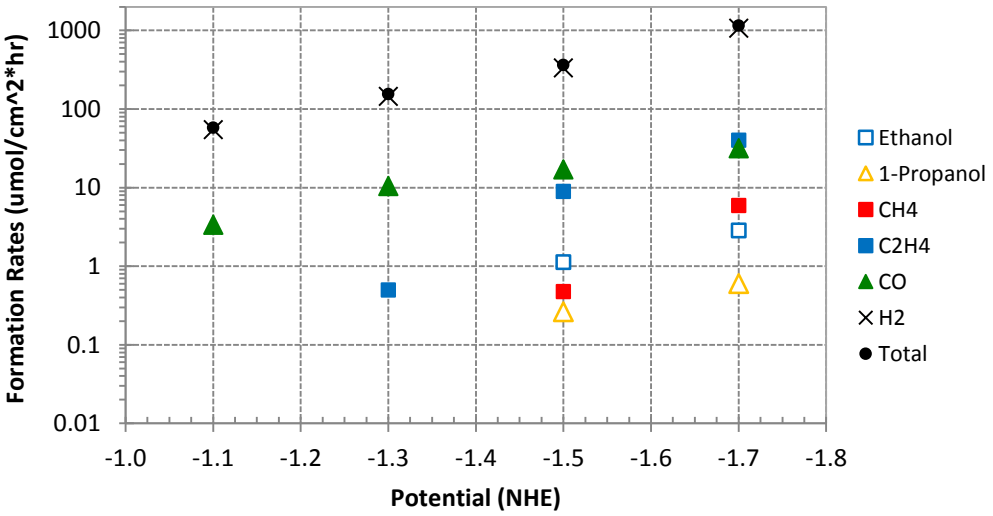


Figure 6.78. Formation rate of products during $CO_2$ reduction on GL/Nafion/$Cu_2O$ electrode at different potentials.

Between -1.3$V_{NHE}$ and -1.5$V_{NHE}$, CO had higher measured formation rate than ethylene but was slightly exceeded by the latter at -1.7$V_{NHE}$. CO formation rate was 32 µmol/$cm^2$*hr at -1.7$V_{NHE}$. The products methane, ethanol and n-propanol were first measured at -1.5$V_{NHE}$ at rates of 0.5, 1.1 and 0.3 µmol/$cm^2$*hr respectively. Their productivity increased to 6.0, 2.9 and 0.6 µmol/$cm^2$*hr respectively at -1.7$V_{NHE}$.

We now looked at the faradaic efficiency of these products at different potential. From Figure 6.79, we observed a peak in CO selectivity of 9.5% at -1.3$V_{NHE}$. At this potential, ethylene had a lower selectivity of 2.7%. At -1.5$V_{NHE}$, ethylene became a major product and showed the highest current efficiency among the $CO_2$ products at 25%. This was followed by CO at 7.8%, ethanol at 3.2%, n-propanol at 1.1% and $CH_4$ at 0.9%. Meanwhile, at the more negative potential of -1.7$V_{NHE}$, the ethylene selectivity continued to improve, increasing to 37%. The methane selectivity also improved to 3.6%. At this potential, the CO efficiency further decreased to 4.9%.

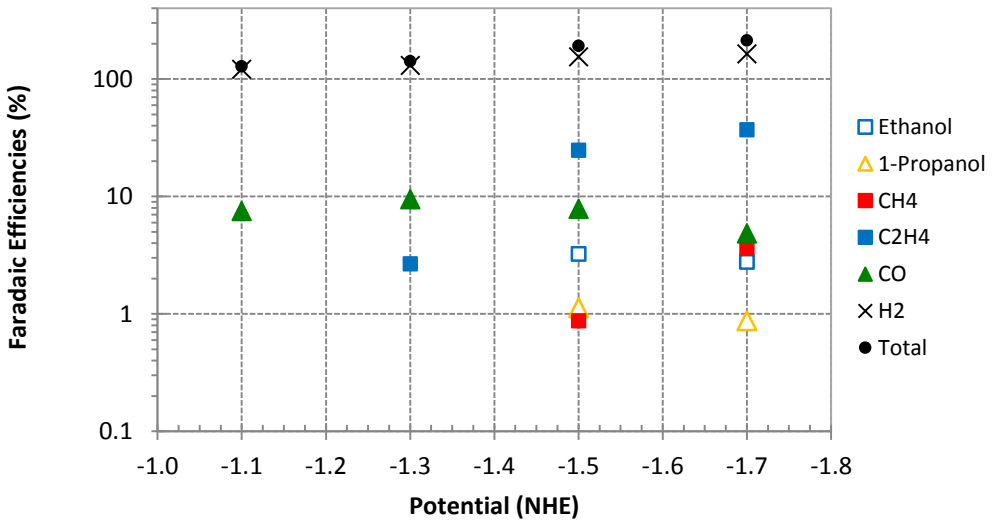


Figure 6.79. Faradaic efficiency of products during $CO_2$ reduction on GL/Nafion/$Cu_2O$ electrode at different potentials.

The shift in selectivity from CO to $C_2H_4$ and $CH_4$ at more negative potentials is consistent with the results observed by Hori's group and also supports a key step in the $CO_2$ reaction pathway proposed by Hori, Kuhl, Schouten and Nie. In particular, the branch point between the formation of CO versus the reduction of $CO_{ads}$ to hydrocarbons.

### *6.3.4. $CO_2$ Reduction on Copper Supported $Cu_2O$ Particles*

Finally, we examined the electrocatalytic activity of $Cu_2O$ supported on polycrystalline Cu substrate. With the previous $Cu_2O$ electrode, we observed that the oxide derived Cu showed different selectivity towards $C_2H_4$ and $CH_4$ compared to polycrystalline Cu. These electrodes consisted of Cu-carbon, Cu-Nafion and Cu-carbon-Nafion interfaces. At this point, it is not clear if the Cu-carbon interface also contributed to enhanced ethylene selectivity. With this $Cu_2O$ electrode, we replaced the carbon support substrate with a copper support substrate and examined any changes on the product distribution.

The $Cu_2O$ particles were synthesized according to the method described by Chang et al. (2009). They were then physically deposited to Cu using a Nafion binder. The Cu substrate had a $Cu_2O$ loading of 1.8 mg and a Nafion/$Cu_2O$ ratio of 4.8.

#### 6.3.4.1. SEM Analysis

The SEM of fresh Cu/Nafion/$Cu_2O$ electrode is shown in Figure 6.80. The left image has a 50,000x magnification while the right image has a 10,000x magnification. The particles were made up mostly of cubes with a few dual cube structures. The average particle size was approximately 600 nm. Some of the particles were fully covered by Nafion while those at the surface were partially covered by Nafion.

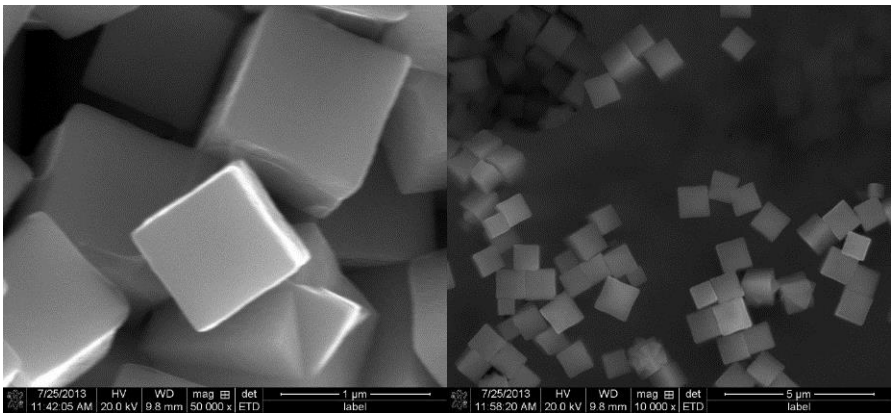


Figure 6.80. SEM of Cu/Nafion/$Cu_2O$ electrode before $CO_2$ reduction at -1.5$V_{NHE}$, (left) at 50,000x magnification and (right) at 10,000x magnification.

Figure 6.81 shows the morphology of $Cu_2O$ particles after $CO_2$ reduction. We observed decorations at the surface of the cube. Some cubes were partially deformed with decorations more confined at the side that was in contact with the electrolyte. The other cubes exhibited less distortion in their structure. About 35% of the $Cu_2O$ particles were lost during electrolysis due to aggressive $H_2$ evolution. Similar to our GL-supported $Cu_2O$, the Cu substrate was not fully covered.

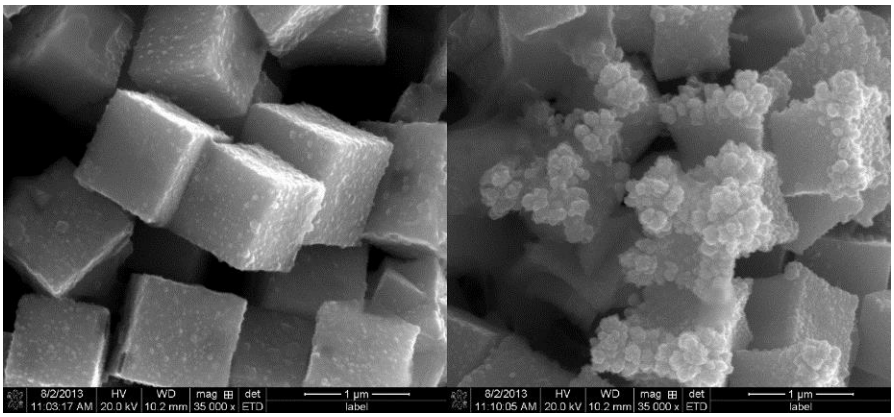


Figure 6.81. SEM of Cu/Nafion/$Cu_2O$ electrode after $CO_2$ reduction at -1.5$V_{NHE}$, (left) at area 1, 35,000x magnification and (right) at area 2, 35,000x magnification.

6.3.4.2. XRD Analysis

The XRD scan before and after $CO_2$ reduction generated peaks for a variety of Cu and $Cu_2O$ crystal planes (refer to Figure 6.82). Before $CO_2$ reduction, the $Cu_2O$(200) particles showed the highest intensity, followed by $Cu_2O$(111) and $Cu_2O$(220) particles. After $CO_2$ reduction, the XRD scan indicated that $Cu_2O$ particles were present since most of the original $Cu_2O$ peaks were still detected except $Cu_2O$(110).

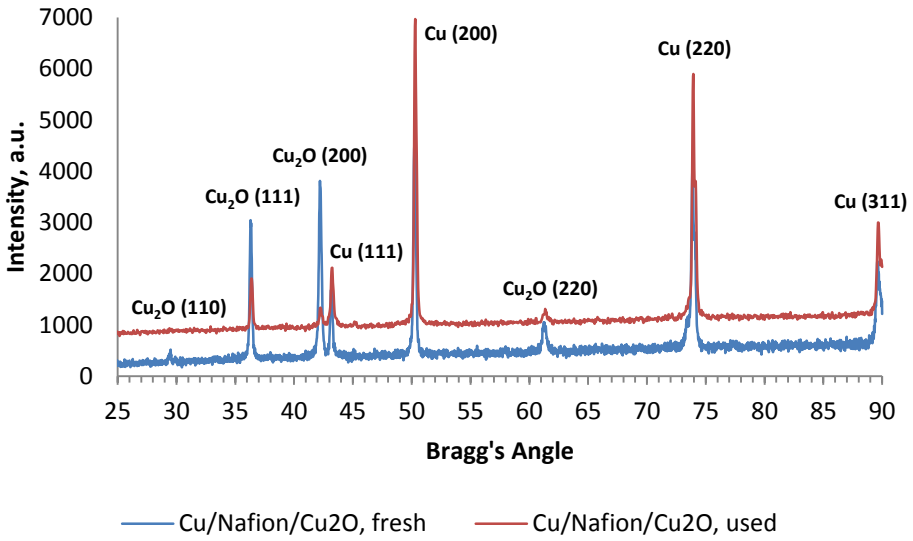


Figure 6.82. XRD profile of Cu/Nafion/$Cu_2O$ electrode before and after $CO_2$ reduction.

6.3.4.3. Current Profile

The $CO_2$ reduction on Cu/Nafion/$Cu_2O$ electrode generated a current profile shown in Figure 6.83. The data on Cu studied in Chapter 4 was also included for reference point. While the charge transfer on the Cu electrode decreased with time, the charge transfer on the Cu/Nafion/$Cu_2O$ electrode was relatively constant around 13 mA/cm$^2$. However, we observed a noise in the current between 0 and 65 minutes which disappeared from 65 to 110 minutes.

The presence of instability in the current during the first part of the process can be attributed to physical movements at the surface as a result of the electrode losing $Cu_2O$ particles. When the electrode surface reached a mechanically stable condition, bubbles became smaller in size. Transient current related to $Cu_2O$ reduction to Cu was not observed from the graph although SEM and XRD showed evidence of partial $Cu_2O$ reduction to Cu.

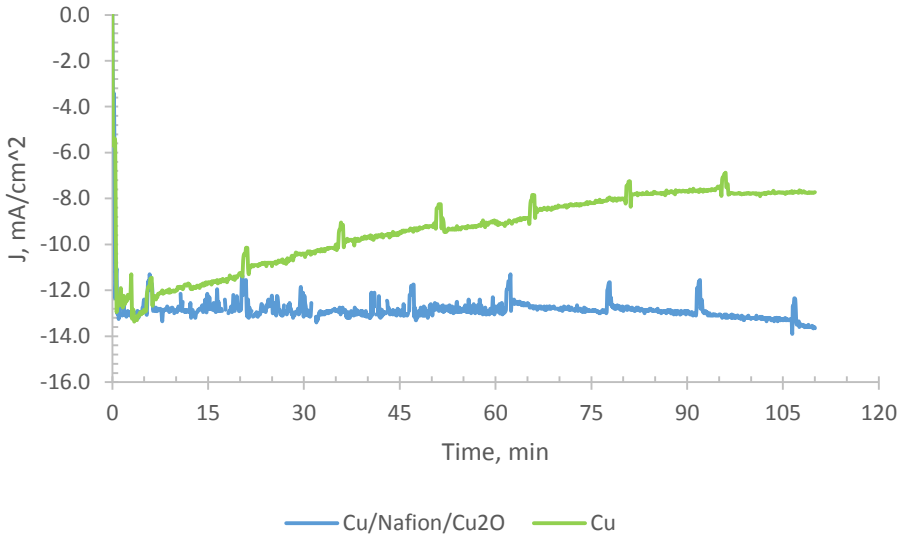


Figure 6.83. Current density profile of Cu/Nafion/$Cu_2O$ and Cu electrodes during $CO_2$ reduction at -1.5$V_{NHE}$.

6.3.4.4. Comparison of Product Formation Rates with Cu

We then compared the formation rates of products between Cu/Nafion/$Cu_2O$ electrode shown in Figure 6.84 and Cu electrode shown in Figure 6.85 (also given in Figure 4.5). The sampling points before 65 minutes were omitted because the high noise in current on the Cu/Nafion/$Cu_2O$ electrode caused uncharacteristic pattern on its product distribution.

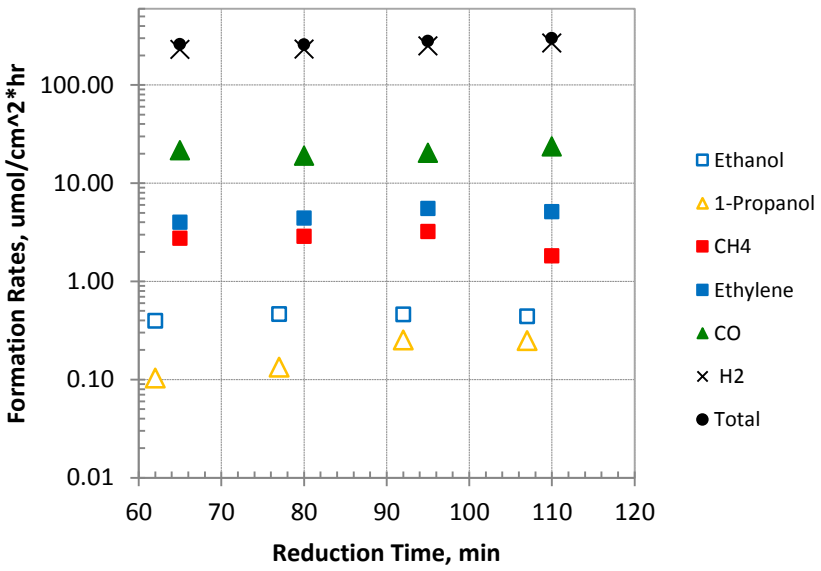


Figure 6.84. Formation rate of products during $CO_2$ reduction on Cu/Nafion/$Cu_2O$ electrode at -1.5$V_{NHE}$.

With our Cu electrode in Chapter 4, we observed methane, ethylene and CO products but did not detect any alcohol products. With our Cu/Nafion/$Cu_2O$ electrode, we observed ethanol and n-propanol, in addition to methane, ethylene and CO.

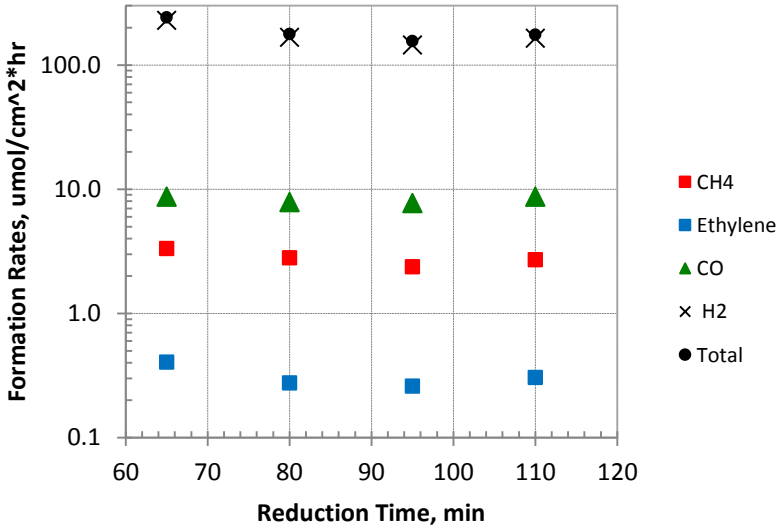


Figure 6.85. Formation rate of products during $CO_2$ reduction on Cu electrode at -1.5$V_{NHE}$.

We obtained higher CO formation rate of 21 µmol/cm$^2$*hr versus 8.3 µmol/cm$^2$*hr on Cu. We also achieved higher ethylene formation rate of 4.8 µmol/cm$^2$*hr versus 0.3 µmol/cm$^2$*hr on Cu. However this rate was not as high as those we have obtained on Toray supported and glassy carbon supported $Cu_2O$ particles. Meanwhile, the methane rates were about the same at 2.7 µmol/cm$^2$*hr versus 2.8 µmol/cm$^2$*hr.

6.3.4.5. Comparison of Product Faradaic Efficiencies with Cu

We then compared the faradaic efficiencies of $CO_2$ products on Cu/Nafion/$Cu_2O$ electrode shown in Figure 6.86 and on Cu electrode shown in Figure 6.87 (also given in Figure 4.6).

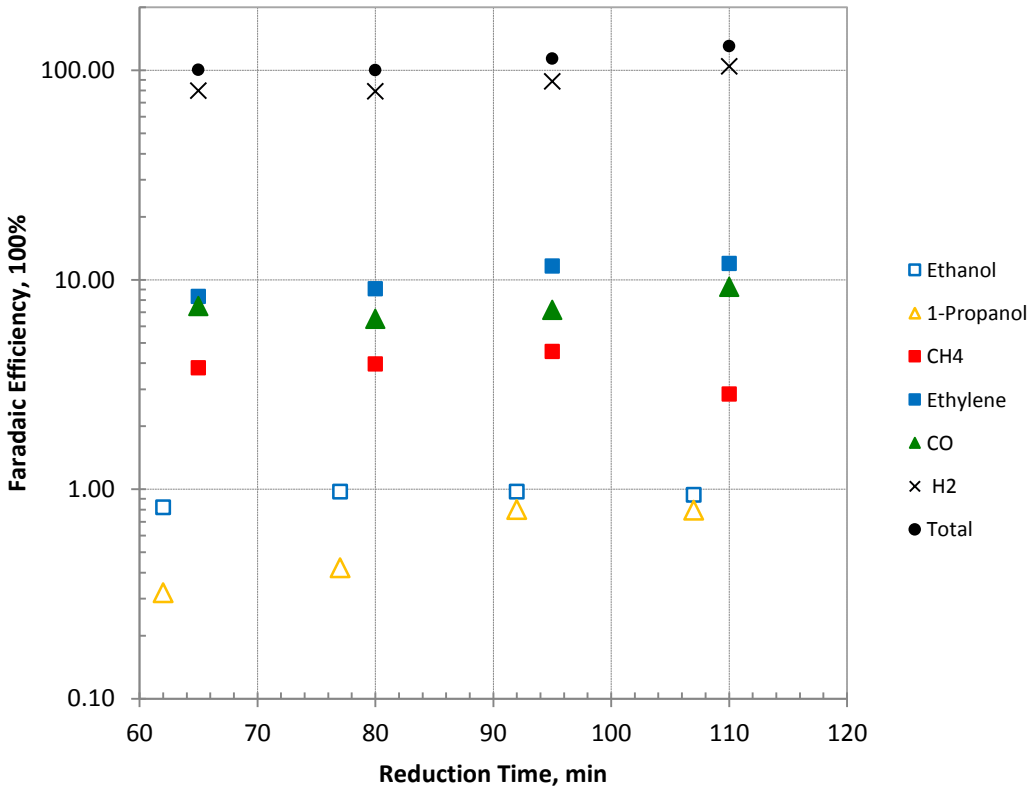


Figure 6.86. Faradaic efficiency of products during $CO_2$ reduction on Cu/Nafion/$Cu_2O$ electrode at -1.5$V_{NHE}$.

The Cu/Nafion/$Cu_2O$ and Cu electrodes showed completely different product distribution. With Cu, all products were at intermediate level, with selectivity in the order of 7.5% methane > 5.5% CO > 1.2% ethylene. With Cu/Nafion/$Cu_2O$ electrode, the selectivity was in the order of 10% ethylene > 7.6% CO > 3.8% methane.

With these data, we computed the selectivity ratio $C_2H_4/CH_4$ and $(C_2H_4 + CH_4)/CO$. The $C_2H_4/CH_4$ selectivity ratio at $-1.5V_{NHE}$ was 2.6 which is higher than 0.9 on Hori's polycrystalline Cu sample at the same applied potential but lower than 14 on Hori's single crystal high index Cu(711) electrode.

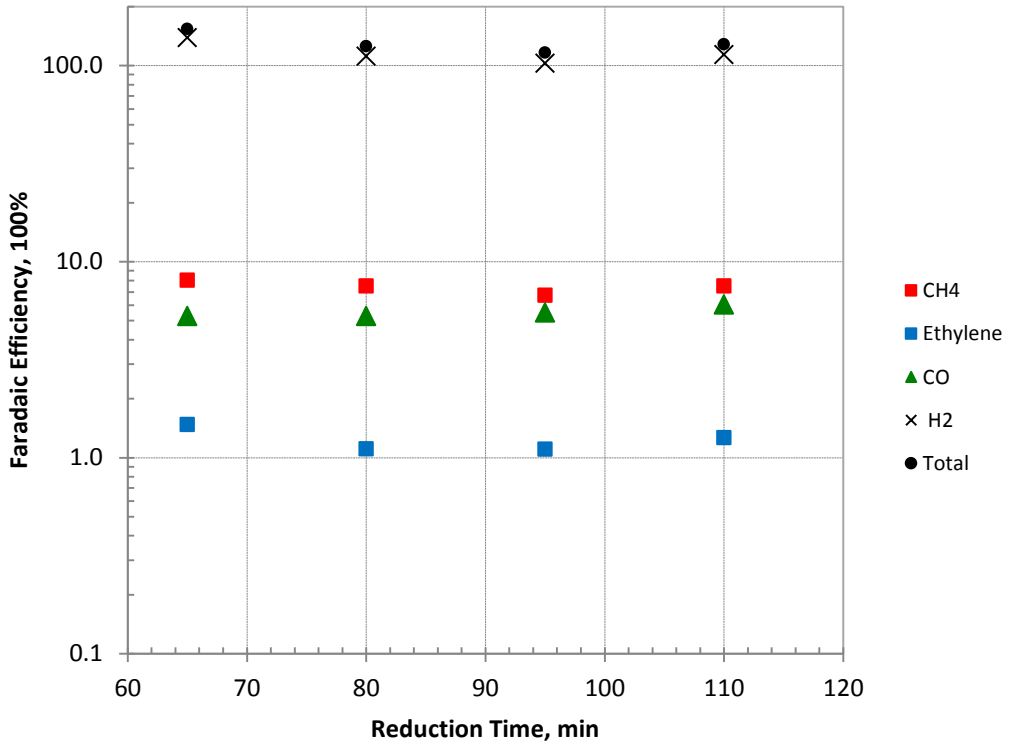


Figure 6.87. Faradaic efficiency of products during $CO_2$ reduction on Cu electrode at $-1.5V_{NHE}$.

The $C_2H_4/CH_4$ ratio was also lower compared to our Toray and glassy carbon supported $Cu_2O$ catalysts. Meanwhile, the average $(C_2H_4 + CH_4)/CO$ selectivity ratio was 1.8

compared to 32 (upper limit range of 9-32) on Hori's polycrystalline Cu sample at the same applied potential.

The lower $C_2H_4/CH_4$ ratio compared to our Toray and glassy carbon supported $Cu_2O$ catalysts was expected because of the additional methane products generated by the Cu support substrate. Since we observed higher ethylene formation rates and better ethylene faradaic efficiencies with our Toray and glassy carbon supported $Cu_2O$ particles, these results suggest that ethylene formation may also be promoted at the Cu-carbon interfaces.

### 6.4. Summary and Conclusion

To summarized, we examined the electrocatalytic activity of colloidal $Cu_2O$ particles deposited on Toray, GL, and Cu support substrate. We looked at the products of $CO_2$ reduction on the Toray and GL support substrate and found that they only made trace amounts of $CH_4$ and CO.

With our baseline Toray/Nafion/$Cu_2O$ electrode, we reproducibly achieved CO and hydrocarbon selectivity up to 50%, led by ethylene and CO. We obtained a $C_2H_4/CH_4$ selectivity ratio of 58.7 which was significantly higher than in Hori's polycrystalline Cu and Cu(711).

We observed better CO and ethylene selectivity with our baseline Toray/Nafion/$Cu_2O$ sample ($Cu_2O$-360B) compared to the $Cu_2O$-0 and $Cu_2O$-30 electrodes. The reduction of larger $Cu_2O$ particles may have resulted in the formation of denser grain boundaries which enhanced CO formation and selectivity to ethylene.

We have evidences which suggest that Nafion may be stabilizing the formation of ethylene by minimizing the degradation of $Cu_2O$ sites that promote the latter. In the absence

of Nafion, hydrocarbon formation may be stabilized alternatively by applying an oscillating current flow. We have shown that the precipitating agent NaOH influenced the morphological uniformity of $Cu_2O$ at higher concentration and consequently lowered the selectivity of $Cu_2O$ to CO and hydrocarbon. As such, cubic $Cu_2O$ particles perform better if they are not mixed with degenerate particles.

Finally, we obtained the $CO_2$ product distribution from two distinct $Cu_2O$ particles at different potentials. We achieved 48% ethylene faradaic efficiency on reduced $Cu_2O$ NP at -1.7$V_{NHE}$. These reduced $Cu_2O$ particles consisted of Cu(111) surfaces which are known to preferably make methane, but may immediately be adjacent to Cu(100) surfaces. We also observed that in $Cu_2O$ NP particles, high $C_2H_4$ selectivity was maintained even at more negative potential but not in the $Cu_2O$ MP particles. Other effects may be influencing this difference and we have not monitored them at this point.

With our GL/Nafion/$Cu_2O$ sample, we also observed similar $CO_2$ product distribution in that the ethylene to methane selectivity ratio was higher compared to that of polycrystalline Cu. We obtained higher ethylene and methane selectivity versus our Toray supported $Cu_2O$ particles. Meanwhile our results on Cu/Nafion/$Cu_2O$ suggest that ethylene formation may be promoted both at the oxide derived Cu surfaces and Cu-carbon boundaries.

# CHAPTER 7
# SUMMARY, CONCLUSIONS AND RECOMMENDATIONS

## 7.1. Summary and Conclusions

We have compared the electrocatalytic activity of polycrystalline Cu, electrochemically deposited $Cu_2O$ and colloidal $Cu_2O$ particles using kinetics and potential dependence experiments in order to determine the role of oxide during the electrochemical reduction of $CO_2$. The $Cu_2O$ particles were made up of low index cubes with size ranging from 40 nm to 900 nm, depending on the catalyst preparation condition. The $Cu_2O$ electrodes were deposited to Toray carbon fiber, glassy carbon and polycrystalline copper support substrates using different Nafion/$Cu_2O$ mass ratios.

With polycrystalline Cu, we achieved 7.5% methane faradaic efficiency with formation rate of 2.8 μmol/$cm^2$*hr, 5.5% CO faradaic efficiency with formation rate of 8.3 μmol/$cm^2$*hr and 1.2% ethylene faradaic efficiency with formation rate of 0.3 μmol/$cm^2$*hr during $CO_2$ reduction at -1.5$V_{NHE}$. Our potential dependence results showed methane formation started at -1.3$V_{NHE}$ while ethylene formation started at -1.5$V_{NHE}$. The methane faradaic efficiency was higher than ethylene faradaic efficiency at the potential range considered (-1.30$V_{NHE}$ to -1.75$V_{NHE}$). We did not detect ethanol and n-propanol.

With electrodeposited $Cu_2O$ film supported on Cu ($Cu/_{ECD}Cu_2O$), we achieved 0.09% methane faradaic efficiency with formation rate of 0.06 μmol/$cm^2$*hr, 1.5% CO faradaic efficiency with formation rate of 4.3 μmol/$cm^2$*hr, 5.2% ethylene faradaic efficiency with formation rate of 2.5 μmol/$cm^2$*hr, 1.1% ethanol faradaic efficiency with formation rate of 0.5 μmol/$cm^2$*hr and 0.6% n-propanol faradaic efficiency with formation rate of 0.2 μmol/$cm^2$*hr during $CO_2$ reduction at -1.5$V_{NHE}$.

We obtained better ethylene formation with $Cu_2O$ film electrodeposited on CuO sublayer ($Cu/_{TH}CuO/_{ECD}Cu_2O$ electrode). The product distribution was 9.5% ethylene faradaic efficiency with formation rate of 9.0 μmol/cm$^2$*hr, 3.7% ethanol faradaic efficiency with formation rate of 3.0 μmol/cm$^2$*hr, 3.0% CO faradaic efficiency with formation rate of 17 μmol/cm$^2$*hr, 2.8% n-propanol faradaic efficiency with formation rate of 1.5 μmol/cm$^2$*hr and 0.05% methane faradaic efficiency with formation rate of 0.05 μmol/cm$^2$*hr.

With colloidal $Cu_2O$ particles supported on Cu, we achieved 3.8% methane faradaic efficiency with formation rate of 2.7 μmol/cm$^2$*hr, 7.6% CO faradaic efficiency with formation rate of 21 μmol/cm$^2$*hr, 10% ethylene faradaic efficiency with formation rate of 4.8 μmol/cm$^2$*hr, 1.0% ethanol faradaic efficiency with formation rate of 0.5 μmol/cm$^2$*hr and 0.5% n-propanol faradaic efficiency with formation rate of 0.2 μmol/cm$^2$*hr during $CO_2$ reduction at -1.5$V_{NHE}$.

We achieved better ethylene formation with $Cu_2O$ NP particles supported on Toray. The product distribution was 38% ethylene faradaic efficiency with formation rate of 18 μmol/cm$^2$*hr, 5.1% CO faradaic efficiency with formation rate of 18 μmol/cm$^2$*hr and 0.6% methane faradaic efficiency with formation rate of 0.5 μmol/cm$^2$*hr.

The baseline Toray/Nafion/$Cu_2O$ electrode showed the best over-all hydrocarbon formation. The product distribution was 28% ethylene faradaic efficiency with formation rate of 13 μmol/cm$^2$*hr, 4.8% ethanol faradaic efficiency with 2.3 μmol/cm$^2$*hr, 16.0% CO faradaic efficiency with formation rate of 41 μmol/cm$^2$*hr and 0.5% methane faradaic efficiency with formation rate of 0.4 μmol/cm$^2$*hr.

These results show that $Cu_2O$ catalysts are different from Cu catalysts. Particularly, Cu catalysts have better methane selectivity while $Cu_2O$ catalysts have better ethylene selectivity. Quantitatively, the $C_2H_4/CH_4$ ratio on Cu was 0.2 while the ratio on both electrodeposited $Cu_2O$ film and colloidal $Cu_2O$ particles was near 60. The $Cu_2O$ particles were reducible and the derived particles consisted of higher number of low-coordinated active sites than Cu which we propose were responsible for the increased ethylene selectivity. The colloidal $Cu_2O$ particles also showed better hydrocarbon formation than electrodeposited $Cu_2O$ film and better CO selectivity than Cu. Meanwhile, a number of SEM images indicated that Nafion preserved some of the $Cu_2O$ particles and helped improve and stabilize hydrocarbon formation, particularly ethylene.

Our different kinetics and potential dependence studies have shown that $Cu_2O$ particles reduce $CO_2$ differently than Cu particles. The results were consistent with the most agreed aspects of the $CO_2$ reduction pathways. The first one is the branch point between desorption of $CO_{ads}$ intermediate and further reduction of $CO_{ads}$ intermediate to hydrocarbons/alcohols. The second one is the C-C coupling step. The reduced $Cu_2O$ particles produced catalytic sites that better promote the coupling of $C_{ads}$ intermediate to form $C_{2+}$ products such as ethylene, ethanol and n-propanol. At this point, it is not clear which $C_{ads}$ intermediates participate in the coupling step and could possibly be via the dimerization of $CO_{ads}$ as suggested by Schouten's group or coupling of $CH_{2ads}$ as suggested by Nie's group. In addition to coupling step, the additional steps to ethanol and n-propanol also remain unclear. Our results showed that ethanol and n-propanol were kinetically more difficult routes than ethylene.

Besides the type of catalyst used, the product distribution was kinetically dynamic and primarily influenced by potential. At low cathodic potential (less than -1.25$V_{NHE}$), we only observed $H_2$ and CO. $H_2$ is produced from reduction of $H_2O$ while CO is the first step of $CO_2$ activation. At high cathodic potential (greater than -1.25$V_{NHE}$), ethylene, methane, ethanol and n-propanol were also produced. At these potentials, $CO_{ads}$ intermediates acquired sufficient potential energy to undergo several hydrogenation steps.

**7.2. Recommendations**

We have provided multiple quantitative results that showed $Cu_2O$ catalysts have significantly higher $C_2H_4/CH_4$ selectivity ratio than polycrystalline Cu. Colloidal $Cu_2O$ particles would be the preferred catalyst to improve production of the industrially important product ethylene.

For future work, we suggest two ways of stabilizing the active sites. The first one involves controlling the size of the oxide-derived Cu particles. Since dispersed Cu particles are more active towards ethylene formation due to the presence of greater fraction of low coordinated Cu atoms, the surface area of these nanoparticles must be maintained. We suggest introducing carbon black during the wet reduction synthesis of $Cu_2O$.

The second one involves stabilizing the Cu(I) active site by adding an ALD layer of $TiO_2$. We have observed unreduced $Cu_2O$ particles that have been subjected to high potential electrolysis. Meanwhile, Li and Kanan (2012) never ruled out the possibility of residual oxide. If the oxidized state of Cu can be maintained, the role of oxide on the electrocatalytic activity of Cu can be better understood. Cu supported on $TiO_2$ was observed to lower the activation energy towards $CO_2$ formation in Water Gas Shift Reaction (WGS). In particular, the metal-oxide interface improved the dissociation of $H_2O$

to OCOH intermediate (Rodriguez et al. 2009). We suggest dipping a thermally oxidized Cu electrode in 1% titanium isopropoxide, $Ti[OCH(CH_3)_2]_4$ solution followed by a second thermal oxidation.

We also suggest further examining the role of Nafion on the enhancement and stabilization of ethylene (and ethanol) formation observed in Chapter 5 Section 5.3.3 and Chapter 6 Section 6.3.2.4 by performing $CO_2$ reduction on Nafion-coated colloidal $Cu_2O$ electrode and Cu foil.

Finally, we suggest applying electrochemical preparation techniques to synthesize $ZnO/Cu_2O$ catalyst used in other energy applications e.g. water gas shift reactions and methanol synthesis. Reports have suggested that ZnO stabilizes oxidized Cu in hydrogenation reactions (Le et al. 2011). Introduction of Zn helped disperse Cu atoms and enhanced binding of intermediates in methanol synthesis (Behrens et al. 2012). Suggested technique is to electrodeposit a thin layer of ZnO to electrodeposited $Cu_2O$ film from a plating bath consisting of 0.01M $Zn(NO_3)_2.6H_2O$. We had performed preliminary studies on ZnO electrochemical deposition.

# BIBLIOGRAPHY


Aurian-Blajeni, B., M.H. Habib, I. Taniguchi and J.O'M. Bockris. 1983. "The Study of Adsorbed Species During the Photoassisted Reduction of Carbon Dioxide at a p-Cadmium Telluride Electrode." *Journal of Electroanalytical Chemistry and Interfacial Electrochemistry* 157(2): 399-404.

Aylmer-Kelly, A.W.B., A. Bewick, P.R. Cantrill and A.M. Tuxford. 1973. "Studies of Electrochemically Generated Reaction Intermediates Using Modulated Specular Reflectance Spectroscopy." *Faraday Discussions of the Chemical Society* 56: 96-107.

Bard, A. J. and L. R. Faulkner. 2001. "Electrochemical Methods: Fundamentals and Applications." *John Wiley and Sons, Inc.*

Bard, A. J., R. Parsons and J. Jordan. 1985. "Standard Potentials in Aqueous Solutions." *CRC Press.*

Beden, B., A. Bewick, M. Razaq and J. Weber. 1982. "On the Nature of Reduced Carbon Dioxide: An IR Spectroscopic Investigation." *Journal of Electroanalytical Chemistry and Interfacial Electrochemistry* 139(1): 203-206.

Behrens, M., F. Studt, I. Kasatkin, S. Kühl, M. Hävecker, F. Abild-Pedersen, S. Zander, F. Girgsdies, P. Kurr, B-L Kniep, M. Tovar, R.W. Fischer, J.K. Nørskov and R. Schlögl. 2012. "The Active Site of Methanol Synthesis over $Cu/ZnO/Al_2O_3$ Industrial Catalysts." *Science* 336: 893-897.

Bidault, F., D.J.L. Brett, P.H. Middleton and N.P. Brandon. 2009. "Review of Gas Diffusion Cathodes for Alkaline Fuel Cells." *Journal of Power Sources* 187: 39–48.

Bowker, M., R.A. Hadden, H. Houghton, J.N.K. Hyland, K.C. Waugh. 1988. "The Mechanism of Methanol Synthesis on Copper/Zinc Oxide/Alumina Catalysts." *Journal of Catalysis* 109 (2): 263–273.

Bugayong, J. and G.L. Griffin. 2013. "Electrochemical Reduction of $CO_2$ using Supported $Cu_2O$ Nanoparticles." Electrochemical Synthesis of Fuels 2, *Electrochemical Society Transactions* 58 (2): 81-89.

Bugayong, J. and G.L. Griffin. 2013. "Electrochemical Reduction of $CO_2$ using Supported $Cu_2O$ Catalysts." Electrochemical Interfaces for Energy Storage and Conversion - Fundamental Insights from Experiments to Computations, *Materials Research Society Proceedings* 1542.

Chandrasekaran, K. and J.O'M. Bockris. 1987. "In-situ Spectroscopic Investigation of Adsorbed Intermediate Radicals in Electrochemical Reactions: Carbon Dioxide(1-) (CO2-) on Platinum." *Surface Science* 185(3): 495-514.

Chang, T. Y., R. M. Liang, P. W. Wu, J. Y. Chen and Y. C. Hsieh. 2009. "Electrochemical Reduction of $CO_2$ by $Cu_2O$-Catalyzed Carbon Clothes." *Materials Letters* 63: 1001-1003.

Chen, K. and D. Xue. 2013. "Crystallisation of Cuprous Oxide." *International Journal of Nanotechnology* 10 (1/2): 4-12.

Ciobica, I.M. and R. A. van Santen. 2003. "Carbon Monoxide Dissociation on Planar and Stepped Ru(0001) Surfaces." *Journal of Physical Chemistry B* 107 (16): 3808–3812.

Cook, R. L., R. C. MacDuff and A. F. Sammells. 1988. "On the Electrochemical Reduction at Carbon Dioxide at In Situ Electrodeposited Copper." *Journal of the Electrochemical Society* 135(6): 1320-1326.

De Jongh, P. 2012. "Porous Materials as Catalysts and Catalyst Supports." *Catalysis*: 431-444.

Desimoni, E. and B. Brunetti. 1980. "Glassy Carbon as Electrode Material in Electroanalytical Chemistry." *Analytica Chimica Acta* 119: l-24.

Det Norske Veritas. 2011. "Carbon Dioxide Utilization: Electrochemical Conversion of $CO_2$ – Opportunities and Challenges." *Research and Innovation*, Position Paper 07-2011: 1-20.

DeWulf, D.W. and A.J. Bard. 1988. "The Electrochemical Reduction of $CO_2$ to $CH_4$ and $C_2H_4$ at Cu/Nafion Electrodes (Solid Polymer Electrolyte Structures)." *Catalysis Letters* 1: 73-80.

DeWulf, D. W., T. Jin and A. J. Bard. 1989. "Electrochemical and Surface Studies of Carbon Dioxide Reduction to Methane and Ethylene at Copper Electrodes in Aqueous Solutions." *Journal of the Electrochemical Society* 136(6): 1686-1691.

Durand, W. J., A. A. Peterson, F. Studt, F. Abild-Pederson and J. K. Norskov. 2011. "Structure Effects on the Energetics of the Electrochemical Reduction of $CO_2$ by Copper Surfaces." *Surface Science* 605: 1354-1359.

Filipic, G. and U. Cvelbar. 2012. "Copper Oxide Nanowires: A Review of Growth." *Nanotechnology* 23: 1-16.

Frese, K. W. 1991. "Electrochemical Reduction of $CO_2$ at Intentionally Oxidized Copper Electrodes." *Journal of Electrochemical Society* 138 (11): 3338 – 3344.

Frese Jr, K.W. in: B.P. Sullivan, K. Krist, H.E. Guard (Eds.). 1993. "Electrochemical and Electrocatalytic Reactions of Carbon Dioxide." Electrochemical Reduction of $CO_2$ at Solid Electrodes (Chapter 6): Elsevier, Amsterdam, 145.

Friebe, P., P. Bogdanoff, N. Alonso-Vante and H. Tributsch. 1997. "A Real-Time Mass Spectroscopy Study of the (Electro)chemical Factors Affecting $CO_2$ Reduction at Copper." *Journal of Catalysis* 168: 374-385.

Gabriele, C., E.A. Quadrelli and S. Perathoner. 2013. "Catalysis for $CO_2$ Conversion: A Key Technology for Rapid Introduction of Renewable Energy in the Value Chain of Chemical Industries." *Energy and Environmental Science* 6: 1711-1731.

Gattrell, M., N. Gupta and A. Co. 2006. "A Review of the Aqueous Electrochemical Reduction of $CO_2$ to Hydrocarbons at Copper." *Journal of Electroanalytical Chemistry* 594: 1-19.

Ghadimkhani, G., N. R. de Tacconi, W. Chanmanee, C. Janaky and K. Rajeshwar. 2013. "Efficient Solar Photoelectrosynthesis of Methanol from Carbon Dioxide Using Hybrid CuO-$Cu_2O$ Semiconductor Nanorod Arrays." *Chemical Communications* 49: 1297-1299.

Golden, T.D., M.G. Shumsky, Y. Zhou, R.A. VanderWerf, R.A. Van Leeuwen and J.A. Switzer. 1996. "Electrochemical Deposition of Copper (I) Oxide Films." *Chemistry of Materials* 8: 2499.

Griffin, G.L. and J. Bugayong. 2014. "Electrochemical Reduction of $CO_2$ Using Copper Oxide Nanoparticles Supported on Glassy Carbon Electrodes." Electrochemical Interfaces for Energy Storage and Conversion - Fundamental Insights from Experiments to Computations, *Materials Research Society Proceedings* 1677.

Henrie, J., S. Kellis, S.M. Schultz and A. Hawkins. 2004. "Electronic Color Charts for Dielectric Films on Silicon." *Optics Express* 12 (7): 1464-1469.

Hori Y., K. Kikuchi, A. Murata and S. Suzuki. 1986. "Production of Methane and Ethylene in Electrochemical Reduction of Carbon Dioxide at Copper Electrode in Aqueous Hydrogencarbonate Solution." *Chemistry Letters* 897-898.

Hori, Y., A. Murata, R. Takahashi and S. Suzuki. 1988. "Enhanced Formation of Ethylene and Alcohols at Ambient Temperature and Pressure in Electrochemical Reduction of Carbon Dioxide at a Copper Electrode." *Journal of the Chemical Society, Chemical Communications*: 17-19.

Hori, Y., A. Murata and R. Takahashi. 1989. "Formation of Hydrocarbons in the Electrochemical Reduction of Carbon Dioxide at a Copper Electrode in Aqueous Solution." *Journal of the Chemical Society, Faraday Transactions* 85(8): 2309-2326.

Hori, Y., R. Takahashi, Y. Yoshinami and A. Murata. 1997. "Electrochemical Reduction of CO at a Copper Electrode." *The Journal of Physical Chemistry B* 101 (36): 7075–7081.

Hori Y., O. Koga, Y. Watanabe and T. Matsuo. 1998. "FTIR Measurements of Charge Displacement Adsorption of CO on Poly- and Single Crystal (100) of Cu Electrodes." *Electrochimica Acta* 44 (8–9): 1389–1395.

Hori, Y. 2008. "Electrochemical $CO_2$ Reduction on Metal Electrodes." Edited by C. Vayenas et al.. *Modern Aspects of Electrochemistry* 42: 89 – 189.

Hori, Y., I. Takahashi, O. Koga and N. Hoshi. 2002. "Selective Formation of $C_2$ Compounds from Electrochemical Reduction of $CO_2$ at a Series of Copper Single Crystal Electrodes." *Journal of Physical Chemistry* 106: 15-17.

Hori, Y., I. Takahashi, O. Koga and N. Hoshi. 2003. "Electrochemical Reduction of Carbon Dioxide at Various Series of Copper Single Crystal Electrodes." *Journal of Molecular Catalysis A:* Chemical 199 (1-2): 39-47.

Hori, Y. in: W. Vielstich, H.A. Gasteiger, A. Lamm (Eds.). 2003. Handbook of Fuel Cells (Chapter 48), Vol. 2, Wiley, West Sussex, England, 720–733.

Huanga, H. and X. Wang. 2014. "Recent progress on carbon-based support materials for electrocatalysts of direct methanol fuel cells." *Journal of Materials Chemistry A* 2 (18): 6266-6291.

Inderwildi, O.R.; S.J. Jenkins and D.A. King. 2008. "Fischer−Tropsch Mechanism Revisited: Alternative Pathways for the Production of Higher Hydrocarbons from Synthesis Gas." *Journal of Physical Chemistry C* 112 (5): 1305–1307.

Intergovernmental Panel on Climate Change. 2007. "Climate Change 2007: Synthesis Report." *An assessment of the Intergovernmental Panel on Climate Change* 1-73.

Ito, H., T. Maeda, A. Nakano and H. Takenaka. 2011. "Properties of Nafion Membrane Under PEM Water Electrolysis Conditions." *International Journal of Hydrogen Energy* 36: 10527-10540.

Jermann, B. and J. Augustynski. 1994. "Long-term Activation of the Copper Cathode in the Course of $CO_2$ Reduction." *Electrochimica Acta* 39 (11-12): 1891-1896.

Kostecki, R. and J. Augustynski. 1994. "Electrochemical Reduction of $CO_2$ at an Activated Silver Electrode." *Berichte der Bunsen-Gesellschaft* 98(12): 1510-15.

Kuhl, K. P., E. R. Cave, D. N. Abram and T. F. Jaramillo. 2012. "New Insights into the Electrochemical Reduction of Carbon Dioxide on Metallic Copper Surfaces." *Energy and Environmental Science* 10: 1039 – 1048.

Kuo, C. H. and M. H. Huang. 2010. "Morphologically Controlled Synthesis of $Cu_2O$ Nanocrystals and their Properties." *Nano Today* 5: 106-116.

Kyriacou, G. and A. Anagnostopoulos. 1992. "Electroreduction of $CO_2$ on Differently Prepared Copper Electrodes. The Influence of Electrode Treatment on the Current Efficiencies." *Journal of Electroanalytical Chemistry* 322: 233-246.

Le, M., M. Ren, Z. Zhang, P. T. Sprunger, R. L. Kurtz and J. C. Flake. 2011. " Electrochemical Reduction of $CO_2$ to $CH_3OH$ at Copper Oxide Surfaces." *Journal of the Electrochemical Society* 158(5): E45-E49.

Lewis, N. S. 2007. "Powering the Planet." *Engineering and Science* 2: 12-23.

Lewis, N. S. and D. G. Nocera. 2006. "Powering the Planet: Chemical Challenges in Solar Energy Utilization." *Proceedings of the National Academy of Sciences* 103(43): 15729-15735.

Li, C. W. and M. W. Kanan. 2012. "$CO_2$ Reduction at Low Overpotential on Cu Electrodes Resulting from the Reduction of Thick $Cu_2O$ Films." *Journal of the American Chemical Society* 134: 7231-7234.

Li, C.W., J. Ciston and M.W. Kanan. 2014. "Electroreduction of Carbon Monoxide to Liquid Fuel on Oxide-Derived Nanocrystalline Copper." *Nature*: 1-5.

Li, Q., P. Xu, B. Zhang, H. Tsai, S. Zheng, G. Wu and H.L. Wang. 2013. "Structure-Dependent Electrocatalytic Properties of $Cu_2O$ Nanocrystals for Oxygen Reduction Reaction." *The Journal of Physical Chemistry C* 117: 13872−13878.

McQuillan, A.J., P.J. Hendra and M. Fleischmann. 1975. "Raman Spectroscopic Investigation of Silver Electrodes." *Journal of Electroanalytical Chemistry and Interfacial Electrochemistry* 65(2): 933-44.

Meyer, B.K., A. Polity, D. Reppin, M. Becker, P. Hering, B. Kramm, P.J. Klar, T. Sander, C. Reindl, C. Heiliger, M. Heinemann, C. Muller and C. Ronning. 2013. "The Physics of Copper Oxide ($Cu_2O$)." *Semiconductors and Semimetals* 88 (Oxide Semiconductors): 201-226.

Nakatsuji, H. and Z-M Hu. 2000. "Mechanism of Methanol Synthesis on Cu(100) and Zn/Cu(100) Surfaces: Comparative Dipped Adcluster Model Study." *International Journal of Quantum Chemistry* 77 (1): 341–349.

Nie, X., M. R. Esopi, M. J. Janik and A. Ashtagiri. 2013. "Selectivity of $CO_2$ Reduction on Copper Electrodes: The Role of the Kinetics of Elementary Steps." *Angewandte Chemie International Edition* 52: 2459-2462.

Noda, H., S.Ikeda, Y. Oda and K. Ito. 1989. "Potential Dependencies of the Products on Electrochemical Reduction of Carbon Dioxide at a Copper Electrode." *Chemistry Letters*: 289-292.

Nogami, G., H. ltagaki and R. Shiratsuch. 1994. "Pulsed Electroreduction of on Copper Electrodes-II." *Journal of the Electrochemical Society* 141 (5): 1138-1142.

Oda, I., H. Ogasawara and M. Ito. 1996. "Carbon Monoxide Adsorption on Copper and Silver Electrodes during Carbon Dioxide Electroreduction Studied by Infrared Reflection Absorption Spectroscopy and Surface-Enhanced Raman Spectroscopy." *Langmuir* 12 (4): 1094–1097.

Peighambardoust, S.J., S. Rowshanzamir and M. Amjadi. 2010. "Review of the Proton Exchange Membranes for Fuel Cell Applications." *International Journal of Hydrogen Energy* 35: 9349-9384.

Peterson, A. A., F. Abild-Pederson, F. Studt, J. Rossmeisl and J. K. Norskov. 2010. "How Copper Catalyzes the Electroreduction of Carbon Dioxide Into Hydrocarbon Fuels." *Energy and Environmental Science* 3: 1311-1315.

Rapier, R. and M. Thurber. 2013. "The Experts: What's the Best Way Forward on Nuclear Power?" *Journal Reports: Energy of The Wall Street Journal*. http://online.wsj.com/article/SB10001424127887323809304578428570153032936.html.

Rodrıguez, J.A., J. Evans, J. Graciani, J-B Park, P. Liu, J. Hrbek and J.F. Sanz. 2009. "High Water-Gas Shift Activity in $TiO_2$(110) Supported Cu and Au Nanoparticles: Role of the Oxide and Metal Particle Size." *Journal of Physical Chemistry C* 113: 7364–7370.

Roy, Somnath C., Oomman K. Varghese, Maggie Paulose and Craig A. Grimes. 2010. "Toward Solar Fuels: Photocatalytic Conversion of Carbon Dioxide to Hydrocarbons." *ACSNano* 4 (3): 1259-1278.

Schouten, K. J. P., Y. Kwon, C. J. M. Van der Ham, Z. Qin and M. T. M. Koper. 2011. "A New Mechanism for the Selectivity to $C_1$ and $C_2$ Species in the Electrochemical Reduction of Carbon Dioxide on Copper Electrodes." *Chemical Science* 2: 1902-1909.

Sharma, S. and B.G. Pollet. 2012. "Support Materials for PEMFC and DMFC Electrocatalysts—A Review." *Journal of Power Sources* 208: 96–119.

Shetty, S.G., A.P.J. Jansen and R.A. van Santen. 2009. "Direct Versus Hydrogen-assisted CO Dissociation." *Journal of the American Chemical Society* 131(36): 12874-12875.

Shetty, S.G. and R.A. van Santen. 2010. "Hydrogen Induced CO Activation on Open Ru and Co Surfaces." *Physical Chemistry Chemical Physics* 12(24): 6330-6332.

Shiratsuchi, R., Y. Aikoh and G. Nogami. 1993. "Pulsed Electroreduction of C02 on Copper Electrodes." *Journal of the Electrochemical Society* 140 (12): 3479-3482.

Smith, B.D., D. E. Irish, P. Kedzierzawski and J. Augustynski. 1997. "A Surface Enhanced Roman Scattering Study of the Intermediate and Poisoning Species Formed during the Electrochemical Reduction of $CO_2$ on Copper." *Journal of the Electrochemical Society* 144 (12): 4288-4296.

Tang, W., A. A. Peterson, A. S. Varela, Z. P. Jovanov, L. Bech, W. J. Durand, S. Dahl, J. K. Norskov and I. Chorkendorff. 2012. "The Importance of Surface Morphology in Controlling the Selectivity of Polycrystalline Copper for $CO_2$ Electroreduction." *Physical Chemistry Chemical Physics* 14: 76-81.

Taniguchi, I. in: J.O'M. Bockris, R.E. White, B.E. Conway (Eds.). 1989. "Electrochemical and Photoelectrochemical Reduction of Carbon Dioxide." Modern Aspects of Electrochemistry: 20, 327-400.

Tsai, C-C., J. Bugayong, G.L. Griffin. 2012. "Role of Surface Oxide Layer during $CO_2$ Reduction at Copper Electrodes." Materials for Catalysis in Energy: Jiang, D., H.K. Kung, R. Jin, R.M. Rioux. *Materials Research Society Proceedings* 1446:59-64.

US Energy Information Administration. 2009. "Emissions of Greenhouse Gases in the United States 2009." *Independent Statistics and Analysis* March 2011: 1-78.

US Energy Information Administration. 2013. "February 2013 Monthly Energy Review." *Independent Statistics and Analysis* February 2013: 1-201.

Van der Linden, W.E. and J.W. Dieker. 1980. "Glassy Carbon as Electrode Material in Electroanalytical Chemistry." *Analytica Chimica Acta* 119: l-24.

Varcoe, J. R. and R. C. T. Slade. 2004. "Prospects for Alkaline Anion-Exchange Membranes in Low Temperature Fuel Cells." *Fuel Cells* 5: 187–200.

Wang, J., M. Musameh and Y. Lin. 2003. "Solubilization of Carbon Nanotubes by Nafion Towards the Preparation of Amperometric Biosensors." *Journal of the American Chemical Society* 25 (9): 2408-2409.

Wasmus, S., E. Cattaneo and W. Vielstich. 1990. "Reduction of Carbon Dioxide to Methane and Ethene - An On-line MS Study with Rotating Electrodes." *Electrochimica Acta* 35 (4): 771-775.

Whipple, D. T. and P. J. A. Kenis. 2010. "Prospects of $CO_2$ Utilization via Direct Heterogeneous Electrochemical Reduction." *The Journal of Physical Chemistry Letters* 1: 3451 – 3458.

Working Group III of the Intergovernmental Panel on Climate Change [Metz, B., O. Davidson, H.C. de Coninck, M. Loos, and L.A. Meyer (Eds.)]. 2005. "IPCC Special Report on Carbon Dioxide Capture and Storage." *Cambridge University Press,* Cambridge, United Kingdom and New York, NY, USA, 1-442.

Yaroslavtsev, A.B. 2013. "Perfluorinated Ion-Exchange Membranes." *Polymer Science, Ser. A* 55 (11): 674–698.

Zhao, Y.F., Y. Yang, C. Mims, C.H.F. Peden, J. Li and D. Mei. 2011. "Insight into Methanol Synthesis from $CO_2$ Hydrogenation on Cu(111): Complex Reaction Network and the Effects of $H_2O$." *Journal of Catalysis* 281(2): 199-211.

Zoolfakar, A.S., R.A. Rani, A.J. Morfa, A.P. O'Mullane and K. Kalantar-zadeh. 2014. "Nanostructured Copper Oxide Semiconductors: A Perspective on Materials, Synthesis Methods and Applications." *Journal of Materials Chemistry C* 2: 5247–5270.

# APPENDIX I

# PERMISSION TO REPRODUCE

**ELSEVIER LICENSE**
**TERMS AND CONDITIONS**

Sep 24, 2014

This is a License Agreement between Joel Bugayong ("You") and Elsevier ("Elsevier") provided by Copyright Clearance Center ("CCC"). The license consists of your order details, the terms and conditions provided by Elsevier, and the payment terms and conditions.

**All payments must be made in full to CCC. For payment instructions, please see information listed at the bottom of this form.**

| | |
|---|---|
| Supplier | Elsevier Limited<br>The Boulevard,Langford Lane<br>Kidlington,Oxford,OX5 1GB,UK |
| Registered Company Number | 1982084 |
| Customer name | Joel Bugayong |
| Customer address | W209 Chem Engg Bldg S Stadium Dr<br>Baton Rouge, LA 70803 |
| License number | 3456280895249 |
| License date | Aug 26, 2014 |
| Licensed content publisher | Elsevier |
| Licensed content publication | Journal of Molecular Catalysis A: Chemical |
| Licensed content title | Electrochemical reduction of carbon dioxide at various series of copper single crystal electrodes |
| Licensed content author | Y. Hori,I. Takahashi,O. Koga,N. Hoshi |
| Licensed content date | 16 May 2003 |
| Licensed content volume number | 199 |
| Licensed content issue number | 1-2 |
| Number of pages | 9 |
| Start Page | 39 |
| End Page | 47 |
| Type of Use | reuse in a thesis/dissertation |
| Portion | figures/tables/illustrations |
| Number of figures/tables /illustrations | 3 |
| Format | both print and electronic |
| Are you the author of this Elsevier article? | No |
| Will you be translating? | No |
| Title of your thesis/dissertation | Electrochemical Reduction of CO2 on Supported Cu2O Catalysts |
| Expected completion date | Nov 2014 |
| Estimated size (number of pages) | 140 |
| Elsevier VAT number | GB 494 6272 12 |
| Permissions price | 0.00 USD |
| VAT/Local Sales Tax | 0.00 USD / 0.00 GBP |
| Total | 0.00 USD |
| Terms and Conditions | |

## ROYAL SOCIETY OF CHEMISTRY LICENSE TERMS AND CONDITIONS

Sep 24, 2014

This is a License Agreement between Joel Bugayong ("You") and Royal Society of Chemistry ("Royal Society of Chemistry") provided by Copyright Clearance Center ("CCC"). The license consists of your order details, the terms and conditions provided by Royal Society of Chemistry, and the payment terms and conditions.

**All payments must be made in full to CCC. For payment instructions, please see information listed at the bottom of this form.**

| | |
|---|---|
| License Number | 3456191077337 |
| License date | Aug 25, 2014 |
| Licensed content publisher | Royal Society of Chemistry |
| Licensed content publication | Energy & Environmental Science |
| Licensed content title | New insights into the electrochemical reduction of carbon dioxide on metallic copper surfaces |
| Licensed content author | Kendra P. Kuhl,Etosha R. Cave,David N. Abram,Thomas F. Jaramillo |
| Licensed content date | Feb 24, 2012 |
| Volume number | 5 |
| Issue number | 5 |
| Type of Use | Thesis/Dissertation |
| Requestor type | academic/educational |
| Portion | figures/tables/images |
| Number of figures/tables /images | 2 |
| Format | print and electronic |
| Distribution quantity | 7 |
| Will you be translating? | no |
| Order reference number | None |
| Title of the thesis/dissertation | Electrochemical Reduction of CO2 on Supported Cu2O Catalysts |
| Expected completion date | Nov 2014 |
| Estimated size | 140 |
| Total | 0.00 USD |

Terms and Conditions

This License Agreement is between {Requestor Name} ("You") and The Royal Society of Chemistry ("RSC") provided by the Copyright Clearance Center ("CCC"). The license consists of your order details, the terms and conditions provided by the Royal Society of Chemistry, and the payment terms and conditions.

RSC / TERMS AND CONDITIONS

## ROYAL SOCIETY OF CHEMISTRY LICENSE TERMS AND CONDITIONS

Sep 24, 2014

This is a License Agreement between Joel Bugayong ("You") and Royal Society of Chemistry ("Royal Society of Chemistry") provided by Copyright Clearance Center ("CCC"). The license consists of your order details, the terms and conditions provided by Royal Society of Chemistry, and the payment terms and conditions.

**All payments must be made in full to CCC. For payment instructions, please see information listed at the bottom of this form.**

| | |
|---|---|
| License Number | 3456251337487 |
| License date | Aug 25, 2014 |
| Licensed content publisher | Royal Society of Chemistry |
| Licensed content publication | Journal of the Chemical Society, Faraday Transactions 1: Physical Chemistry in Condensed Phases |
| Licensed content title | Formation of hydrocarbons in the electrochemical reduction of carbon dioxide at a copper electrode in aqueous solution |
| Licensed content author | Yoshio Hori,Akira Murata,Ryutaro Takahashi |
| Licensed content date | Dec 31, 1969 |
| Volume number | 85 |
| Issue number | 8 |
| Type of Use | Thesis/Dissertation |
| Requestor type | academic/educational |
| Portion | figures/tables/images |
| Number of figures/tables /images | 3 |
| Format | print and electronic |
| Distribution quantity | 7 |
| Will you be translating? | no |
| Order reference number | None |
| Title of the thesis/dissertation | Electrochemical Reduction of CO2 on Supported Cu2O Catalysts |
| Expected completion date | Nov 2014 |
| Estimated size | 140 |
| Total | 0.00 USD |
| Terms and Conditions | |

## ROYAL SOCIETY OF CHEMISTRY LICENSE TERMS AND CONDITIONS

Sep 24, 2014

This is a License Agreement between Joel Bugayong ("You") and Royal Society of Chemistry ("Royal Society of Chemistry") provided by Copyright Clearance Center ("CCC"). The license consists of your order details, the terms and conditions provided by Royal Society of Chemistry, and the payment terms and conditions.

**All payments must be made in full to CCC. For payment instructions, please see information listed at the bottom of this form.**

| | |
|---|---|
| License Number | 3456290752570 |
| License date | Aug 26, 2014 |
| Licensed content publisher | Royal Society of Chemistry |
| Licensed content publication | Chemical Science |
| Licensed content title | A new mechanism for the selectivity to C1 and C2 species in the electrochemical reduction of carbon dioxide on copper electrodes |
| Licensed content author | K. J. P. Schouten,Y. Kwon,C. J. M. van der Ham,Z. Qin,M. T. M. Koper |
| Licensed content date | Jul 21, 2011 |
| Volume number | 2 |
| Issue number | 10 |
| Type of Use | Thesis/Dissertation |
| Requestor type | academic/educational |
| Portion | figures/tables/images |
| Number of figures/tables /images | 1 |
| Format | print and electronic |
| Distribution quantity | 7 |
| Will you be translating? | no |
| Order reference number | None |
| Title of the thesis/dissertation | Electrochemical Reduction of CO2 on Supported Cu2O Catalysts |
| Expected completion date | Nov 2014 |
| Estimated size | 140 |
| Total | 0.00 USD |
| Terms and Conditions | |

## JOHN WILEY AND SONS LICENSE TERMS AND CONDITIONS

Sep 24, 2014

This is a License Agreement between Joel Bugayong ("You") and John Wiley and Sons ("John Wiley and Sons") provided by Copyright Clearance Center ("CCC"). The license consists of your order details, the terms and conditions provided by John Wiley and Sons, and the payment terms and conditions.

**All payments must be made in full to CCC. For payment instructions, please see information listed at the bottom of this form.**

| | |
|---|---|
| License Number | 3456291307793 |
| License date | Aug 26, 2014 |
| Licensed content publisher | John Wiley and Sons |
| Licensed content publication | Angewandte Chemie International Edition |
| Licensed content title | Selectivity of CO2 Reduction on Copper Electrodes: The Role of the Kinetics of Elementary Steps |
| Licensed copyright line | Copyright © 2013 WILEY-VCH Verlag GmbH & Co. KGaA, Weinheim |
| Licensed content author | Xiaowa Nie,Monica R. Esopi,Michael J. Janik,Aravind Asthagiri |
| Licensed content date | Jan 23, 2013 |
| Start page | 2459 |
| End page | 2462 |
| Type of use | Dissertation/Thesis |
| Requestor type | University/Academic |
| Format | Print and electronic |
| Portion | Figure/table |
| Number of figures/tables | 1 |
| Original Wiley figure/table number(s) | Scheme 1 |
| Will you be translating? | No |
| Title of your thesis / dissertation | Electrochemical Reduction of CO2 on Supported Cu2O Catalysts |
| Expected completion date | Nov 2014 |
| Expected size (number of pages) | 140 |
| Total | 0.00 USD |
| Terms and Conditions | |

COPYRIGHT PERMISSION REQUEST FORM

Date: August 25 2014

To: The Chemical Society of Japan
5,Kanda-Surugadai,Chiyoda-ku,
Tokyo 101-8307, Japan

Fax: +81-3-3292-6318
E-mail: info@chemistry.or.jp

From: Joel Nino G. Bugayong
W339 Chemical Engineering Bldg.
Louisiana State University
South Stadium Drive,
Baton Rouge, LA, USA, 70803

Phone: 765-714-7882
Fax: 225-578-1476
E-mail: jbugay1@lsu.edu

I am preparing a paper entitled:

Electrochemical Reduction of $CO_2$ on Supported $Cu_2O$ Catalysts

to appear in

Ph.D. Dissertation

which is published by

Louisiana State University Graduate School

Expected publication date: November 2014

I request your permission to include the following material in this and in all subsequent editions of this work to be published by Joel Nino G Bugayong or its licensees for distribution throughout the world, in all media including electronic/online and microfilm.

Title of Publication: Potential Dependencies of the Products on Electrochemical Reduction of Carbon Dioxide at a Copper Electrode

Author(s)/Editor(s): Hidetomo NODA, Shoichiro IKEDA, Yoshiyuki ODA and Kaname ITO

Title of Selection: Chemistry Letters

Year: 1989 Vol.: 18 No.: 2

Figure(s)/Table(s): 1, 2 and 3 Page(s): 291-292

---

We hereby grant permission for the use of the material requested above.

Nobuyuki Kawashima
Executive Director
The Chemical Society of Japan

Date: August. 26. 2014

Our Ref. No. CY-RT 14 - 224

**CAMBRIDGE UNIVERSITY PRESS LICENSE**
**TERMS AND CONDITIONS**

Oct 27, 2014

This is a License Agreement between Joel Bugayong ("You") and Cambridge University Press ("Cambridge University Press") provided by Copyright Clearance Center ("CCC"). The license consists of your order details, the terms and conditions provided by Cambridge University Press, and the payment terms and conditions.

**All payments must be made in full to CCC. For payment instructions, please see information listed at the bottom of this form.**

| | |
|---|---|
| License Number | 3497391045498 |
| License date | Oct 27, 2014 |
| Licensed content publisher | Cambridge University Press |
| Licensed content publication | MRS Online Proceedings Library |
| Licensed content title | Electrochemical Reduction of $CO_2$ using Supported $Cu_2O$ Catalysts |
| Licensed content author | Joel Bugayong and Gregory L. Griffin |
| Licensed content date | Jun 28, 2013 |
| Volume number | 1542 |
| Issue number | -1 |
| Start page | 0 |
| End page | 0 |
| Type of Use | Dissertation/Thesis |
| Requestor type | Author |
| Portion | Full article |
| Author of this Cambridge University Press article | Yes |
| Author / editor of the new work | Yes |
| Order reference number | None |
| Territory for reuse | World |
| Title of your thesis / dissertation | Electrochemical Reduction of CO2 on Supported Cu2O Catalysts |
| Expected completion date | Nov 2014 |
| Estimated size(pages) | 140 |
| Billing Type | Invoice |
| Billing address | W209 Chem Engg Bldg S Stadium Dr<br>Baton Rouge, LA 70803<br>United States |
| TAX (0.00%) | 0.00 USD |
| Total | 0.00 USD |

Terms and Conditions

# CAMBRIDGE UNIVERSITY PRESS LICENSE TERMS AND CONDITIONS

Oct 27, 2014

This is a License Agreement between Joel Bugayong ("You") and Cambridge University Press ("Cambridge University Press") provided by Copyright Clearance Center ("CCC"). The license consists of your order details, the terms and conditions provided by Cambridge University Press, and the payment terms and conditions.

**All payments must be made in full to CCC. For payment instructions, please see information listed at the bottom of this form.**

| | |
|---|---|
| License Number | 3497390558356 |
| License date | Oct 27, 2014 |
| Order Content Publisher | Cambridge University Press |
| Order Content Publication | MRS Online Proceedings Library |
| Order Content Title | Electrochemical Reduction of $CO_2$ using Copper Oxide Nanoparticles supported on Glassy Carbon Electrodes |
| Order Content Author | Gregory L. Griffin and Joel Bugayong |
| Order Content Date | Jun 9, 2014 |
| Volume number | 1677 |
| Issue number | -1 |
| Start page | 0 |
| End page | 0 |
| Type of Use | Dissertation/Thesis |
| Requestor type | Author |
| Portion | Full article |
| Author of this Cambridge University Press article | Yes |
| Author / editor of the new work | Yes |
| Order reference number | None |
| Territory for reuse | World |
| Title of your thesis / dissertation | Electrochemical Reduction of CO2 on Supported Cu2O Catalysts |
| Expected completion date | Nov 2014 |
| Estimated size(pages) | 140 |
| Billing Type | Invoice |
| Billing address | W209 Chem Engg Bldg S Stadium Dr<br>Baton Rouge, LA 70803<br>United States |
| TAX (0.00%) | 0.00 USD |
| **Total** | **0.00 USD** |

**CAMBRIDGE UNIVERSITY PRESS LICENSE**
**TERMS AND CONDITIONS**

Oct 27, 2014

This is a License Agreement between Joel Bugayong ("You") and Cambridge University Press ("Cambridge University Press") provided by Copyright Clearance Center ("CCC"). The license consists of your order details, the terms and conditions provided by Cambridge University Press, and the payment terms and conditions.

**All payments must be made in full to CCC. For payment instructions, please see information listed at the bottom of this form.**

| | |
|---|---|
| License Number | 3497390708087 |
| License date | Oct 27, 2014 |
| Licensed content publisher | Cambridge University Press |
| Licensed content publication | MRS Online Proceedings Library |
| Licensed content title | Role of Surface Oxide Layer during $CO_2$ Reduction at Copper Electrodes |
| Licensed content author | Cheng-Chun Tsai, Joel Bugayong and Gregory L. Griffin |
| Licensed content date | Jul 11, 2012 |
| Volume number | 1446 |
| Issue number | -1 |
| Start page | 0 |
| End page | 0 |
| Type of Use | Dissertation/Thesis |
| Requestor type | Author |
| Portion | Full article |
| Author of this Cambridge University Press article | Yes |
| Author / editor of the new work | Yes |
| Order reference number | None |
| Territory for reuse | World |
| Title of your thesis / dissertation | Electrochemical Reduction of CO2 on Supported Cu2O Catalysts |
| Expected completion date | Nov 2014 |
| Estimated size(pages) | 140 |
| Billing Type | Invoice |
| Billing address | W209 Chem Engg Bldg S Stadium Dr<br>Baton Rouge, LA 70803<br>United States |
| TAX (0.00%) | 0.00 USD |
| Total | 0.00 USD |
| Terms and Conditions | |

## Request for Permission to Reproduce or Re-Publish ECS Material

**Please fax this form to**: The Electrochemical Society (ECS). Attn: Permissions Requests. 1.609.730.0629. You may also e-mail your request to: copyright@electrochem.org. Include all the information as required on this form. Please allow 3-7 days for your request to be processed.

I am preparing a (choose one): ☐ paper ☐ chapter ☐ book ☑ thesis

entitled: ELECTROCHEMICAL REDUCTION OF CO2 ON SUPPORTED Cu2O CATALYSTS

to be published by: Joel Nino G Bugayong

in an upcoming publication entitled: LSU Electronic Thesis and Dissertation

I request permission to use the following material in the publication noted above, and request nonexclusive rights for all subsequent editions and in all foreign language translations for distribution throughout the world.

**Description of material to be used**—Indicate what material you wish to use (figures, tables, text, etc.) and give the full bibliographic reference for the source publication. You may attach a separate list, organized by ECS title.

Full Article of Bugayong, J. and G.L. Griffin. 2013. "Electrochemical Reduction of CO2 using Supported Cu2O Nanoparticles," Electrochemical Synthesis of Fuels 2, Electrochemical Society Transactions 58 (2): 81-89.

Signature: Joel Nino Bugayong Digitally signed by Joel Nino Bugayong DN: cn=Joel Nino Bugayong, o, ou, email=jbugay1@lsu.edu, c=US Date: 2014.10.27 22:00:32 -05'00' Date: October 27, 2014

Name: Joel Nino Bugayong

Address: W339 Chemical Engineering Bldg South Stadium Drive Baton Rouge LA 70803

Telephone: 7657147882 Fax:

E-mail: jbugay1@lsu.edu

Permission is granted to reproduce the above-referenced material. Please acknowledge the author(s) and publication data of the original material, and include the words: "Reproduced by permission of The Electrochemical Society."

10/30/14
Date

John Lewis, Associate Director of Publications

Joel Bugayong <jbugay1@tigers.lsu.edu>

## permission to reproduce content

3 messages

**Joel Bugayong** <jbugay1@tigers.lsu.edu> Thu, Oct 30, 2014 at 11:01 AM
To: Narasi.Sridhar@dnv.com, Davion.M.Hill@dnv.com

Dear Sridhar and Hill,

Greetings from Louisiana.

I would like to obtain your permission to reproduce Figure 2 from your paper in 2011 on:

"Carbon Dioxide Utilization Electrochemical Conversion of CO2 – Opportunities and Challenges."

I will be using this figure for my Ph.D dissertation.

Thank you for your attention. I look forward to hearing from you.

Sincerely yours,

Joel

---

**Sridhar, Narasi** <Narasi.Sridhar@dnvgl.com> Thu, Oct 30, 2014 at 12:26 PM
To: Joel Bugayong <jbugay1@tigers.lsu.edu>, "Hill, Davion M." <Davion.M.Hill@dnvgl.com>

Yes, you may do so with proper attribution. Thank you.

Best regards

Sridhar

**Dr. Narasi Sridhar, FNACE**

**Director, Materials and Sensors Program**
**DNV GL - Strategic Research & Innovation**

E-mail narasi.sridhar@dnvgl.com
Mobile +1 614 787 8249 | Direct +1 614 761 6920| Fax +1 614 761 1633

**From:** Joel Bugayong [mailto:jbugay1@tigers.lsu.edu]
**Sent:** Thursday, October 30, 2014 12:01 PM
**To:** Sridhar, Narasi; Hill, Davion M.
**Subject:** permission to reproduce content

[Quoted text hidden]



**Joel Bugayong** <jbugay1@tigers.lsu.edu> Thu, Oct 30, 2014 at 12:31 PM
To: "Sridhar, Narasi" <Narasi.Sridhar@dnvgl.com>

Thank you very much Dr. Sridhar!

[Quoted text hidden]

# VITA

Joel, a graduate student from the Philippines, is in the process of completing his Ph.D. degree in Chemical Engineering at Louisiana State University (LSU). He is married to Dr. Patrisha. They are expecting a baby boy around December of 2014 and will be given the name Lorenzo Theodore.

Joel earned his Bachelor's degree in Chemical Engineering at the University of the Philippines Los Baños (UPLB) in 2004 with the distinction *magna cum laude* and *#1 ranking* from the engineering class of 175 students. While in college, he participated in a study abroad program at Michigan State University in spring of 2002 where he experienced his first ever snow. After college, he taught at the UPLB Institute of Chemistry as an Instructor for 2 ½ years. He then pursued further studies in the United States where he finished his Master's degree in Chemical Engineering at LSU in 2011.

Joel is a lifetime member of the Phi Kappa Phi Honor Society and received the Phi Kappa Phi Award of Excellence in 2007 and the Chevron Engineering Graduate Assistantship Supplement Award in 2014. His interests include catalysis, renewable energy, electrochemical processes, separation methods, interface phenomena, semiconductor device fabrication, analytical techniques and teaching.

During his free time, he was actively engaged in both on campus and off campus volunteer works. Among his most memorable participations were during the grass planting activities at the Barataria Waterway in Lafitte, Louisiana in August of 2010 and at the Bayou Sauvage National Wildlife Refuge in Lacombe, Louisiana in May of 2011. In those activities, he was half submerged in muddy swamp.